KERNFORSCHUNGSZENTRUM

KARLSRUHE

September 1976

KFK 2357

Institut für Angewandte Kernphysik

# Progress Report of the Teilinstitut Nukleare Festkörperphysik
# 1. 6.1975 — 31. 5.1976

Editor: G. Heger

GESELLSCHAFT
FÜR
KERNFORSCHUNG M.B.H.

KARLSRUHE

GESELLSCHAFT FÜR KERNFORSCHUNG M. B. H.
KARLSRUHE

KERNFORSCHUNGSZENTRUM KARLSRUHE

KFK 2357

Institut für Angewandte Kernphysik

# PROGRESS REPORT

of the

Teilinstitut Nukleare Festkörperphysik

1.6.1975 - 31.5.1976

Editor: G. Heger

Gesellschaft für Kernforschung mbH., Karlsruhe

Wir danken Frau J. Steigleder für die umfangreichen Schreibarbeiten im Zusammenhang mit diesem Report.

This progress report of the Teilinstitut Nukleare Festkörperphysik covers the period from 1st June 1975 - 31st May 1976. The arrangement has been chosen to emphasis the main areas of research in which the institute is presently involved.
These areas are Dynamics of Solids and Liquids, Electronic Structure and Magnetism of Solids and Development of Materials. Some of the technical developments relevant to these topics are also included.

Dieser Progress-Report des Teilinstituts Nukleare Festkörperphysik erfaßt den Zeitraum vom 1. Juni 1975 - 31. Mai 1976. Die Darstellung betont die Hauptforschungsgebiete, auf denen das Institut zur Zeit tätig ist. Diese sind: Dynamik von Festkörpern und Flüssigkeiten, Elektronenstruktur und Magnetismus von Festkörpern und die Entwicklung neuer Materialien. Einige technische Entwicklungen, die für die Forschungsarbeiten wichtig sind, wurden ebenfalls in den Bericht aufgenommen.

In dem vorliegenden Bericht gibt das Teilinstitut IAK I "Nukleare Festkörperphysik" einen Überblick über die wissenschaftlichen Arbeiten in dem Zeitraum vom 1. Juni 1975 bis 31. Mai 1976. Das Forschungsprogramm des Instituts hat derzeit folgende drei Hauptrichtungen:

- Untersuchungen zur Struktur und Dynamik von kondensierter Materie

- Untersuchungen der elektronischen und magnetischen Eigenschaften von Festkörpern

- Herstellung neuer Materialien mittels Ionenimplantation, Kathodenzerstäubung und simultanem Aufdampfen.

Mit den Methoden der Neutronenspektroskopie werden am Forschungsreaktor FR2 in Karlsruhe und am Hochflußreaktor in Grenoble Experimente zur Bestimmung der Phononendispersion und Phononenzustandsdichten von Festkörpern sowie der Streugesetze von Flüssigkeiten durchgeführt. Zur Zeit stehen Untersuchungen an supraleitenden Materialien im Vordergrund. Hierdurch soll ein Beitrag zum besseren Verständnis der Wechselwirkung zwischen gitterdynamischen und supraleitenden Eigenschaften von Festkörpern geleistet werden. Von besonderem Interesse ist ferner das Studium der Dynamik von eindimensionalen metallischen Systemen.

Bei den Untersuchungen von elektronischen und magnetischen Eigenschaften von Festkörpern werden die Methoden der $^{61}$Ni-Mößbauerspektroskopie und der Neutronenstreuung eingesetzt, um Information über Hyperfeinfelder, Spindichteverteilungen und magnetische Anregungen zu erhalten. Es wird hier die Möglichkeit genutzt, die sehr kurzlebigen $^{61}$Ni-Quellen am Zyklotron des Kernforschungszentrums herzustellen. Daher werden zur Zeit vorwiegend Verbindungen und Legierungen des Nickels untersucht.

Die Methoden der Ionenimplantation, Kathodenzerstäubung und des simultanen Aufdampfens werden derzeit ausschließlich zur Herstellung von Supraleitern und zur gezielten Veränderung ihrer supraleitenden Eigenschaften eingesetzt. Im Rahmen dieses Programms werden auch Fragen der Strahlenschädigung untersucht. Als wichtiges Hilfsmittel für die Charakterisierung der hergestellten Materialien dient die He-Rückstreutechnik. Diese Arbeiten werden am Van-de-Graaff Beschleuniger des Institutes durchgeführt.

Die experimentellen Arbeiten werden durch eine kleine Theoriegruppe unterstützt, die sich zur Zeit vorwiegend mit Fragen der Elektron-Phonon Wechselwirkung sowie der Dynamik von Festkörpern und Flüssigkeiten beschäftigt.

Das Institut betrachtet es als eine wesentliche Aufgabe, auswärtige Forschungsgruppen bei der Nutzung der Experimentiereinrichtungen am Reaktor FR2 zu unterstützen. Ein Mitarbeiter ist nahezu ausschließlich für die Betreuung von Gastgruppen bei der Durchführung von Experimenten an zwei Strukturspektrometern des FR2 eingesetzt. Experimente zur unelastischen Neutronenstreuung erfolgen häufig auf der Basis einer Zusammenarbeit. Insbesondere werden Experimente vorbereitet, die anschließend am Hochflußreaktor in Grenoble weitergeführt werden.

Das IAK I hat zur Zeit 22 wissenschaftlich-technische Mitarbeiter. Dies bedeutet einen Rückgang um 4 Mitarbeiter gegenüber dem Vorjahr, wodurch hauptsächlich die Arbeiten auf dem Gebiet der Neutronenstreuung beeinträchtigt wurden.

Der größte Teil der Arbeiten zur elastischen Neutronenstreuung von Gastgruppen erfolgt außerhalb des Forschungsprogramms des IAK I und wird daher in dem vorliegenden Bericht nicht berücksichtigt.

Von den Arbeiten, die bereits veröffentlicht bzw. zur Veröffentlichung eingereicht sind, werden nur Kurzfassungen oder Literaturhinweise angegeben. Erste Ergebnisse von laufenden Arbeiten werden dagegen etwas ausführlicher beschrieben.

# CONTENTS

## 1. INVESTIGATIONS ON THE DYNAMICS OF SOLIDS AND LIQUIDS

Investigations of the Perovskite-Type Layer Structures $(C_nH_{2n+1}NH_3)_2MnCl_4$ with n = 1, 2

## 2. ELECTRONIC STRUCTURE AND MAGNETISM OF SOLIDS

## 3. MATERIALS RESEARCH

## 4. DATA PROCESSING

## 5. DEVELOPMENT OF MEASURING DEVICES AND TECHNIQUES

6. PUBLICATIONS, CONFERENCE CONTRIBUTIONS AND SEMINARS

# 1. INVESTIGATIONS ON THE DYNAMICS OF SOLIDS AND LIQUIDS

## 1.1. Phonon Dispersion of Titanium Carbide

*L. Pintschovius and W. Reichardt*

Our study of the phonon dispersion of TiC /1/ has been completed last year, mainly by measurements on the triple-axis spectrometer IN1 at the HFR in Grenoble.

Our results are in good accordance with the experimentally determined phonon density of states of TiC$_{.98}$ /2/ (see Fig. 1). As has been expected the dispersion of TiC looks similar to that of ZrC, in particular it does not exhibit any anomalies and is very well described by a shell model. The large splitting of the optical modes is another characteristic of a non-superconducting representative of these materials. Furthermore the concentration dependence of the acoustic frequencies is much smaller than in the case of the superconductor NbC$_x$, whereas the concentration dependence of the optic modes is approximately the same in both cases: With decreasing carbon content the lowest frequencies are lifted while the highest frequencies remain essentially unaffected.

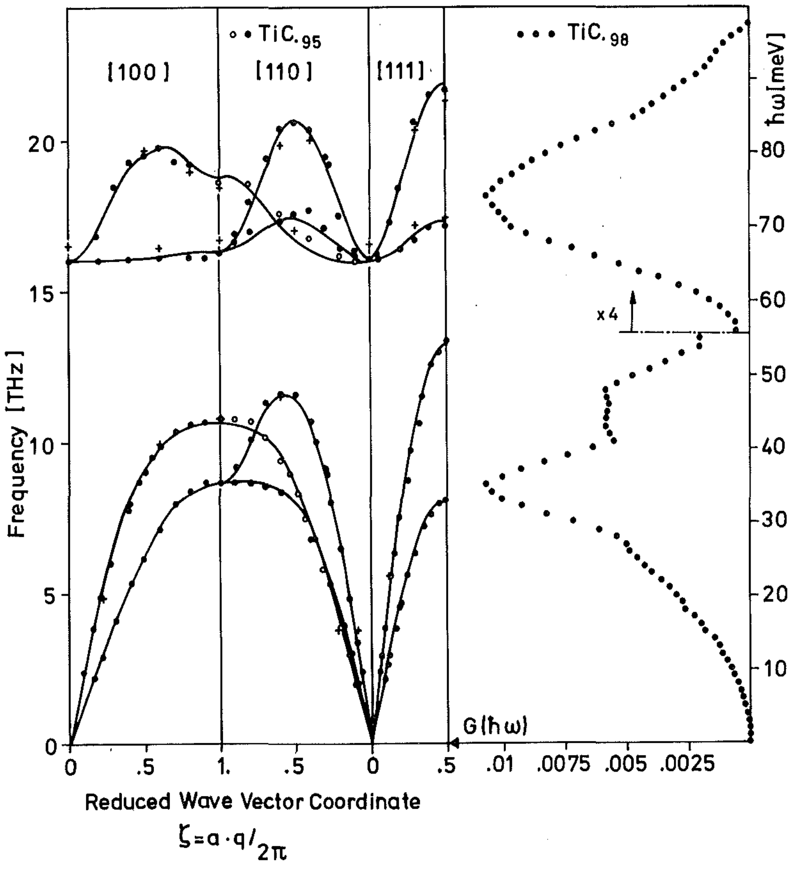

Fig. 1. Phonon dispersion of TiC$_{.95}$ (circles) and TiC$_{.98}$ (crosses). The solid lines are the result of a fit on the basis of a shell model for TiC$_{.95}$. For a comparison the experimentally determined phonon density of states of TiC$_{.98}$ is plotted on the right side.

Table I Experimental and calculated /3/ differences between the velocities of sound of $TiC_{.95}$ and $TiC_{.89}$.

| Phonon branch | $(C_{TiC_{.95}}/C_{TiC_{.89}} - 1) \cdot 100$ | |
|---|---|---|
| | experimental | calculated |
| LA [100] | 3.5 ± 1 | 2.2 |
| TA [100] | 0.5 ± 1 | 0 |
| LA [110] | 0 ± 3 | 1.0 |
| $TA_1$ [110] | 0 ± 1 | 0 |
| LA [111] | 0 ± 2 | 1.5 |
| TA [111] | 3 ± 1 | 2.5 |

The dependence of the acoustic frequencies on the carbon concentration has been calculated by Splettstößer and Leibfried /3/ for both $TiC_x$ and $NbC_x$ (see also p. X). However, up to now quantitative predictions are given only for $TiC_x$ which is the simpler case. They are in fair agreement with our experimental results as can be seen from a compairson of calculated and measured shifts of the velocities of sound (Tab. I). Moreover theory and experiment agree that the frequencies at the zone boundary are not dependent on the carbon content.

Table II Parameters of the screened shell model for $TiC_{.95}$ (force constants in units of $e^2/2r_o^3$, charge in units of e, $k_S$ and $k_F$ in units of $2\pi/a$). For a comparison Weber's results for ZrC and HfC are given.

| | $TiC_{.95}$ | ZrC | HfC |
|---|---|---|---|
| A(12) | 25.31 | 23.82 | 22.5 |
| B(12) | .65 | 3.47 | 4.6 |
| A'(22) | 8.09 | 10.02 | 13.08 |
| B'(22) | -3.02 | -1.02 | -1.77 |
| C'(22) | 1.41 | -1.02 | -1.77 |
| Z | -1.03 | -1.08 | -1.08 |
| $Y_1$ | 3.41 | 0 | 0 |
| $Y_2$ | -.46 | -2 | -1.3 |
| $K_1$ | 760 | 309 | 180 |
| $K_2$ | 107.3 | 123.5 | 107 |
| $k_F$ | .318 | .4 | .4 |
| $k_S$ | .509 | .4 | .4 |

The model mentioned above is the screened shell model which was used by Weber /5/ to analyse the dispersion relation of HfC and ZrC. We tried to fit our data by varying 8 parameters (A(12), B(12), A'(22), B'(22) = C'(22), Z, $Y_2$, $k_1$, $k_2$), while for $Y_1$, $k_F$ and $k_S$ the values given by Weber for other refractory carbides were used. However, these results were not quite satisfactory and the variation of all twelve parameters listed in Tab. II improved the fit considerably.

A part of these results has been presented at the Conference on Neutron Scattering in Gatlinburg /4/.

## REFERENCES

/1/ L. Pintschovius and W. Reichardt, in Progress Report of the Teilinstitut Nukleare Festkörperphysik, Ges. f. Kernforschung Karlsruhe (KFK 2183) p. 6 (1975).

/2/ F. Gompf and W. Reichardt, this report.

/3/ B. Splettstößer and W. Leibfried, to be published.

/4/ F. Gompf, L. Pintschovius, W. Reichardt and B. Scheerer, in Proc. of the Intern. Conf. on Neutron Scattering, Gatlinburg (USA), June 1976, in press.

/5/ W. Weber, Phys. Rev. B8, 5082 (1973).
Thesis, München (1972).

## 1.2. Lattice Dynamics of Vanadium Carbide

*L. Pintschovius, W. Reichardt and B. Scheerer*

VC has 9 valence electrons and therefore is expected to become superconducting at $T_c \gtrsim 5$ K like other transition metal carbides and nitrides with 9 valence electrons, e.g. NbC and TiN. Indeed superconductivity has been observed recently in VC but the maximum $T_c$ was only 2.3 K /1/. These samples have been prepared by ion implantation to get a stoichiometric compound. Chemical methods invariably lead to samples whose content of carbon vacancies is at least 11 % which in contrast to the case of $NbC_{.89}$ do not show superconductivity. Therefore a single crystal neutron scattering study has to be performed on a non-superconducting specimen. Nevertheless from our knowledge of the system $NbC_x$ we expect to be able to show whether the lattice dynamics of VC are similar to the superconducting or the non-superconducting representatives of the transition metal carbides.

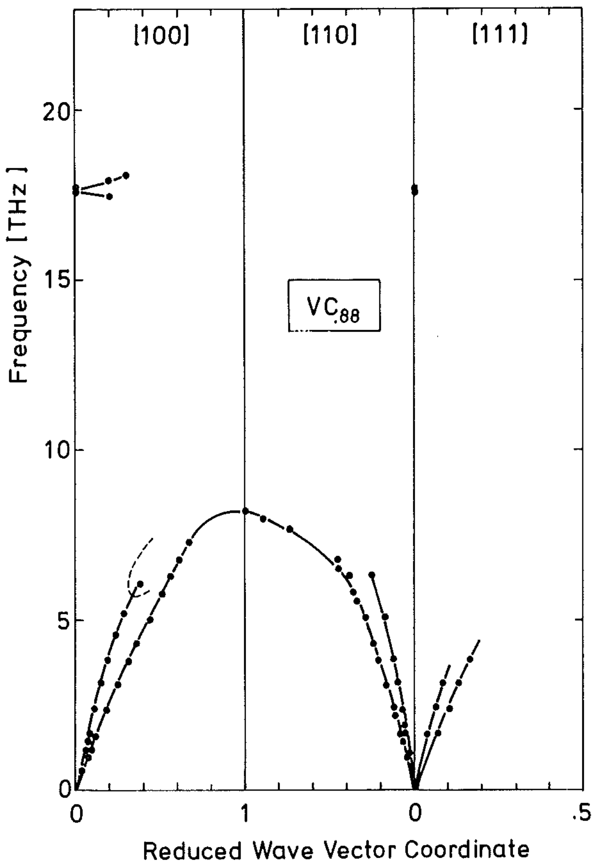

Fig. 1. Phonon dispersion of $VC_{.88}$

Our crystal was grown by the floating zone melting technique /2/ and has a volume of ca. 1 $cm^3$. Its composition was determined by chemical methods to be $VC_{.873}$. Unfortunately the measurements of the acoustic branches are particularly difficult due to the fact that the scattering from the vanadium atoms is almost completely incoherent and that the amplitudes of carbon atoms are small for these modes. Especially in those regions in q-space where the superconducting carbides show large anomalies in their dispersion relation the coherent scattering cross section is extremely small.

Therefore up to now only two branches could be followed to the zone boundary (see Fig. 1). As has been expected the TA branch in [100]-direction does not exhibit any anomaly. At a first glance this seems to be true also for the TA branch in [110]-direction but when compared to the same branch in TiC it shows a reminiscence of the anomaly which has been observed in the superconducting refractory carbides. For a comparison Fig. 2 shows the results for $NbC_x$ with different carbon concentrations after rescaling the frequencies to account for the differences in atomic mass between Nb and V.

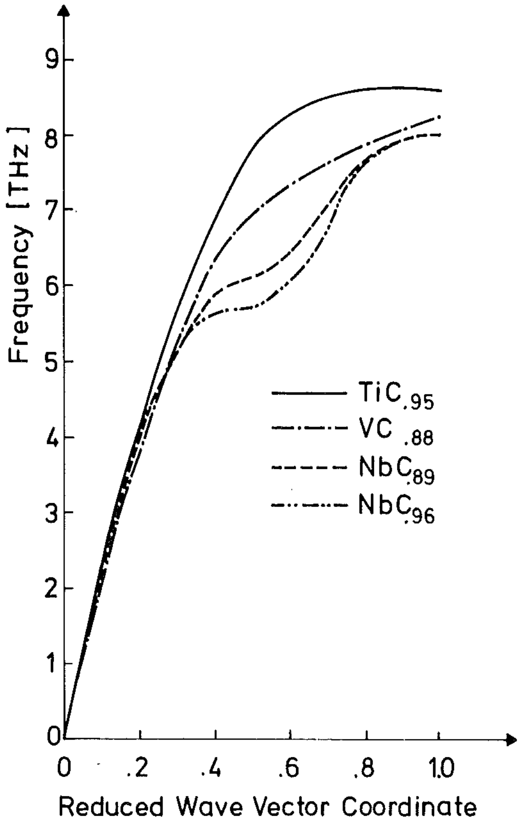

Fig. 2. Comparison of the TA (110) branch with polarisation $\vec{e}$ = (110) for $TiC_{.95}$, $VC_{.88}$, $NbC_{.89}$ and $NbC_{.96}$. The frequencies of $NbC_x$ are rescaled to account for the differences in atomic mass between Nb and V.

The few points yet measured of the optical dispersion suggest a rather small splitting of the optical branches what is typical for the superconducting carbides.

Thus we draw the preliminary conclusions that the lattice dynamics of VC are different from those of the non-superconducting carbides but these differences are much smaller than in the case of other carbides with higher $T_c$.

These investigations will be continued at the HFR Grenoble in the near future.

REFERENCES

/1/ K.-G. Langguth and O. Meyer, this report.

/2/ B. Scheerer, in Progress Report of the Teilinstitut Nukleare Festkörperphysik, Ges. f. Kernforschung Karlsruhe (KFK 2183), p. 89 (1975).

## 1.3. Lattice Dynamics of Non-Stoichiometric Niobium Carbide

*L. Pintschovius, W. Reichardt and R. Currat*[(a)]

[(a)] Institut Laue-Langevin, Grenoble, France

Our investigations on the lattice dynamics of $NbC_{.89}$ /1/ have been completed by measurements on the triple-axis spectrometers IN8 at the HFR in Grenoble and TAS1 at the FR2 in Karlsruhe.

The main result of the measurements at Grenoble is plotted in Fig. 1 which shows the intensity contours of the longitudinal phonon in [100]-direction . The intensity values have been corrected for the energy - and q-dependent factors of the differential cross section (except the structure factor) and for the luminosity of the spectrometer, but not for resolution effects.

From linewidths measurements of the Bragg reflections on a high resolution diffractometer we could ensure that the large linewidths are not due to inhomogeneities of the carbon concentration. Recently Splettstößer and Leibfried /2/ tried to explain the line shapes using a simplified version of the double shell

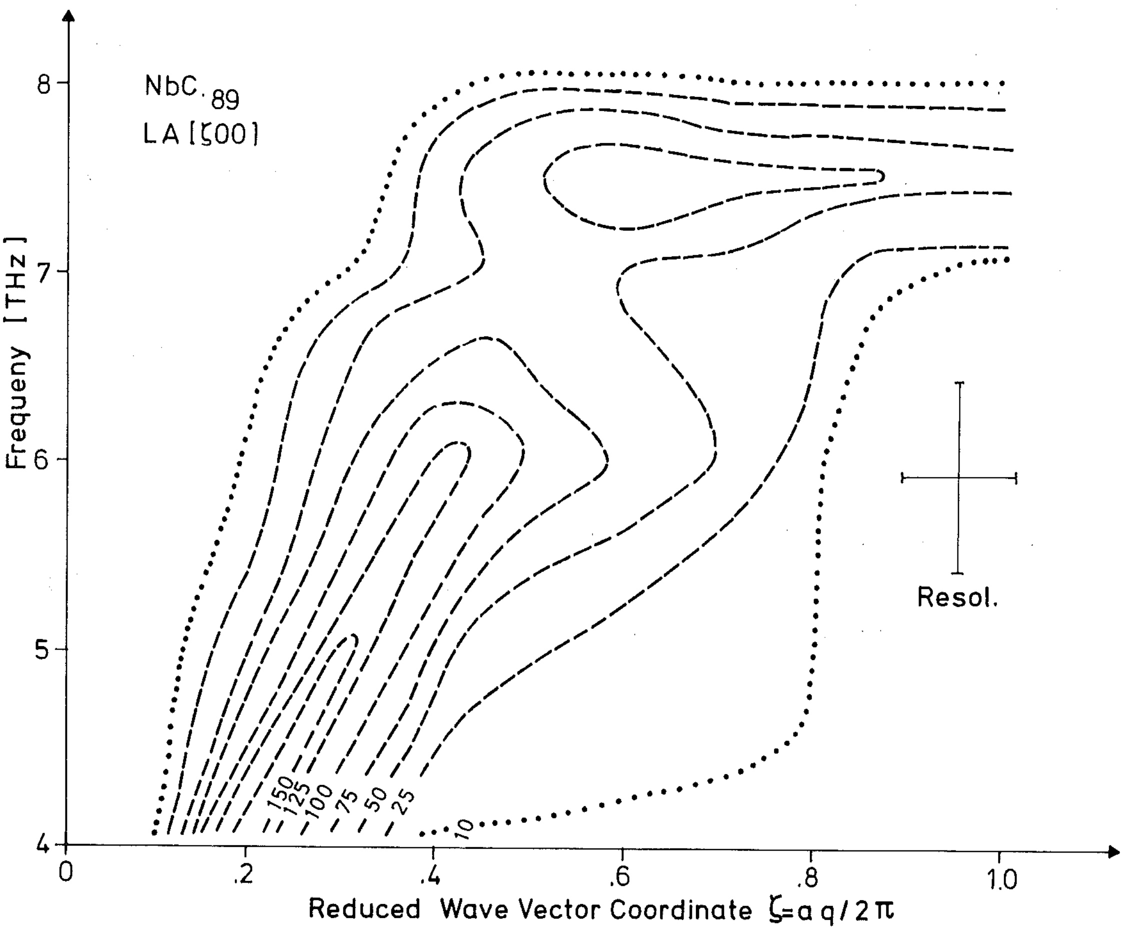

Fig. 1. Normalized intensity contours of the neutron scattering from the excitations of wave vector $\vec{q}$ = (ξ,0,0) and polarization $\vec{e}$ = (1,0,0). The background has been substracted.

model of Weber /3/ and the Single T-matrix Approximation. Their results seem to be qualitatively correct but further investigations are necessary to draw final conclusions.

The optical dispersion has been measured at the FR2 using incident energies up to 130 meV and a sample consisting of two co-aligned crystals with a total volume of 2 $cm^3$. As the optical branches are rather flat the large mosaic spread ( ≈ 1.5 $^{o}$) of the second crystal which was not used before did not affect the results significantly.

Fig. 2 shows the experimental data of both the acoustic and optical region and a fit based on the double shell model of Weber /3/.

A short summary of our results has been presented at the conference on neutron scattering at Gatlinburg /5/.

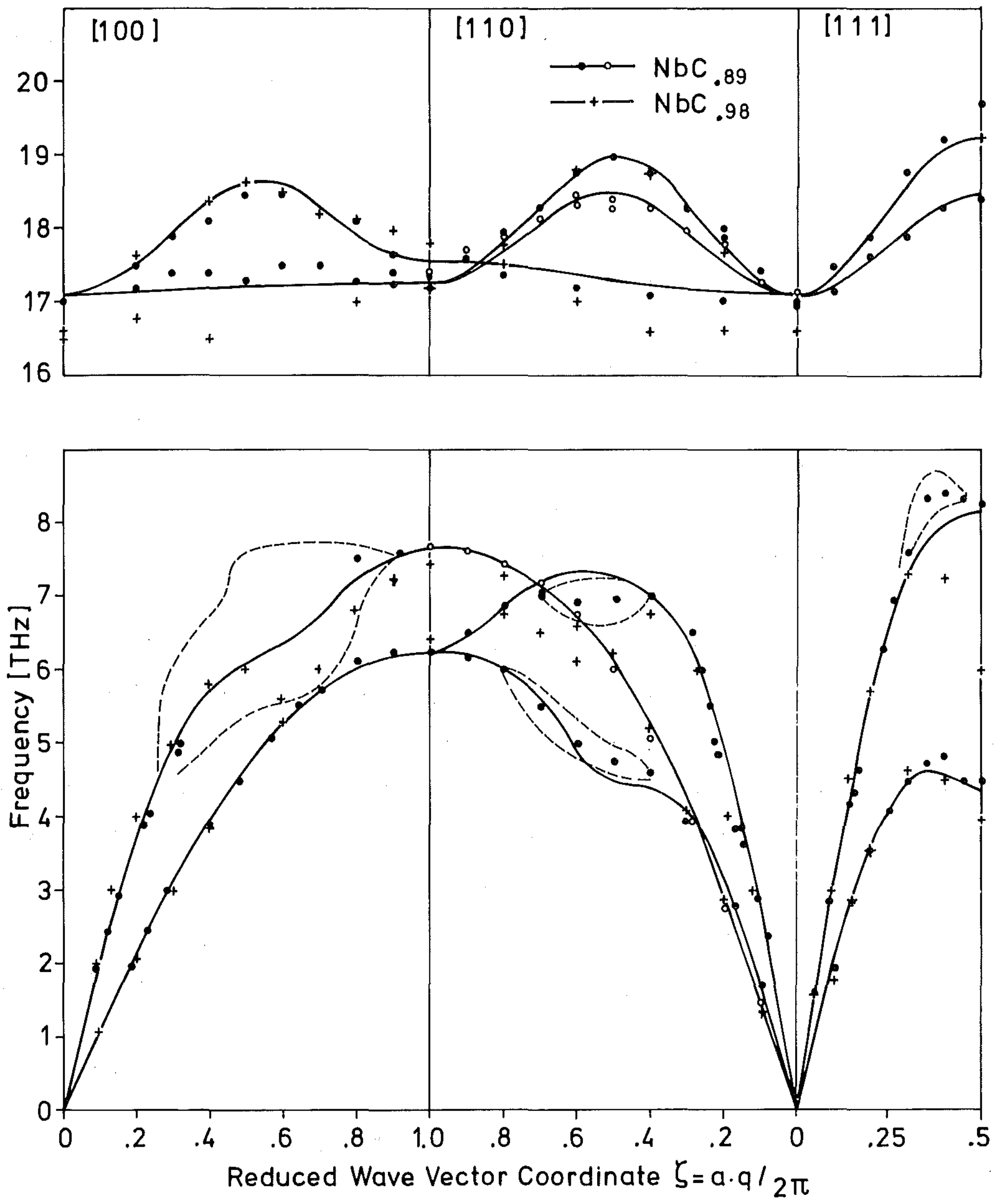

Fig. 2. Phonon dispersion of $NbC_{.89}$. The solid line shows a fit using the double shell model of Weber /3/. The dotted lines indicate the width of the neutron groups corrected for resolution effects. For a comparison the data of Smith and Gläser /2/ for $NbC_{.98}$ are included in the figure.

## REFERENCES

/1/ L. Pintschovius and W. Reichardt, in Progress Report of the Teilinstitut Nukleare Festkörperphysik, Ges. f. Kernforschung Karlsruhe (KFK 2183), p. 4 (1975).

/2/ B. Splettstößer and W. Leibfried, to be published.

/3/ W. Weber, Phys. Rev. B8, 5082 (1973).

/4/ H. G. Smith and W. Gläser, Phys. Rev. Lett. 25, 1611 (1975).

/5/ F. Gompf, L. Pintschovius, W. Reichardt and B. Scheerer, in Proc. of the Internat. Conference on Neutron Scattering, Gatlinburg (USA), June 1976, in press.

## 1.4. Comparison of the Phonon Densities of States of Non Superconducting NbC$_{.76}$ and Superconducting NbC$_{.96}$

*F. Gompf*

NbC$_{.76}$ has 8 valence electrons (V.E.) and is a non-superconductor. With rising carbon content (i.e. rising V.E. number) superconductivity sets in and reaches 11 K for stoichiometric NbC. It is known from NbC single crystal measurements /1, 2/ that with decreasing carbon content the anomalies found in the phonon dispersions also decrease. In some regions of the anomalies however the phonons could not be defined due to an extreme strong broadening of their line widths and there the shape of the dispersion curves is uncertain. In order to learn more about this frequency shift and in order to compare it with model calculations we determined the phonon density of states for NbC$_{.76}$ on TOF 1 under the same experimental conditions as for NbC$_{.96}$ /3/. The generalised G(ħω) was converted into the true phonon density of states F(ħω) as described in /3/. A comparison of our results which in this case are partly corrected for the resolution of the spectrometer is given in Fig. 1. The whole spectrum of NbC$_{.76}$ is strongly shifted to higher frequencies. Its shape is actually better described by Weber's shell model calculation for ZrC /4/ - which is also a non-superconductor with 8 V.E. and which shows no phonon anomalies. With the help of model calculations Weber had stated that for the refractory materials with 8 and 9 V.E. McMillans hypothesis $\eta = N(o) \cdot J^2 = \text{const.}$ does not hold. Our direct determination of

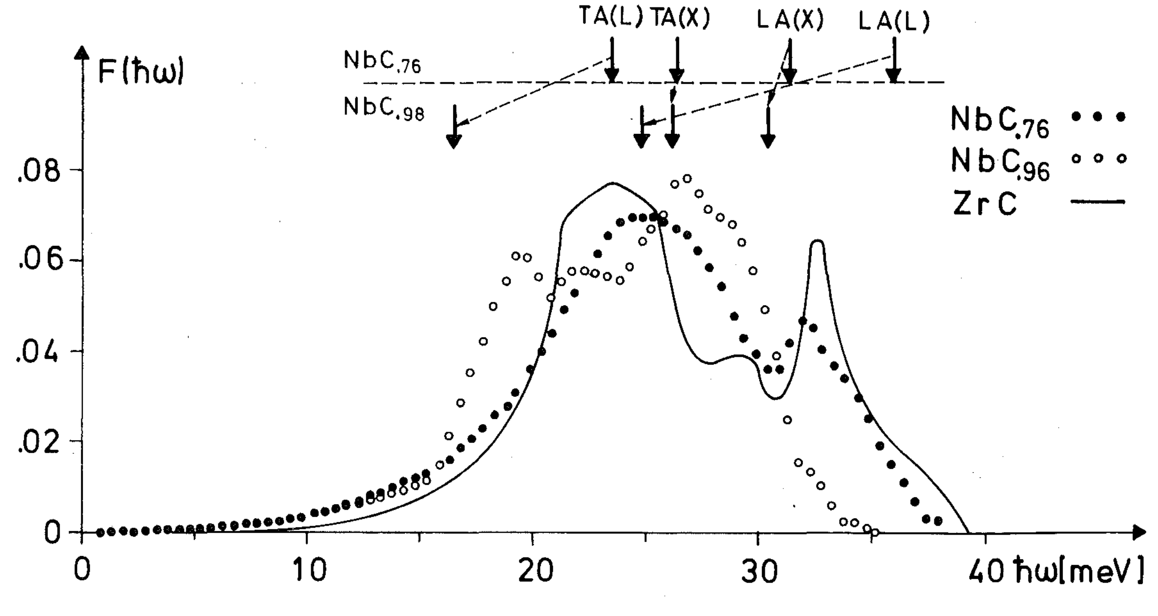

Fig. 1. The phonon density of state for NbC$_{.76}$ compared to that of NbC$_{.96}$ and to a shell model calculation for ZrC (the arrows indicate the zone boundery frequencies at the X and L point for NbC$_{.76}$ and NbC$_{.96}$ taken from Ref. /1/ and /2/ respectively).

the phonon densities of states for $NbC_{.76}$ and $NbC_{.96}$ confirm these results and show that the difference of the mean square frequencies defined in the sense of McMillan is still not large enough to explain the $T_c$ value ( ≈ 10 K) of $NbC_{.96}$.

REFERENCES

/1/ H. G. Smith and W. Gläser, Phys. Rev. Lett. 25, 1611 (1970).

/2/ L. Pintschovius and W. Reichardt, in Progress Report of the Teilinstitut Nukleare Festkörperphysik, Ges. f. Kernforschung Karlsruhe (KFK 2183), p. 4 (1975).

/3/ J. Geerk, F. Gompf, W. Reichardt and E. Schneider, in Progress Report of the Teilinstitut Nukleare Festkörperphysik, Ges. f. Kernforschung Karlsruhe (KFK 2183), p. 31 (1975).

/4/ W. Weber, Phys. Rev. B8, 5082 (1973).

## 1.5. Phonon Density of States for ZrN

F. Gompf

ZrN is a superconductor with a $T_c$ of 10 K. It has 9 valence electrons like some other superconducting refractory materials such as NbC and TiN. In order to compare it with them and to have a more detailed knowledge of the phonon density of states we performed a room temperature measurement of $ZrN_{.87}$ at TOF1 with better accuracy and higher resolution than before /1/.

The acoustic part of the spectrum is shown in Fig. 1 and compared with the generalized phonon density of states for $NbC_{.96}$ /2/. In this case both spectra are partially corrected for resolution of the TOF-spectrometer. The phonon densities of states cover approximately the same range of frequencies for both materials, the only significant difference is that the ZrN spectrum shows a peak around 21 meV whereas $NbC_{.96}$ peaks towards the end of the spectrum. A larger resemblance in shape and intensities is found with the TiN-spectrum /3/ after the mass difference has strong hint that the anomalies for the nitride family differ in size and position from those of the carbides. That the nitrides have larger intensities for small frequencies can be attributed to the stronger scattering power of N in comparison to C, since both light masses are vibrating in phase with the heavy metal atoms for low frequencies. In order to convert $G(\hbar\omega)$ for ZrN to

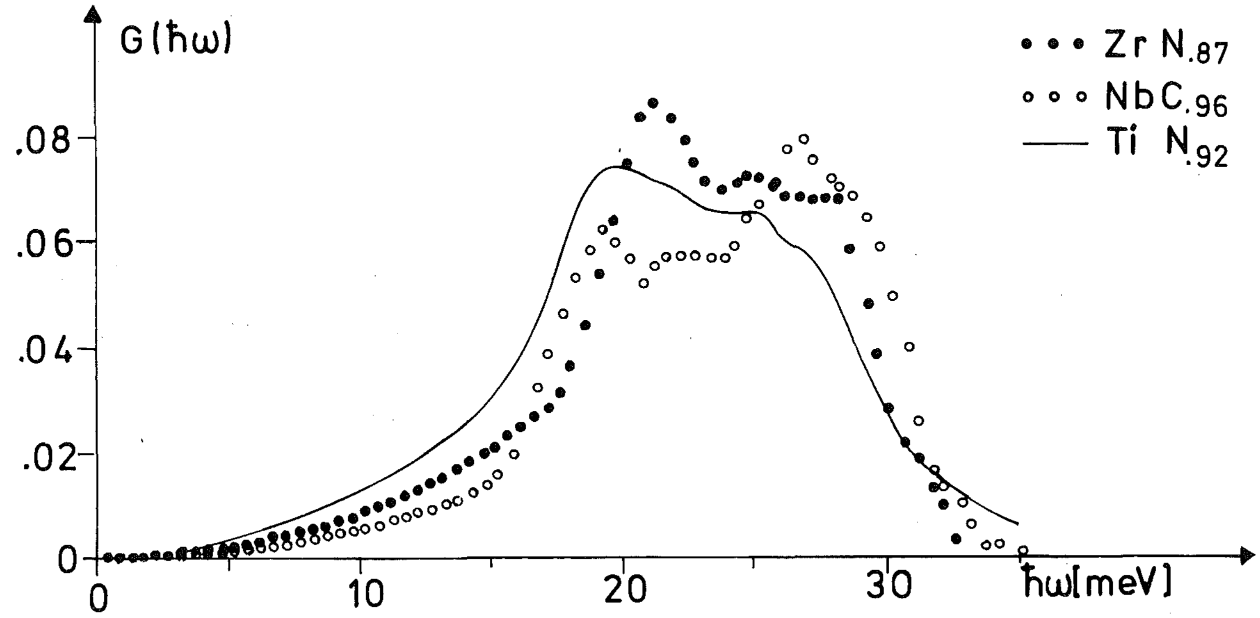

Fig. 1. Comparison of the phonon density of states for ZrN$_{.87}$ with that of NbC$_{.96}$ and the "mass-scaled" (see text) frequency distribution of TiN$_{.92}$.

the true phonon density of states F(ħω) a correction factor G(ħω)/F(ħω) must be derived with the help of a model calculation. In this case Weber's double shell model /4/ must be modified to meet the particularities of the nitride family. This correction decrease the spectra only for low frequencies and is not expected to change the overall shape.

## REFERENCES

/1/ F. Gompf, J. Salgado and W. Reichardt, in Progress Report of the Teilinstitut Nukleare Festkörperphysik, Ges. f. Kernforschung Karlsruhe (KFK 2054), p. 21 (1974).

/2/ J. Geerk, F. Gompf, W. Reichardt and E. Schneider, in Progress Report of the Teilinstitut Nukleare Festkörperphysik, Ges. f. Kernforschung Karlsruhe (KFK 2183), p. 31 (1975).

/3/ F. Gompf, in Progress Report of the Teilinstitut Nukleare Festkörperphysik, Ges. f. Kernforschung Karlsruhe (KFK 2183), p. 29 (1975).

/4/ W. Weber, Phys. Rev. B8, 5082 (1973).

## 1.6. Investigations on the Phonon Density of States of Cubic δ-NbN

*F. Gompf, W. Reichardt and A. N. Christensen*[a]

[a] Aarhus University, Aarhus, Dänemark

In extension to our former investigations of δ-$NbN_{.84}$ /1/ we determined the phonon density of states of a sample with higher nitrogen concentration. Measurements on a high resolution powder diffractometer showed that the sample was purely cubic δ-phase. From the lattice constant a N-concentration of $X = .94$ was determined. A preliminary analysis of the intensities of the diffraction peaks yielded $X = .96$.

The measurement of the scattering law of $NbN_{.95}$ at room temperature was performed under identical experimental conditions as for $NbN_{.84}$. The results for the acoustic parts of the generalized phonon density of states $G(h\omega)$ of the two samples are compared in Fig. 1. A distinct softening of the phonon frequencies is observed for $NbN_{.95}$ compared to $NbN_{.84}$; the mean square frequencies defined in the sense of McMillan by $\langle\omega\rangle/\langle\frac{1}{\omega}\rangle$ differ by 10 %. This result will be

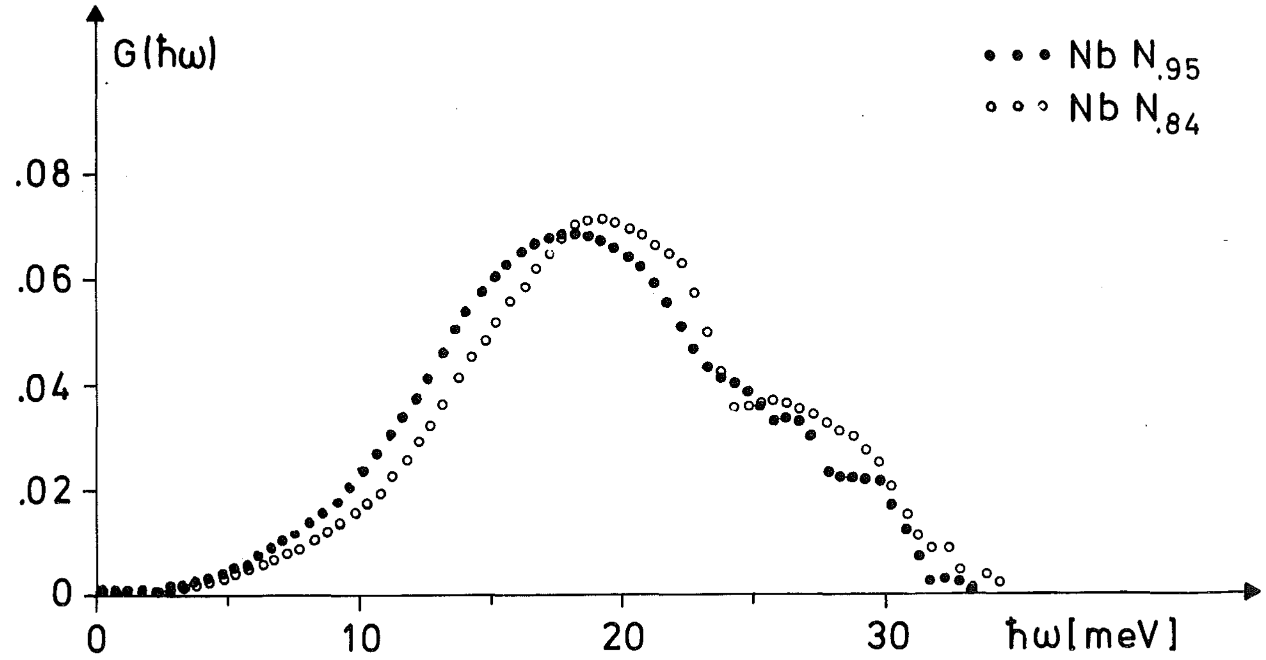

Fig. 1. Comparison of the phonon densities of states of $NbN_{.95}$ and $NbN_{.84}$.

essentially unaffected by the corrections which have to be applied if the experimental results are converted to the true phonon densities of states. Using McMillan's $T_c$-formula together with the assumption that $\eta$ is the same for both N-concentrations a difference between the $T_c$-values of $\Delta T_c = 2.5$ K is calculated which is in very good agreement with the experimentally determined dependence of $T_c$ on the N-concentration /2/. We had found earlier that, going from $NbC_{.96}$ ($T_c \approx 10$ K) to $NbN_{.84}$ ($T_c \approx 15$ K), the change in $T_c$ can be explained solely by the change of the phonon spectrum keeping $\eta$ constant. For representatives with low $T_c$ however $\eta$ increases with increasing $\lambda$ (see also Ref. /4/). Thus one is tempted to conclude that for the refractory materials the relation between $\eta$ and $\lambda$ has a general behaviour as shown in Fig. 2.

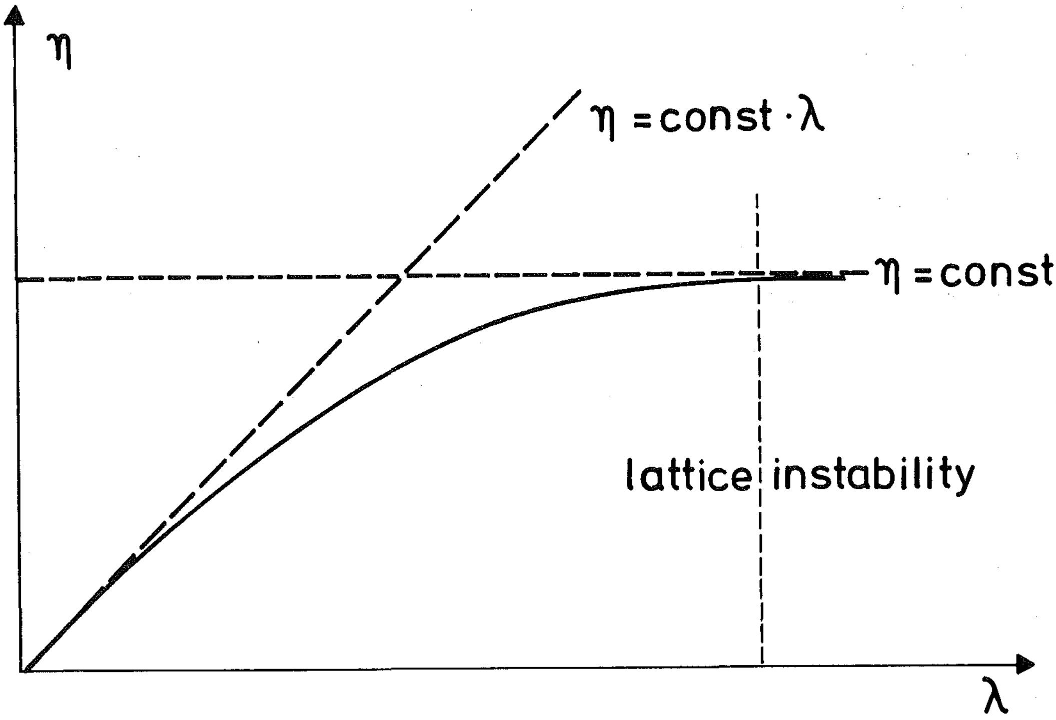

Fig. 2. Relation between $\lambda$ and $\eta$ for the refractory materials.

REFERENCES

/1/ F. Gompf and W. Reichardt, in Progress Report of the Teilinstitut Nukleare Festkörperphysik, Ges. f. Kernforschung Karlsruhe (KFK 2054), p. 28 (1975).

/2/ L. E. Toth, Transition Metal Carbides and Nitrides, Academic Press, New York and London (1971).

/3/ F. Gompf and W. Reichardt, Vergleich der Phononenzustandsdichten von NbN und NbC, Vortrag DPG Freudenstadt (1976).

/4/ W. Weber, Phys. Rev. B8, 5093 (1973).

## 1.7. Phonon Dispersion of Tetragonal γ-NbN

*W. Reichardt*

We have started measurements of the phonon dispersion curves of tetragonal γ-NbN. The sample used in the experiment is a multi-domain crystal; therefore only averages of the dispersion curves in the [100] and [001] directions can be obtained. The same is true for the [110] and [101] directions. The measurements are further complicated by the presence of a considerable amount of the hexagonal β-phase and by the splitting of the Bragg-reflections due to the tetragonal distortion which causes a reduction of the q-resolution.

The results obtained so far are shown in Fig. 1. They are compared with the acoustic part of the phonon density of states of cubic NbN$_{.84}$ /1/. The apparent correspondence between the zone boundary frequencies and the structure in the phonon density of states suggests that the dispersion curves of the tetragonal and the cubic phase are not markedly different (the tetragonal distortion from the cubic symmetry is only about 1 %). At small wave vectors the dispersion curves are very similar to those of NbC$_{.89}$ /2/, whereas an unusual behaviour is observed for the TA-branch in the [110] direction, which bends down when approaching the zone boundary. For the LA-branch in the [100] direction no

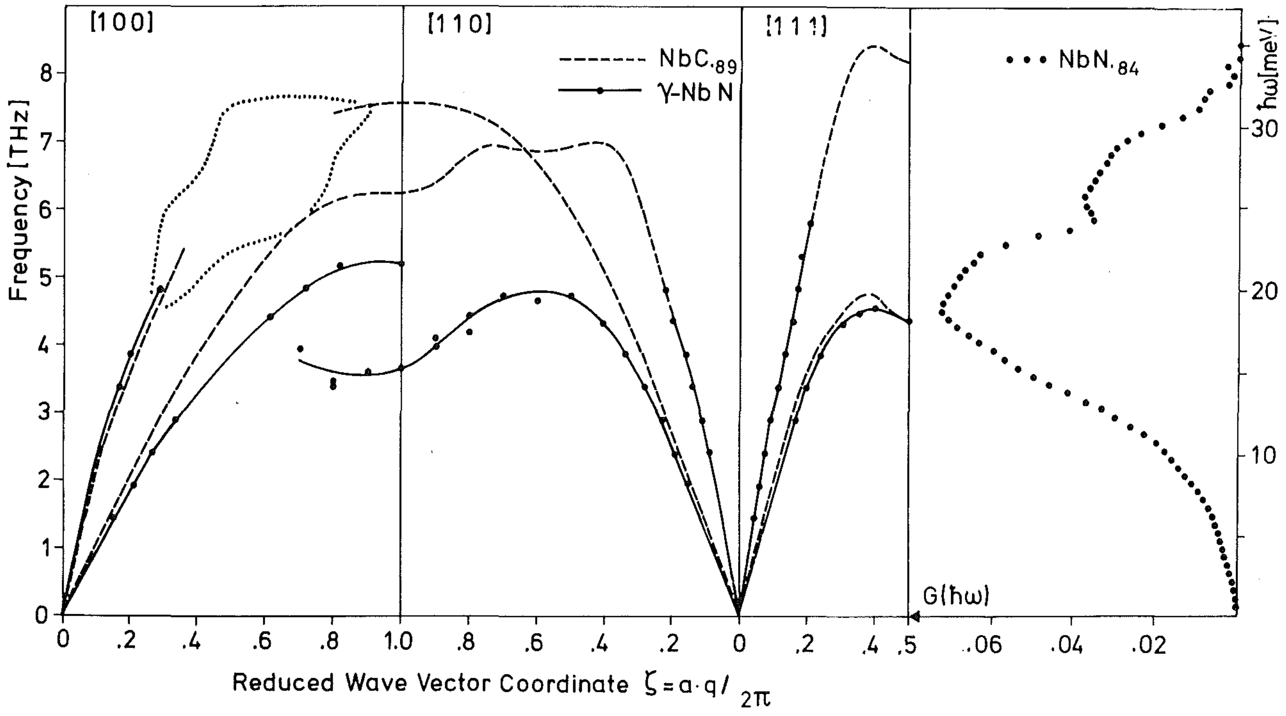

Fig. 1. Phonon dispersion of tetragonal γ-NbN.
For comparison the dispersion curves of NbC$_{.89}$ and the phonon density of states of cubic NbN$_{.84}$ are shown in the figure.

clearly defined phonon peaks could be detected in the middle of the zone. At present it is not clear whether this is due to a tremendeous broadening of the neutron groups as has been observed in non-stoichiometric NbC /2, 3/ or caused by a contamination of the scans by phonons of the β-phase.

## REFERENCES

/1/ F. Gompf and W. Reichardt, in Progress Report of the Teilinstitut Nukleare Festkörperphysik, Ges. f. Kernforschung Karlsruhe (KFK 2183), p. 28 (1975).

/2/ L. Pintschovius and W. Reichardt, in Progress Report of the Teilinstitut Nukleare Festkörperphysik, Ges. f. Kernforschung Karlsruhe (KFK 2183), p. 4 (1975).

/3/ H. G. Smith, in "Superconductivity in d- and f-Band Metals", AIP Conference Proceedings No. 4, N.Y., p. 321 (1972).

## 1.8. Phonon Densities of States of the Thorium Hydrides

*M. Dietrich*[(a)]*, W. Reichardt and H. Rietschel*

(a) Institut für Experimentelle Kernphysik, GfK

Besides PdH and its alloys ($T_c$ up to about 17 K), $Th_4H_{15}$ is the only metal hydride known to become superconducting ($T_c \sim 8$ K). Superconducting hydrides provide a particularly appropriate example to clarify the role of optical phonons in superconductivity. Tunneling experiments have shown the electron-optical phonon interaction to be strong and of importance for the high $T_c$ in PdH /1/, but so far have not performed on $Th_4H_{15}$. As we shall discuss below, more indirect information on electron-optical phonon coupling is available through an investigation of the lattice dynamics.

Using inelastic scattering of neutron we have determined the optical phonon density of states in both $Th_4H_{15}$ and $ThH_2$ (not superconducting above 1 K). The samples have been prepared by direct reaction of pure hydrogen with thorium metal /2/. The resulting optical phonon densities of states are shown in Fig. 1 together with the resolution of the spectrometer (triangles). There are two remarkable features:

1. While in $ThH_2$ the optical phonons are distributed within a Gaussian of the width 30 meV, they are spread over about 170 meV in $Th_4H_{15}$. This spread

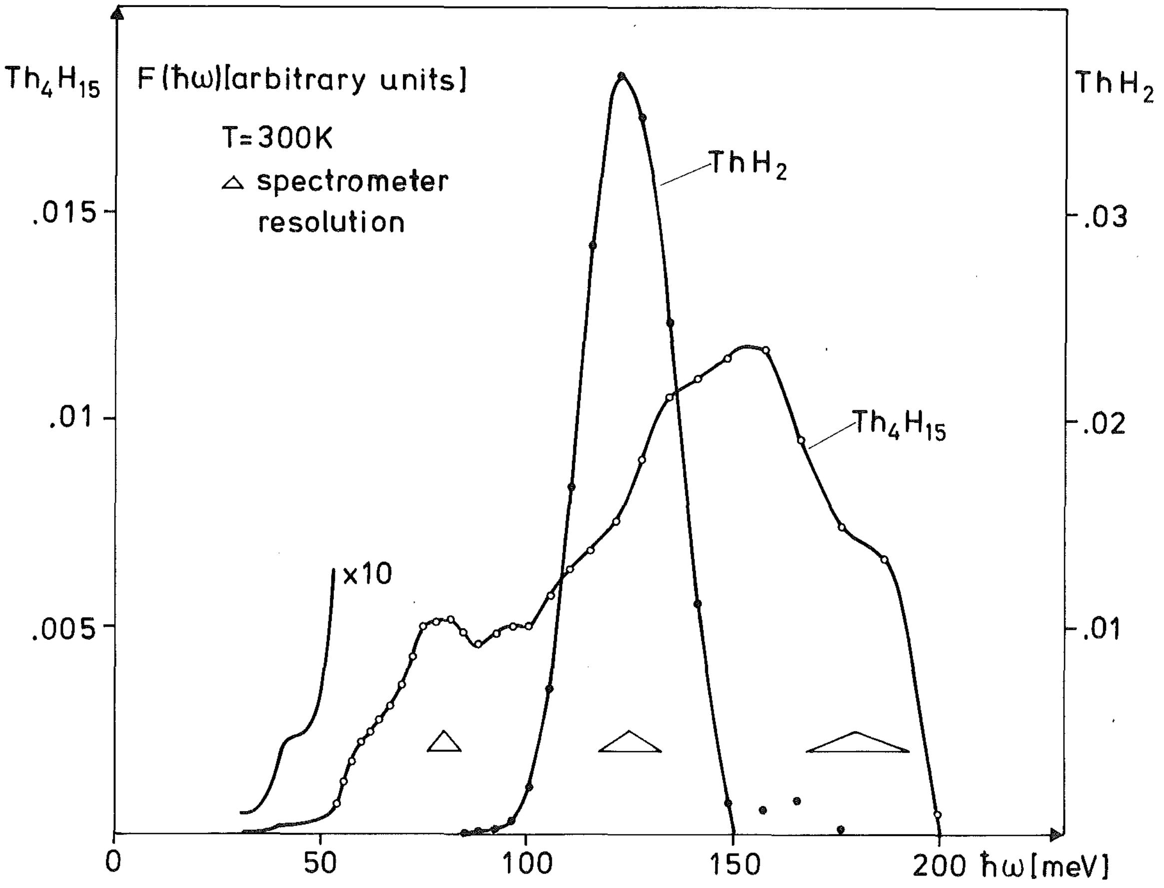

Fig. 1. Comparison of the optical phonon densities of states of $ThH_2$ and $Th_4H_{15}$ at 297 K.

cannot be explained by a superposition of two Gaussians due to the two inequivalent H-positions.

2. There is an optical phonon group of very low frequencies down to 30 meV in $Th_4H_{15}$.

We interpret these findings as follows:

1. In $Th_4H_{15}$ the energy spread of the optical phonons is caused by their strong dispersion which, in turn, has its origin in a strong electron-optical phonon interaction. The same interaction may be the reason for the rather high $T_c$. This conclusion is supported by the fact that the optical phonon dispersion is much weaker (narrow density of states) in $ThH_2$ which is not superconducting above 1 K.

2. In $Th_4H_{15}$ at least one optical phonon branch undergoes softening thereby creating the low energy shoulder of weak intensity in the density of states. Such a phonon anomaly may be the precursor of a lattice instability within the hydrogen sublattice.

In summary, we assume $Th_4H_{15}$ to be an optical phonon mediated high $T_c$ superconductor with some tendency towards lattice instabilities.

REFERENCES

/1/ A. Eichler, H. Wühl, B. Stritzker, Sol. State Commun. 17, 213 (1975).

/2/ C. B. Satterthwaite, D. T. Peterson. J. Less-Common Metals 26, 361 (1972).

## 1.9. Phonon Density of States of Some Chevrel Phase Molybdenum Compounds

*B. P. Schweiss and B. Renker*

Among the high field superconductors the ternary molybdenum compounds have become of considerable interest. Compounds with transition temperatures as high as 15.5 K /1/ and critical fields up to 700 KG /2/ have been found. The ideal formula is $XMo_6Y_8$ where X represents one of the metal atoms Pb, Sn, Cu, Ag, Co, Ni etc. and Y is either S, Se or Te /3/. The crystal structure is rhombohedral with one X atom (or two in the case of small cations) and one $Mo_6Y_8$ cluster per unit cell. A framework of X atoms with approximately cubic symmetry surrounds each $Mo_6S_8$ unit which consists of a $Mo_6$ octahedron within a slightly distorted $S_8$ cube that is tilted $\approx 15^\circ$ from the rhombohedral axis /4/. $T_c$ measurements of Fischer et al. /5/ on the rare earth compounds indicate that the Mo electrons with negligible overlap on the X sites are important for the superconducting properties. In a crude approximation $T_c$ depends on the Mo-Mo spacing between neighbouring $Mo_6Y_8$ units which is approximately optimal for $PbMo_6S_8$ with 3.26 Å. As more detailed investigations within different series of those compounds show, variations in the electron phonon interaction may additionally account for the observed differences in $T_c$ /6/. Indeed lattice instabilities /7/, pronounced phonon softening /8/ and anomalous large values for the low temperature specific heat /8/ have been observed for a number of ternary molybdenum compounds.

In the present investigation we have studied the phonon density of states for a number of related compounds in order to locate contributions of the various atoms to the lattice vibrational spectrum and to see whether any correlations between the phonon spectra and the striking physical properties of these compounds can be found.

Powder samples of $PbMo_{6.35}S_8$ ($T_c$ = 14 K), $SnMo_6S_7$ (13 K), $Pb_{1.2}Mo_6Se_8$ (not superconducting above 4 K) and $Mo_6Se_8$ (6.5 K) were prepared using a method which is described by Marezio et al. /4/. The Chevrel phases exist as defect structures and the quoted chemical formulas give the initial composition. Neutron diffraction patterns were taken for all of the samples and did not show any appreciable amount of other phases. The transition temperatures in the brackets were measured by the inductive method. The values indicate the midpoints of the transition region which was typically of the order 0.5 K. Measurements of the phonon density of states $G(\hbar\omega)$ were performed with the time-of-flight spectrometer TOF2 at the cold source using 5 meV neutron incident energy and neutron upscattering. The data were corrected for background, counter efficiency, an average Debye-Waller factor, multiphonon contributions and converted to a generalized $G(\hbar\omega)$ spectrum. Fig. 1 shows the results obtained for $PbMo_{6.35}S_8$ and $SnMo_6S_7$ respectively. The $G(\hbar\omega)$ results for $Pb_{1.2}Mo_6Se_8$ and $Mo_6Se_8$ are compared in Fig. 2.

As it was discussed in a previous paper /8/ the interpretation of the complex spectra may be facilitated by a simple molecular crystal model which assumes an arrangement of single X atoms and rigid $Mo_6Y_8$ "molecules". Then the 45 normal modes group into 36 high frequency internal and 9 low frequency external modes which consist of 3 acoustical, 3 optical modes and 3 torsional modes of the molecule. Within this picture the intersection between high internal and low external modes is probably indicated by the gap at 18 meV shown in Fig. 1. The relation of the areas is indeed approximately 9 : 36 as must be expected and this value is even better approximated if we try to correct for the different atomic scattering cross sections. The most prominent feature within the region of the external modes is the extremely sharp peak at 4.3 and 4.7 meV respectively. A corresponding sharp excitation is absent in the $Mo_6Se_8$ spectrum and it seems natural to correlate this excitation with movements of the metal atoms in the open channels between the $Mo_6Y_8$ clusters. The mass ratio $(M_{Pb}/M_{Sn})^{1/2} = 1.32$ is not fully displayed by the shift of the peak positions in Fig. 1 but the difference in masses may be partly compensated by a smaller spring constant caused by the smaller atomic radius of Sn. The lack of any coherent effects in the single TOF spectra taken at different scattering angles and the much larger partial Debye-Waller factors of these metal atoms which were found by X-ray analysis /3/ also point to an Einstein mode like behaviour.

The position of the second maximum near 10 meV is also sensitive to an exchange of the central metal atom as Fig. 1 shows. This does not seem to be the case for the third smaller maximum at ≈ 14 meV. This frequency is lower for the compound with $Mo_6Se_8$ as a comparison of Fig. 1 and 2 shows. Therefore within the simple model one might assign the latter peak to the vibrational excitations

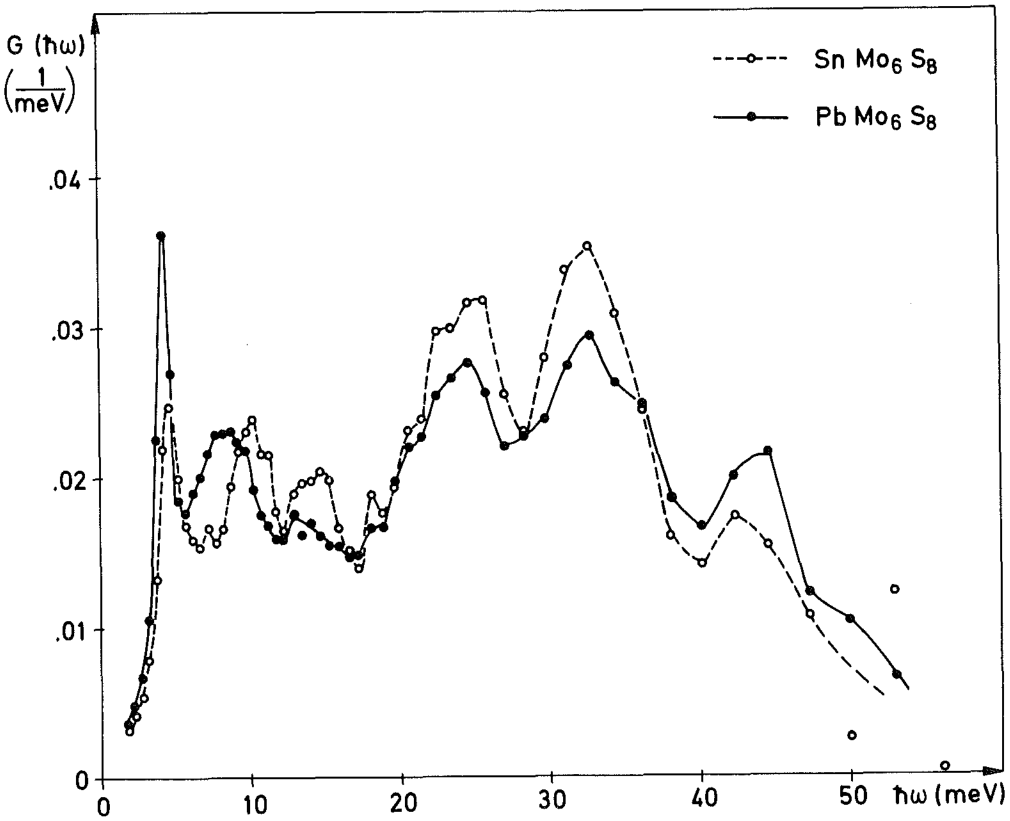

Fig. 1. Phonon density of states of $PbMo_6S_8$ and $SnMo_6S_8$.

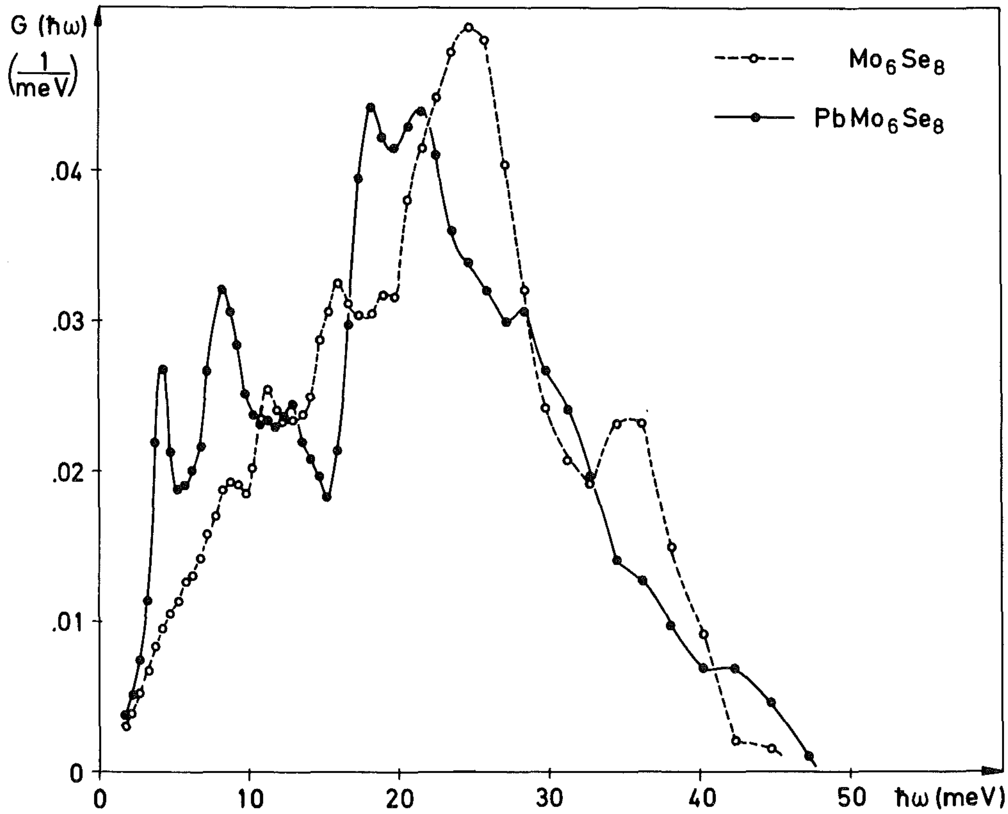

Fig. 2. Phonon density of states of $Mo_6Se_8$ and $PbMo_6Se_8$.

of the $Mo_6Y_8$ units. Of course the molecular crystal model is only a very crude approximation since a sharp distinction between external and internal modes is not strictly possible as the spectrum of $Mo_6Se_8$ in Fig. 2 shows.

The region of internal vibrations exhibits a three peak structure. The peak at about 43 meV in Fig. 1 corresponds mainly to vibrations of the sulfur atoms. The shift in frequency and the change in intensity supports this conclusion when the sulfur atoms are replaced by Se with the larger mass and the larger scattering cross section.

In conclusion we have seen that the molecular crystal model which allows a general understanding of the lattice dynamics of these compounds /8/ only provides a crude model. The movement of the metal atoms within the open channels leads to Einstein mode like excitations which to a large extend explain the anomalously large low temperature specific heat of the ternary molybdenum compounds. But these frequencies do not seem to be responsable for the superconducting properties of the compounds as the comparison of the low $T_c$ = 3.9 K /3/ for $PbMo_6Se_8$ and the higher $T_c$ = 6.5 K for $Mo_6Se_8$ shows. One might speculate that this might be the case for the low lying torsional vibrations which set up displacements in the important Mo-Mo-spacing between neighbouring $Mo_6S_8$ clusters.

## REFERENCES

/1/ B. T. Matthias, M. Marezio, E. Corenzwit, A. S. Cooper and H. E. Barz, Science 175, 1465 (1972).

/2/ 0. Fischer, M. Decroux, S. Roth, R. Chevrel and M. Sergent, J. Phys. C: Sol. State Phys. 8, L474 (1975).

/3/ R. Chevrel, M. Sergent and J. Prigent, J. Sol. State. Chem. 3, 515 (1971).
R. Chevrel, Thèse, Rennes, France (1974).
G. Guillevic, Thèse, Rennes, France (1974).

/4/ M. Marezio, P. D. Dernier, J. P. Remeika, E. Corenzwit and B. T. Matthias, Mat. Res. Bull. 8, 657 (1973).

/5/ 0. Fischer, A. Treyvaud, R. Chevrel and M. Sergent, Sol. State Commun. 17, 721 (1975).

/6/ R. Chevrel, M. Sergent and 0. Fischer, Mat. Res. Bull. 10, 1169 (1975).

/7/ C. W. Kimball, L. Weber, G. van Landuyt, F. Y. Fradin, B. D. Dunlap and G. K. Shenoy, Phys. Rev. Lett. 36, 412 (1976).

/8/ S. D. Bader, G. S. Knapp, S. K. Sinha, B. P. Schweiss and B. Renker, submitted to Phys. Rev. Lett.

## 1.10. Phonon Spectra of Chevrel-Phase Lead and Tin-Molybdenum Sulfides: A Molecular Crystal Model and its Implications for Superconductivity

*S. D. Bader*[(a)], *G. S. Knapp*[(a)], *S. K. Sinha*[(a)], *P. Schweiss and B. Renker*

[(a)] Argonne National Laboratory, Argonne, Illinois 60439

to be published in Phys. Rev. Lett.

ABSTRACT

Heat-capacity (2 - 400 K) and inelastic neutron scattering studies of the phonon spectra are reported for high-critical field, Chevrel-phase lead and tin-molybdenum sulfide superconductors ($T_c \sim 11 - 15$ K). Nine phonon modes per unit cell are identified whose frequencies are in the immediate region Bergmann and Rainer indicate is necessary to optimize $T_c$. Dramatic acoustic phonon softening on cooling is observed. A molecular-crystal model is proposed for the lattice dynamics of these materials.

## 1.11. Temperature Dependence of the Phonon Density of States of $Nb_3Al$

*E. Schneider*[+]

The measurements of the phonon density of states $G(\hbar\omega)$ by inelastic neutron scattering from $Nb_3Al$ /1/ have been completed by an experiment at 4.2 K. For comparison the results for room temperature and 4.2 K from TOF 1 are shown in Fig. 1. The range of scattering angles was from 35 ° to 147.4 °, the incoming energy was 65 meV.

The drastic changes in $G(\hbar\omega)$ by the variation of the sample temperature which we already found in our preparatory experiments occur between 20 and 30 meV and

---

[+] Present address: Physik Department, TU München

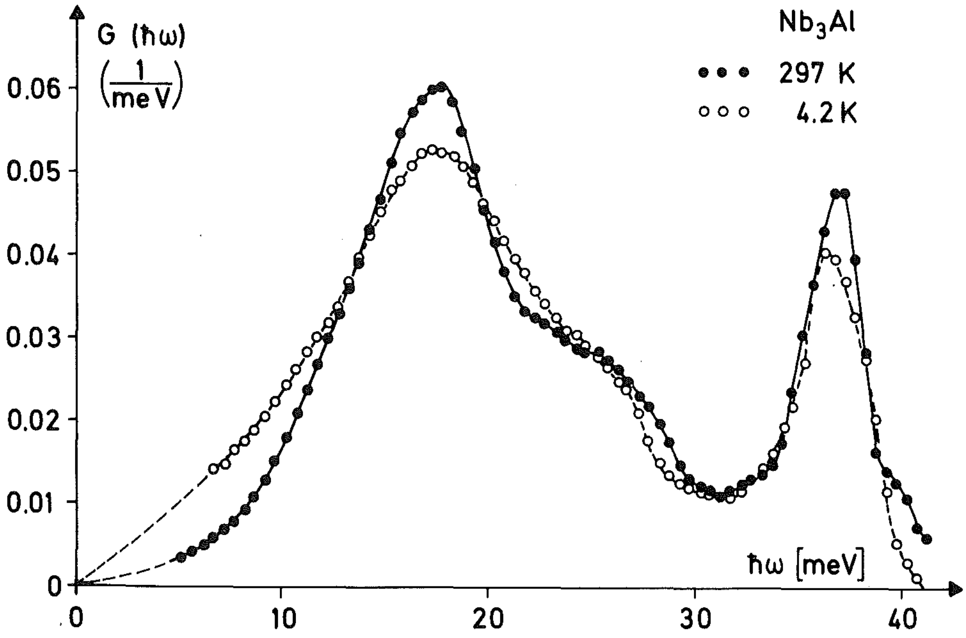

Fig. 1. Phonon density of states of $Nb_3Al$ for 4.2 and 297 K.

below 12 meV in the range of the niobium vibrations. Up to 10 meV the enhancement of the frequency spectrum amounts to more than a factor of two on cooling, whereas the peak at 37 meV which we ascribe to the lighter aluminium atoms is somewhat lowered but its position is not changed.

From the two phonon spectra we have calculated the lattice specific heat and Debye temperatures. The two curves shown in Fig. 2 hold only for the limiting cases of high temperatures (upper curve) and low temperatures (lower curve). For intermediate temperatures $\Theta_D$ lies in between these two curves. The value of $\Theta_D$ = 290 K which we found in the literature /2/ is well above our low temperature limit of 240 K. However, the calculated Debye temperatures are not very accurate below about 30 K as the TOF-spectrum below 5 meV was contaminated with elastically scattered neutrons and thus the low frequency part of the phonon density of states could not be determined reliably.

On the other hand it seems that the extrapolation method, where the slope of the experimental $c_V/T$ - versus $T^2$ - curve at low temperatures is used to determine $\Theta_D$, is not applicable for this compound. With the $c_V/T$ - values calculated from our phonon spectrum at 4.2 K we obtained different slopes and hence different $\Theta_D$ values depending on the temperature range from which the linear extrapolation was performed.

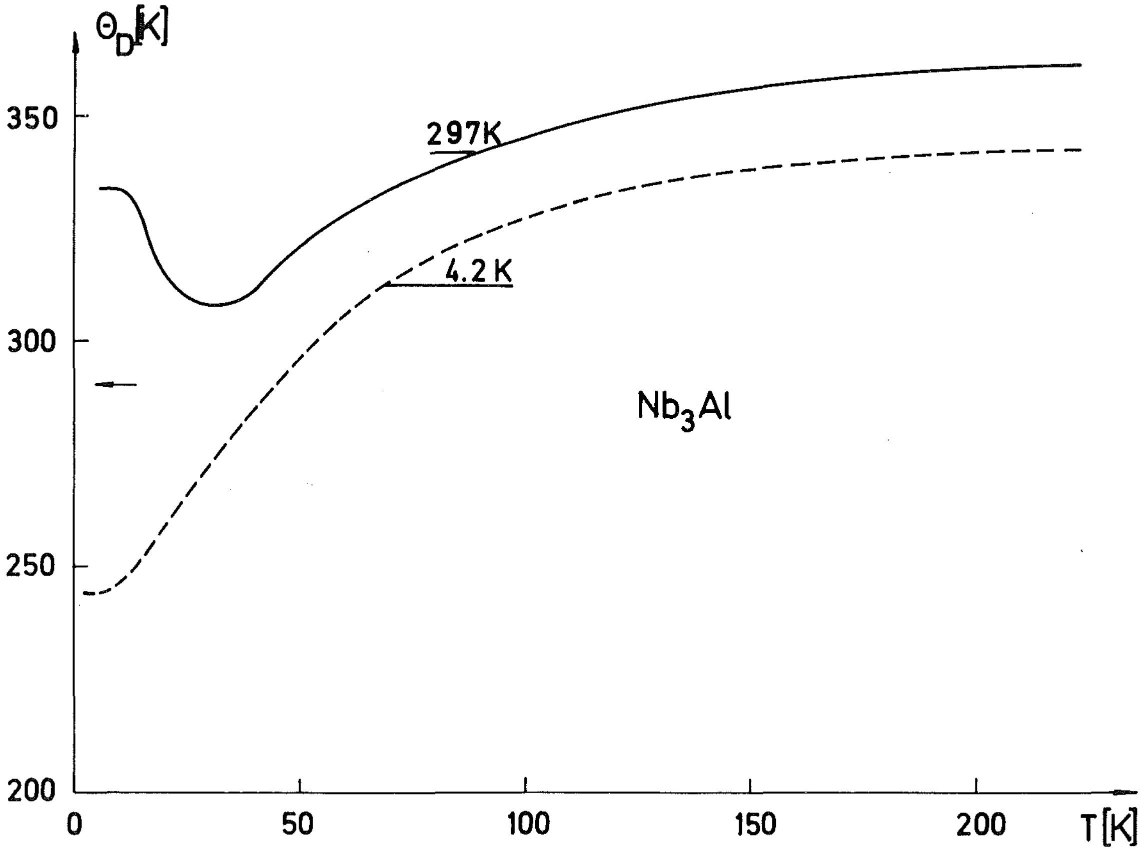

Fig. 2. Temperature dependence of the Debye temperature of $Nb_3Al$

REFERENCES

/1/ E. Schneider and W. Reichardt, in Progress Report of the Teilinstitut Nukleare Festkörperphysik, Ges. f. Kernforschung Karlsruhe, (KFK 2183), p. 26 (1975).

/2/ R. H. Willens, T. H. Geballe, A. C. Gossard, J. P. Maita, A. Menth, G. W. Hull, Jr. and R. R. Soden, Sol. State Commun. 7, 837 (1969).

## 1.12. Phonon Density of States of dhcp Lanthanum

*N. Nücker*

Phonon densities of states of dhcp Lanthanum were measured using the time-of-flight instruments IN4 at the HFR Grenoble and TOF 2 at the FR2 Karlsruhe. The polycrystalline dhcp Lanthanum sample was prepared by melting 99.999 % pure Lanthanum in a vacuum better than $10^{-5}$ mbar to remove Hydrogen. The transformation to the dhcp phase was achieved by cold working the material in an Argon atmosphere.

The experiments on IN4 were done with an incident neutron energy of $E_o = 27.6$ meV. Fig. 1 compares the results obtained from energy loss and energy gain spectra respectively. The two curves give slightly different intensities due to an incomplete sampling obtained in the experiment. The spectra resemble the phonon density of states of the related element Yttrium. We have done computer simulations of our Lanthanum experiments using the force constants of Sinha et al. /1/ for Y adapted to La by inserting a higher mass to adjust the energy scale. The model calculation gives the general features of the measured density of states and allows to calculate the influence of the incomplete sampling of the experiment, which is found to be less than 10 %. The deviations between the true phonon density of states and that obtained by the computer experiments have been used to correct our experimental results. After these corrections very satisfactory agreement between the energy gain and energy loss data is obtained (see Fig. 2). The final result for the phonon density of states of dhcp La is given in Fig. 3 by the full curve. It is the average of the two curves of Fig. 2 including the result of an additional measurement performed on TOF 2 at the FR2 with $E_o = 5.0$ meV. It is compared with the result of a measurement at 4.5 K. The two spectra differ only slightly, in particular no hardening of the phonon density of states on cooling is observed.

In Fig. 4 the low temperature results are compared with the Eliashberg-function $\alpha^2F(\omega)$ determined from superconducting tunneling measurement by Wühl et al. /2/. While the two spectra have very similar structures there is a remarkable shift of the Eliashberg-function to lower energies compared to the neutron results. This shift is well outside the uncertainties associated with the energy calibration of both experiments. Thus it has to be considered as real. Correspondingly the electron phonon coupling function $\alpha^2(\omega)$ determined from these two results decreases strongly with increasing energy. The analysis of the tunneling measurement yielded a rather low value for the coulomb repulsion term $\mu^*$ of 0.02. This may be a hint that the high frequency part of $\alpha^2F(\omega)$ has been measured too low and consequently the true $\alpha^2(\omega)$ does not show such a drastic decrease.

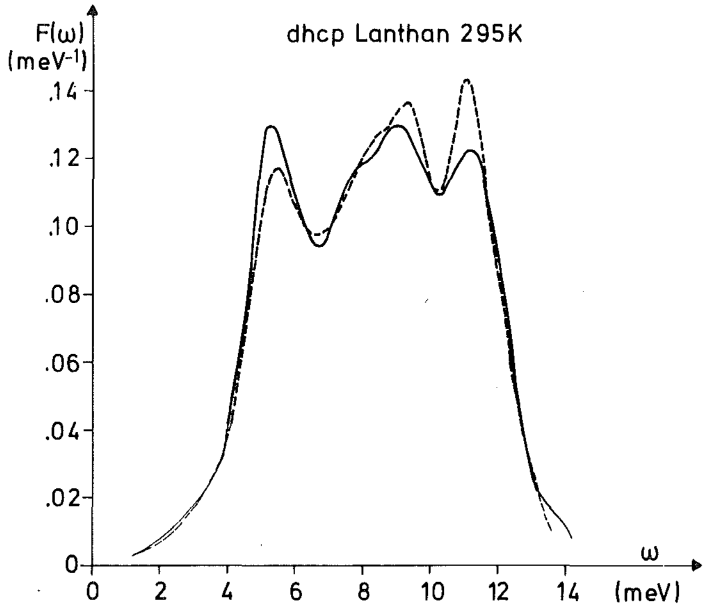

Fig. 1.

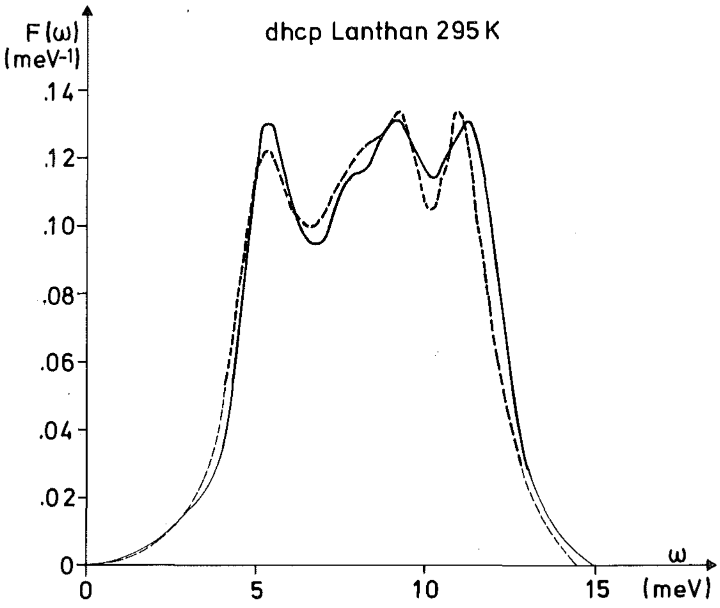

Fig. 2.

Phonon density of states of Lanthanum at 295 K.

—— Results from energy gain measurement.

--- Results from energy loss measurement.

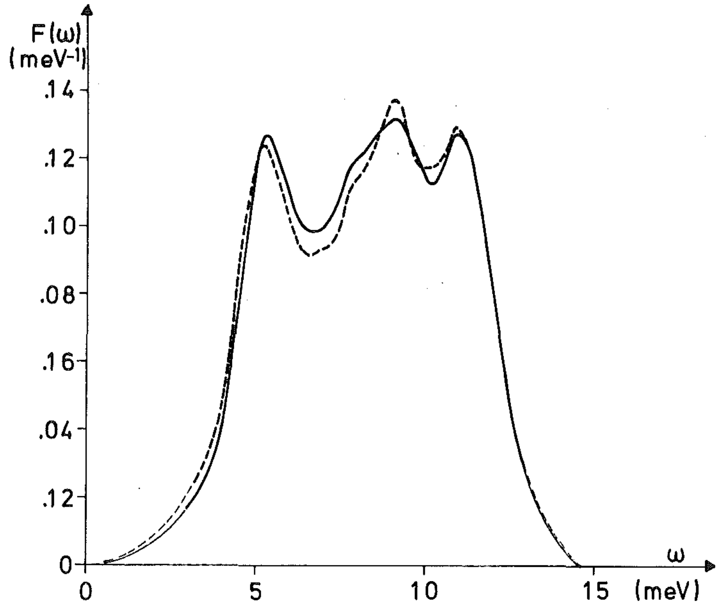

Fig. 3. Phonon density of states of Lanthanum (—— 295 K, --- 4.5 K).

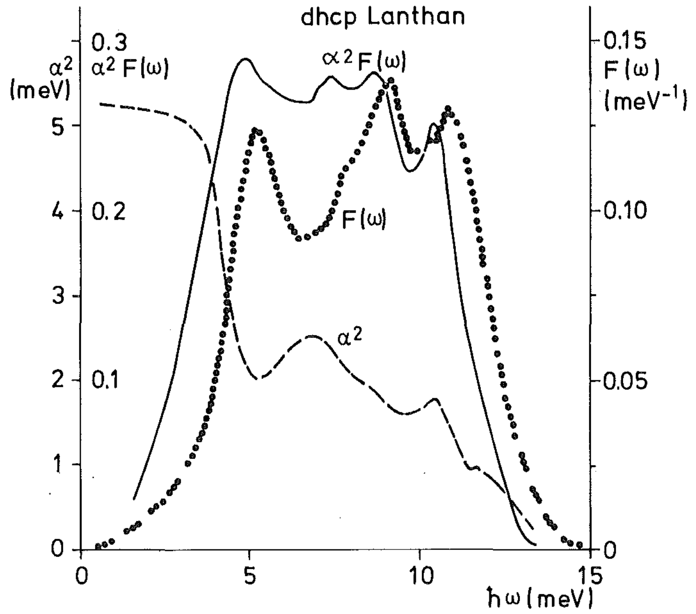

Fig. 4. Phonon density of states of dhcp Lanthanum F(ω) at 4.5 K (•••) compared to the Eliashberg-function $\alpha^2F(\omega)$ (——) and resultant electron phonon coupling function $\alpha^2$ (----).

REFERENCES

/1/ H. Wühl, A. Eichler and J. Wittig, Phys. Rev. Lett. 31, 1393 (1973).

/2/ S. K. Sinha, T. O. Brun, L. D. Muhlestein and J. Sakurai, Phys. Rev. B1, 2430 (1970).

## 1.13. Phonon Density of States of $LaAl_2$

*K. Knorr*[(a)] *and N. Nücker*

(a) Institut für Physik der Universität Mainz

Heat capacity measurements of the laves phase compound $LaAl_2$ /1, 2/ plotted in the usual $C_p/T$ versus $T^2$ scale show an abrupt change in slope at about 7.5 K corresponding to a change in the $T^3$ coefficient by approximately a factor of 2.

Phonon densities of states were determined from time-of-flight measurements on $LaAl_2$ at 5 K and 20 K using the IN4/HFR Grenoble. Due to elastic scattering contributions of the sample and the cryostat it was not possible to evaluate the phonon density of states below 7 meV. Since we did not observe any difference between the results for the two temperatures at higher frequencies the reported change in the heat capacity coefficient must be caused by lower lying modes.

In order to improve statistics we summed the results of the 5 K and 20 K measurement. Fig. 1 gives the generalized phonon density of states G(ω) of $LaAl_2$ for temperatures between 5 K and 20 K.

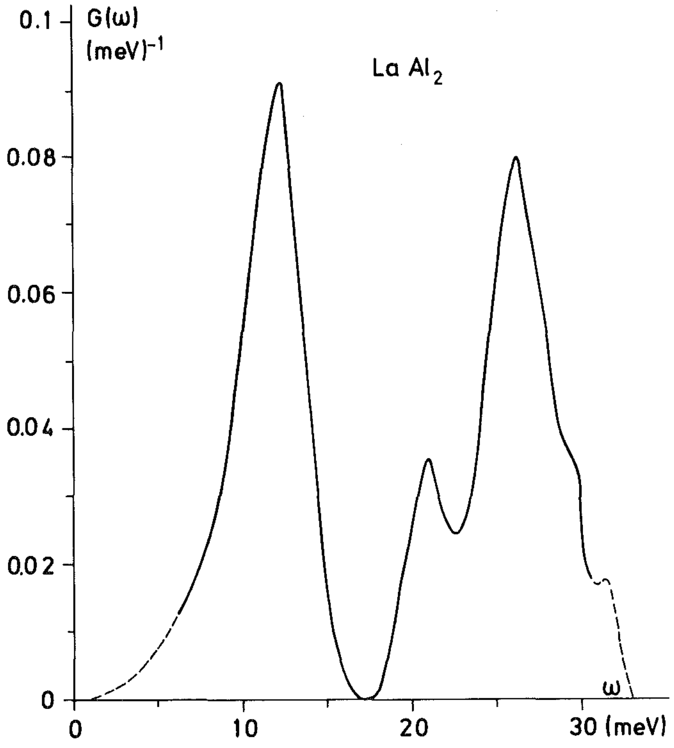

Fig. 1. Generalized phonon density of states of $LaAl_2$ ($5\ K \leq T \leq 20\ K$).

REFERENCES

/1/ R. E. Hungsberg, K. A. Gschneider, J. Phys. Chem. Solids 33, 401 (1972).

/2/ H. Happel, Dissertation, Universität Frankfurt (1975).

## 1.14. Measurement of the Phonon Density of States of Al at 297 K

*J.-B. Suck, E. Schneider*$^+$ *and W. Reichardt*

Extensive studies on the lattice dynamics of Al have been reported in the literature by several authors. Stedman et al. /1,2/ have determined the dispersion surface at 80 K for a large number of wave vectors in the entire Brillouin zone. By interpolating the experimental data they determined the phonon density of states directly without using a lattice dynamical model. Model calculations by Cowley /3/ are in rather good agreement with Stedman's results. Thus the phonon density of states of Al at 80 K is rather well known and therefore Al provides a good example to study how well the phonon density of states of a coherent scatterer can be determined by an experimental sampling method /4/.

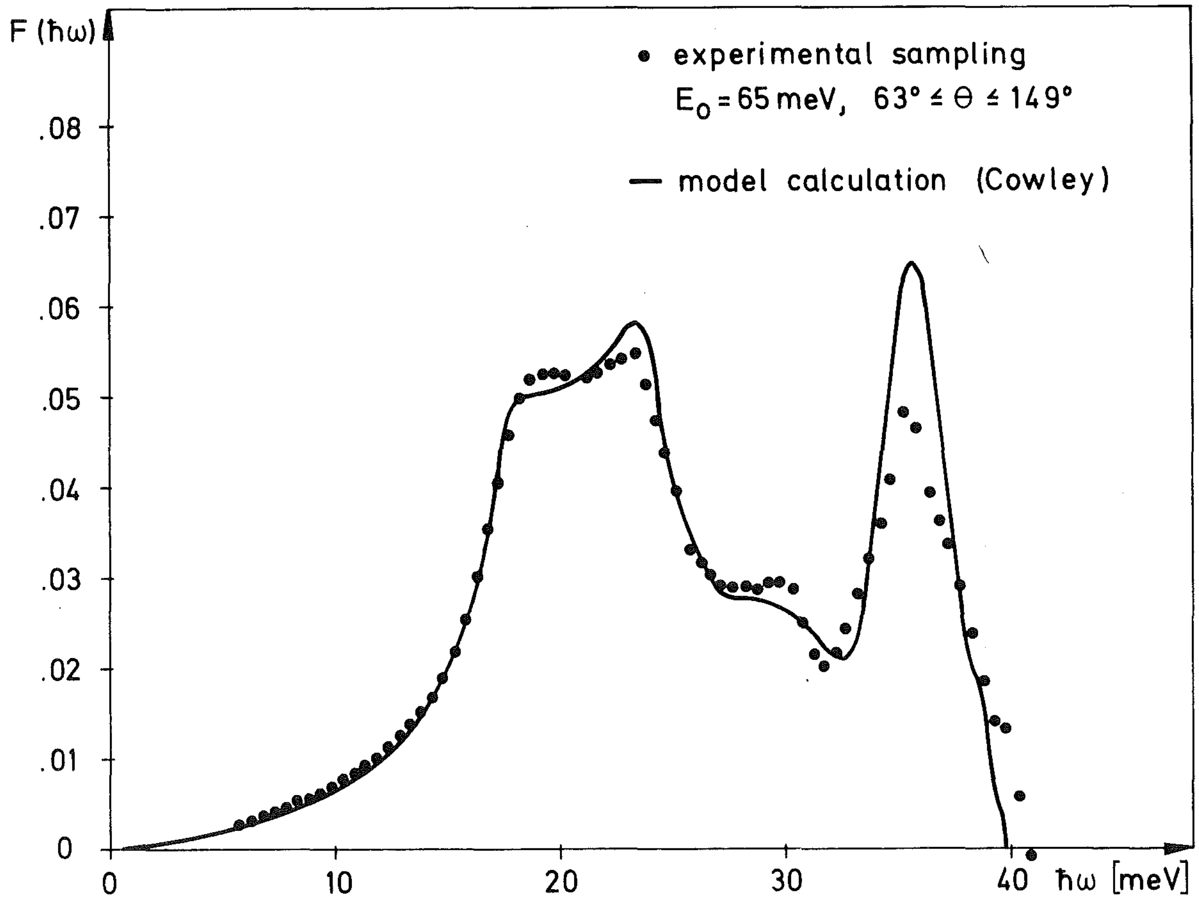

Fig. 1. Al at 297 K: Comparison of the experimentally determined phonon density of states with the result of a calculation using a slightly modified version of Cowley's model.

---

[+] Present address: Physik Department, TU München

We performed such an experiment at 297 K on the time-of-flight spectrometer TOF1 at the FR2. The primary energy was 65 meV. In addition we simluated the experiment on a computer using Cowley's model in order to obtain information about the systematic errors inherent in the experimental method.

The sample was prepared from filings obtained from a 99.9 pure Al block. In order to eliminate lattice defects introduced by the filing process the sample was annealed about 50 hours at 800 K. No differences were observed between the TOF-spectra before and after annealing. The experimental results of Fig. 1 were partly corrected for the resolution of the spectrometer by an iterative procedure where the original TOF spectrum was reconstructed within the statistical errors of the experiment. Thus the resolution of the experimental result depends on the counting statistics of the individual time channel.

For the calculation of the phonon density of states shown in Fig. 1 we used Cowley's model reducing the original force constants by 3.5 % in order to account for the softening of the phonon frequencies when going from 80 K to 297 K. Furthermore the phonon line broadening as observed by Stedman was approximately taken into account. According to the computer simulation studies the systematic errors of the experiment were smaller than 4 % over the whole frequency range.

## REFERENCES

/1/ R. Stedman and G. Nilsson, Phys. Rev. 145, 492 (1966).
/2/ R. Stedman, L. Almquist and G. Nilsson, Phys. Rev. 162, 549 (1967).
/3/ E. R. Cowley, Can. J. Phys. 52, 1714 (1974).
/4/ V. S. Oskotskii, Soviet Phys. Solid State 9, 420 (1967).

## 1.15. Phonon Dispersion of NiO at Small Wave Vectors

*W. Reichardt*

Our former measurements of the dispersion curves of NiO at 297 K /1, 2/ have shown that there were considerable discrepancies between the elastic constants deduced from the neutron data and those obtained from ultrasonic measurements /3, 4/. As the neutron measurements were performed in the antiferromagnetic state ($T_N = 523$ K) the observed differences may be due to the magnetic ordering. If this is true the discrepancies should disappear above the Nêel temperature.

For a more reliable determination of the elastic constants we have extended our former measurements at 297 K to smaller wave vectors using improved resolution in the experiment. The results for three independent runs under different experimental conditions are shown in the upper part of Fig. 1. The straight lines are the slopes of the dispersion curves as determined from the elastic constants which gave the best fit to our experimental results. Their values are listed in Table I together with the ultrasonic data of Refs. /3/ and /4/.

Table I Elastic constants of NiO (units: $10^{12}$ dyn cm$^{-2}$).

| | $c_{11}$ | $c_{12}$ | $c_{44}$ | $\frac{1}{2}(c_{11} - c_{12})$ |
|---|---|---|---|---|
| this work | 4.24 | 1.66 | 0.97 | 1.29 |
| Ref./3/ 297 K | 2.24 | 0.97 | 1.10 | |
| Ref./4/ 297 K | 2.70 | 1.25 | 1.05 | |
| Ref./3/ 570 K | 3.21 | 0.53 | 1.16 | 1.34 |

The results of measurements at 570 K - i.e. about 50 degrees above $T_N$ - are given in the lower part of Fig. 1. They are compared with the slopes of the dispersion curves at 297 K. One observes that there is almost no change of the phonon frequencies when going from the antiferromagnetic to the paramagnetic state. This shows that the small rhombohedral distortion of 0.15 % which accompanies the magnetic ordering has a negligible effect on the dispersion curves. As the elastic constants obtained from the neutron measurements are almost the same for both temperatures considerable deviations from the ultrasonic data of Ref. /3/ exist in the paramagnetic region too (see Table I). From Table I it is seen that the values for $\frac{1}{2}(c_{11} - c_{12})$ are in reasonable agreement; thus the discrepancies occur essentially for the longitudinal sound velocities.

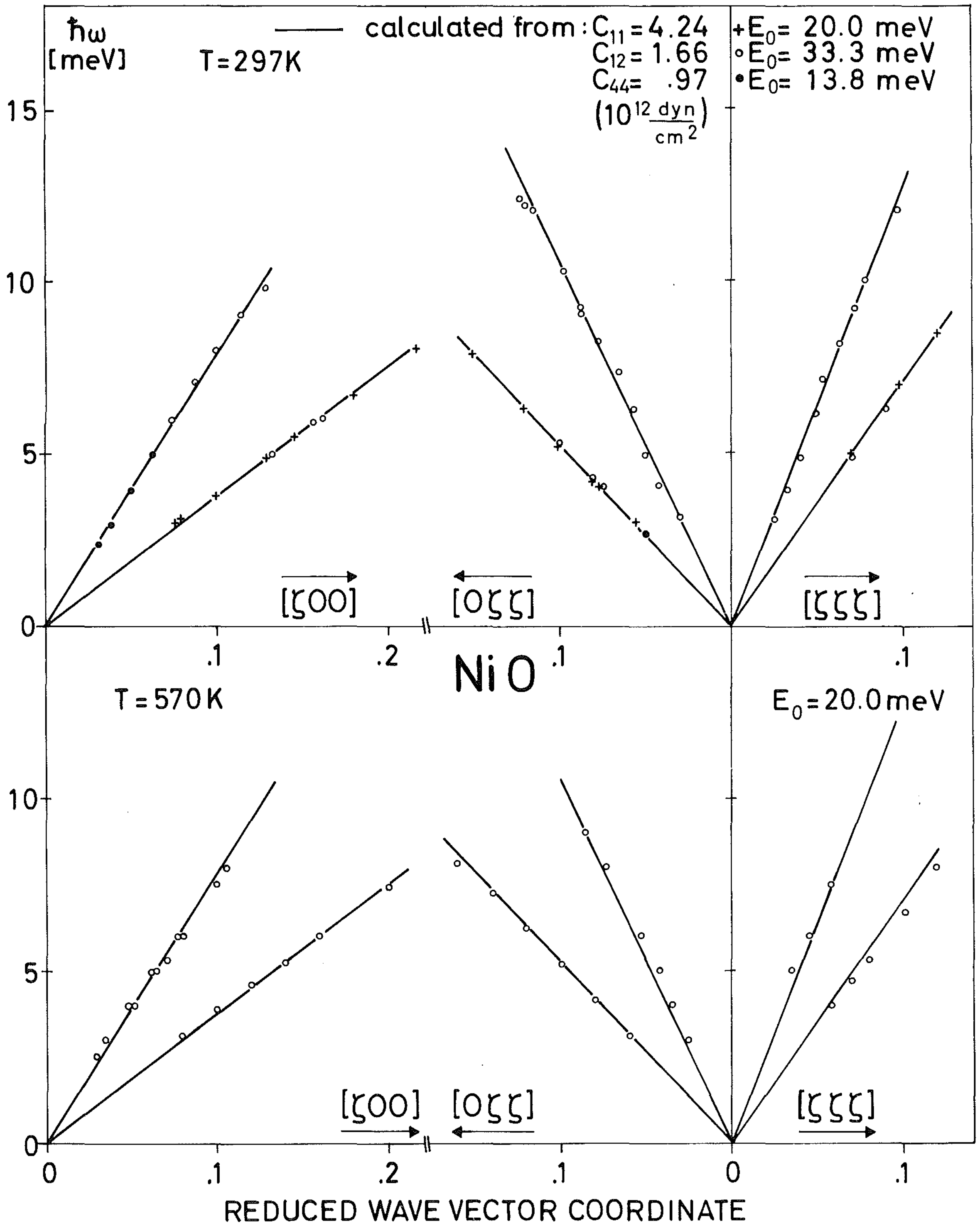

Fig. 1. Phonon frequencies of NiO at small wave vectors in the antiferromagnetic state (T = 297 K) and the paramagnetic state (T = 570 K).

## REFERENCES

/1/ W. Reichardt, in Progress Report of the Teilinstitut Nukleare Festkörperphysik, Ges. f. Kernforschung Karlsruhe (KFK 2054) (1974).

/2/ W. Reichardt, V. Wagner and W. Kress, J. Phys. C8, 3955 (1975).

/3/ P. de V. du Plessis, S. I. Van Tonder and L. Alberts, J. Phys. C4, 1983 (1971).

/4/ N. Uchida and S. Saito, J. Acoust. Soc. Am. 51, 1602 (1972).

## 1.16. Lattice Dynamics of MnO

*V. Wagner*[(a)], *W. Reichardt and W. Kress*[(b)]

(a) Institut Laue-Langevin, Grenoble and Universität Würzburg

(b) MPI für Festkörperforschung, Stuttgart

Measurements of the phonon dispersion curves of MnO were first reported by Haywood and Collings /1/. Their results seem to indicate that the phonon dispersion is quite different from those of the other divalent transition metal oxides with NaCl structure and that a simple shell model is not applicable. Therefore we have remeasured the phonon dispersion curves of MnO on the triple axis spectrometer TAS1 at the FR2 with the main emphasis on the optical branches.

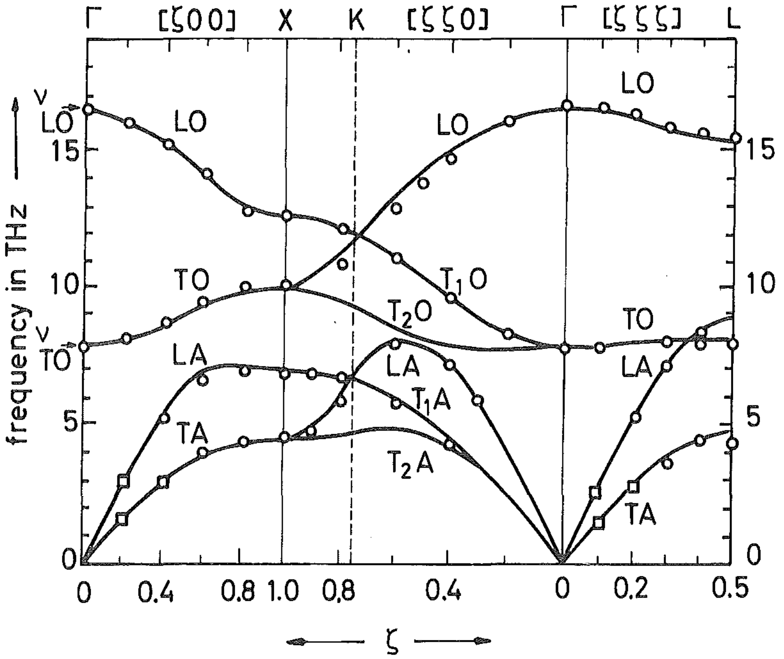

Fig. 1. Fit of a simple shell model with 9 parameters to the phonon frequencies of MnO.

The experimental results for 296 K are shown in Fig. 1. Rather good agreement is found between the optical frequencies at the Γ-point and the values reported from IR reflection measurements /2/. A simple shell model with 9 parameters has been fitted to the experimental data. Both ions were allowed to be polarizable. The model parameters are listed in Table 1. An essential feature of the model is the positive shell charge of the $Mn^{2+}$ which accounts for the overlap polarization /3/.

In Table II the elastic and dielectric properties of MnO calculated from our model are compared with the results of ultrasonic /4/ and IR reflection measurements /2/.

Table I Model parameters of the shell model.
($A_{22}$ and $B_{22}$ describe the short range interaction between the $O^{2-}$).

| $A_{12}$ | $B_{12}$ | $A_{22}$ | $B_{22}$ | $Z$ | $Y_1$ | $Y_2$ | $k_1$ | $k_2$ |
|---|---|---|---|---|---|---|---|---|
| 33.8 | -5.6 | -3.1 | 0.3 | 1.98 | 2.96 | -3.96 | 94.2 | 163.2 |
| $e^2/v$ | | | | $e$ | | | $e^2/v$ | |

Table II Elastic and dielectric properties of MnO.

| | $C_{11}$ | $C_{12}$ | $C_{44}$ | $E_{oo}$ | $E_o$ |
|---|---|---|---|---|---|
| model | 2.57 | 0.98 | 0.80 | 4.95 | 21.5 |
| experimental | 2.23 | 1.20 | 0.79 | 4.95 | 22.5 |
| | $10^{12}$ dyn $cm^{-2}$ | | | | |

Considering that only few experimental data in the low frequency region have been used in the fit the agreement of the elastic constants with the ultrasonic results is quite satisfactory.

In conclusion we can say that the phonon dispersion curves of MnO are very similar to those of the related compounds NiO, FeO and CoO and that they are very well described by a simple shell model.

## REFERENCES

/1/ B. C. Haywood and M. F. Collins, J. Phys. C4, 1299 (1971).

/2/ J. N. Plendl, L. C. Mansw, S. S. Mitra and I. F. Chang, Sol. State Commun. 7, 109 (1969).

/3/ H. Bilz, M. Buchmann, R. Haberkorn and U. Schroeder, Sol. State Commun. 16, 1023 (1975).

/4/ D. W. Oliver, J. Appl. Phys. 40, 893 (1969).

## 1.17. Phonon Dispersion of α-Arsenic

*W. Reichardt and K. H. Rieder*[a]

[a] MPI für Festkörperforschung Stuttgart[+]

The measurements of the phonon dispersion curves of α-Arsenic at 296 K reported in the previous progress report /1/ have been completed. The results for the directions ΓT, ΓL, ΓX and ΓKX are shown in Fig. 1. The optical frequencies at the Γ-point (24.0 meV and 31.2 meV) are in very good agreement with the values obtained by Lannin et al. /2/ from first order Raman scattering measurements (24.0 meV and 31.5 meV). Furthermore the highest and lowest optical frequencies of our measurements occuring at T and X respectively coincide well with the upper and lower limits of the second order Raman spectrum of Ref. /2/.

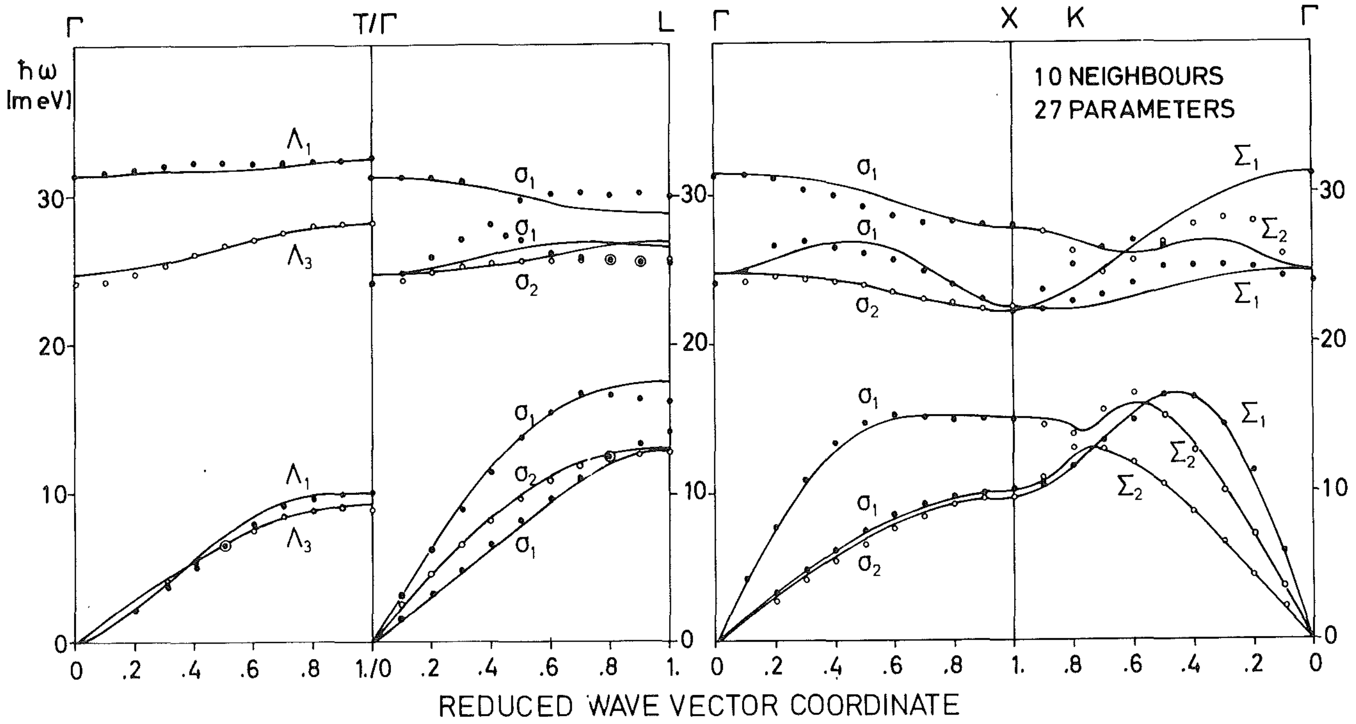

Fig. 1. Phonon dispersion of α-As at 297 K.
The curves are calculated with a Born von Kármán model extending to the tenth nearest neighbors with 27 fit parameters.

No measurements of the elastic constants by ultrasonic methods have been reported yet. Therefore we tried to determine the elastic constants from our phonon data at small wave numbers. The results obtained from a fit to the slopes of 16 acoustic branches are listed in Table I together with the data for the related elements Bi and Sb taken from the literature /3/.

---

[+] Present address: IBM Research Laboratory, Rüschlikon, Switzerland

Table I Elastic constants of the group Vb semimetals (units $10^{11}$ dyn/cm$^2$).

| | $c_{11}$ | $c_{33}$ | $c_{44}$ | $c_{12}$ | $c_{13}$ | $c_{14}$ |
|---|---|---|---|---|---|---|
| Bi | 6.37 | 3.82 | 1.123 | 2.49 | 2.47 | .72 |
| Sb | 10.13 | 4.50 | 3.93 | 3.45 | 2.92 | 2.09 |
| As | 16.2 | 3.0 | 3.8 | 6.1 | 2.7 | 2.0 |

The marked anisotropy of the interatomic forces is demonstrated by the large difference between $c_{11}$ and $c_{33}$. The unusual behaviour that $c_{33}$ is smaller than $c_{44}$ has also been obtained when the slope of the LA-branch in the ΓT-direction has been excluded from the fit.

The curves in Fig. 1 were obtained from a calculation using a Born von Kármán model with interactions up to the tenth nearest neighbours and 27 parameters fitted to the experimental data. The model has been used to calculate the phonon density of states. In Fig. 2 it is compared with the phonon density of states determined by Salgado /3/ from a neutron scattering experiment on a powder sample.

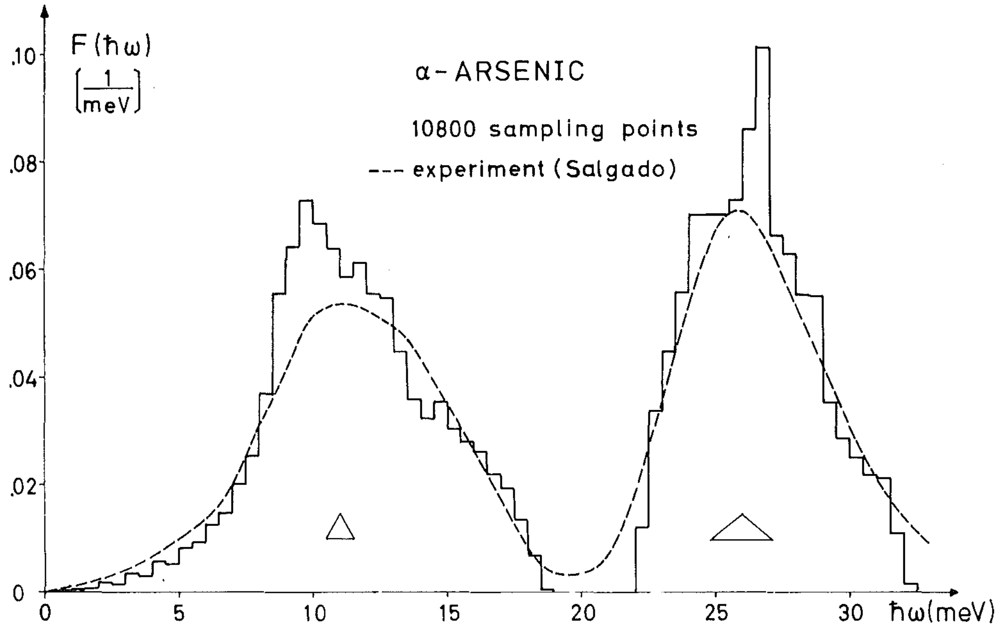

Fig. 2. Comparison of the phonon density of states calculated from our model with that determined directly from a neutron scattering experiment.

REFERENCES

/1/ W. Reichardt and K. H. Rieder, in Progress Report of the Teilinstitut Nukleare Festkörperphysik, Ges. f. Kernforschung Karlsruhe, (KFK 2183), p. 14 (1975).

/2/ J. S. Lannin, J. M. Calleja and M. Cardonna, Phys. Rev. B12, 585 (1975).

/3/ J. Salgado, KFK Report 1954 (1974).

## 1.18. Impurity Effects in $Bi_{1-x}Sb_x$ Alloys

*B. Hofmann, H. Rietschel and R. Kuhn*

Previous measurements with BiSb samples of not quite satisfactory homogeneity /1/ gave strong hints that the lattice dynamics of this alloy system is mainly determined by impurity effects due to the high mass defect concentration of the Sb atoms. Therefore efforts were made to obtain reliable experimental data for the localized modes and phonon line shapes.

Considerable improvement could be achieved in preparing homogeneous single crystals of an appreciable size (20 $cm^3$). The repeated zone levelling technique was used followed by a growing process with slow drawing velocities (≈ 1 mm/h). Composition and perfection of the samples were analysed by measuring intensity reliefs of the (0015) Bragg-reflection (Fig. 1) on a high resolution neutron diffractometer.

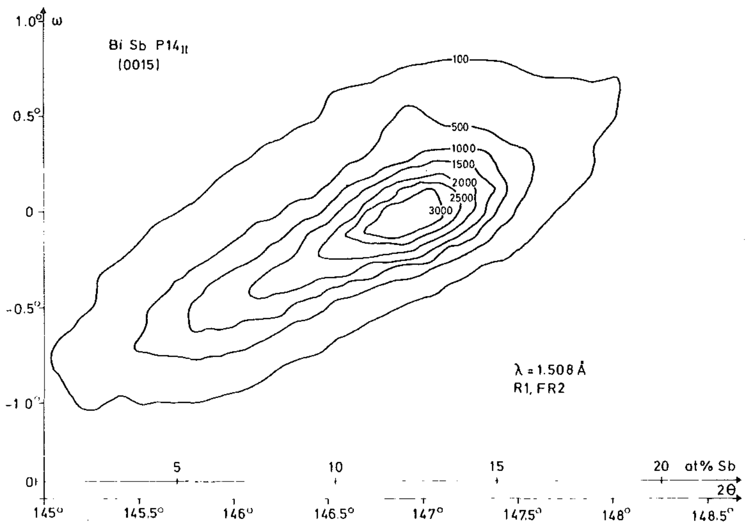

Fig. 1 Intensity relief of the (0015) Bragg-reflection for a BiSb single crystal with a mean Sb concentration of 12 at. %.

For an alloy sample with a mean Sb concentration of 12 ± 1 at. % the neutron scattering laws $S(\vec{q},\omega)$ were measured in the main symmetry direction ΓT parallel to the trigonal axis (Fig. 2). Comparing the results with those for pure Bi, measured under the same experimental conditions, additional scattering intensity is found beyond the optical frequency range of the vibrational spectrum of Bi. This effect is attributed to localized modes of Sb-atoms within a Bi-matrix.

Form and intensity of the impurity induced neutron spectra depend on the polarisation and the wave vector of the in-band modes where they are attached to:

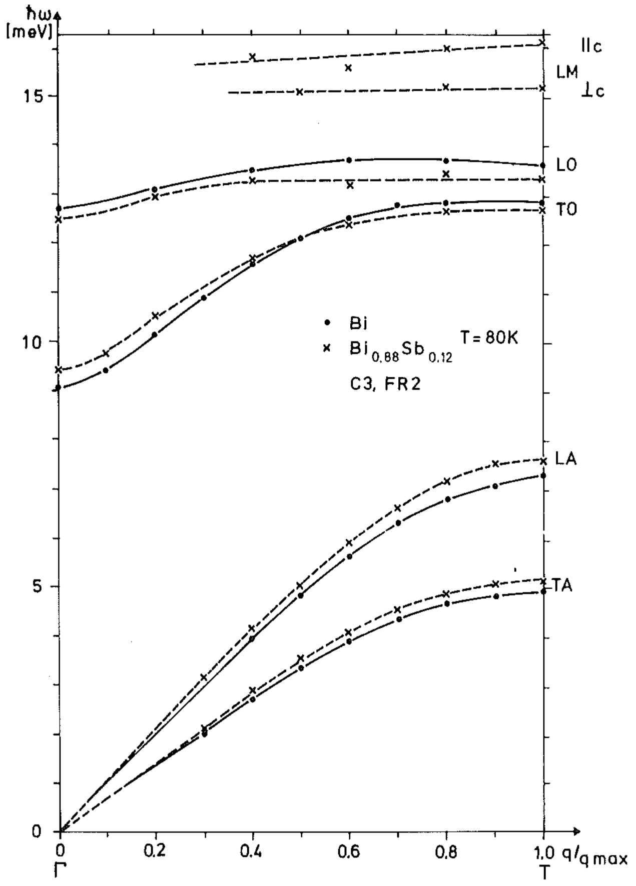

Fig. 2. Phonon dispersions in ΓT direction for pure Bi ( —●— ) and $Bi_{0.88}Sb_{0.12}$ ( --x-- ).

i) In the TO branch with polarisation perpendicular to the trigonal axis the localized modes appear as small extended shoulders, which merge into the background at about 16 meV (Fig. 3a). They are more pronounced for the LO branch where they yield a peak structure located between 15.5 meV and 16 meV (Fig. 3b).

ii) Due to the low counting rates in the region of the impurity modes and the limited experimental resolution (≈ 1.5 meV), it is rather difficult to determine the localized mode energy, especially for the TO branch.

iii) Other effects, which showed up in single phonon measurements are line broadening and energy shifts of the in-band modes (Fig. 4).

In order to get more insight into the dynamics of mass disordered alloys, neutron scattering laws been calculated using two standard methods, based on the Green's function formalism:

i) The Coherent Potential Approximation (CPA) developed by Taylor /2/.

ii) The Average T-matrix Approximation (ATA) by Leath and Goodman /3/.

The predictions of both theories are compared in Figs. 4 and 5a, b. ATA calculations give δ-function contributions in the region of the localized modes while CPA results show a strong coupling between in-band and impurity modes. Projected density of states for Bi obtained by the dynamical model of Czachor et al. /4/ were used for these calculations. There is only qualitative agreement with the experiment after folding the results with the resolution of the spectrometer (dashed curves in Figs. 3a, 3b). The cut off frequency of the calculated distributions is about 1 meV lower than the measured ones. Better agreement with theory is found for the energy shifts of the in-band modes especially in the optical mode region, where both theories give the same result (Fig. 4).

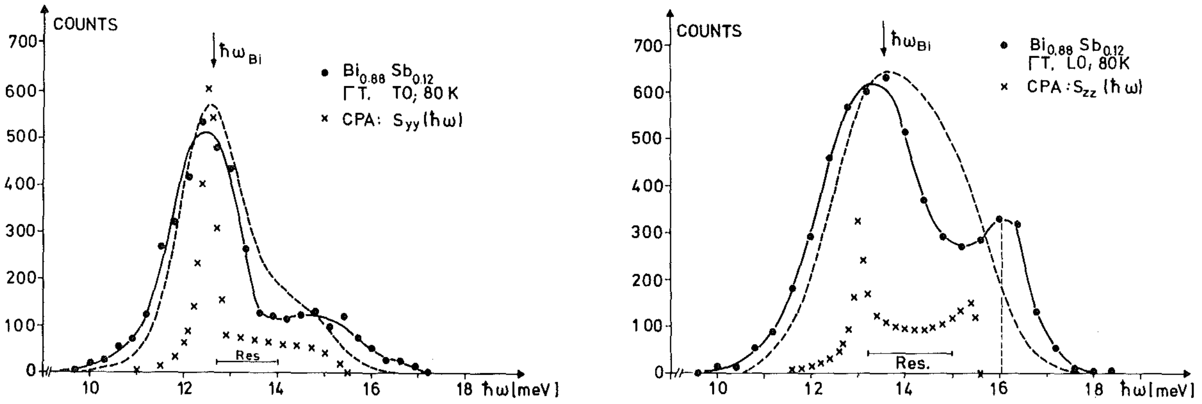

Fig. 3. —— • —— Impurity induced neutron spectra of zone boundary optical phonon for $Bi_{0.88}Sb_{0.12}$. xxxx CPA calculations using projected phonon density of states, ---- folded with the experimental resolution.

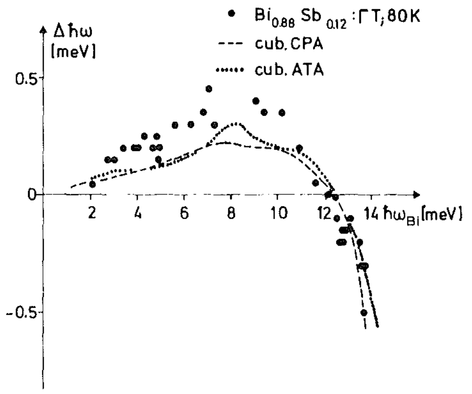

Fig. 4. Energy shifts of the in-band modes for $Bi_{0.88}Sb_{0.12}$:
● experimental data,
---- CPA and .... ATA calculations using the Bi phonon density of states.

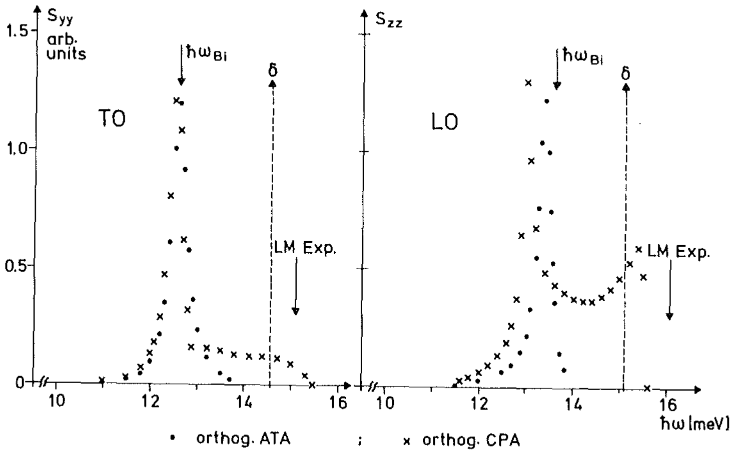

Fig. 5. Comparison of scattering laws S(ω) calculated by the CPA (x) and ATA (●) formalism for $Bi_{0.88}Sb_{0.12}$. The arrows indicate the position of the corresponding Bi resonance and the experimentally detected localized mode energy. The δ-contributions are predicted by ATA theory.

## REFERENCES

/1/ B. Hofmann, in Progress Report of the Teilinstitut Nukleare Festkörperphysik, Ges. f. Kernforschung Karlsruhe (KFK 2183), p. 16 (1975).

/2/ D. W. Taylor, Phys. Rev. 156, 1017 (1967).

/3/ P. L. Leath, B. Goodman, Phys. Rev. 181, 1062 (1969).

/4/ A. Czachor et al., Acta Phys. Pol. A43, 37 (1973).

## 1.19. Study of the Sb Contributions to the Vibrational Spectrum of $Bi_{0.89}Sb_{0.11}$

*B. Hofmann and F. Gompf*

The phonon density of states of a BiSb powder sample with a mean Sb content of 11 at. % was measured on TOF 1 at liquid nitrogen temperature. The powder sample was prepared from the same ingot as the single crystal used for the phonon dispersion measurement (page 35 ). We chose a primary energy of 31.15 meV in order to have good resolution of energy transfers around 14 - 16 meV since a measurement with the TOF 2 spectrometer /1/ seemed to indicate additional impurity-mode contributions in this region. For comparison the frequency spectrum of pure Bi was measured under the same experimental conditions. Both measurements are compared in Fig. 1. The acoustic part of the BiSb-spectrum is noticeably shifted to higher frequencies. The optical peak is not shifted but an additional intensity is found around 14.7 meV which is almost separated from the optical modes when the spectrum is corrected for resolution.

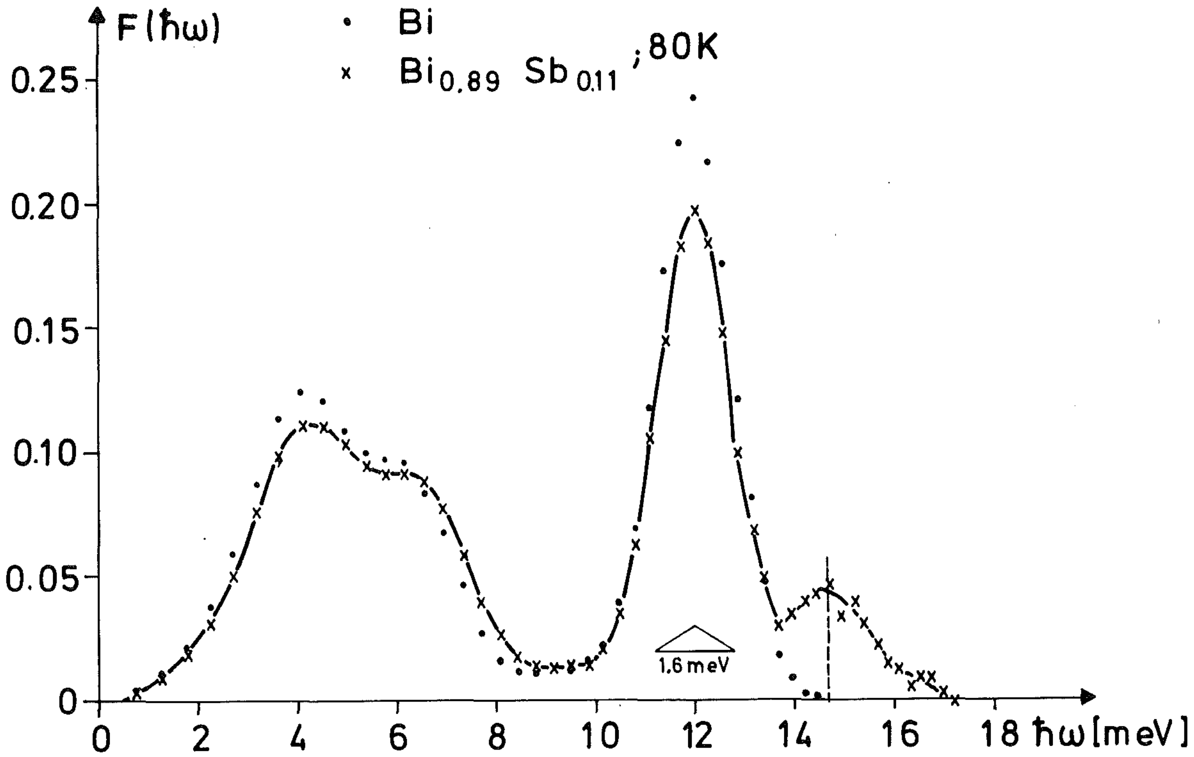

Fig. 1. Comparison of the phonon density of states for Bi with that of $Bi_{.89}Sb_{.11}$ at 80 K.

The experimental results are compared with calculations based on the CPA and ATA theories for which different expressions for the phonon density of states are derived. Fig. 2 shows the calculated phonon spectra starting from the measured Bi phonon density of states and assuming cubic symmetry. Comparing into account only the mass difference of the two scatterers Bi and Sb nut negled the different neutron scattering lengths which tend to reduce the experimental intensities in the impurity mode range by more than a factor of two. The agreement between experiment and theory is quite good in the in-band region of the spectrum: the shift of the upper side of the acoustical peak and the unchanged position of the optical peak is equally well described by both theories.

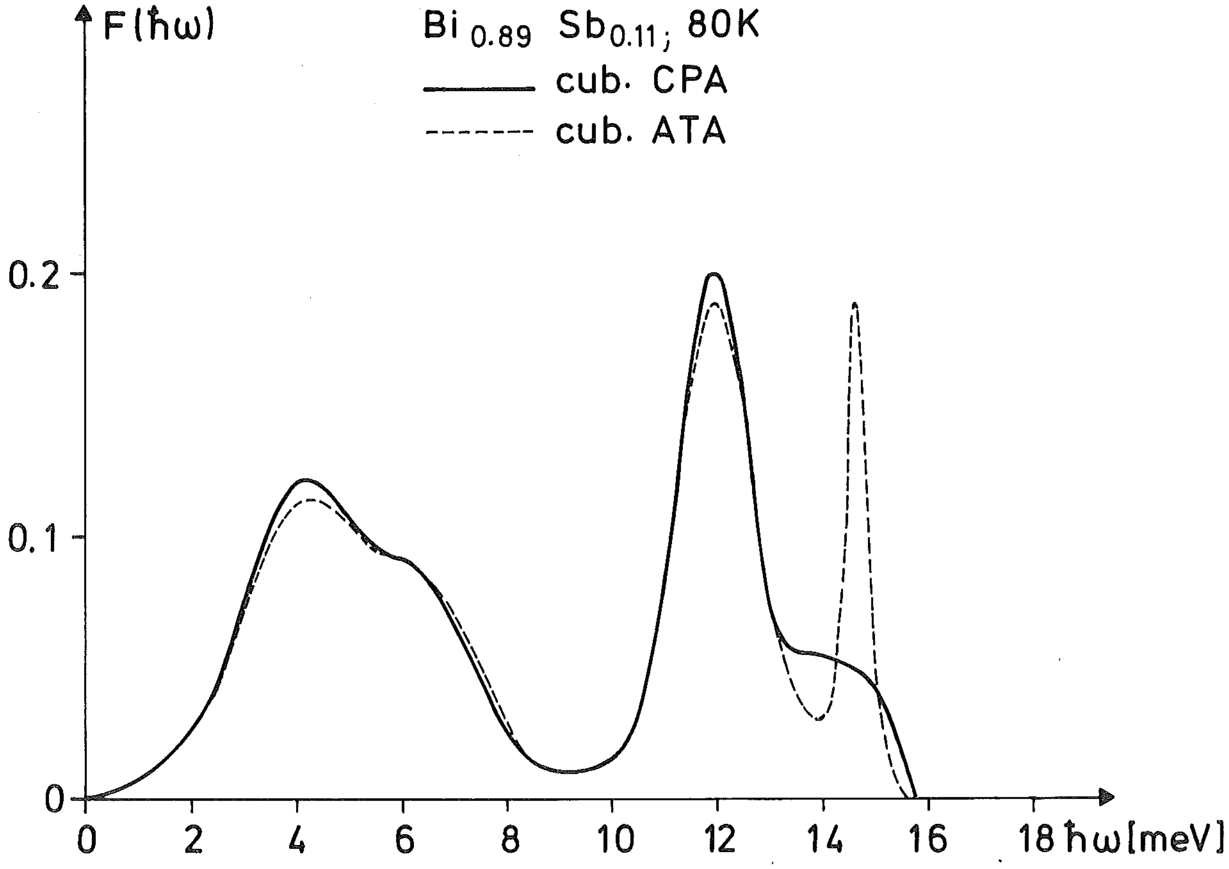

Fig. 2. Calculated phonon spectra for $Bi_{0.89}Sb_{0.11}$ starting from the Bi phonon density of states and assuming a cubic lattice: —— CPA; --- ATA.

The main discrepancies between both models occur in the upper part of the spectrum, the impurity band region. While CPA predicts only an additional shoulder attached to the high energy side of the optical peak, ATA gives a sharp extra peak centered at 14.7 meV almost separated from the in-band-spectrum, in good agreement with the experimental results. Taking into account a reduction of the impurity mode intensity by the smaller scattering cross section of Sb and resolution effects it may be suggested that the ATA model gives a more realistic description of the measured data than the CPA calculations.

## REFERENCES

/1/ F. Gompf, B. Hofmann and E. Schneider, in Progress Report of the Teilinstitut Nukleare Festköprperphysik, Ges. f. Kernforschung Karlsruhe (KFK 2183), p. 35 (1975).

## 1.20. $2k_F$-Modes in an One-Dimensional Peierls-System

*K. Käfer*

If an one-dimensional (1-D) electron-jellium system undergoes a Peierls distortion, i.e. develops a sinusoidal superstructure, the now broken continuous symmetry leads to a zero-frequency boson, which has been described by Fröhlich as a translation of the electronic charge-density wave (CDW) on a merely rearranging positive background /1/. Lee et al. have shown that this "Fröhlich mode" is identical with the phase mode, one of the two $2k_F$ phonons of the Peierls-phase ("phase mode" and "amplitude mode") which are generated by interaction of the $+2k_F$ and $-2k_F$ modes of the undistorted system /2/.

Substituting a lattice for the jellium, the distortion-induced gap in the electronic dispersion and thus the total energy of the system becomes dependent on the phase of the CDW: the travelling CDW is pinned and the Fröhlich mode reduces to an oscillation with a finite frequency $\omega_p$ around an energetically favourable position. The magnitude of $\omega_p$ depends on the commensurability of the original lattice constant with $\frac{2\pi}{2k_F}$. (A rough sketch is given in Fig. 1).

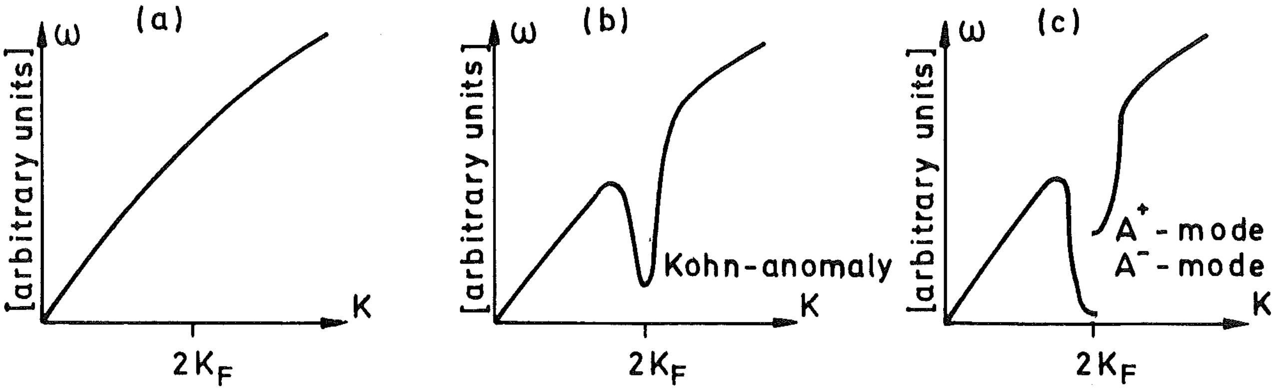

Fig. 1. (a) Bare phonon dispersion

(b) Screening by the electron system produces a Kohn-anomaly with $\omega(2k_F) = \sqrt{\frac{1}{2}\lambda}\ \Omega$.

(c) In the Peierls-phase coupling between the degenerate $2k_F/-2k_F$ phonons leads to a gap in the dispersion with the commensurability-pinned phase mode ($A^-$-mode), $\omega_- = \omega_p$, and the amplitude mode ($A^+$-mode), $\omega_+ = \sqrt{\lambda}\ \Omega$.

$\lambda$ is a measure for the electron-phonon coupling, $\Omega$ the unrenormalized phonon frequency.

Coulomb interaction has not been taken into account.

For a better understanding of this phenomenon we wanted to find out which mechanism in the "phonon picture" produces such a commensurability-dependent pinning. We could show that the above-mentioned $+2k_F/-2k_F$ coupling is still sufficient to explain this type of pinning. The finite frequency $\omega_p$ is due to the commensurability-enlarged gap in the electronic dispersion which leads to a reduced polarisability of the electron system.

Introducing coulomb forces into this 1-D model, the phase mode frequency is raised from the pinning frequency $\omega_p$ to $\sqrt{\frac{3}{2}\lambda}\ \Omega$, while the amplitude mode is unaffected /2/. Since in the Peierls phase the $2k_F$ modes can be regarded as zone-center optical modes, in a 3-D system of parallel chains the longitudinal and transversal phase mode are split (in analogy to the ionic crystal), and we expect three frequencies at $\underline{k} = (0,0,\pm 2k_F) + \underline{G}$ ($\underline{G}$ : reciprocal lattice vector of the undistorted system):

a) $\omega_p$ : transversal phase mode ($\underline{q} = \lim_{\varepsilon\to 0} (\varepsilon,\varepsilon,2k_F)$)
b) $\sqrt{\frac{3}{2}\lambda}\ \Omega$ : longitudinal phase mode ($\underline{q} = \lim_{\varepsilon\to 0} (0,0,2k_F+\varepsilon)$)
c) $\sqrt{\lambda}\ \Omega$ : longitudinal and transversal amplitude mode.

Since in KCP at temperatures below 100 K a Peierls correlation length of more than 100 Pt-Pt distances is well established /3/, we think that at those temperatures fluctuations no longer play an essential rôle, and the $2k_F$ neutron data /4/ should be explicable in terms of the above mean-field model. Preliminary calculations have shown that, despite the nominally steep dispersion of these modes, the horizontal tangents at $2k_F$ lead to intensities detectable by inelastic neutron scattering. Further investigations along these lines are in progress.

## REFERENCES

/1/ H. Fröhlich, Proc. R. Soc. A223, 296 (1954).

/2/ P. A. Lee, T. M. Rice and P. W. Anderson, Sol. State Commun. 14, 703 (1974).

/3/ J. W. Lynn, M. Iizumi, G. Shirane, S. A. Werner and R. B. Saillant, Phys. Rev. B12, 1154 (1975).

/4/ R. Comès, B. Renker, L. Pintschovius, R. Currat, W. Gläser and G. Scheiber, phys. stat. sol. B71, 171 (1975).
K. Carneiro, G. Shirane, S. A. Werner and S. Kaiser, Phys. Rev. B13, 4258 (1976).

## 1.21. Phonon Density of States of $K_2Pt(CN)_4Br_{.3} \cdot 3H_2O$ (KCP)

*F. Gompf and B. Renker*

The phonon density of states of the quasi one dimensional conductor $K_2Pt(CN)_4Br_{.3} \cdot 3D_2O$ has been studied by inelastic neutron scattering with special attention to the movements of the water molecules.

It is well known that the water in KCP is of large influence on the physical properties of the crystal. The transport properties change for instance by orders of magnitude dependent on the humidity /1/. By neutron structure analysis and NMR measurements /2, 3/ it is obvious that at least two essentially different binding potentials for water molecules exist in KCP. At room temperature the water molecules in the (110) plane are partially free for rotation whereas the onset of free rotation for the water molecules within the (100) plane has been observed only above 310 K /3/. The aim of the present experiments was to study these effects in the neutron time-of-flight (TOF) spectra by a comparison of the results for deuterated and non-deuterated samples. Hereby we make use of the large difference in the scattering cross sections $\sigma_{H_2O}/\sigma_{D2O} \approx 8$ and the difference in mass. Both measurements were performed at room temperature on the TOF 2 spectrometer with a primary energy of 5.05 meV.

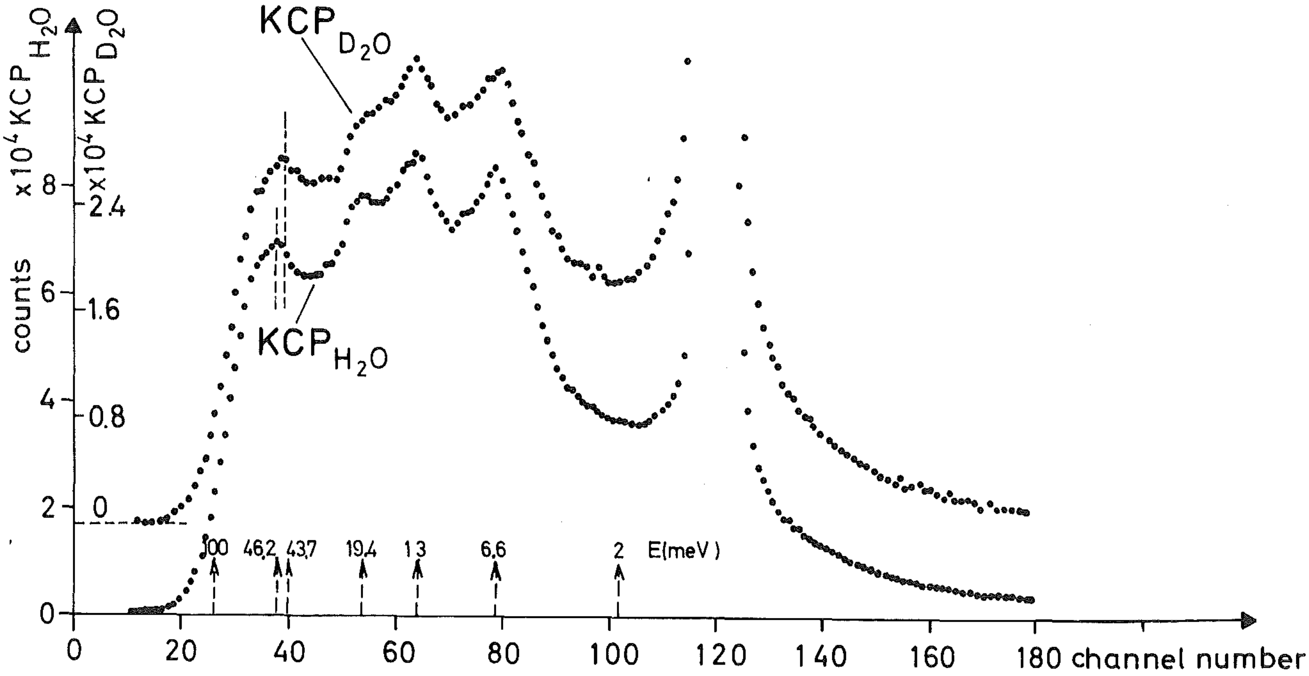

Fig. 1. Comparison of the TOF spectra of KCP with $H_2O$-content and $D_2O$-content.

Fig. 1 shows a comparison of the TOF spectra of both samples. Generally both spectra look very similar. No pronounced coherent scattering contributions were measured in the single detector TOF spectra and for all frequencies the ratio in the $KCP_{H_2O}$ and $KCP_{D_2O}$ scattering intensities is about the same and proportional to the different scattering amplitudes which means that the water molecules participate in most of the lattice modes.

The position of the first maximum at bout 6 meV agrees well with the frequency of the LA branch in [100] direction and the horizontal part of the dispersion branch at $q_z = 0.25$ where the curvature changes caused by the pronounced Kohn anomaly. The higher frequency peaks are due to optical modes. The $KCP_{H_2O}$ spectrum exhibits a maximum at 46.2 meV. This peak is likely to be caused by vibrations of the water molecules since, in fair agreement with the mass ratio of $\sqrt{78/20}$ and the smaller scattering cross section, a similar but less pronounced peak at 43.7 meV is measured in the $KCP_{D_2O}$ spectrum. Torsional excitations are expected at much lower frequencies. For these modes the shift in frequency should be about $\sqrt{2}$. Intensity which certainly can be attributed to such scattering processes is not found in the spectra of Fig. 1. The larger scattering close to the elastic line in $KCP_{D_2O}$ is probabely an effect of multiple scattering due to the thicker sample dimensions.

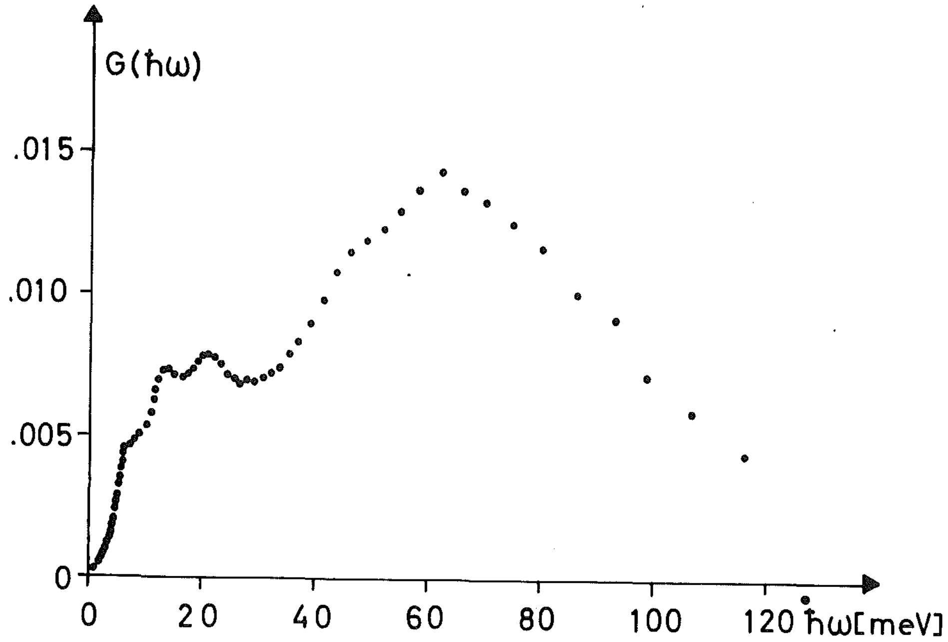

Fig. 2. The phonon density of states for $K_2Pt(CN)_4Br_{.3} \cdot 3H_2O$.

Fig. 2 shows the conversion of the TOF spectrum of $KCP_{H_2O}$ to the generalized phonon density of states G(ħω). Here Debye-Waller factor and multi-phonon corrections were taken into account.

These measurements will be extended by a more extensive study of the low frequency part of the G(ħω) spectrum.

REFERENCES

/1/ P. Würfel, H. D. Hausen, K. Krogmann and P. Stampfel, phys. stat. sol. 10, 537 (1972).

/2/ G. Heger, B. Renker, H. J. Deiseroth and H. Schulz, Mat. Res. Bull. 10, 217 (1975).

/3/ H. Launois and H. Njedoba, Nato Advantaged Study Institute on Low-Dimensional Cooperative Phenomena, Starnberg 1974, Ed. H. J. Keller, Plenum Press, N.Y., p. 259 (1975).

# Investigations of the Linear Conductor $(SN)_x$

## 1.22. Part I: Optical Studies of Electronic Transport Properties

*H. P. Geserich*[(a)], *W. Möller*[(a)] *and L. Pintschovius*

[(a)] Institut für Angewandte Physik der Universität Karlsruhe

Our efforts to grow large single crystals and thin films of $(SN)_x$ have been continued /1/. We succeeded in preparing orientated $(SN)_x$-films and investigated their optical properties in the visible and near infrared region. The results are published in a paper the abstract of which is given below.

### Optical Properties of Oriented $(SN)_x$-Films in the Visible and Near Infrared Region

*W. Möller, H. P. Geserich and L. Pintschovius*

Solid State Commun. 18, 791 (1976).

ABSTRACT:

Optical reflectance and transmittance measurements between 0.3 and 5.5 eV were performed on $(SN)_x$-films which showed a parallel orientation of the crystallites with respect to their polymer chain axis.

The optical behaviour below 3 eV for light polarized parallel to the chain axis, and in particular a strong absorption peak between 1 and 2 eV is explained to be a Maxwell-Garnett resonance of the free carriers. The influence of the free carriers is also observed for light polarized perpendicular to the chains and is analysed by the same model. From the anisotropy of the transport properties the interchain coupling is inferred.

These investigations have been continued on single crystals. Fig. 1 shows a plot of the reflectivity versus phonon energy for two different crystal faces. The fact that the reflectivity curves exhibit a plasma edge not only for light polarized parallel but also for light polarized perpendicular to the chains confirm our data taken from measurements on orientated films. It means that $(SN)_x$ has to be regarded as a highly anisotropic metal rather than a quasi one-dimensional conductor. The differences between the curves R 1 and R 2 is related to the anisotropy of the electronic transport properties within the plane perpendicular to the chains. The discussion of these results is included in a review with the following summary.

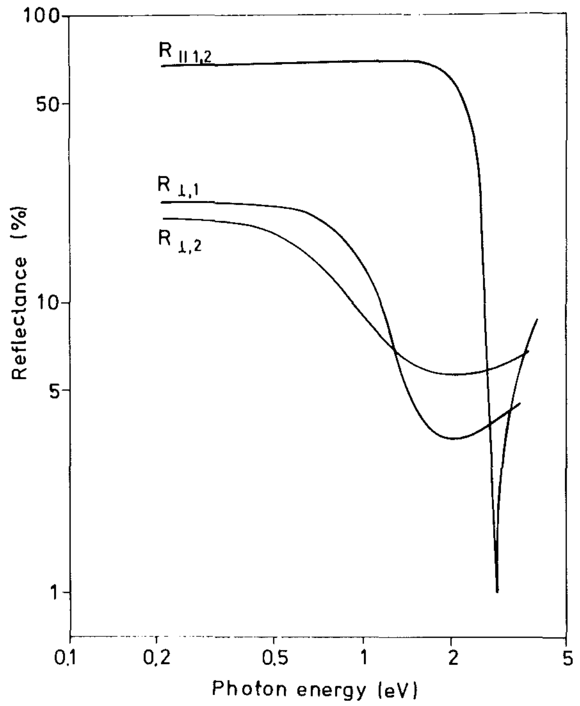

Fig. 1. Reflectance of $(SN)_x$ single crystals with different crystallographic orientation of the investigated surface. The surface corresponds to an (100) plane (1) and to a 50 percent mixing of (002) and $(\bar{1}02)$ planes (2). This mixing is due to the twinning of the crystals. $R_\parallel$ and $R_\perp$ : incident light polarized parallel and perpendicular to the chain axis.

### Polysulfur Nitride, A New Type of a One-Dimensional Conductor

*H. G. Geserich and L. Pintschovius*

in Festkörperprobleme XVI, Advances in Solid State Physics, E. Treusch, Pergamon-Vieveg, Braunschweig (1976).

Summary:

Polymeric sulfur nitride was the first substance of the class of quasi-one-dimensional metals which did not become insulating at low temperatures. It does not only retain its metallic transport properties but even becomes superconducting. The preparation and crystal structure is described and a review is given in the physical investigations of this material. Particular emphasis will lie on the influence of the real structure of the crystals on the physical properties and on their anistropy. This discussion makes comprehensible why the attribute "one-dimensional" should be used with caution for this particular material.

## 1.23. Part II: Lattice Dynamics

*L. Pintschovius, H. J. Stolz*[(a)], *H. Wendel*[(a)], *A. Otto*[(a)] *and H. Kahlert*[(b)]

[(a)] Max-Planck-Institut für Festkörperforschung, Stuttgart

[(b)] Ludwig-Boltzmann-Institut für Festkörperforschung, Wien (Austria)

The first attempt to investigate the lattice dynamics of $(SN)_x$ was made by Raman and IR measurements on polycrystalline films. The results are collected in the following publication:

On the Interaction between Chains in $(SN)_x$

*H. J. Stolz, A. Otto and L. Pintschovius*

Proc. III Int. Conf. Light Scatt. Solids, July 1975,
Campinas (Brasil.), Ed. M. Balkanski, R. C. C. Leite,
S. P. S. Porto, Flammarion Sciences, Paris (1976).

In this paper a number of phonon frequencies have been reported but their assignment remained doubtful due to the high number of defects present in these films. After the preparation of single crystals with volumes of a few mm$^3$ we started IR and Raman measurements on these samples and furthermore a neutron scattering study of their structure and lattice dynamics. The neutron investigations are extremely difficult not only because of the small size but also because of the poor quality of the crystals: In accordance with the findings of other authors /2, 3/ all crystals were found to be twinned and to have a very large mosaic spread for directions perpendicular to the chains (7 - 9$^\circ$ f.w.h.m.).

The first inelastic neutron scattering study was performed at the ILL Grenoble on a crystal of 5 mm$^3$ volume. In spite of the small size of the sample we were able to remeasure some of the results at the FR2 in Karlsruhe.

Later on the experimental conditions have been improved considerably when larger crystals with volumes up to 80 mm$^3$ became available. Nevertheless they are still very small for their use in an inelastic neutron scattering experiment

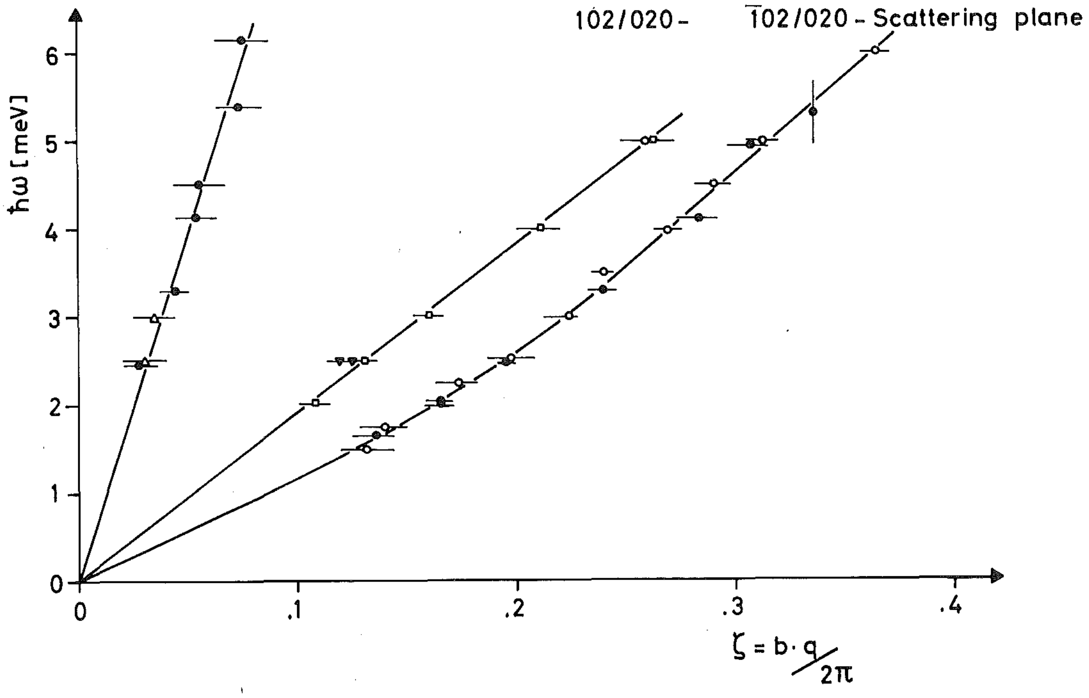

Fig. 2. Dispersion curve of phonons traveling in chain direction. Points refer to measurements at the HFR in Grenoble other symbols to measurements at the FR2 in Karlsruhe.

and therefore twelve crystals have been equally aligned with respect to all crystallographic axes and so we ended up with a sample of 0.2 cm$^3$ volume. The next run of the experiment has been performed at the FR2.

An important part of the data is plotted in Fig. 2, which shows the dispersion relation of phonons traveling in chain direction. The large differences between the slopes of the longitudinal and transverse branches and the upward curvature of the lower transverse branch point to a clear distinction in the strength of the interchain- and intrachain force constants. This is confirmed by a comparison of the velocities of sound for different crystallographic directions (see Table I).

Table I  Velocities of sound for different crystallographic directions measured in longitudinal (L) and transverse (T) configuration.

| Direction | $\upsilon_L$ (m/s) | $\upsilon_T$ (m/s) |
|---|---|---|
| [020] | 8300 ± 800 | 2000 ± 100<br>1200 ± 100 |
| [102] | 4000 ± 500 | 2400 ± 300<br>1350 ± 150 |
| $[\bar{1}02]$ | 3200 ± 200 | |
| $[\bar{2}02]$ | 2600 ± 300 | 1300 ± 200 |

Taking the optical and neutron data together, a preliminary analysis using a valence force model yielded the following results /4/.

1. The by far strongest forces connect atoms within the same chain.
2. The strongest interchain binding forces connect atoms within the $(\bar{1}02)$-plane, which is the plane of the polymer chains. The corresponding force constants are by one order of magnitude smaller than the largest intrachain force constants.
3. In directions approximately perpendicular to the $(\bar{1}02)$-plane the binding forces are rather weak. The corresponding force constants are by a factor of about 3 smaller than the largest interchain force constants.

Therefore, with respect to the lattice dynamics $(SN)_x$ can be regarded either as a quasi-one-dimensional system or as a layer-type crystal.

## 1.24. Part III : Neutron Diffraction Study of the Crystal Structure of $(SN)_x$

*G. Heger, S. Klein*[a]*, L. Pintschovius and H. Kahlert*[b]

[a] Sonderforschungsbereich 127, Fachbereich Geowissenschaften der Universität Marburg

[b] Ludwig-Boltzmann Institut für Festkörperforschung, Wien, Austria

The two available structure analysis of $(SN)_x$ by electron /2/ and X-ray diffraction /3/ led to considerably different results. Therefore we started a neutron diffraction study using the large crystals of the inelastic neutron scattering experiments. These measurements turned out to be particularly difficult due to the twinning and the very large mosaic spread of the crystals.

Powder measurements which can be performed more easily were not applicable for a structure determination due to the following reasons:

(i) Microcrystalline powders usually contain admixtures of several $(SN)_x$ modifications.

(ii) Single crystals of $(SN)_x$ consist of the wanted modification only, but nevertheless severe texture problems remain when pulverizing due to the chain structure.

(iii) As all crystals can be regarded as a parallel bundle of fibers, the diameters of which are typically a few 100 Å only, the Debye-Scherrer lines are considerably broadened.

Ten single crystals of $(SN)_x$ with volumes between 5 and 60 $mm^3$ were tested leading to the following overall results:

(i) The crystals are twinned with respect to the (100) mirror-plane. The two twinning components are almost equally sized.

(ii) Reflex-scanning around the chain direction (b-axis) leads to huge line widths (up to $9^\circ$ f.w.h.m.). The chain reflexes (OkO) on the other hand show normal linewidths. This strongly anisotropic mosaic spread means, that the crystal fibers are bundled together with large angles of tolerancy.

A complete three-dimensional data set of integral intensities was measured of both twinning domains using a 15 $mm^3$ $(SN)_x$ crystal. Particular precaution was taken to collect the entire intensity of each reflex.

With this set of relative intensities a structure analysis has been started. Preliminary results point to a good agreement with the model of Cohen et al. /3/ from their X-ray studies.

## REFERENCES

/1/ L. Pintschovius, in Progress Report of the Teilinstitut Nukleare Festkörperphysik, Ges. f. Kernforschung Karlsruhe (KFK 2183), 90 (1975).

/2/ M. Boudeulle, Thesis (unpublished), Lyon (1974).

/3/ M. J. Cohen, A. F. Garito, A. J. Heeger, A. G. MacDiarmid, C. M. Mikulski, M. S. Saran and J. Kleppinger, J. Am. Chem. Soc. 98, 3844 (1976).

/4/ H. Wendel, H. J. Stolz and L. Pintschovius, to be published.

## 1.25. Inelastic Neutron Scattering Study of β-Eucryptit ($LiAlSiO_4$)

*B. Renker, B. P. Schweiss and H. Schulz* [(a)]

[(a)] Max-Planck-Institut für Festkörperforschung, Stuttgart

Solid electrolyts - especially systems with high mobile $Li^+$ ions - are of considerable technical and theoretical interest because of possible applications in futural battery systems.

It has been shown that β-eucryptit ($LiAlSiO_4$) is a good $Li^+$ ionic conductor at high temperatures /1/. The crystal structure of this material corresponds to that of high quartz when half of the $Si^{4+}$ ions are replaced by $Al^{3+}$ ions. The charge is balanced by the incorporation of $Li^+$ ions in the main channels of the structure which are parallel to the c-axis /2/. Thus β-eucryptit is an example for an one-dimensional ionic conductor for temperatures above ≈ 460 °C.

The aim of the present investigation is to study the $Li^+$ motion below and above this transition temperature. Our measurements were up to now concentrated on polycrystalline material only and yield a generalized phonon density of states $G(\hbar\omega)$. Measurements were performed at the time of flight spectrometer TOF2 at the cold source with 5 meV incident neutron energy in the neutron upscattering mode. The average over a large region of scattering angles was taken in order to eliminate coherence effects. Fig. 1 shows the generalized $G(\hbar\omega)$ spectra obtained at 23 °C and at 500 °C. In the room temperature spectrum a sharp maximum in the scattering intensity is found at 10 meV a broader one at 25 meV and two less pronounced peaks around 40 and 55 meV. The open circles show the spectrum at 500 °C. This temperature is well above 460 °C where the superstructure reflections which correspond to an ordered arrangement of the $Li^+$ ions within the channels have disappeared. Both spectra were corrected for multiphonon contributions. The most pronounced change in the spectrum occurs around 10 meV, where the peak observed at room temperature has almost vanished.

We conclude from these first results that low lying optical vibrations of Li atoms in the room temperature phase are located mainly around 10 meV. Raman spectra /3/ show a broad asymmetric line at ≈ 20 meV which was tentatively attributed to the motion of the Li atoms. The reason for this discrepancy may be that we sample the whole Brillouin zone whereas the R-measurements register the zone center frequencies only.

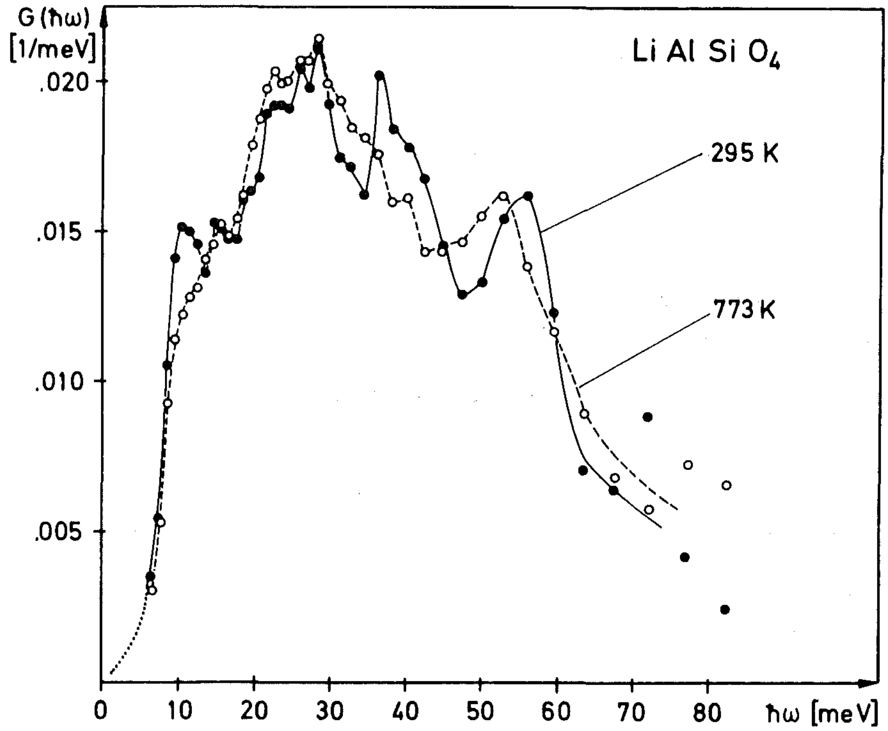

Fig. 1. Phonon density of states of β-eucryptit.

The diffusion of $Li^+$ ions in the channels should give rise to a diffusive broadening of the elastic line. Because of the small scattering cross section of Li compared to the rest of the atoms the corresponding effect may be small and difficult to observe. At least at 500 °C we do not observe a significant broadening which indicates a small diffusion constant at this temperature.

These measurements will be extended to higher temperatures. Furthermore detailed studies of dispersion branches and the diffusive motion of the $Li^+$ ions using a single crystal are in progress.

REFERENCES

/1/ R. T. Johnson, B. Morosin, M. L. Lnotek and R. M. Biefeld, Bull. Amer. Phys. Soc. 20, 330 (1975).
/2/ H. Schulz, J. Amer. Ceramic Soc. 57, 313 (1974).
/3/ B. Morosin and P. S. Peercy, Phys. Lett. 53A, 147 (1975).

## 1.26. Phonon Density of States of KCN

*K. Knorr*[a] *and N. Nücker*

[a] Universität Mainz, Institut für Physik

KCN shows some striking features due to the rotational degrees of freedom of the CN-molecules. At room temperature the CN-molecules are randomly orientated. Some low energy acoustic phonons could be measured by inelastic neutron scattering /1, 2/.The width of these phonons increases with energy making it difficult to observe the librational mode of the CN-molecules and the optical phonons. When lowering the temperature the $C_{44}$ elastic constant softens and becomes nearly zero at the first order phase transition at 168 K. The structure changes from cubic (NaCl like) to monoclinic and the crystal looses its transparency due to formation of domains. In this phase the CN-molecules are aligned in the $[110]$ direction. An isostructural phase transition occurs at 83 K when the CN-molecules order with respect to head and tail.

We have determined phonon densities of states using inelastic neutron scattering with time-of-flight technique. Measurements at 5 K, 145 K and 180 K were performed on IN4/HFR Grenoble and at 77 K on TOF2/FR2 Karlsruhe. The time-of-flight data were corrected for background (empty cryostat measurement) and counter efficiencies. Multiphonon scattering was taken into account in computing the phonon density of states. The resultant distributions (Fig. 1) contain the phonon contribution of potassium weighted by its scattering cross section to mass ratio $\sigma/M$ and of the CN-molecules weighted by their $\sigma/M$ ratio. The reliability of the experimental method is the better the more Brillouin zones are involved in the sampling process i.e. the greater the volume in Q-space. In the IN4 experiments the incident neutron energy was $E_o = 39.5$ meV and scattered neutrons were measured in an angular range from $8^o$ to $158.5^o$. According to this the sampling volume was limited to Q values: $0.6\ \text{Å}^{-1} < Q < 8.6\ \text{Å}^{-1}$. The data of the FR2 experiment at 77 K were: $E_o = 72$ meV and $7\ \text{Å}^{-1} < Q < 10\ \text{Å}^{-1}$.

The distribution of the 5 K result is dominated by three well defined peaks at 8, 16 and 21 meV. According to the phonon dispersion curves the structure at 8 meV has to be assigned to the transverse acoustic modes at the zone boundary while the longitudinal modes presumably contribute to the density beyond the first dip. Raman measurements by Dultz /3/ confirm that the peak at 16 meV is due to the librational modes of the CN-molecules. The peak at 21 meV is caused by the bulk of the optical modes. At higher temperatures the structure in the spectra is continuously washed out. This trend seems to be independent of the phase transitions and may be explained by severe damping of phonons due to large amplitudes of rotation of the CN-molecules. We still have some problems in determining the upper cutoff frequency due to a high frequency tail which may be caused by multiple scattering or incorrect multi-phonon corrections.

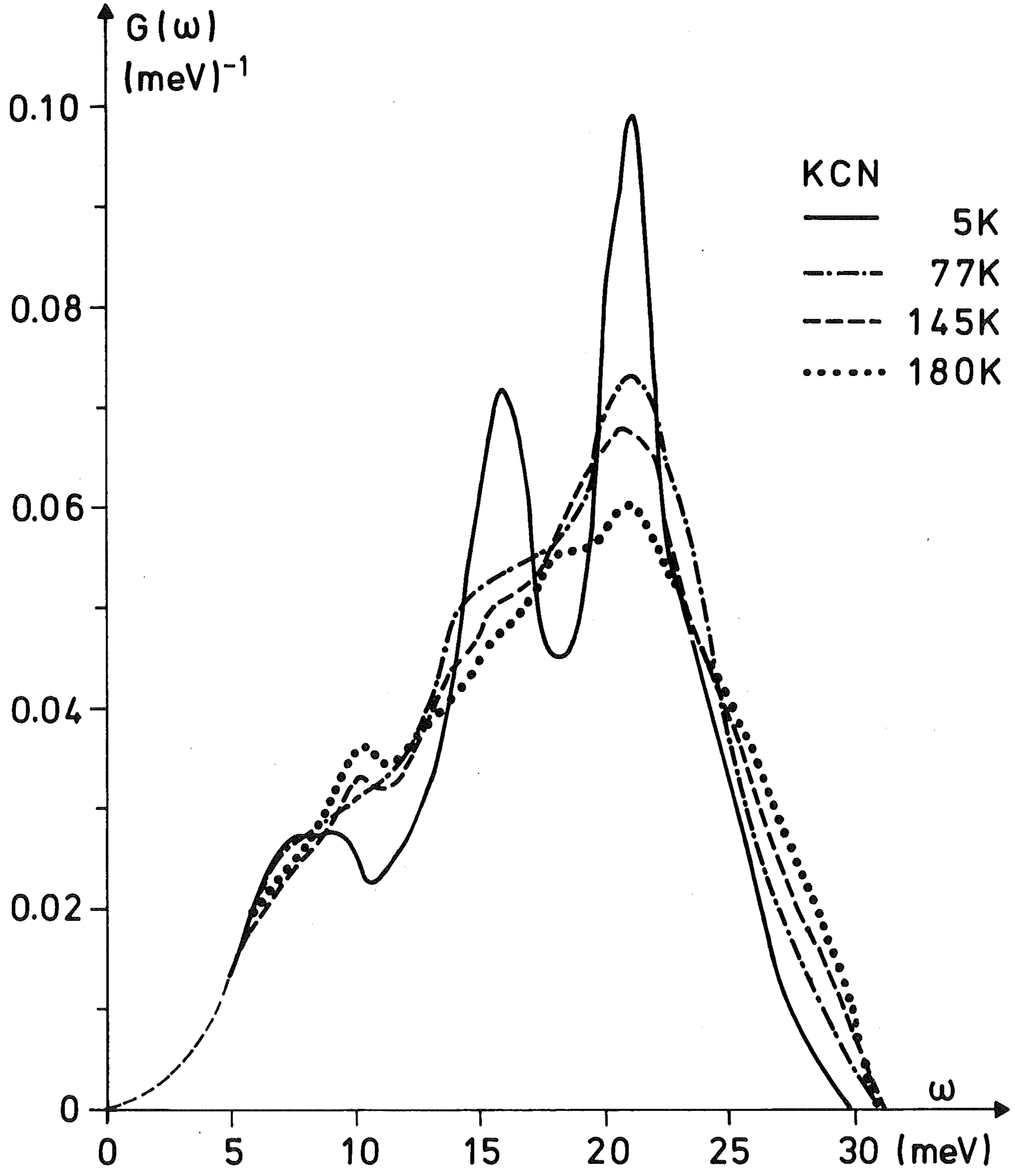

Fig. 1 Phonon density of states of KCN at 5 K, 77 K, 145 K and 180 K.

REFERENCES

/1/ J. M. Rowe, et al., J. Chem. Phys. 62, 4551 (1975).

/2/ J. Daubert, private communication.

/3/ W. Dultz, Sol. State Commun. 15, 595 (1974).

# Investigations of the Perovskite-Type Layer Structures $(C_nH_{2n+1}NH_3)_2MnCl_4$ with n = 1, 2.

## 1.27. Part I: Crystal Structures and Phase Transitions of $(CH_3NH_3)_2MnCl_4$ (≡ MAMC)

*G. Heger, D. Mullen*[(a)] *and K. Knorr*[(b)]

[(a)] Sonderforschungsbereich 127, Fachbereich Geowissenschaften der Universität Marburg

[(b)] Institut für Kristallographie der Universität Tübingen

The perovskite-type layer compounds $(C_nH_{2n+1}NH_3)_2MnCl_4$ show a variety of different structural modifications. For methyl-ammonium manganese chloride $(CH_3NH_3)_2MnCl_4$, abbreviated as MAMC, we continued our neutron diffraction investigations on the sequence of phase transitions /1 - 3/. Detailed structure analysis on single crystals lead to a complete description of these transitions including the special role of hydrogen bonding. The abstract of a publication is given below.

### On the Importance of Hydrogen Bonding for the Structural Phase Transitions in $(CH_3NH_3)_2MnCl_4$. A Single Crystal Neutron Diffraction Study

*G. Heger, D. Mullen and K. Knorr*

phys. stat. sol. (a) 35, 627 (1976).

ABSTRACT

The crystal structure of $(CH_3NH_3)_2MnCl_4$ (MAMC) was determined by neutron diffraction at 188 K in the low temperature tetragonal phase ($P4_2/ncm$). The sequence of structural phase transitions of MAMC can be discussed in terms of N-H...Cl bridges between $NH_3$ and certain $Cl^-$-ions. The order of the room temperature orthorhombic structure is determined by one dominant H-band and that of the low temperature tetragonal structure by three equivalent H-bridges.

## 1.28. Part II : Lattice Dynamics in Perovskite-Type Layer Structures: The Phonon Density of States of $(CH_3NH_3)_2MnCl_4$ ( ≡ MAMC)

*N. Lehner and G. Heger*

To study the lattice dynamics of MAMC we have extended our far infrared (= FIR) reflection investigations /4/ using inelastic neutron scattering. Powder measurements by the time-of-flight (TOF) technique on nondeuterated MAMC have been performed at 405 K of the high temperature tetragonal (I4/mmm), at 300 K of the orthorhombic (Abma), and at 77 K of the monoclinic modification.

Fig. 1 shows e.g. a time-of-flight distribution at 405 K measured in upscattering at the cold source of the FR2 with a primary energy of 5 meV. At this temperature the crystal has 27 degrees of freedom (including rotations of the $(CH_3NH_3)$-molecule as a whole, but excluding its internal vibrations). According to a high phonon damping the whole spectrum is smeared out. Additionally, there is a large number of multiphonon-excitations, so that the expected gap between 40 and 100 meV (i.e. between the external and internal vibrations) cannot be seen.

For the calculation of the phonon density of states from the measured TOF-spectra the program MUPHOCOR /5/ was used. There have been great difficulties because of the extraordinary large amount of multiphonon contributions and the

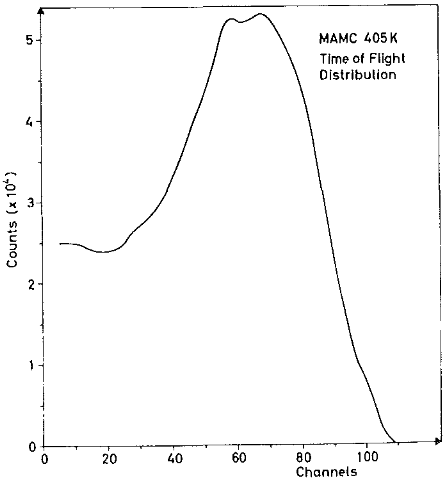

Fig. 1

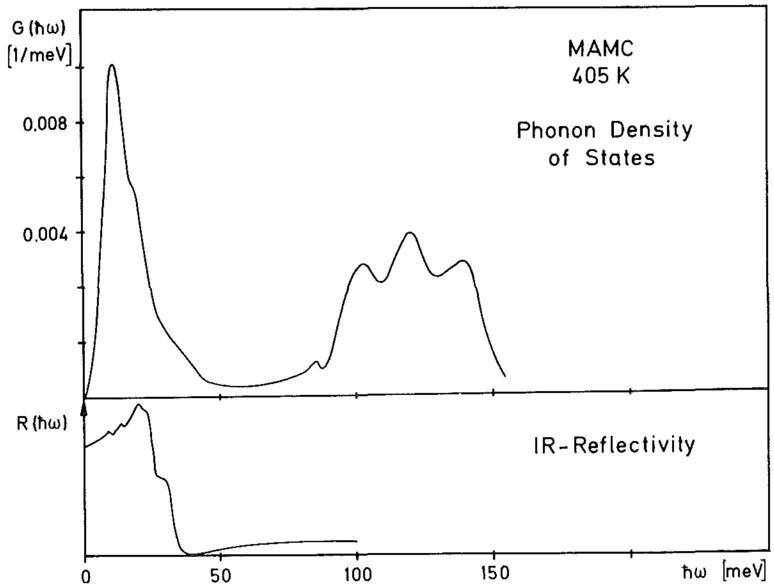

Fig. 2. Comparison of the results from neutron scattering and IR-measurements for $(CH_3NH_3)_2MnCl_4$ at 405 K.

high energy (up to 200 meV) of the internal vibrations. The resulting G(ħω)-curve is plotted in Fig. 2 together with the IR-reflection-spectrum for 405 K. At high frequencies it corresponds also with IR-data from Arend et al. /6/, which show that the IR-active internal vibrations lie above about 100 meV. Thus the neutron data give evidence for the same energy gap between the external and internal modes. Our results at 300 K exhibit the same general structure of the spectrum.

To get more detailed informations about the external vibrations, the TOF-measurements have been analysed again - only up to 50 meV - using a smaller energy mesh size in this region of good experimental resolution. The results are shown in Fig. 3 together with the measured IR-active vibrations in the upper part. It can be seen, that the region of the acoustic phonons ends at about 10 meV. At the same energy a high phonon density can be observed and the vibrations of the whole MnCl$_6$-octahedra are supposed at these frequencies. A comparison with the data for 300 K shows a hardening of the phonon modes at about 30 meV where the eigenfrequencies of the vibrations inside the MnCl octahedra are expected.

Fig. 4 shows the resulting G(ħω) for 77 K derived from energy loss TOF-measurements with a primary energy of 71 meV. Here the indicated hardening has continued and the concentration of the phonon density has drastically increased.

From the low temperature tetragonal modification (P4$_2$/ncm), the phase transition at 96 K leads to the monoclinic phase /7/. The resulting tilted arrangement within the layers of the MnCl$_6$-octahedra may cause the pronounced hardening observed at low temperatures.

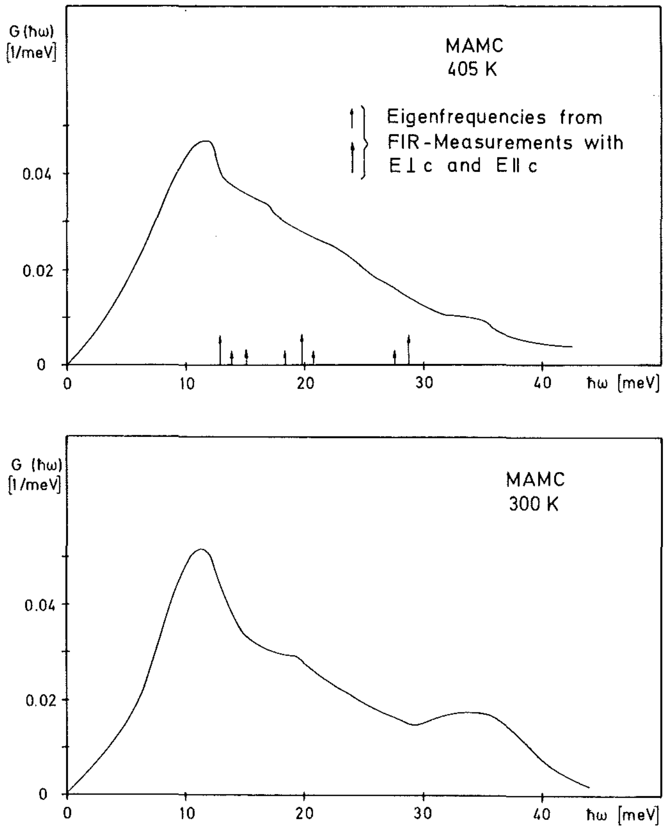

Fig. 3. Phonon density of states for (CH$_3$NH$_3$)$_2$MnCl$_4$ at 405 K and 300 K calculated only up to 50 meV.

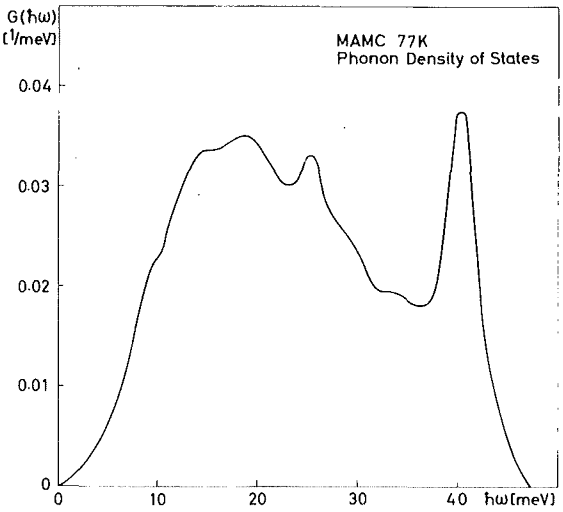

Fig. 4

## 1.29. Part III : Lattice Dynamics of Perovskite-Type Layer Structures: FIR-Studies of $(C_2H_5NH_3)_2MnCl_4$ ( ≡ EAMC)

*N. Lehner, R. Geick*$^{(a)}$*, K. Strobel*$^{(a)}$ *and E. Neumann*$^{(b)}$

$^{(a)}$Physikalisches Institut der Universität Würzburg

$^{(b)}$Laboratorium für Festkörperchemie, Universität Konstanz

In the family of the perovskite-type layer structures $(C_nH_{2n+1}NH_3)_2MnCl$ the first member is the MAMC (n = 1), which has been studied intensively e.g. by means of neutron diffraction (see this report), or FIR (= far infrared) reflection measurements /4/. Analogous FIR-experiments have been performed on ethyl-ammonium manganese chloride $(C_2H_5NH_3)_2$ $MnCl_4$ (≡ EAMC), the second member (n = 2).

The crystal structure of EAMC, shown in Fig. 1, is closely related to that of MAMC. At room temperature both have the same symmetry (space group Abma-$D_{2h}^{18}$). The only differences originates from the longer $C_2H_5NH_3$-molecules in EAMC, which separate the $MnCl_4$-layers even more than in MAMC. From X-ray investigations /8/ only the positions of the nitrogen- and carbon-atoms of these molecules are known, which stand for the $CH_3$-$CH_2$-$NH_3$-groups in the plot.

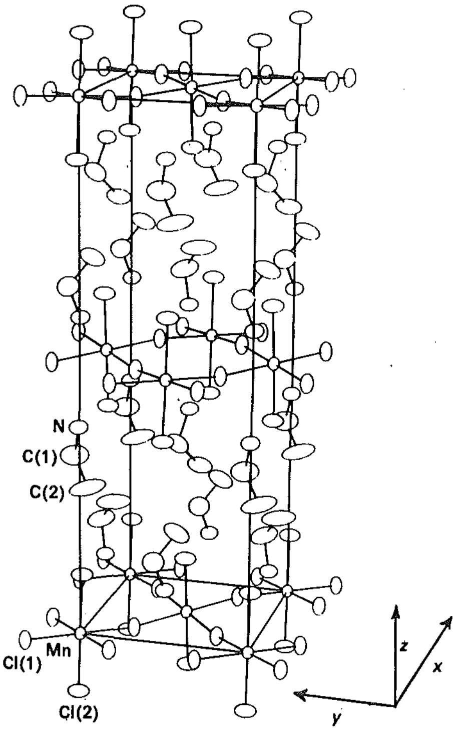

Fig. 1. Crystal structure of $(C_2H_5NH_3)_2MnCl_4$ at T = 300 K (W. Depmeier)

While MAMC is twinned at room temperature and lower temperatures, EAMC is not twinned and therefore it should be possible to separate the vibrations with E||a and E||b. Moreover in EAMC there is no monoclinic phase at lower temperatures /9/. For MAMC the continuous phase transition at 394 K is of special interest /2, 3/; a similar discontinuous transition takes place in EAMC /9/. For a better understanding of this phase transition the influence of the length of the organic chains on the frequencies of the IR-active lattice vibrations should be explored.

A set of reflection spectra for E||c is given in Fig. 2. The temperature dependence is similar to that in MAMC: at higher temperatures the spectrum is smeared out and the single modes are strongly damped, whereas at lower temperatures a number of sharp peaks is found. For EAMC at room tempereature group theory predicts 7 IR-active lattice vibrations, which can easily be found. For temperatures lower than 222 K there should be 14 IR-active lattiece vibrations, but some of them obviously have a very small oscillator strength and cannot be seen.

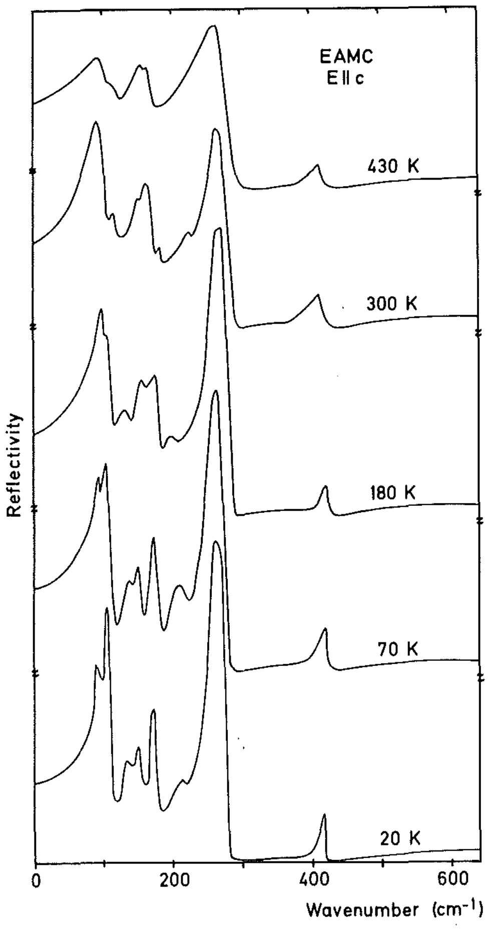

Fig. 2. FIR-reflection-spectra with $E\|c$ of $(C_2H_5NH_3)_2MnCl_4$ at various temperatures.

For a direct comparison of results from the isomorphous compounds MAMC and EAMC at room temperature the imaginary part of the dielectric constant is shown in Fig. 3. Whereas for MAMC the 14 expected frequencies $E\perp c$ are not resolvable (because of twinning $E\|a$ and $E\|b$ are mixed), for EAMC the results differ clearly. Nearly all the expected eigenfrequencies can be determined for $E\|a$ and $E\|b$. For $E\|c$ the 7 expected eigenfrequencies are found in the region of the external vibrations up to 300 $cm^{-1}$. The eighth at about 400 $cm^{-1}$ is found for all three polarisations. It is supposed to be an internal bending mode of the $C_2H_5NH_3$-molecule. This soft internal vibration, not present for the $CH_3$— $NH_3$ dump-bell molecules of MAMC, hinder the mobility of the $CH_3$-$CH_2$-$NH_3$-groups in EAMC. From this picture it can be understood that the phase transition is shifted to higher temperatures and at the same time becomes discontinuous.

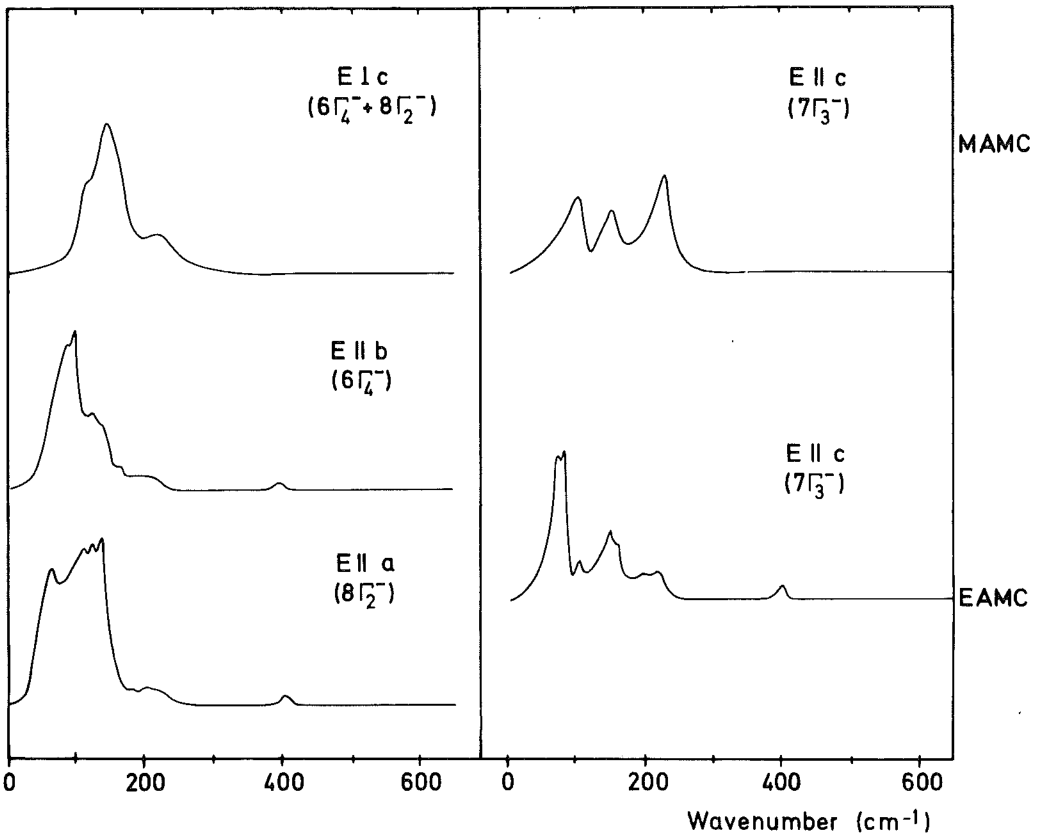

Fig. 3. Comparison of the room temperature FIR-results for MAMC and EAMC: imaginary part $\varepsilon_2$ of the dielectric constant.

REFERENCES

/1/ G. Heger, E. Henrich and B. Kanellakopulos, Sol. State Commun. <u>12</u>, 1157 (1973).

/2/ K. Knorr, I.R. Jahn and G. Heger, Sol. State Commun. <u>15</u>, 231 (1974).

/3/ G. Heger, D. Mullen and K. Knorr, phys. stat. sol. (a) <u>31</u>, 455 (1975).

/4/ N. Lehner, K. Strobel, R. Geick and G. Heger, J. Phys. C<u>8</u>, 4096 (1975).

/5/ J.-B. Suck and W. Reichardt, in Progress Report of the Teilinstitut Nukleare Festkörperphysik, Ges. f. Kernforschung Karlsruhe (KFK <u>2183</u>), p. 94 (1975).

/6/ H. Arend, J. Schoenes and P. Wachter, phys. stat. sol. (b) <u>69</u>, 105 (1975).

/7/ G. Chapüis, R, Kind and H. Arend (to be published in phys. stat. sol.)

/8/ W. Depmeier, Acta Crystl. B<u>32</u>, 303 (1976).

/9/ W. Depmeier, private communications.

## 1.30. Measurement of the Structure Factor of Liquid Rubidium by Neutron Diffraction up to 1400 K and 200 bar

*R. Block, W. Freyland*[(a)]*, W. Gläser*[(b)]*, F. Hensel*[(a)] *and J.-B. Suck*

[(a)]Fachbereich Physikalische Chemie der Universität Marburg

[(b)]Physik Department, Technische Universität München

The structure factor S(Q) is an important quantity in studies of the physical properties of a liquid between its triple and critical point. It gives information about the order of the system as a function of temperature and density; furthermore the electrical transport properties depend on the variations of the structure in a liquid metal. The knowledge of S(Q) may also allow to investigate the density dependence of the interaction potentials between the particles. In contrast to the liquid rare gases (e.g. Ar) a different behaviour is expected for a liquid metal when going to its critical point (for example a metal-non metal transition).

As a first step we measured the density dependence of the structure factor of liquid Rubidium by neutron diffraction techniques. 17 measurements were made near the saturation curve of the liquid-gas system in the temperature range between 450 K and 1400 K corresponding to a density from 1.42 $g/cm^3$ to 0.98 $g/cm^3$. The momentum transfers Q covered the range from 0.2 $Å^{-1}$ to 2.4 $Å^{-1}$.

To demonstrate the characteristic changes found for the structure factor of liquid Rb, 4 curves have been selected in Fig. 1. As a function of temperature and density the following significant changes in S(Q) have been observed: the height of the first maximum decreases from about 2.0 at 450 K to 1.12 at 1400 K. It also broadens with decreasing density. In the same temperature range the value of S(Q) for the lowest Q measured increases by a factor of 6. This is in good agreement with the compressibility data /1/. Furthermore we observe a clear shift in the position of the first maximum from 1.525 $Å^{-1}$ to 1.43 $Å^{-1}$. This reflects the change in mean distance due to the expansion of the liquid. It is interesting to note that a calculation with a hard sphere model /2/ gives the opposite results. The variations of the hard core radius going from $\sigma = 4.2245$ Å at 450 K to $\sigma = 3.75$ Å at 1400 K. Thus the hard sphere model seems not to give good results for the density dependence of S(Q). A realistic potential has to be chosen.

Having covered a large range in density for the structure factor it is interesting to compare the electrical conductivity determined by experiment /1/

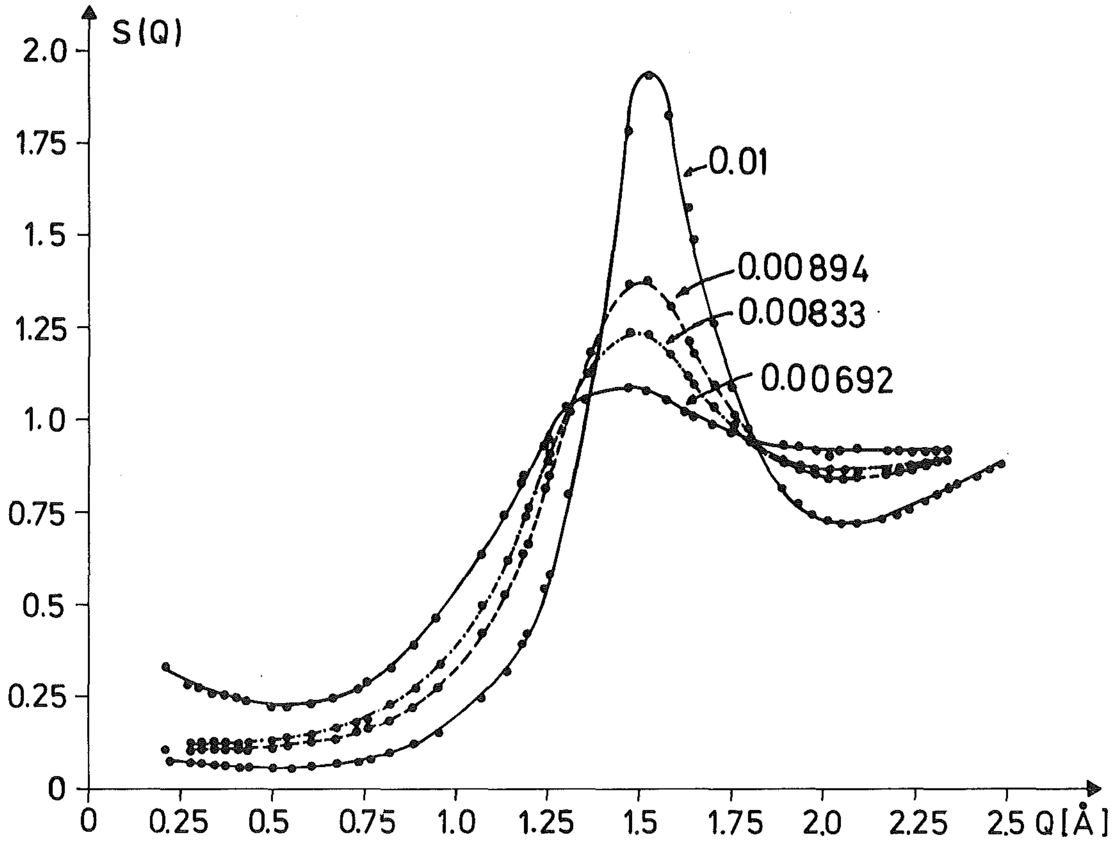

Fig. 1. S(Q) for liquid Rb at different densities.

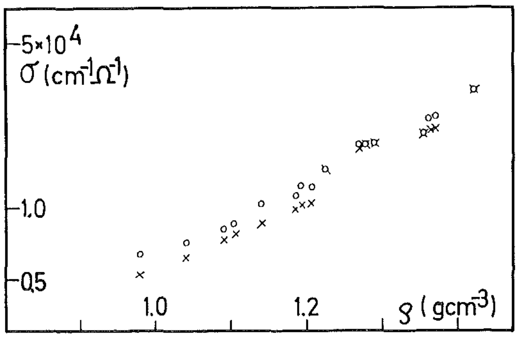

Fig. 2. o Ziman theory
x experimental data /1/

with the values predicted by Ziman theory /3/. For the pseudopotential we have taken the Ashcroft model with $r_c = 2.2$ a.u. screened by a dielectric function proposed by Heine and Abarenkov /4/. The results are plotted in Fig. 2. There is a good agreement with the theory.

## REFERENCES

/1/ N. Freyland (private communications).

/2/ N. W. Ashcroft and J. Lenkov, Phys. Rev. 145, 83 (1966).

/3/ J. M. Ziman, Phil. Mag. 6, 1013 (1961).

/4/ V. Heine and I. Abarenkov, Phil. Mag. 9, 451 (1964).

## 1.31. Extended Born-Green Equation: A New Approach for Determining Pair Potentials in Disordered Systems

*W. Abel, R. Block and W. Schommers*

The Born-Green equation was tested using molecular dynamics data for liquid rubidium at 319 K. The unsatisfactory results of this equation for the pair potential are caused by the insufficient precision of the Kirkwood approximation for describing the triplet correlation function $g_3(r,s,t)$.

In order to get a better pair potential it is necessary to improve the Born-Green equation. To obtain an extended Born-Green equation the ansatz /1/

$$g_3(r,s,t) = g(r)g(s)g(t) - \gamma(r)\gamma(s)\gamma(t) \tag{1}$$

was chosen because (i) the correction function $\gamma(r)$ can be determined experimentally and (ii) all calculated $\gamma(r)$ are similar. The latter point needs further

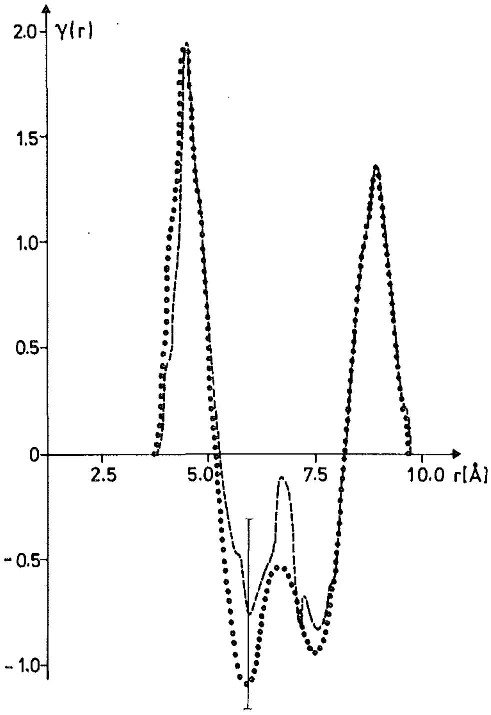

Fig. 1. The function $\gamma(r)$

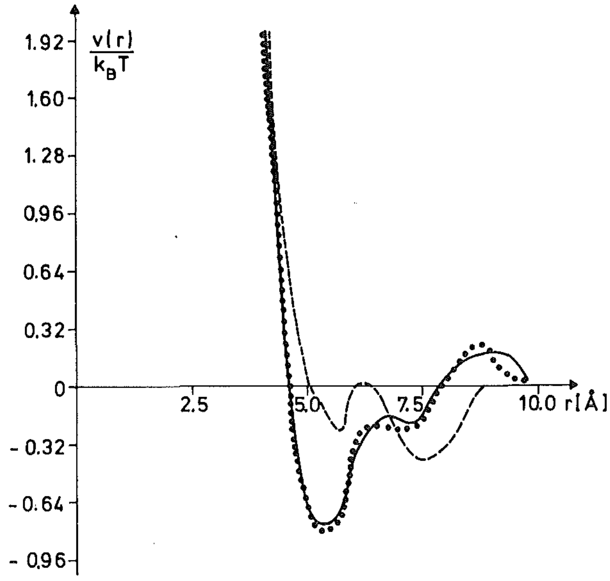

Fig. 2. Pair potential for Pb

explanation: using Eq. (1) and the molecular dynamics data for $g_3(r,s,t)$ and $g(r)$ one can determine $\gamma(r)$ directly. However, there are as many functions $\gamma(r)$ as configurations exist for $g_3(r,s,t)$. But it has been demonstrated /2/ that these functions are very much the same over large r-ranges.

The broken line in Fig. 1 shows the molecular dynamics results for a special $\gamma(r)$ with the best statistics. Already with this $\gamma(r)$ the extended Born-Green equation leads to an improvement of the potential compared to the results following from the simple Born-Green equation. By variation of $\gamma(r)$ (using an interactive graphical method /3/) within its error limits it is possible to generate a potential, which is in good agreement with the reference potential. Such a potential is shown in Fig. 2 by a dotted line. The corresponding function $\gamma(r)$ has been plotted in Fig. 1. From Fig. 2 it can be seen that the extended Born-Green equation leads to much better results for the pair potential than the simple Born-Green equation. Even the details in the reference potential are reproduced very well.

In order to get $\gamma(r)$ one has to know $\left[\partial g(r)/\partial p\right]_T$ which means that the pair correlation function $g(r)$ has to be studied as a function of pressure p at constant temperature T /4/.

## REFERENCES

/1/ P. A. Egelstaff, D. I. Page and C. R. Heard, J. Phys. C4, 1453 (1971).

/2/ R. Block, in Progress Report of the Teilinstitut Nukleare Festkörperphysik, Ges. f. Kernforschung Karlsruhe (KFK 2054), p. 35 (1974).

/3/ W. Abel, in Progress Report of the Teilinstitut Nukleare Festkörperphysik, Ges. f. Kernforschung Karlsruhe (KFK 2183), p. 93 (1975).

/4/ P. Schofield, Proc. Phys. Soc. 88, 149 (1966).

## 1.32. The Effect of van der Waals-Type Interactions in Metals: A Pseudopotential Model

*W. Schommers*

Z. Phys. B 24, 171 (1976)

ABSTRACT

A model has been developed for the long-range part of the ion-ion interaction of simple metallic many-particle systems. The investigation is based on the local pseudopotential theory. The essential point in the examination is the consideration of interactions of van der Waals-type in the determination of the direct ion-ion potential and the ion-electron pseudopotential. Numerical calculations performed for liquid rubidium near the melting point show that these interactions are distinctly reflected in the long-range part of the ion-ion potential. The reference potential used in the study had been calculated without parameters by means of the experimentally determined pair correlation function.

# 2. ELECTRONIC STRUCTURE AND MAGNETISM OF SOLIDS

## 2.1 Hyperfine Interactions at $^{61}$Ni Nuclei in the Mixed Compounds $Dy(Fe_xNi_{1-x})_2$ and $Dy(Fe_xNi_{1-x})_3$

*J. Fink, G. Czjzek, H. Schmidt and M. Morariu*[+]

A study of the mixed compounds $Dy(Fe_xNi_{1-x})_2$ (cubic C15 structure) and $Dy(Fe_xNi_{1-x})_3$ (rhombohedral $PuNi_3$ structure) by $^{61}$Ni Mössbauer spectroscopy was performed in supplement to an investigation of these materials by X-ray diffraction and Mössbauer spectroscopy with $^{161}$Dy and $^{57}$Fe at the Institut für Festkörperforschung, Kernforschungsanlage Jülich /1/.

The results obtained in this study for $Dy(Fe_{1-x}Ni_x)_2$ are summarized in Fig. 1 those for $Dy(Fe_{1-x}Ni_x)_3$ are shown in Fig. 2. In both cases we find for x = 1 a magnetic hyperfine field at $^{61}$Ni near 20 kG. The contribution due to Dy dipolar fields has been calculated to be between 5 and 10 kG in both compounds, the remaining field can be viewed as a transferred hyperfine field. The values indicate a 3d-moment at the nickel sites near 0.1 $\mu_B$ or less. The relatively large value of the effective electric quadrupole coupling constant in the cubic compound $DyNi_2$ indicates the presence of a noncollinear arrangement of the Dy moments. This could also explain the discrepancy between the bulk magnetic moment of 7 $\mu_B$ per Dy atom and the magnetic hyperfine field at $^{161}$Dy in $DyNi_2$ which corresponds to the free-ion moment of 10 $\mu_B$. The difference cannot be accounted for by a ferrimagnetic ordering of Dy and Ni moments, since the Ni moments certainly are too small.

The magnetic hyperfine fields at $^{61}$Ni rise rapidly upon addition of iron to both compounds (Figs. 1a, 2a) and also the effective electric quadrupole coupling constant changesstrongly at low Fe concentrations remaining approximately constant for $x \geq 0.3$ (Figs. 1b, 2b). In the mixed compounds we find quite large distributions of the magnetic hyperfine fields, with maximum width near x = 0.5, as expected in a random alloy.

For the compounds $Dy(Fe_xNi_{1-x})_3$ better fits to the spectra are obtained if we assume two nickel sites distinguished by different average values of the magnetic

---

[+] Guest scientist from: Institute for Atomic Physics, Bukarest, Rumänien hyperfine fields. These results are presented in Fig. 2a as well as the total averages assuming the same average field on all nickel sites. The difference between the fields on the 2 sites is (40 ± 2) kG, independent of iron concentration. As shown in Fig. 2c, however, the relative intensity $f_h$ of the high-field component does depend on x. This variation can in principle be explained by preferred occupation of one of the inequivalent lattice sites by Fe atoms. Yet no model based on this assumption gave quantitative agreement with the experimental variation of $f_h$ with x. The observed concentration dependence of $f_h$ can be explained quantitatively (continuous curve in Fig. 2c) if we assume that all sites are occupied at random by Fe or Ni atoms, and the low-field sites correspond to those Ni atoms on crystallographic h-sites having 2 or more Ni neighbours in the planes formed by these sites.

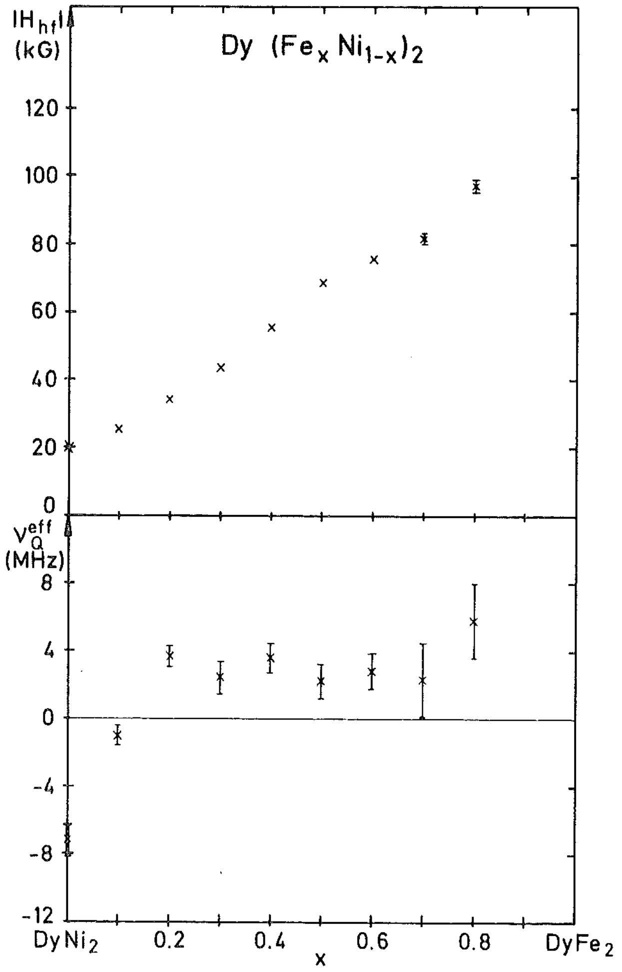

Fig. 1. Variation of hyperfine interactions at $^{61}$Ni with x in $Dy(Fe_xNi_{1-x})_2$ at 4.2 K. a) Average magnetic hyperfine field. b) Effective quadrupole coupling constants $\nu_Q^{eff} = \frac{1}{2} e^2 q Q \cdot (3 \cos^2 \theta - 1)$.

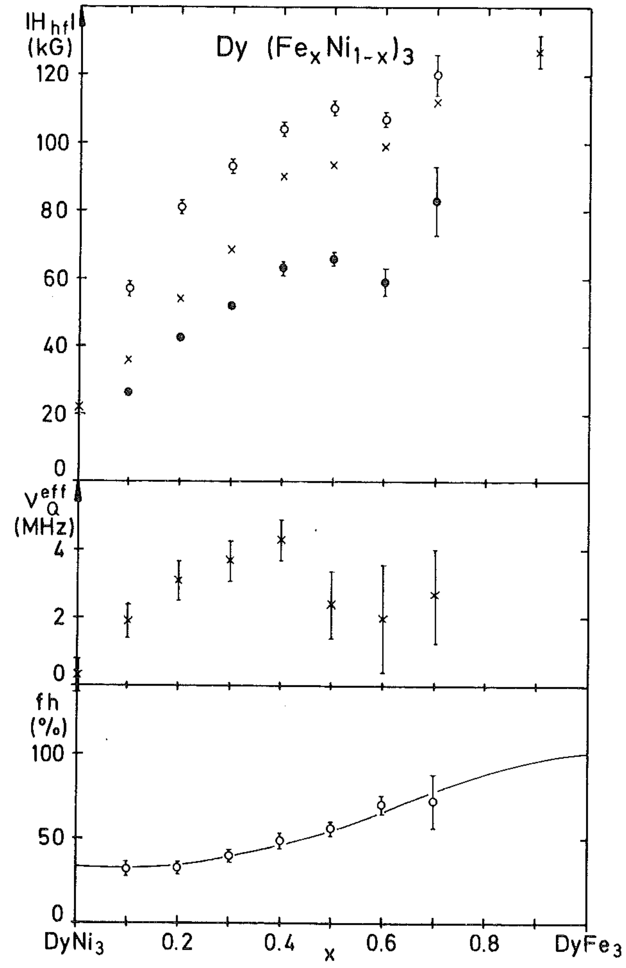

Fig. 2. Variation of hyperfine interactions at $^{61}$Ni with x in $Dy(Fe_xNi_{1-x})_3$ at 4.2 K. a) Magnetic hyperfine fields: x average values, o high-field sites, ● low field sites. b) Effective quadrupole coupling constants (only average values are shown as no significant differences between the 2 sites were found). c) Fractional intensity $f_h$ of the high-field sites.

REFERENCES

/1/ H. Maletta, G. Crecelius and J. Hauck, Institut für Festkörperforschung der KFA Jülich. All investigations were performed on the same samples, prepared at KFA Jülich. A preliminary report on the results obtained by $^{161}$Dy and $^{57}$Fe Mössbauer spectroscopy in Dy$(Fe_xNi_{1-x})_3$ was given by G. Crecelius and H. Maletta, Proceedings of the International Conference on Mössbauer Spectroscopy, Cracow, p. 149 (1975).

## 2.2 Hyperfine Interactions at $^{61}$Ni Nuclei in a PdNiFe Alloy

*G. Czjzek, J. Fink, H. Schmidt and I.A. Campbell*[(a)]

(a) Laboratoire de Physique des Solides, Université Paris-Sud, Orsay, France

In Pd-Ni alloys, the magnetic hyperfine field at $^{61}$Ni nuclei changes rather drastically from its value of -75 kG in pure nickel to about +175 kG in $Pd_{0.9}Ni_{0.1}$ /1/. One explanation for the large positive value could be given by a strong orbital field due to enhanced spin-orbit coupling in Pd-rich alloys. As this should also lead to a considerable electric field gradient and thus to a measurable quadrupole interaction, this hypothesis can be checked experimentally. We have begun a new study of this alloy system taking Mössbauer spectra with a sample of composition $Pd_{0.97}Ni_{0.015}Fe_{0.015}$, prepared with nickel enriched to 62 % $^{61}$Ni.

The spectrum taken at 4.2 K (Fig. 1) does show some asymmetry, however, the least-squares fit revealed, that the net electric field gradient is zero. The average magnetic hyperfine field is (159 ± 1) kG, smaller than the field in binary Pd-Ni alloys near the composition $Pd_{0.9}Ni_{0.1}$. There is a rather large distribution of magnetic hyperfine fields, the second moment of the distribution being (780 ± 60) $(kG)^2$. The asymmetry of the spectrum can be ascribed to a simultaneous distribution of electric field gradients with zero average, which however is correlated with the distribution of magnetic hyperfine fields. Such a correlation leads to an asymmetric broadening of the lines which can be described in the following way: For the $\ell$-th line whose position is $\upsilon_\ell = c_\ell \cdot H_{hf} + d_\ell E_Q$ ($H_{hf}$ is the magnetic hyperfine field, $E_Q$ the quadrupole interaction energy,

$c_\ell$ and $d_\ell$ are known coefficients determined by the nuclear moments), the linewidth $\Gamma_\ell$ is given by:

$$\Gamma_\ell = \left[\Gamma_0^2 + 8 \cdot M_2(H) \cdot (c_\ell + \beta_{HQ}\, d_\ell)^2\right]^{\frac{1}{2}} \quad ,$$

where $\Gamma_0$ is the natural linewidth, $M_2(H)$ is the second moment of the field distribution, and $\beta_{HQ}$ gives a measure for the correlation between electric field gradients and magnetic hyperfine fields. For $\beta_{HQ} = (-2.4 \pm 0.9)$ µm/sec/kG this field indicates the existence of perturbations of both charge density and spin density in the vicinity of Fe-atoms.

Further investigations of Pd-Ni and Pd-Ni-Fe alloys are in progress.

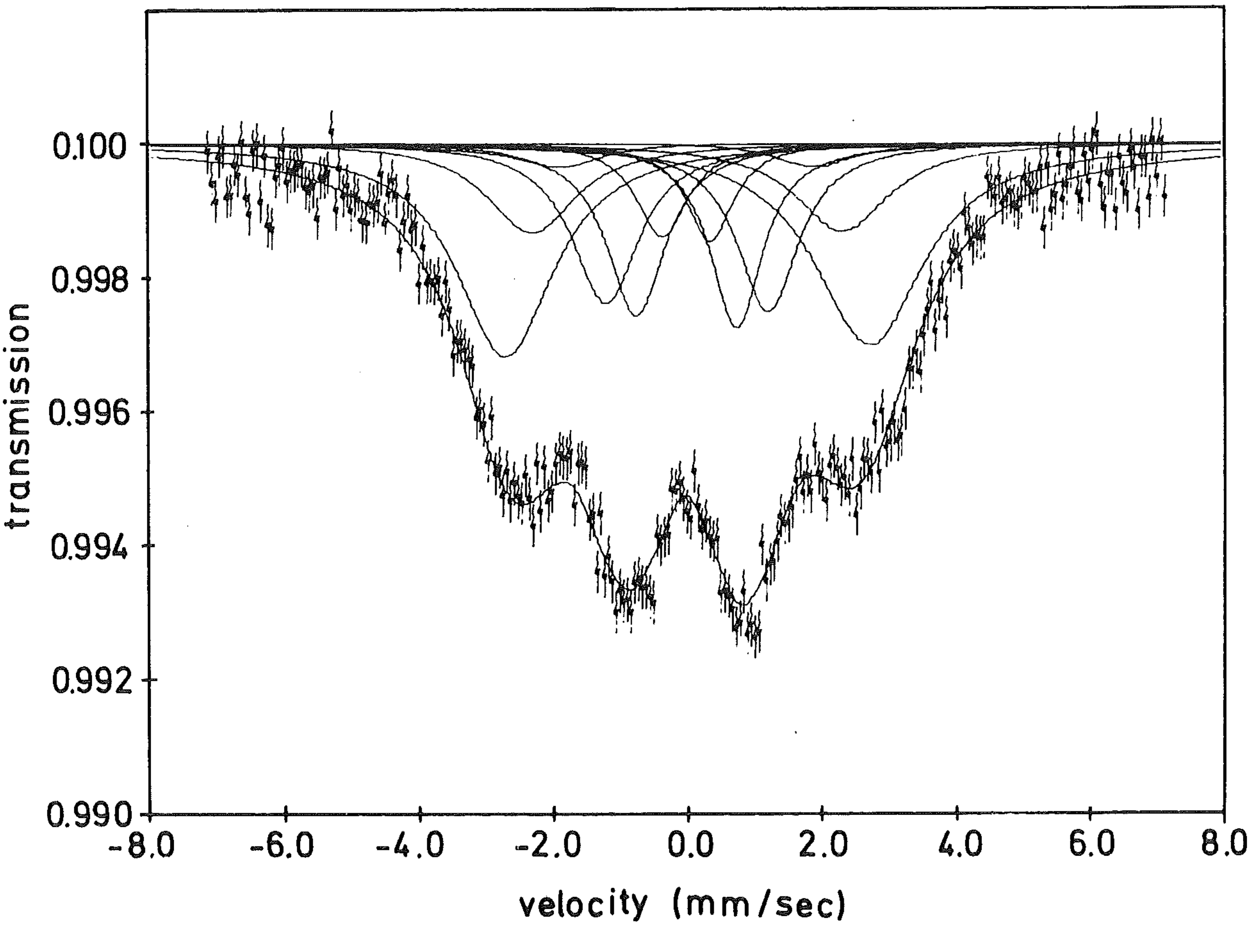

Fig. 1. $^{61}$Ni-Mössbauer spectrum in $Pd_{0.97}Ni_{0.015}Fe_{0.015}$ at 4.2 K. The continuous line is obtained by a least-squares fit with the Mössbauer transmission integral assuming a correlated distribution of hyperfine fields and electric field gradients.

REFERENCES

/1/ J. E. Tansil, F. E. Obenshain and G. Czjzek, Phys. Rev. B6, 2796 (1972).

## 2.3 An Investigation of Magnetic Ordering in $Gd_xCe_{1-x}Ru_2$ by $^{155}$Gd-Mössbauer Spectroscopy

*K. Ruebenbauer*[+]*, J. Fink, H. Schmidt and G. Czjzek*

The hyperfine interactions at $^{155}$Gd nuclei in mixed compounds $Gd_xCe_{1-x}Ru_2$ ($0.05 \leq x \leq 0.5$) with cubic C15-structure were studied by Mössbauer spectroscopy in the temperature region from 1.2 K to 60 K. The single-line $^{155}$Eu:Pd source described previously /1/ was employed in this work.

No change of the isomer shift over the entire range of concentration was found. Therefore, any line broadening observed must be ascribed to magnetic dipole and electric quadrupole interactions; broadening caused by variations of the isomer shift with local environment can be excluded.

At higher temperatures (for x = 0.05 at all temperatures down to 1.2 K) the absorption spectrum consists of a broadened line which could be fitted by a superposition of 2 components: A single line (as expected for the cubic Gd-sites in a pure compound) and a second component corresponding to a temperature-independent quadrupole interaction energy of about $3 \times 10^{-7}$ eV. The variation with x of the fractional intensity of the single-line corresponds quite well to the fraction $f_o$ of Gd atoms having only Ce or only Gd atoms in the first coordination shell as calculated for a random alloy, $f_o = (1 - x)^4 + x^4$.

In all samples with $x \geq 0.11$ an additional broadening of the spectrum occured below a temperature $T_M$ which increases linearly with x (Fig. 1a). For the higher Gd-concentrations ($0.18 \leq x \leq 0.5$) the values of $T_M$ coincide with the magnetic ordering temperatures determined by bulk susceptibility measurements /2/. Below $T_M$ the absorption spectra were fitted with the assumption of a static magnetic hyperfine field at the Gd-nuclei.

The temperature dependence of the magnetic hyperfine field is quite well described by molecular field theory for x = 0.5. However, as shown in Fig. 2, significant deviations from this temperature dependence occur for lower Gd-concentrations. Especially for the most dilute samples the temperature dependence of $H_{hf}$ is very similar to that of the order parameter predicted theoretically by K. H. Fischer for a spin glass /3/ and to experimental results in amorphous ferromagnets /4/. It is also in qualitative agreement with the behaviour inferred by Ø. Fischer and M. Peter from their measurements of the susceptibility above the

---

[+] Guest scientist from: Institute of Nuclear Physics, Crakow, Poland ordering temperature and from the specific heat /5/. We can very well describe our data by a molecular-field model with a temperature-dependent molecular-field constant as proposed in ref. /5/, or equivalently with the ansatz $\Theta(T) = \Theta_o + BT$, the ordering temperature being given by $T_M = \Theta_o + BT_M$. The curves in Fig. 2 are obtained by such fits to our data. The resulting values of B are shown in Fig. 1c, the saturation fields at T = 0 are given in Fig. 1b.

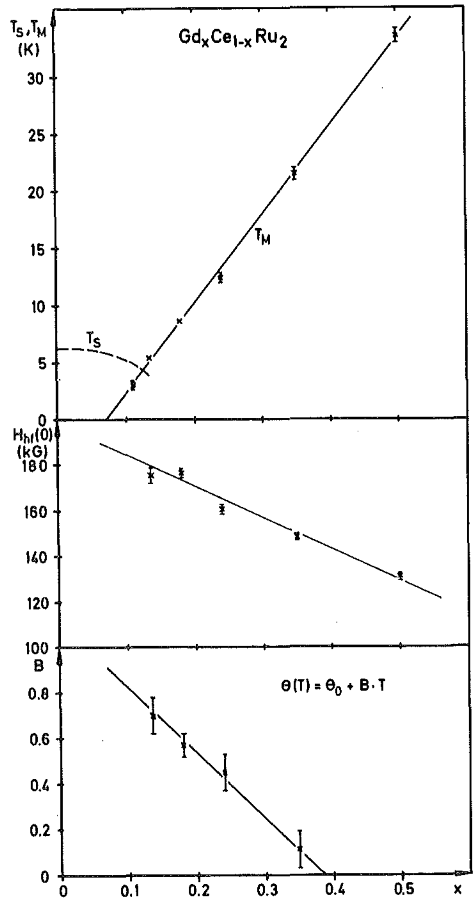

Fig. 1. Concentration dependence of (a) magnetic ordering temperature $T_M$, (b) magnetic hyperfine field at $^{155}Gd$ nuclei for T = 0, and (c) temperature factor B of the variable Curie-Weiß temperature $\Theta(T)$.

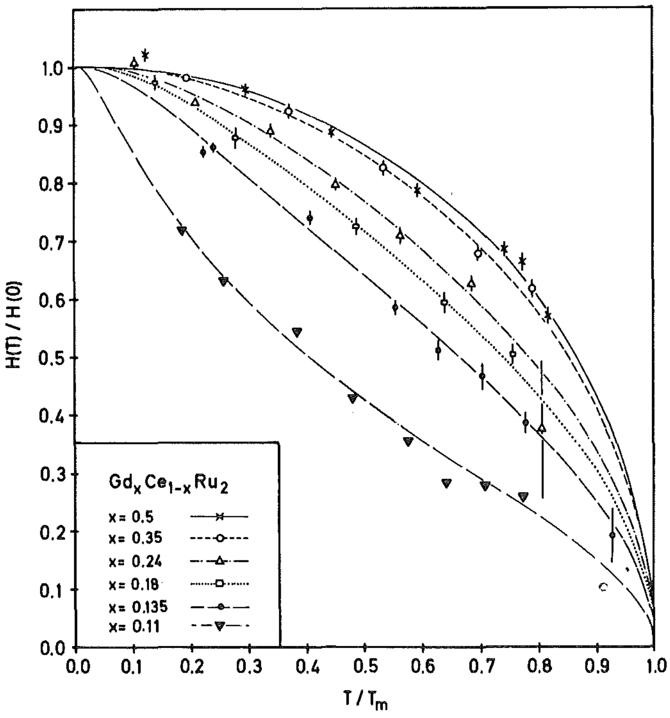

Fig. 2. Temperature dependence of the $^{155}Gd$ hyperfine field for several compounds $Gd_xCe_{1-x}Ru_2$. The solid line corresponds to the Brillouin function for $S = \frac{7}{2}$, the other lines are obtained by least-squares fits to the data as described in the text.

REFERENCES

/1/ J. Fink, K. Ruebenbauer, H. Schmidt, G. Czjzek, U. Berndt and C. Keller, in Progress Report of the Teilinstitut Nukleare Festkörperphysik, Ges. f. Kernforschung Karlsruhe (KFK 2183), p. 56 (1975).

/2/ M. Wilhelm and B. Hillenbrand, Z. Naturforschung 26A, 141 (1971).

/3/ K. H. Fischer, Phys. Rev. Lett. 34, 1438 (1975).

/4/ J. M. D. Coey, J. de Physique Colloque 35, C6 - 89 (1974).

/5/ Ø. Fischer and M. Peter, in Magnetism, Vol. 5, Ed. H. Suhl, Academic Press, New York and London, p. 327 (1973).

## 2.4. Crystal Electric Fields in Rare-Earth-$Al_2$ Compounds

*P. v. Blanckenhagen, H. Happel*$^{(a)}$*, K. Knorr*$^{(a)}$ *and A. Murani*$^{(b)}$

$^{(a)}$Physikalisches Institut der Universität Frankfurt

$^{(b)}$Institut Laue-Langevin, Grenoble, France

Polycrystalline samples of the intermetallic compounds $REAl_2$ (RE = Pr, Ho, Er, Tm) have been investigated by inelastic neutron scattering between 4.2 K and room temperature. Although there are several measurements on this system and on the related pseudobinary compounds $La_{1-y}RE_yAl_2$ and $Y_{1-y}RE_yAl_2$ /1, 2/ (and references therein), the CEF parameters published by different authors scatter considerably. To remove these discrepancies, we have continued the systematic investigation of the $REAl_2$ series by inelastic neutron scattering starting with $ErAl_2$ /3/. The measurements were performed with time-of-flight spectrometers at the FR2 and at the HFR Grenoble (IN7). The samples were investigated in the paramagnetic as well as in the ferromagnetic phase.

In $ErAl_2$ two resolved crystal field transition peaks are observed /3/. The intensity of the first peak at 4.5 meV is strongly temperature dependent. A determination of the crystal field parameters from the new results gives $x = +0.16 \pm 0.02$ and $W = (-0.030 \pm 0.005)$ meV which is a slight modification of the values given in /3/ but corresponds as well to negative CEF-parameters $A_4$ and $A_6$. The spectrum observed for $TmAl_2$ (Fig. 1) above the Curie temperature is consistent with these parameters.

For $PrAl_2$ and $HoAl_2$ in the paramagnetic phase, no crystal field transitions could be resolved due to a large linewidth of the quasielastic scattering. In the ordered phase at 4.2 K, transitions have been detected for all compounds investigated. An analysis of these data taking into account the crystal field parameters deduced from the paramagnetic phase and a molecular field is in progress.

The linewidth of the quasielastic scattered intensity in the paramagnetic phase has been investigated as function of momentum transfer Q and temperature. At $Q > 1$ Å$^{-1}$ the linewidth becomes independent of Q (Fig. 2) and a mean relaxation time may be estimated from it.

The data will be presented at the "2nd Conference on Crystal Field Effects in Metals and Alloys", September, Zürich, Switzerland.

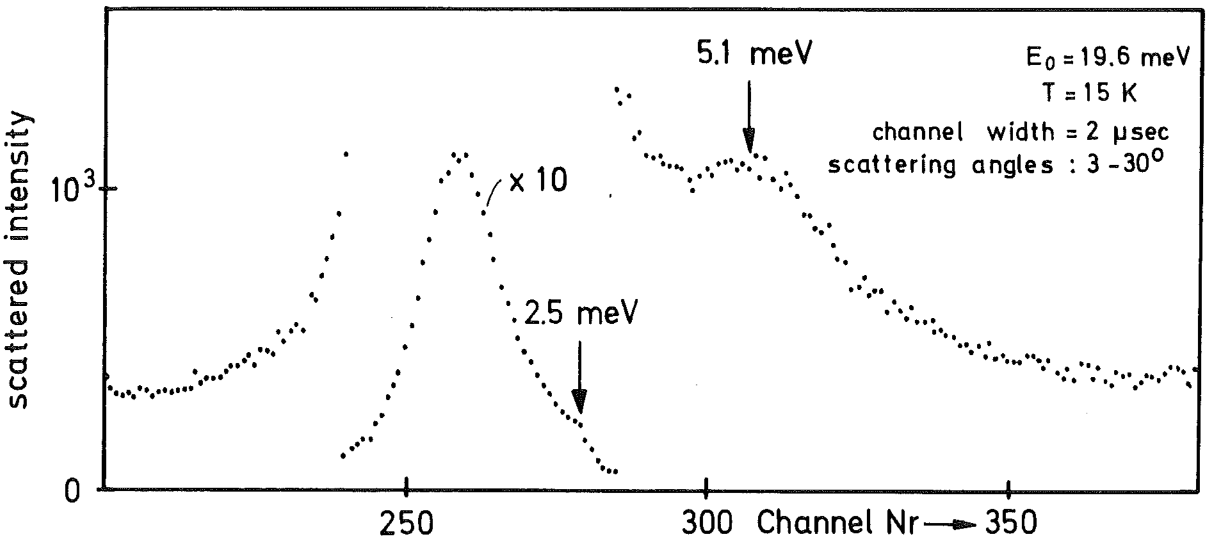

Fig.1: Time-of-flight spectra for Tm $Al_2$ (countingtime: 50 hours)

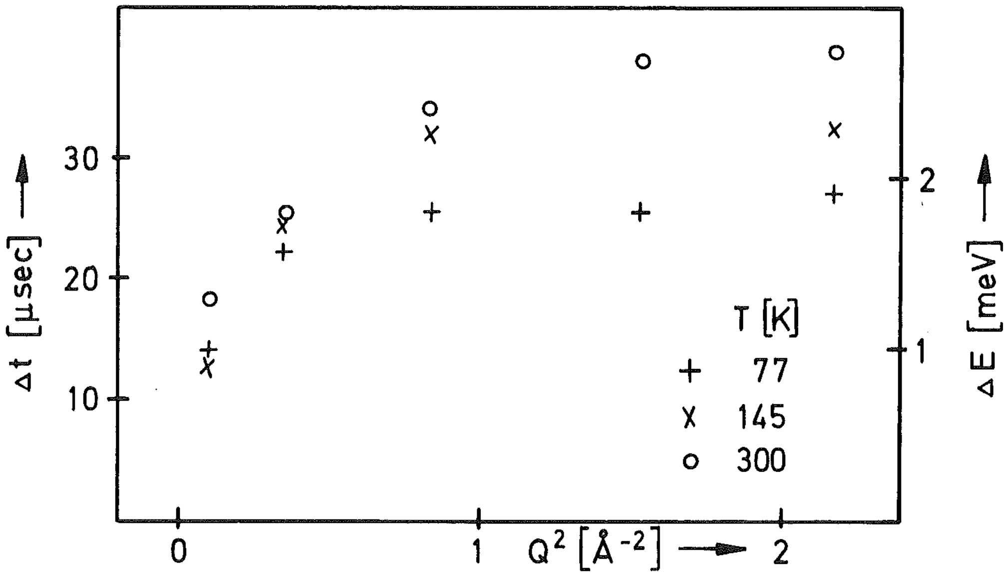

Fig.2: Line width of the quasielastic scattering from Pr $Al_2$ (corrected for instrumental resolution)

REFERENCES

/1/ P. Bak, Excitations and Magnetic Properties of Rare-Earth-$Al_2$ Compounds, Risö Report no. 132 (1974).

/2/ H. Happel, Dissertation, Universität Frankfurt (1975).

/3/ P. v. Blanckenhagen, C. v. Platen, H. Happel and K. Knorr, in Progress Report of the Teilinstitut Nukleare Festkörperphysik, Ges. f. Kernforschung Karlsruhe (KFK 2183), p. 54 (1975).

## 2.5. Short Range Antiferromagnetism in Superconducting $La_{1-y}Tb_ySn_3$ Detected by Neutron Scattering

*P. v. Blanckenhagen and H. E. Hoenig*[a]

[a] Physikalisches Institut der Universität Frankfurt

Measurements of the superconducting transition temperature $T_c$ and the magnetic susceptibility $\chi$ of polycrystalline $La_{1-y}Tb_ySn_3$ indicated a strong influence of the onset of antiferromagnetic coupling as derived from the Curie Weiss-temperature on $T_c$ /1/. From measurements of the susceptibility and the specific heat it is known that the ground state of $Tb^{3+}$ in these series of compounds is nonmagnetic, separated by ≈ 10 K from the next higher crystal field state /2/.

In this investigation we tried to find out what kind of magnetic order within these Van Vleck-ions coexists with the superconducting state (for $y < 0.2$). Therefore we performed neutron scattering experiments on polycrystalline $La_{1-y}Tb_ySn_3$ samples ($y = 0$; 0.085; 0.155; 0.25; 0.35) in the temperature range from 1.7 to 70 K and in magnetic fields ranging up to 4 T. Fig. 1 gives the angular dependence of the scattering intensity for the sample containing 15.4 % Tb. We observe broad peaks near the $(\frac{1}{2}00)$- and the $(\frac{1}{2}10)$-positions. Since these peaks are strongly field dependent (Fig. 3) and disappear at temperatures > 60 K (Fig. 2) we conclude that they are due to an antiferromagnetic superstructure of short range. The magnetic intensity around $(\frac{1}{2}00)$ is 6 % of the (111) nuclear intensity at 1.7 K. In the concentration range $0.15 \leq y \leq 0.35$ the magnetic correlation length is found to be of the order of 30 Å. For $y = 0.154$ and temperatures < 3.5 K the superconductivity coexists with an antiferromagnetic short range order of the Tb-ions. The averaged magnetic moment of the $Tb^{3+}$ ions is about $3\mu$, which is about $\frac{1}{3}$ of the moment of the free $Tb^{3+}$-ion.

We find consistency between the results obtained from neutron scattering and from the measurements of the susceptibility and the specific heat. The enhancement of the pair breaking is understood in the framework of the crystalline field theory for superconductors /3/ as an effect which arises from the moment dispersion of the crystal field excitation caused by exchange coupling of the $Tb^{3+}$ - ions.

### REFERENCES

/1/ H. E. Hoenig et al. Verhandlungen DPG (VI) 7, 720 (1976).

/2/ H. E. Hoenig et al. in Proc. 1. Conf. on CEF in metals and alloys (Ed. E. A. Devine), Montreal, p. 298 (1974).

/3/ P. Fulde and I. Peschel, Adv. Phys. 21, 89 (1972).

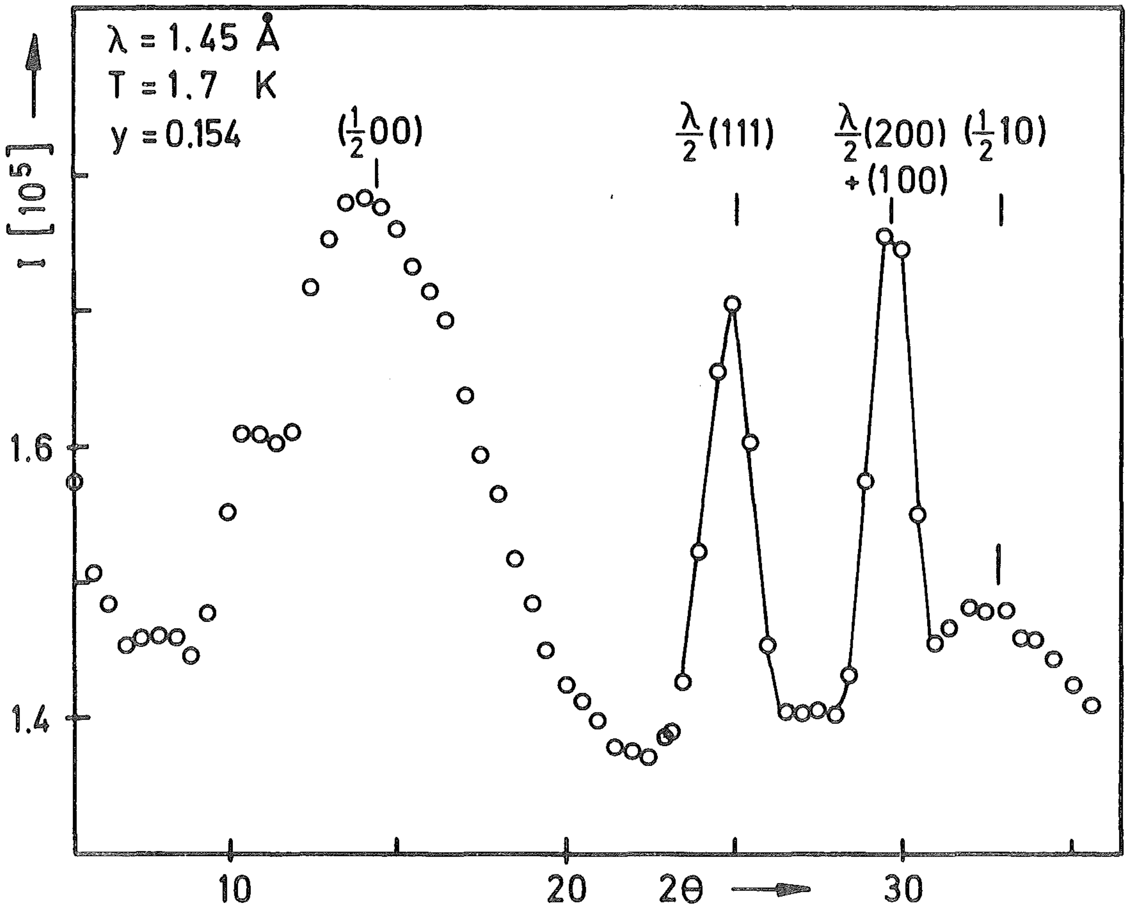

Fig.1: Scattered intensity (instrumental background subtracted)

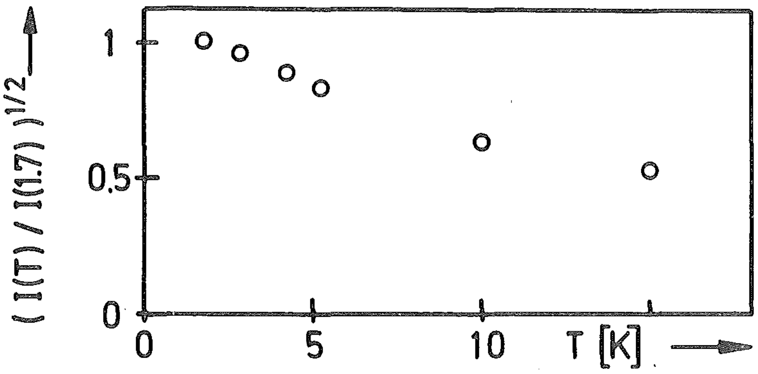

Fig. 2: Temperature - dependence of the magnetic intensity near the $(\frac{1}{2}00)$ position

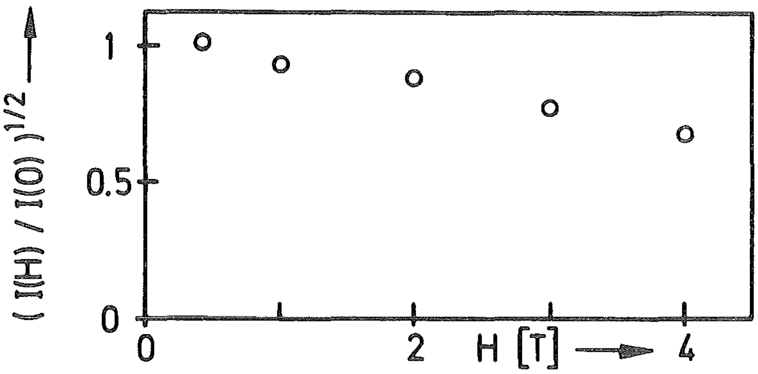

Fig. 3: Fielddependence of the intensity near the $(\frac{1}{2}00)$ position (H ⊥ to the scattering plane)

## 2.6. Investigation on Structural and Magnetic Properties of the Intermetallic System $(Cr_{1-x}Fe_x)_{1+\delta}Sb\,(o \leq x \leq 1)$

*G. Heger, E. Hellner*[(a)]*, D. Mullen*[(a)] *and W. Treutmann*[(a)]

[(a)] Fachbereich Geowissenschaften der Universität Marburg

Combined X-ray and neutron diffraction studies on single crystals of $(Cr_{1-x}Fe_x)_{1+\delta}Sb\,(0 \leq x \leq 1)$ /1/ have now been extended over the whole composition range.

The crystallographic data of the partially filled NiAs-type structures (space group $P6_3/mmc$ - Fig. 1) are summed in Table I. Since iron and chromium have closely similar X-ray scattering factors, it was possible to determine the occupancies of these metals at the interstitial 2(c) sites by X-ray diffraction. Using these $\delta$-values the neutron data yield the chromium-to-iron ratios in the 2(a) $(0,0,0;\ 0,0,\frac{1}{2})$ and 2(c) $(\frac{2}{3},\frac{1}{3},\frac{1}{4};\ \frac{1}{3},\frac{2}{3},\frac{3}{4})$ sites. Samples for X-ray and neutron diffraction were taken from the same run of crystal growth.

Cell constants for the whole overall composition range are plotted in Fig. 2. Fig. 3 shows the variation of $\delta$ with the overall composition. A peak in $\delta\,(\delta \approx 0.26)$ occurs at about 50 % Fe. With $50 < \%\ \text{Fe} < 100$, $\delta$ decrease to values between 0.19 and 0.23. For the range $50 > \%\ \text{Fe} > 20$, $\delta$ falls to values between 0.18 and 0.20. For overall compositions < 20 % Fe a sharp drop to almost zero for pure $Cr_{1+\delta}Sb$ $(\delta = 0.02)$ occurs. For $Fe_{1+\delta}Sb$ values of $\delta$ between 0.20 and 0.25 have been found. Errors for $\delta$ are about 0.02.

The relationship between the Cr : Fe ratios in the 2(a) and 2(c) sites in Fig. 4 shows three different regions: a constant iron content of about 55 % in the 2(c) sites when the 2(a) iron occupancy is between 10 and 30 %; a sharp peak in the iron content of the 2(c) site as the 2(a) iron accupancy changes from 30 to 50 %; and a region of variable 2(c) iron occupancy when the 2(a) occupancy is greater than about 50 % iron.

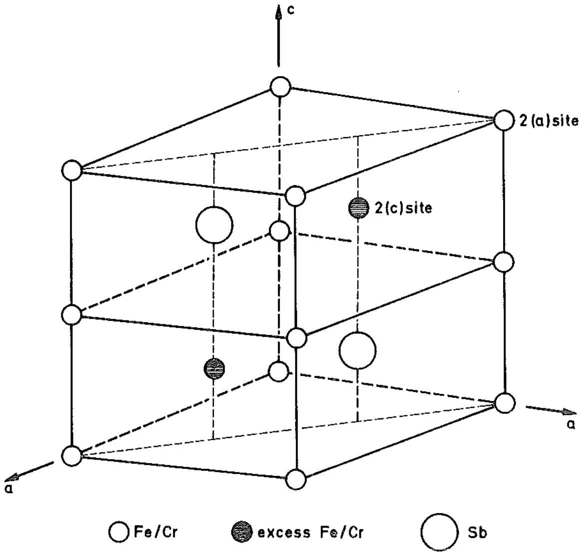

Fig. 1. Unit cell of NiAs-type structure.

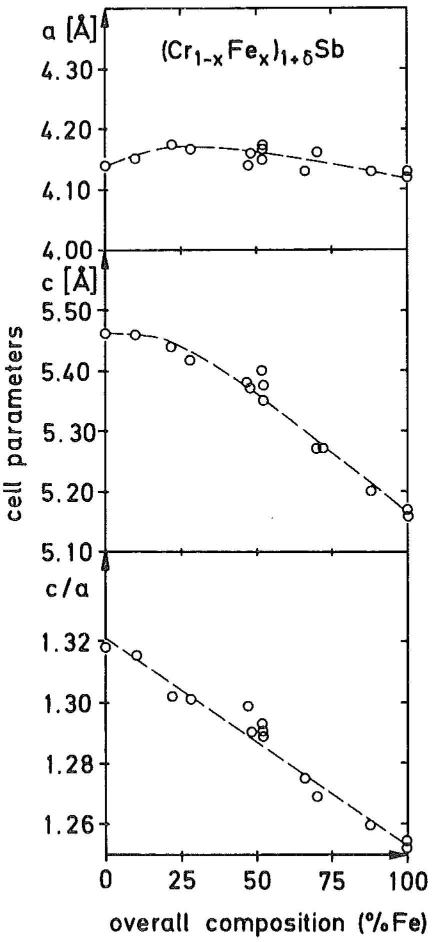

Fig. 2 Cell constants over the composition range 0 ≤ x ≤ 1.

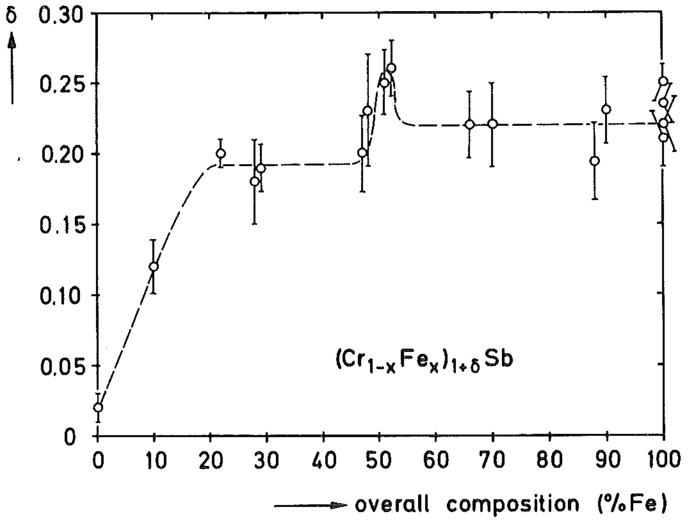

Fig. 3 Variation of δ over the composition range 0 ≤ x ≤ 1.

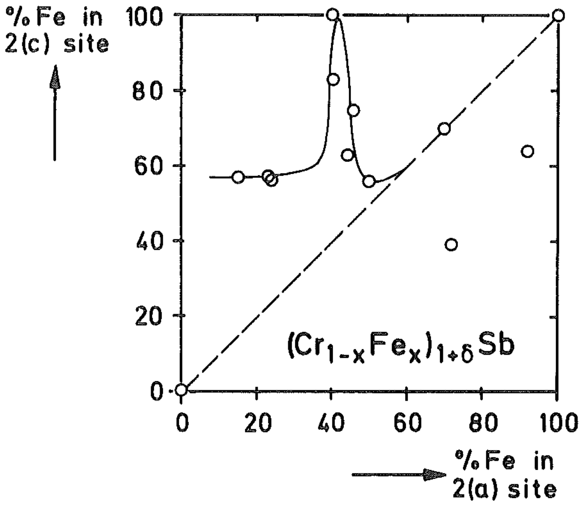

Fig. 4 Variation of Cr:Fe ratios in 2(a) and 2(c) sites (0 ≤ x ≤ 1).

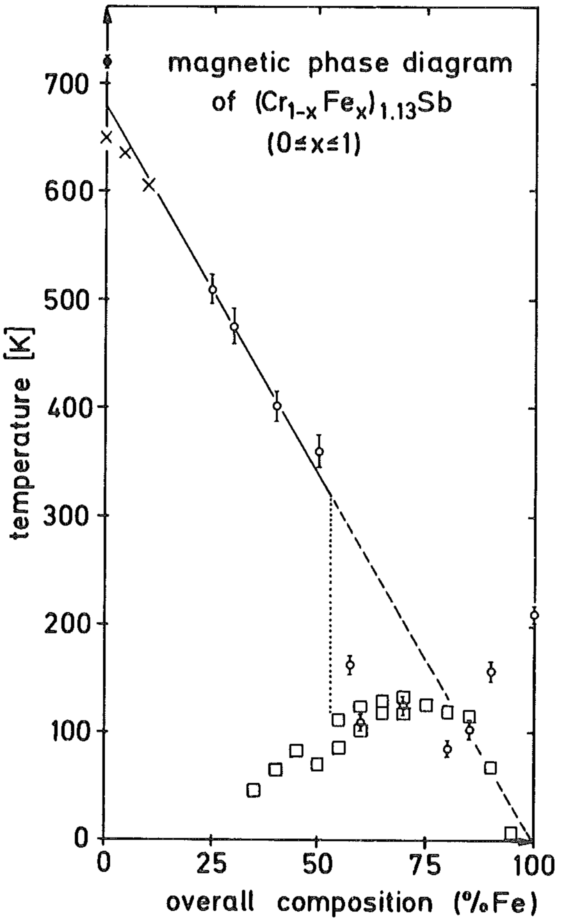

Fig. 5 Magnetic phase diagram. Néel-temperatures (Φ/2/,x/3/) and paramagnetic Curie-temperatures (□/4/) from susceptibility measurements and ordering temperatures (Φ/5/) from Mössbauer spectroscopy.

Table I Structural data for the system $(Cr_{1-x}Fe_x)_{1+\delta}Sb$ ($0 \le x \le 1$).

| Crystal No. | Composition | Occupancy | | Cr : Fe Ratios | |
|---|---|---|---|---|---|
| | | 2(a) Site | 2(c) Site | 2(a) Site | 2(c) Site |
| 10BR1 | $Fe_{1.22}Sb$ | (1.00) | 0.22 ± 0.019 | 0 : 100 | 0 : 100 |
| 10BR6 | $Fe_{1.21}Sb$ | (1.00) | 0.21 ± 0.020 | 0 : 100 | 0 : 100 |
| 10BR8 | $Fe_{1.25}Sb$ | (1.00) | 0.25 ± 0.014 | 0 : 100 | 0 : 100 |
| 10BR11 | $Fe_{1.24}Sb$ | (1.00) | 0.24 ± 0.014 | 0 : 100 | 0 : 100 |
| 9BR1 | $(Cr_{0.12}Fe_{0.88})_{1.19}Sb$ | (1.00) | 0.19 ± 0.028 | 8 : 92 | 36 : 64 |
| 7BR1 | $(Cr_{0.30}Fe_{0.70})_{1.22}Sb$ | (1.00) | 0.22 ± 0.030 | 30 : 70 | 30 : 70 |
| 7BR5 | $(Cr_{0.34}Fe_{0.66})_{1.22}Sb$ | (1.00) | 0.22 ± 0.024 | 28 : 72 | 61 : 39 |
| 5BR1 | $(Cr_{0.53}Fe_{0.47})_{1.20}Sb$ | (1.00) | 0.20 ± 0.027 | 56 : 44 | 37 : 63 |
| 5BR5 | $(Cr_{0.52}Fe_{0.48})_{1.23}Sb$ | (1.00) | 0.23 ± 0.044 | 60 : 40 | 17 : 83 |
| 5BR8 | $(Cr_{0.48}Fe_{0.52})_{1.26}Sb$ | (1.00) | 0.26 ± 0.022 | 50 : 50 | 44 : 56 |
| 4BR2 | $(Cr_{0.48}Fe_{0.52})_{1.25}Sb$ | (1.00) | 0.25 ± 0.023 | 60 : 40 | 0 : 100 |
| 3BR5 | $(Cr_{0.71}Fe_{0.29})_{1.19}Sb$ | (1.00) | 0.19 ± 0.017 | 76 : 24 | 44 : 56 |
| 3BR8 | $(Cr_{0.72}Fe_{0.28})_{1.18}Sb$ | (1.00) | 0.18 ± 0.030 | 77 : 23(1) | 43 : 57(4) |
| 2BR1 | $(Cr_{0.78}Fe_{0.22})_{1.20}Sb$ | (1.00) | 0.20 ± 0.010 | 85 : 15(1) | 43 : 57(4) |
| 0BR03 | $Cr_{1.02}Sb$ | (1.00) | 0.02 ± 0.012 | 100 : 0 | 100 : 0 |

The structural results for the intermetallic compounds $(Cr_{1-x}Fe_x)_{1+\delta}Sb$ ($0 \le x \le 1$), i.e. the occupancies of the interstitial 2(c) sites ($\delta$ - values) and the individual Cr:Fe distributions, can be compared with the magnetic behaviour of the system shown in the phase diagram in Fig. 5. The linear decrease of the Néel-temperatures with increasing overall Fe-composition ends with a discontinuity at about 50 % Fe. This cut off is accompanied by a transition from antiferromagnetic to ferromagnetic behaviour at low temperatures for the range 50 < % Fe < 90. In this region the paramagnetic Curie-temperatures vary markedly depending on different sample preparation. Close to the pure $Fe_{1+\delta}Sb$ another antiferromagnetic phase occurs.

We assume that the discontinuity in the magnetic behaviour at about 50 % Fe is caused by the distribution of the transition metal atoms. This can be clearly seen in the corresponding anomalies of the interstitial site occupancies ($\delta$ - values) and the chromium-to-iron ratios in the 2(a) and 2(c) sites (Fig. 3 and 4).

The two end members ($Cr_{1-\delta}Sb$ and $Fe_{1+\delta}Sb$) have antiferromagnetic structures /2, 6/. While for $Fe_{1+\delta}Sb$ a triangular ordering in the (001) plane is reported, $Cr_{1+\delta}Sb$ has a collinear arrangement of the magnetic moment vectors parallel to the c-axis. Our preliminary measurements on the Cr-rich side of the system indicate that the magnetic structure is basically of the $Cr_{1+\delta}Sb$ type. The decreasing Nêel-temperatures with rising Fe-content are accompanied by an increasing canting angle of the magnetic moments against c.

## REFERENCES

/1/ E. Hellner, G. Heger, D. Mullen and W. Treutmann, Mat. Res. Bull. 10, 91 (1975).

/2/ J. Takei, D. E. Cox and G. Shirane, Phys. Rev. 129, 2008 (1963).

/3/ K. Yamaguchi, H. Watanabe, H. Yamamoto and Y. Yamaguchi, J. Phys. Soc. Japan, 31, 1042 (1971).

/4/ J. Nösselt and U. Sondermann. Int. J. Magnetism 5, 277 (1973).

/5/ F. W. Richter and K. Schmidt, Int. J. Magnetism 5, 283 (1973).

/6/ T. Yashiro, Y. Yamaguchi, S. Tomiyoshi, N. Kazama and H. Watanabe, J. Phys. Soc. Japan 34, 58 (1973).

## 2.7. Spin-Lattice Relaxation of the β-Emitter $^8Li$ in Solid Li-Mg Alloys

*H. Ackermann, D. Dubbers, F. Fujara, M. Grupp, P. Heitjans, A. Koerblein and H.-J. Stoeckmann*

Guest group from: Physikalisches Institut der Universität Heidelberg, Germany; Institut Laue-Langevin, Grenoble, France

By capture of polarized thermal neutrons polarized β-active $^8Li$ nuclei were produced in $^7Li$ alloys containing 0...11 at. % Mg. The polarization was monitored by the asymmetric distribution of the $^8Li$ β-radiation. The spin-lattice relaxation time $T_1$ of $^8Li$, observed via transients of the β-decay asymmetry, was measured for 6 alloys in the temperature range T = 20...450 K at the field $B_o = 0.3385$ T.

The relaxation rate $T_1^{-1}$ consists of a contribution $T_{1e}^{-1}$ from the conduction electrons and - above 250 K - of an additional relaxation rate $T_{1diff}^{-1}$ due to atomic diffusion. In the low T region $\leq 200$ K, $T_1^{-1}$ was found to obey $T^{-1} = T/C$ for each alloy with good accuracy. $C = T_{1e}T$ increased with solute concentration from 292.7 (5.2) sK for pure $^7Li$ to 350.4 (9.4) sK for $^7Li$ with 10.8 at. % Mg. Connecting these results with the known Knightshift K of $^7Li$ in dilute Li-Mg alloys /1/, one finds the Korringa relation $T_{1e}TK^2$ = const. to hold in the concentration range covered.

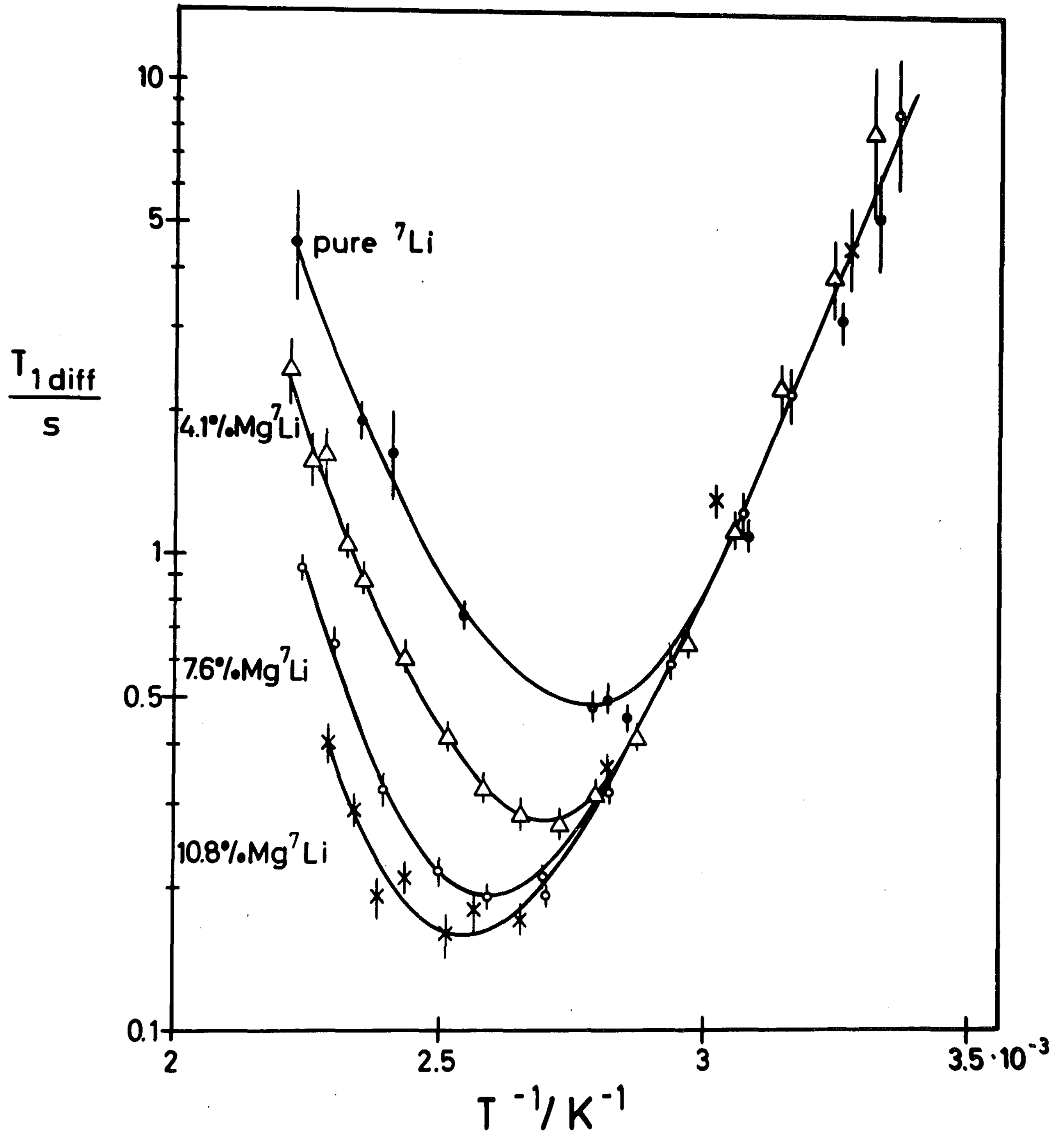

Fig. 1. Diffusion induced part of the spin-lattice relaxation time $T_{1diff}$ of $^8$Li in LiMg-alloys.

$T^{-1}_{1diff}$ was obtained by subtracting $T^{-1}_{1e}$ from $T^{-1}_{1}$. It was found that the $T^{-1}_{1diff}(T)$ curves shift their maxima from about 365 K to 395 K with increasing Mg content, indicating that the effective correlation time for diffusion becomes longer. Further, the maximum value of $T^{-1}_{1diff}$ increases from 2.2 (1) $s^{-1}$ to 6.3 (8) $s^{-1}$ on alloying. Subtracting from $T^{-1}_{1\mathrm{diff}}$ the purely dipolar contribution $T^{-1}_{1d}$, as given by the diffusional relaxation of Li in pure Li /2/, the remaining relaxation rate proves to be proportional to the Mg concentration and reaches twice the value of $T^{-1}_{1d}$. Following the lines of a similar investigation on $^7$Li by NMR /3/, the extra relaxation rate cannot be accounted for by the diffusion induced dipolar interaction between $^8$Li and Mg but is assumed to be due to the quadrupolar interaction of $^8$Li with the fluctuating electric field gradients of the diffusing solute ions. Allowing for the different quadrupole moment and Larmor frequency the measured quadrupolar relaxation rate of $^7$Li as compared to $^8$Li seems to be too small at low solute concentrations and becomes consistent only for about 8 at. % Mg in Li.

REFERENCES

/1/ D.C. Hughes, Phil. Mag. 5, 467 (1960).
/2/ H. Ackermann, D. Dubbers, M. Grupp, P. Heitjans, R. Messer and H.-J. Stoeckmann, phys. stat. sol. (b) 71, K91 (1975).
/3/ J. M. Titmann and B. M. Moores, J. Phys. F 2, 592 (1972).

## 2.8. NMR Multiquantum Transitions of the β-Emitter $^8$Li (0.8 sec) in $LiTaO_3$

*H. Ackermann, K. Doerr, D. Dubbers, F. Fujara, P. Heitjans, M. Grupp and H.-J. Stoeckmann*

Guest group from: Physikalisches Institut der Universität Heidelberg, Germany; Institut Laue-Langevin , Grenoble, France

Polarized β-active $^8$Li (I = 2, $T_{\frac{1}{2}}$ = 0.84 s) nuclei are produced in a single crystal of rhombohedral $LiTaO_3$ at room temperature by capture of polarized thermal neutrons. The nuclear polarization is monitored by the $^8$Li β-decay asymmetry. Saturation of one single-quantum NMR transition between two neighbouring quadrupole shifted Zeeman levels reduces the nuclear polarization only by 5 % and is therefore difficult to detect via the β-decay asymmetry. On the other hand, saturation of two, three and four quanta transitions reduces the polarization by 20 %, 50 % and 100 %, respectively, and hence leads to strong signals in the β-decay asymmetry, see Fig. 1. From the present measurements the electric quadrupole coupling constant of Li in $LiTaO_3$ was determined to be $e^2qQ = (60.3 \pm 0.5)$ kHz.

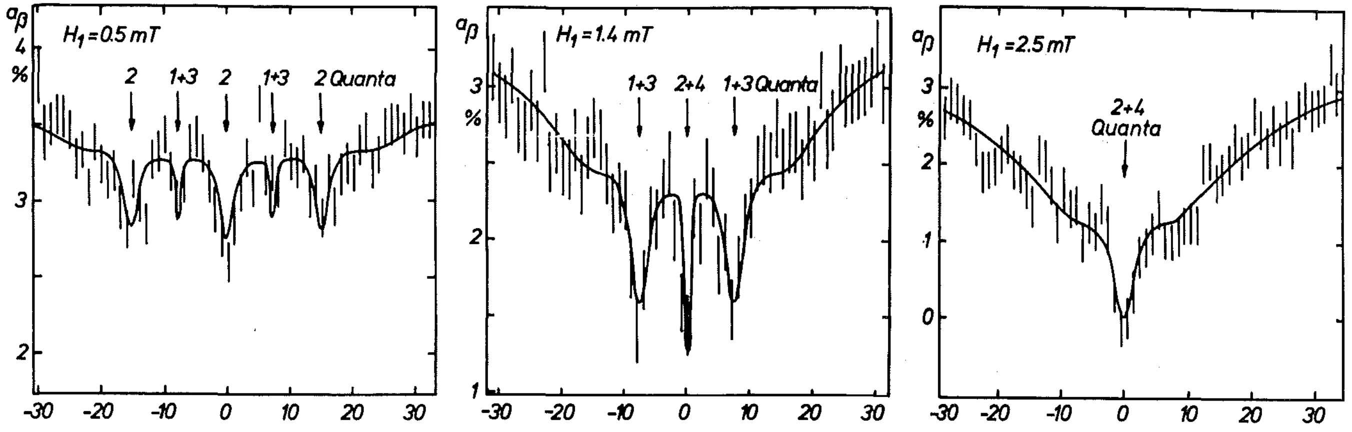

Fig. 1. NMR multiquantum transitions detected in the β-decay asymmetry $a_\beta$ of $^8$Li in $LiTaO_3$; c-axis $\uparrow\uparrow B_o$, $B_o$ = 0.40 T. The curves represent an exact calculation, see D. Dubbers: Z. Physik 276, 245 (1976).

## 2.9. Investigation of the Spin-Flop Transition and the Bicritical Point of the 2-Dimensional Antiferromagnet $(C_2H_5NH_3)_2MnCl_4$

*J. Nösselt*[(a)], *G. Heger and R. Moser*

(a) SFB 127, Fachbereich Geowissenschaften der Universität Marburg

Besides its interesting properties with respect to structural phase transitions /1/, ethyl-ammonium-manganese-chloride $(C_2H_5NH_3)_2MnCl_4$ (≡ EAMC) is a model system of a two-dimensional Heisenberg antiferromagnet. The antiferromagnetic phase transition occurs at $T_N$ = 42.5 K. It is presumably caused by the anisotropic part of the intralayer exchange interaction Mn-Cl-Mn rather than by the very small interlayer coupling.

Below $T_N$ the high field behaviour of the magnetization shows - if the field is applied parallel to the easy $\boxed{001}$ direction - a spin-flop transition at $H_{SF} = (30 \pm 2)$ kOe for $T \to 0$ K; $H_{SF}$ increases slightly with increasing temperature. The transition is not sharp, but smeared out over a certain field range (Fig. 1). The accuracy of the angle between the applied field and the easy axis was better than ± 1°, and small changes of this angle do not seem to alter remarkably the observed behaviour. The transition fields were determined by peaks of the differential susceptibility $\frac{\Delta M}{\Delta H}$ (Fig. 2).

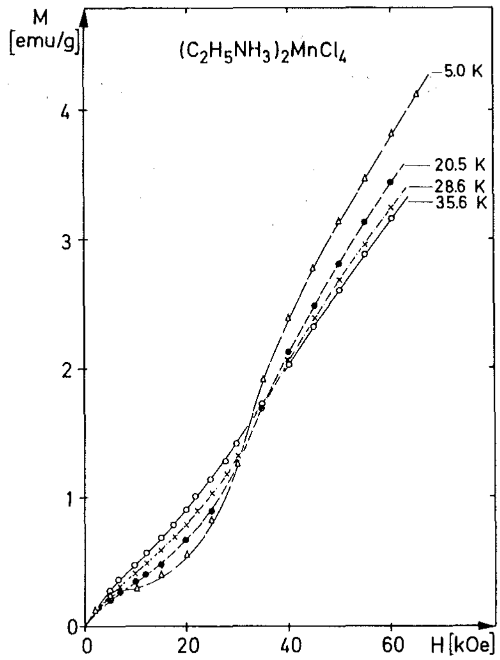

Fig. 1. Magnetization of EAMC for several temperatures as a function of the applied field $H_{||}$.

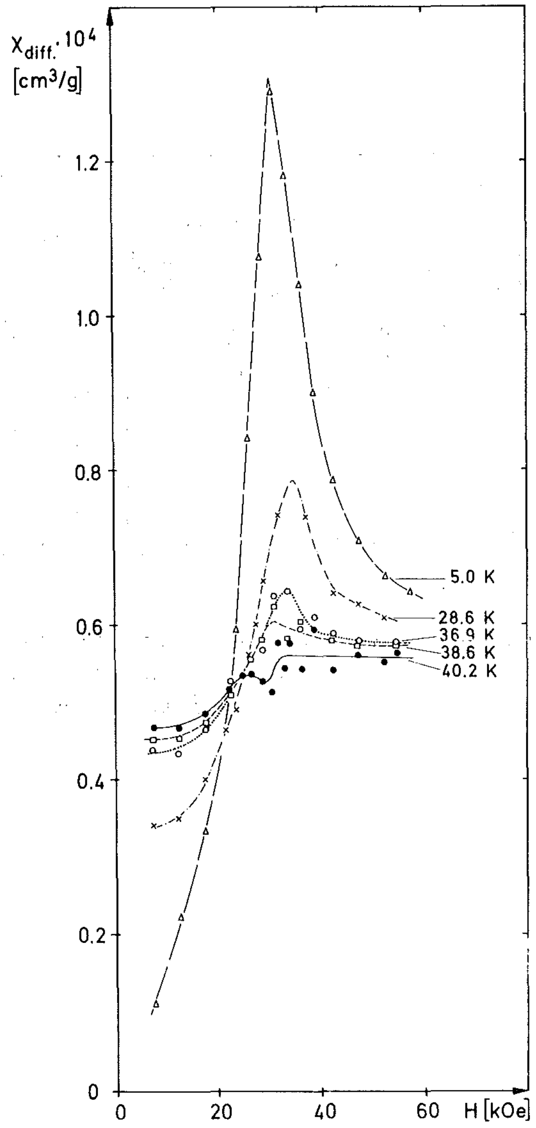

Fig. 2. Differential susceptibility of EAMC for several temperatures as a function of the applied field $H_{||}$.

In applied fields below $H_{SF}$ the parallel susceptibility $\chi_{||}$ shows the known temperature dependence and the phase boundary which separates the antiferromagnetic from the paramagnetic state is determined by the inflection of the $\chi_{||}$ (T) curves. The experimental data were fitted using a power series approximation of the form

$$\chi_{||}(T) \cdot T = A(H) + B(H) \cdot \varepsilon + C(H) \cdot \varepsilon^2 + D(H) \cdot \varepsilon^3 + E(H) \cdot \varepsilon^4$$

with $$\varepsilon = \frac{T - T_c}{T_c} .$$

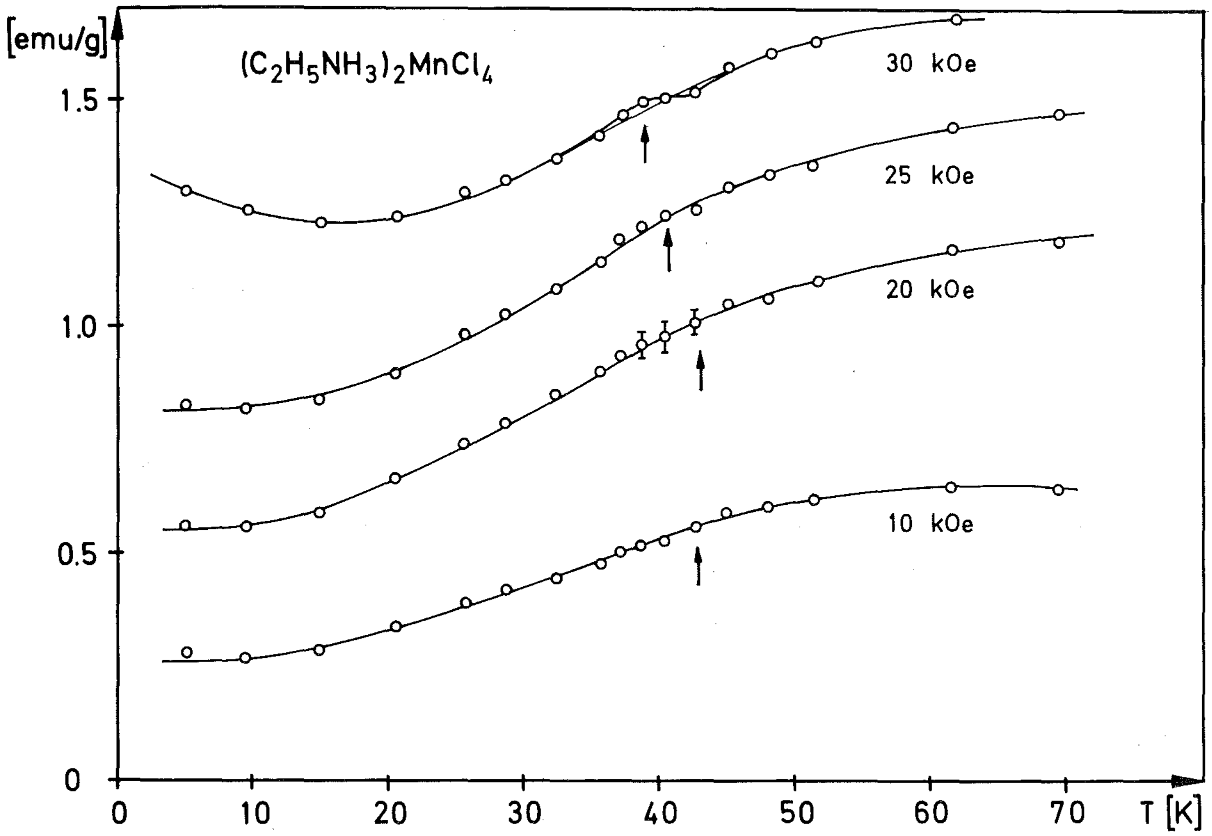

Fig. 3. Magnetization of EAMC for $H_{||} < H_{SF}$; $H_{||}$ = const. as a function of temperature. +

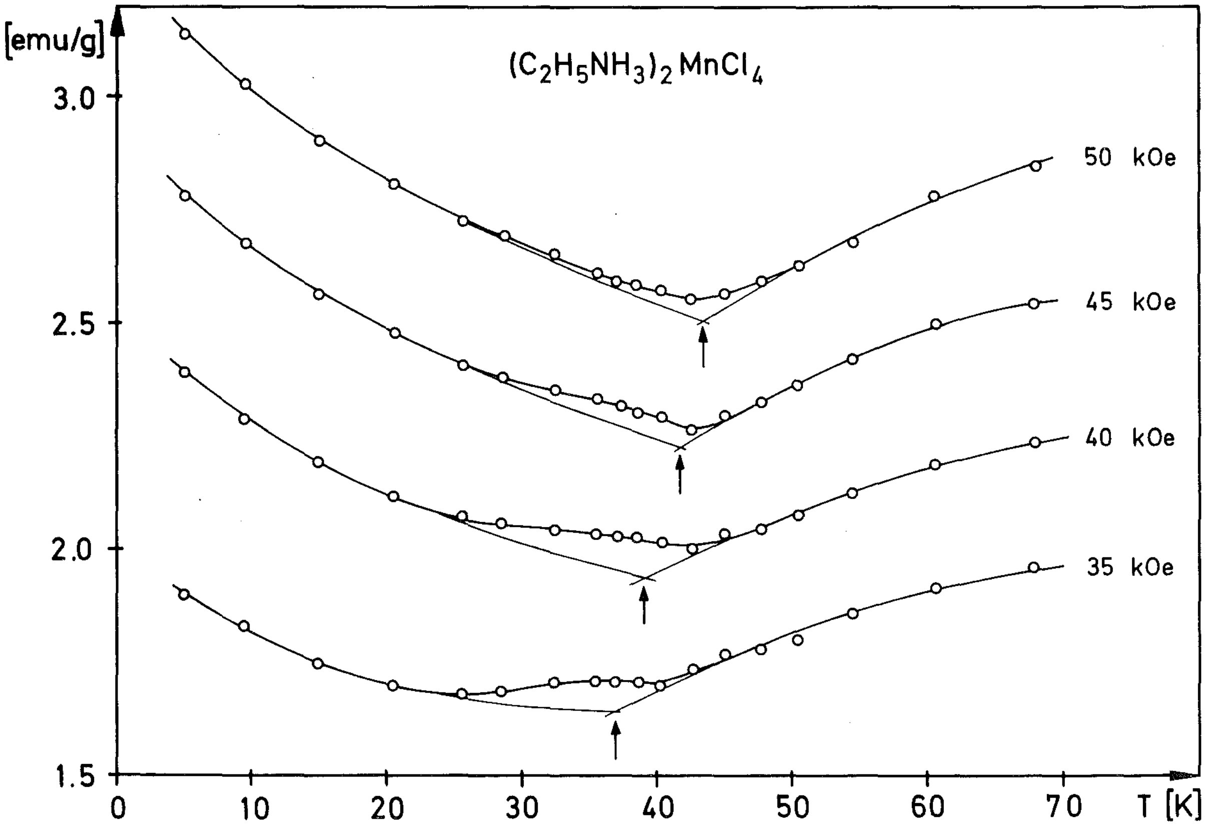

Fig. 4. Magnetization of EAMC for $H_{||} > H_{SF}$; $H_{||}$ = const. as a function of temperature. +

---

+The arrows indicate the individual critical temperatures $T_c$.

The results are shown in Fig. 3. In this way all the curves depend on the same set of parameters A, B, C, D and E with the variables H and $T_c$.

Above $H_{SF}$ the behaviour of the susceptibility in the paramagnetic region has not changed. In the spin-flop state there is an increasing magnetization and so the phase boundary which separates the spin-flop from the paramagnetic state can be determined likewise from the temperature dependence of the susceptibility (Fig. 4).

All the boundaries between different magnetic states meet in one special point, i.e. the bicritical point, where the first order spin-flop transition vanishes. The critical values are $H_c = (34.5 \pm 2)$ kOe and $T_c = (35 \pm 1)$ K. The experimentally magnetic phase diagram for $(C_2H_5NH_3)_2MnCl_4$ shown in Fig. 5 agrees well with that predicted theoretically by Fisher and Nelson /2/.

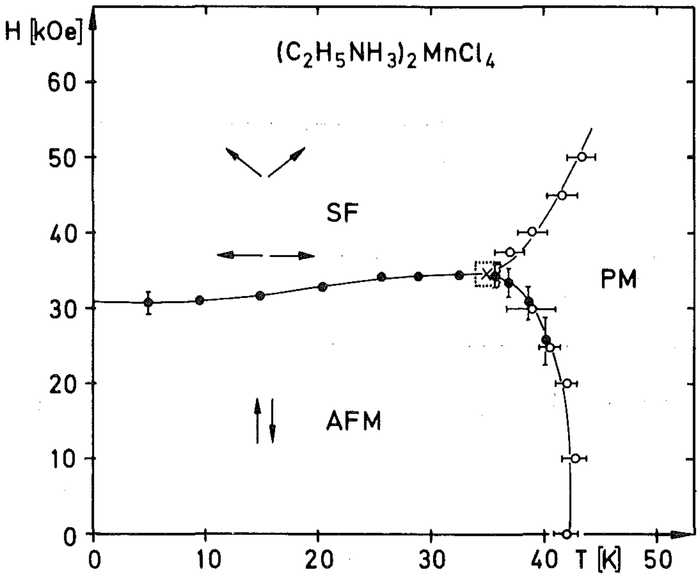

Fig. 5. The magnetic phase diagram of $(C_2H_5NH_3)_2MnCl_4$

REFERENCES

/1/ See e.g.: Investigations of the Perovskite-Type Layer Structures $(C_nH_{2n+1}NH_3)_2MnCl_4$ with n = 1, 2. (1.25 - 1.27 in this report).

/2/ M. E. Fisher and D. R. Nelson, Phys. Rev. Lett. 32, 1350 (1974).

## 2.10. Investigation of the Electron Density of Simple Compounds. A Neutron Diffraction Study of the Crystal Structure of Thiourea ($S=C(NH_2)_2$) at Room Temperature

*G. Heger, D. Mullen*[(a)] *and W. Treutmann*[(a)]

[(a)] SFB 127, Fachbereich Geowissenschaften der Universität Marburg

In order to compare theoretically determined electron densities with experimental results, combined X-ray and neutron diffraction studies of high precision at several temperatures are required. Whereas X-ray measurements yield the total electron density distribution, neutron data give information about the position and thermal vibration of the nuclei which is used to describe the core-electron distribution. An X - N (X-ray - neutron) difference analyses then leads to a description of the bond electron density distributions.

Complementary to existing data, we started measurements on thiourea ($S=C(NH_2)_2$), urea ($O=C(NH_2)_2$) and tetracyanoethylene ($(NC)_2C = C(CN)_2$). The refinement of the crystal structure of thiourea at room temperature is completed. An earlier neutron diffraction study has yielded a high R-factor of 0.107 /1/. ($R = \Sigma||F_o| - |F_c||/\Sigma|F_o|$, with $F_o$ and $F_c$ for the observed and calculated structure factors, respectively).

For our refinement we used a total of 370 independent reflection intensities corrected for absorption /2/. We obtain a final R-factor of 0.057. Thiourea crystalizes in the orthorhombic space group Pnma with 4 molecules per unit cell (a = 7.657, b = 8.558, c = 5.485 Å). The $S=C(NH_2)_2$ molecules, shown in Fig. 1 are nearly coplanar.

The accurate structure factor data obtained are used in calculations of (X - N) difference maps and in various models in which bond electron density distributions are considered.

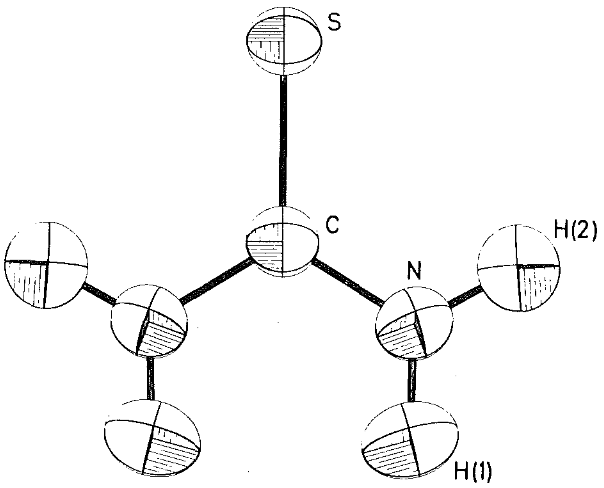

Fig. 1. The thiourea molecule with the thermal ellipsoids.

REFERENCES

/1/ M. N. Elcombe, J. C. Taylor, Acta Crystallogr. A24, 410 (1968).
/2/ C. T. Prewitt, Z. Kristallogr. 122, 24 (1965).

# 3. MATERIALS RESEARCH

## 3.1. Determination of Uniform Implantation Profiles

*G. Linker*

For a single energy implantation profile a gaussian distribution of the implanted ions based on LSS /1/ projected range statistics may be adopted:

$$N(x) = \frac{N_D}{\sqrt{2\pi}\,\Delta R_p} \exp\left[-(x-R_p)^2/2(\Delta R_p)^2\right] \qquad (1)$$

$R_p$ = projected range
$\Delta R_p$ = straggling in projected range
$N_D$ = implantation dose, ions/cm$^2$

In many experiments however a uniform implantation distribution over a certain depth is required. The use of multiple implantations at different energies to achieve this aim has long been recognized. Here a simple approach for the energy and fluence value determination in uniform composite profile calculations is described.

Let denote the heights of the single energy profiles i at their projected ranges $R_{pi}$ by h(i,i) and the contribution of profile k to profile i at $R_{pi}$ by h(k,i); then for m distinct energies the total height of peak i at $R_{pi}$ will be

$$H(i) = \sum_{k=1}^{m} h(k,i) \qquad i = 1, m$$

Let now multiply the above equations for i = 2, m with factors F(j), j = 1, m - 1; then the heights of the composite profile at the depth values $R_{pi}$ are:

$$W(i) = h(1,i) + \sum_{j=1}^{m-1} F(j) \cdot h\,(j+1,\, i) \qquad i=1,m$$

Now we demand that the values W(i) should all be equal, i.e.

$$W(1) \overset{!}{=} W(k) \qquad k = 2, m$$

This constrain leads to a system of m - 1 linear equations for the determination of the factors F(j):

$$\mathfrak{A}\mathfrak{x} = \mathfrak{b} \qquad \text{with}$$

$$\mathfrak{A} = (a(i,j)) \text{ and } a(i,j) = h(j+1,1) - h(j+1\;, i+1);\; i = 1,\, m-1$$
$$j = 1,\, m-1$$

$$\mathfrak{b} = h(1,j) - h(1,1);\; j = 2,\, m$$
$$\mathfrak{x} = (F(j)) \qquad ;\; j = 1,\, m-1$$

The h(i,j) are determined from eq. (1) with $N_D = 1$.

This approach of course only guarantees equal heights of a profile at distinct depth values $R_{pi}$. However, the inspection of a few calculations with different energy value combinations supplies the right energy values for a homogeneous distribution over the whole depth required.

Then the fluence $N_D$ for energy i = 1 for a desired concentration in an ion-target system under consideration is calculated from formula (1) taking into account the contribution of the other profiles. The fluences for the energies i = 2, m are then obtained by multiplying the value for i = 1 with the calculated factors F(j).

An example for a uniform profile calculation for nitrogen implantation into molybdenum is shown in Fig. 1 for three distinct energies. The factors F(1) and F(2) are indicated in the figure and the fluences necessary for a dotation with 10 % impurity are also included.

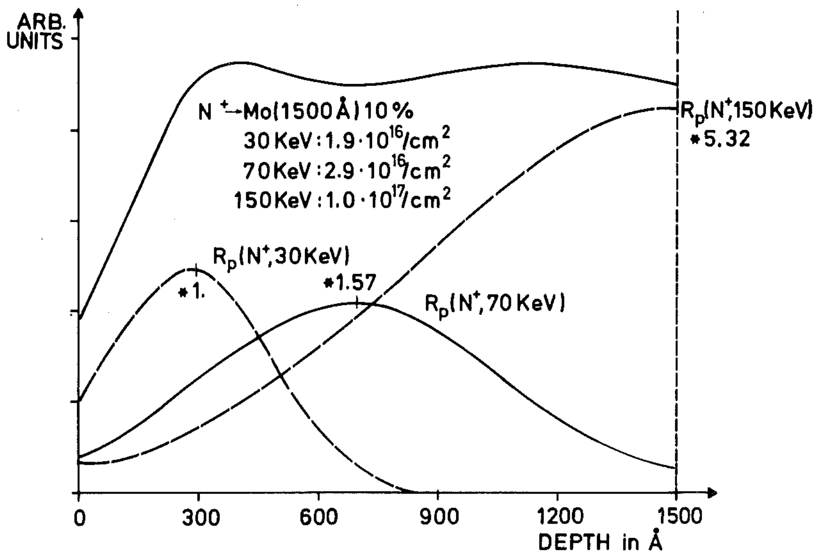

Fig. 1. Single and composite implantation profiles for nitrogen in a 1500 Å thick molybdenum layer.

REFERENCES

/1/ J. Lindhard, M. Scharff, H. E. Schiott, Mat. Fys. Medd. Dan. Vid. Selsk. 33, no. 14 (1961).

## 3.2. Preparation and Analysis of Aluminium Films with Different Contents of Oxygen

*P. Ziemann*

As a first step in a detailed study how the superconducting properties of aluminium films can be changed by either radiation damage or by ion implantation at liquid helium-temperature, Al layers were prepared with different oxygen contents by evaporation and analysed using the Rutherford-backscattering technique.

The Al films were evaporated by a 2 kW-electron gun from a molybdenum boat onto quartz and carbon substrates held at room temperature (R.T.). The films were 0.5 cm wide and 1500 - 3000 Å thick. During evaporation a partial oxygen pressure was maintained by bleeding oxygen into the vacuum chamber and by simultaneously pumping with diffusion pumps at the system. The evaporation data of the films are summarized in Table I.

| SAMPLE | $P_1$ (TORR) | $P_2$ (TORR) | RATE (Å/sec) | THICKNESS (Å) | $T_S$ (K) |
|---|---|---|---|---|---|
| A | $1 \times 10^{-8}$ | $6 \times 10^{-7}$ | 350 | 2500 | 300 |
| B | $2.5 \times 10^{-9}$ | $6 \times 10^{-5}$ | 100 | 1900 | 300 |
| C | $9 \times 10^{-7}$ | $6 \times 10^{-5}$ | 110 | 3200 | 300 |
| D | $8 \times 10^{-7}$ | $4.5 \times 10^{-5}$ | 40 | 1600 | 300 |
| E | $3 \times 10^{-8}$ | $7.5 \times 10^{-5}$ | 110 | 2500 | 300 |
| F | $2 \times 10^{-8}$ | $8.5 \times 10^{-5}$ | 30 | 2000 | 300 |

Table I Evaporation data of the Al Films ($P_1$ pressure before evaporation, $P_2$ pressure during evaporation after bleeding in the oxygen, except sample A, where it is the pressure during evaporation without oxygen inlet, $T_S$ substrate temperature).

From each evaporated charge the films on the carbon substrates were analysed by backscattering of 2 MeV $He^+$-ions. The oxygen content, its distribution and possible heavy atom contamination of the films could be determined from the backscattering spectra. The oxygen distributions were rather homogeneous except sample F, which revealed a nearly linear increase in oxygen concentration from about 32 at. % at the surface to about 48 at. % at the backside of the film. The lowest oxygen concentration, which could be determined was about 1 at. %, typical relative errors in concentration determination are about 10 %.

The transition temperature $T_c$ was determined from half the value of the residual resistance obtained by a standard four point measurement. The temperature is measured by a GaAs-diode calibrated against a Ge-resistor. The results are presented in Figure 1, which shows, that an increasing $T_c$ is correlated with an increasing oxygen content whereas the residual resistivity ratio R = R(R.T.)/R(4 K) increases with a decreasing oxygen content. The high r-value, which is taken as a measure for the layer purity, determined for sample A may be noted. The results of the films with higher oxygen contents are typical for "granular" Al films as given in the literature /1/.

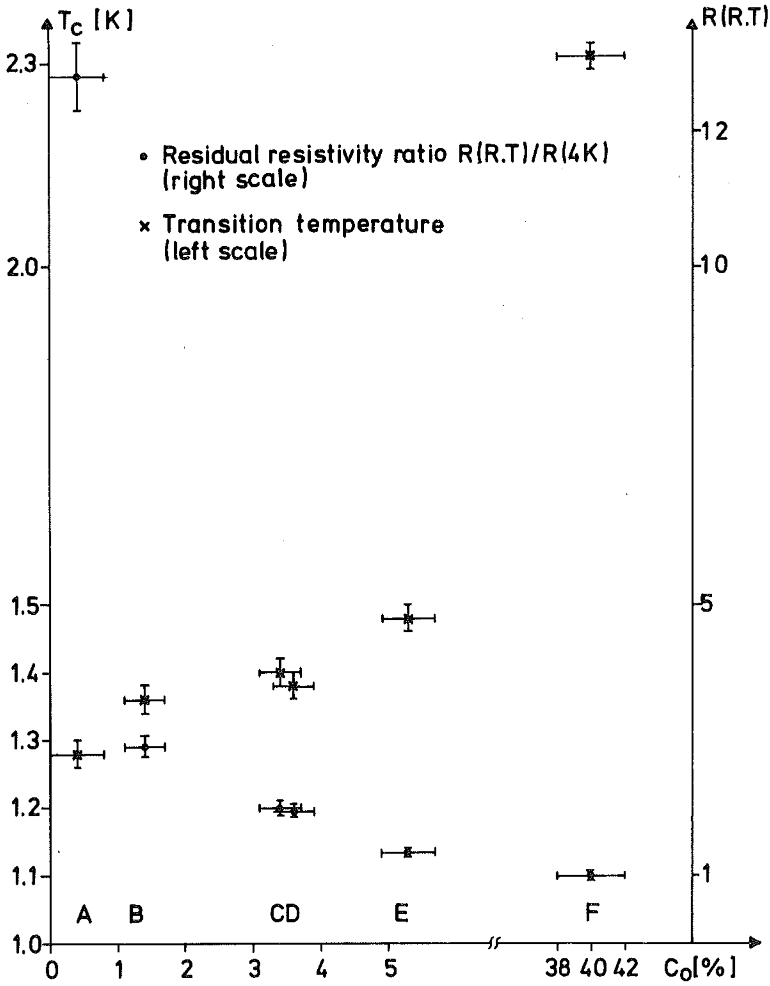

Fig. 1. Dependence of the transition temperature $T_c$ and residual resistivity r on the oxygen concentration $c_o$.

REFERENCES

/1/ R.W. Cohen and B. Abeles, Phys. Rev. 168, 444 (1968).

## 3.3. Determination of Oxygen Distribution in Oxidized $Si_3N_4$

*J. Lombaard* [(a)], *O. Meyer and G. Grathwohl*[(b)]

[(a)] On leave from: Physics Department, University of Pretoria 0002, South Africa

[(b)] Institut für Material und Festkörperforschung, KFZ Karlsruhe

Due to its outstanding mechanical, thermal and corrosive properties silicon nitride is of great importance to industry especially in the manufacturing of gasturbines. Creep deformations occur however when reaction sintered $Si_3N_4$ is heated in air and the extent of internal oxidation is related to the change in creep properties /1/. Up to now the concentration profiles of $Si_2ON_2$ and $SiO_2$ (cristobalite) have been measured by X-ray diffraction which however is insensitive to any possible content of amorphous material /2/. In order to determine the amorphous component, here the total oxygen profile has been measured by Rutherford backscattering.

The $Si_3N_4$ sample (A460) has been oxidized by heating in air for 200 hours at a temperature of 1000 °C. During this procedure the sample was covered with a layer of $SiO_2$. Afterwards the sample has been wedged by grinding one side with SiC. Backscattering measurements were made on different spots along the grinded surface in order to get depth profiles of nitrogen and oxygen. To prevent electrostatic charge build-up during the measurements all samples were partially covered with tin foils.

Typical spectra of 2 MeV alpha particles scattered at an angle of 165 ° from two different spots in the target are given in Fig. 1. The spectra clearly show that the bulk material is contaminated with calcium and other heavier elements. The concentration ratios of oxygen to silicon have been calculated by comparing the oxygen and silicon step heights in the spectra. A similar analysis has been used to determine the nitrogen content and the results are given in Fig. 2. Measurements made at different spots on the oxidized surface show that the $SiO_2$ layer is not of uniform thickness and composition. Different concentration ratios for oxygen to silicon have been obtained at different spots. The ratios given in Fig. 2 at the surface (positions -1, +1) were measured at spots where the $Si_3N_4$ was not yet completely converted to $SiO_2$. Although there is a sharp decrease in the oxidation within the first 0.1 mm below the surface, the oxidation took place throughout the whole sample. In order to compare the results with the oxygen content of an unoxidized sample, the latter has been splitted. The newly formed surface has an oxygen to silicon concentration ratio of less than 0.04.

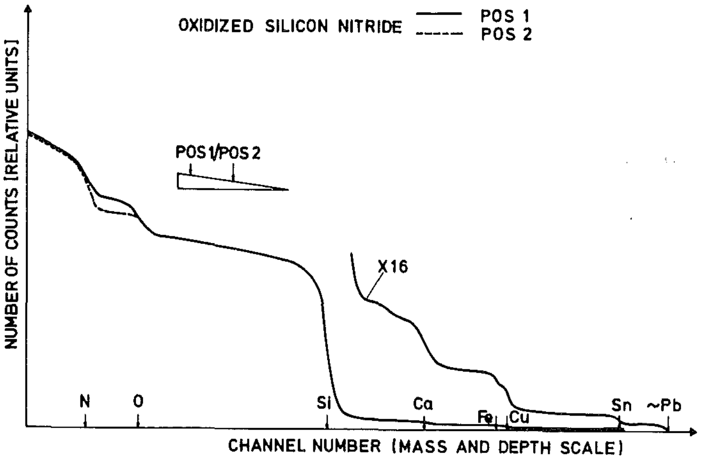

Fig. 1. Backscattering energy spectra from two different spots of an oxidized silicon nitride sample.

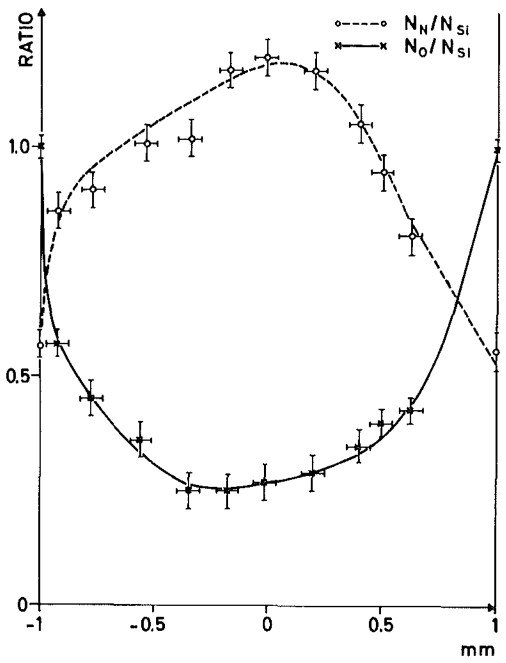

Fig. 2. Oxygen and nitrogen depth profiles of a 2 mm thick wedged sample. The 0-point of the depth scale determines the midpoint of the sample.

The present results give an oxygen to silicon ratio that is 10 % to 20 % higher than those obtained by X-ray diffraction. This clearly indicates that some of the oxygen compounds are in an amorphous state.

The internal oxidation of the $Si_3N_4$ can be reduced by covering the surface with a protective layer. Previous attempts to cover it with a sputtered layer of aluminium oxide were unsuccessful. Backscattering analysis of a $Si_3N_4$ sample protected with a sputtered $Al_2O_3$-layer showed however that the surface before sputtering was already contaminated and that the $Al_2O_3$-layer contains a significant amount of calcium as impurity. Further attempts to produce pure protective $Al_2O_3$-layers are planned. Oxygen profiles of oxidized samples after creep experiments will also be measured by backscattering.

## REFERENCES

/1/ F. Thümmler, F. Porz, G. Grathwohl and W. Engel, Science of Ceramics 8, 133 (1976).

/2/ W. Engel, J. Porz and F. Thümmler, Berichte der Deutschen Keramischen Gesellschaft 52, 296 (1975).

## 3.4. Analysis of Backscattering Spectra Using a NOVA 2 Computer

*E. L. Haase*

For the backscattering measurements at the Van de Graaff accelerator of the IAK a computer-based CAMAC data aquisition and experiment automatisation system is being assembled and tested.

This system will also be employed for the evaluation of the acquired data to speed up the analysis by on-line operation with rapid turn-over, and to improve the accuracy of the analysis.

As part of this effort a program for the theoretical generation of backscattering spectra is being developed. For this purpose , besides the known measurement conditions, one needs to know the scattering cross-section, and the energy loss values and charge state of the projectile as a function of its energy.

For the energy loss the semi-empirical polynomial coefficients based on model fits to experimental data by Ziegler and Chu /1/ are used.

The scattering is essentially given by the Rutherford cross-section with corrections for the equilibrium charge state of $^4$He ions in matter and the screening of the target atoms by their core electrons. The former is based on fits to measurements by Armstrong et al. /2/. The latter is difficult to handle as no analytical expression for the potential exist. Presently an empirical Z-dependent linear correction of the order of a few percent is used. Fig. 1 shows representative results for a backscattering spectrum of 2 MeV $\alpha$-particles from a randomly oriented vanadium single crystal.

Good agreement with the experimental spectrum is obtained down to about 500 keV, where both the energy loss is stated to become unreliable and the screening is expected to become important.

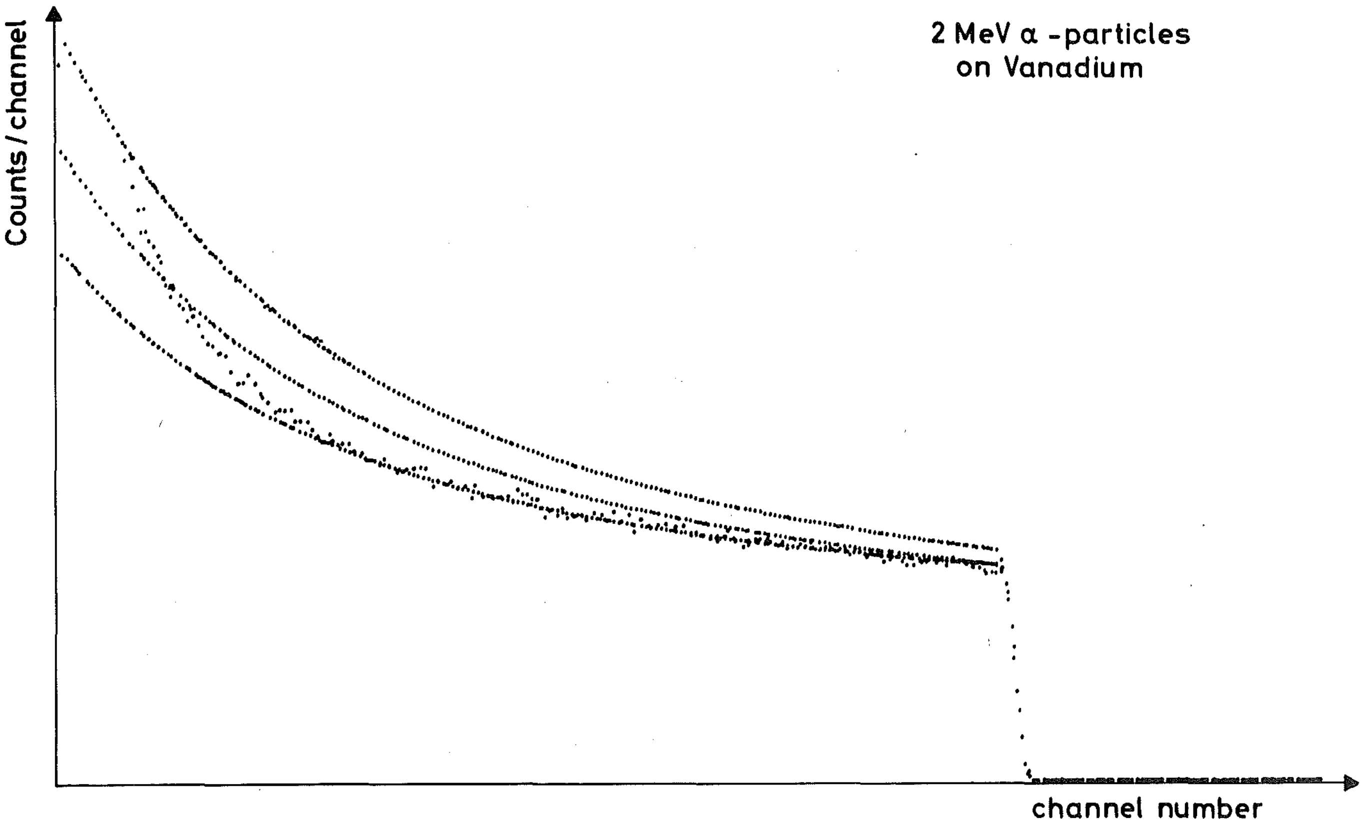

Fig. 1. Measured and generated backscattering spectra for a vanadium sample. The scattered points are experimental data. The top curve is a generated spectrum calculated with the uncorrected Rutherford cross-section and folded with the experimental resolution. The middle curve includes the correction for the equilibrium charge state of the projectile. The bottom curve additionally contains an empirical correction for the electron screening.

## REFERENCES

/1/ J. F. Ziegler and W. K. Chu, Atomic Data Nucl. Data Tabl. 13, 463 (1974).

/2/ J. C. Armstrong et al. Proc. Phys. Soc. 86, 1283 (1965).

## 3.5. Stochiometry Determinations of Pure and Coroded $Si_3N_4$ Samples

*E. L. Haase and J. Lombaard*[(a)]

[(a)] Physics Department, University of Pretoria, Pretoria 0002, South Africa

Presently the backscattering technique is being applied for the analysis of pure and coroded $Si_3N_4$ samples /1/. This material is being tested as it has very interesting technical applications /2/.

To speed up the analysis and to improve its accuracy, the computer program described in the preceeding contribution has been applied to this problem.

Fig. 1 shows an experomental backscattering spectrum from untreated $Si_3N_4$ material and the smooth generated spectrum. The right step stems from silicon. Here the generated spectrum reproduces the experimental data very well. Below the left step originating from nitrogen, the data and the generated curve begin to diverge due to poor knowledge of the energy loss and possible screening effects. The actual stochiometry of $Si_3N_4$ is very well reproduced by the height of the steps, confirming Braggs rule when using the energy loss data for nitrogen in the solid state /3/.

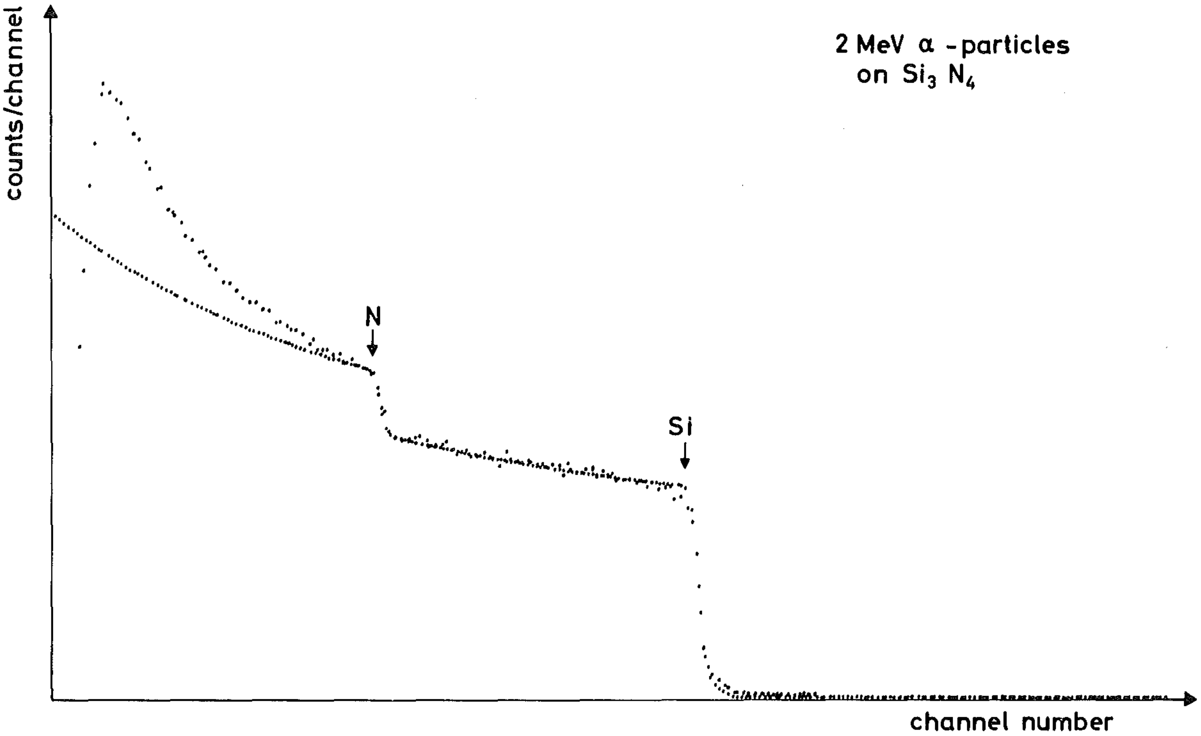

Fig. 1. Experimental data points and generated spectrum for pure $Si_3N_4$. The stochiometry is well reproduced.

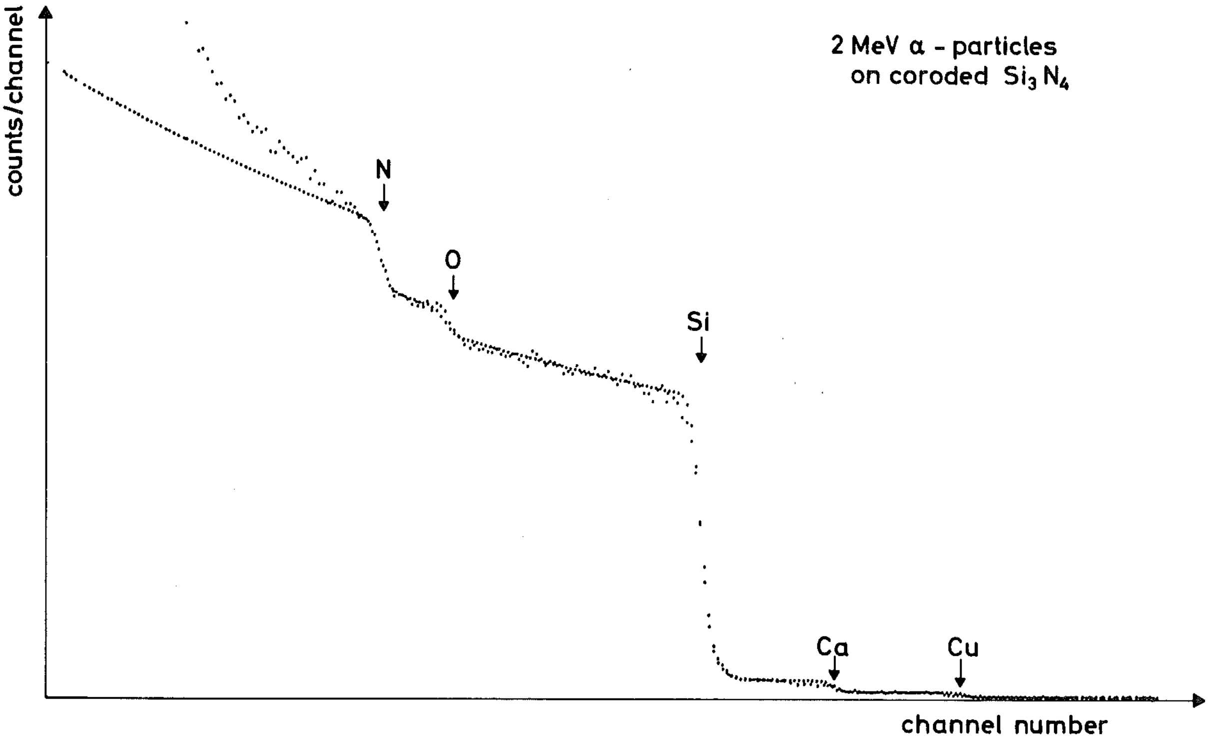

Fig. 2. Experimental data points and theoretical spectrum for coroded $Si_3N_4$. The generated spectrum reproduces very well the shape and the steps from copper, calcium, silicon, oxygen and nitrogen.

Fig. 2 shows both an experimental and a generated spectrum for an oxidized $Si_3N_4$ sample. At the right hand side steps from 0.2 at. % copper and 0.65 at. % calcium can easily be identified. There are three further steps from 39 at. % silicon, 10 at. % oxygen and 50. % nitrogen. Investigations of other samples have shown that for this rather porous material the oxygen concentration is quite uniform within the analysing depth of about 5000 Å. Above the nitrogen step there is good agreement between the theoretical curve and the data points. The fact that the data points at the silicon edge are below the theoretical curve indicates that the surface is rough due to porosity. The analysis of this sample shows that, compared with the untreated material, 5 at. % of the nitrogen is lacking and 10 at. % additional oxygen is bound probably in the form of $SiO_2$. The stoichiometry can be determined quite accurately, as the shape and slope above about 400 keV are well reproduced and one can now determine the contribution of the heavier masses to the lower steps as a function of depth. In fitting the height of the steps one can exclude surface impurity peaks and default regions, and average out statistical fluctuations by averaging over "clean" regions.

REFERENCES

/1/ J. Lombaard, O. Meyer and G. Grathwohl: Determination of Oxygen Distribution in Oxidized $Si_3N_4$ (3.3 in this report).

/2/ F. Thümmler, F. Porz, G. Grathwohl and W. Engel, Science of Ceramics 8, 133 (1976).

/3/ J. F. Ziegler and W. K. Chu, IBM Research Report RC 5742 (1976).

## 3.6. Superconducting Vanadium Carbide Produced by Carbon Ion Implantation

*K.-G. Langguth and M. Kraatz*

In contrast to the other carbides of the group Vb transition metals, vanadium carbide shows no superconductivity down to a temperature of 30 mK /1/. This may be correlated with the exceptional low carbon-to-metal-atom ratio of .875 for vanadium carbide /2/ reachable with conventional metallurgical processes. This is supported also by the strong dependence of the transition temperature $T_c$ upon the carbon-to-metal-atom ratio in NbC and TaC /3/. Therefore $C^+$ ions were implanted into carbon deficient $VC_x$ single crystals at different implantation temperatures and the samples were examined for superconductivity.

The implantations were made into vanadium carbide single crystals grown in our institute by the zone melting method. The C/V-atom-ratio of the single crystals were .875 and the gaseous impurities found by chemical analysis were:
$H \leq 1530$ ppm, $N \leq 370$ ppm and $O \leq 320$ ppm.

The crystals were homogeneously implanted with carbon ions of different energies and fluences over a depth of about 1500 Å which is more than 3 times of the estimated coherence length.

The carbon profile and the radiation damage were measured with backscattering and channelling of 2 MeV $^4He^+$ particles.

To remove the radiation damage the crystals were submitted to an isochronal annealing process. At about 950 °C the radiation damage starts to anneal out but at the same temperature the implanted carbon diffuses to the surface of the crystal. The annealing of the crystal and the outdiffusion of the implanted carbon is completed at about 1130 °C.

In order to detect superconductivity of the implanted samples the resistivity was measured down to a temperature of 1.2 K. The measurements were done with a four point probe and an electronic arrangement which is described in a separate contribution of this volume.

None of the samples which were implanted at room temperature and subsequently annealed showed superconductivity. However, the VC single crystal which were implanted at elevated temperature were superconducting. The maximum $T_c$ found

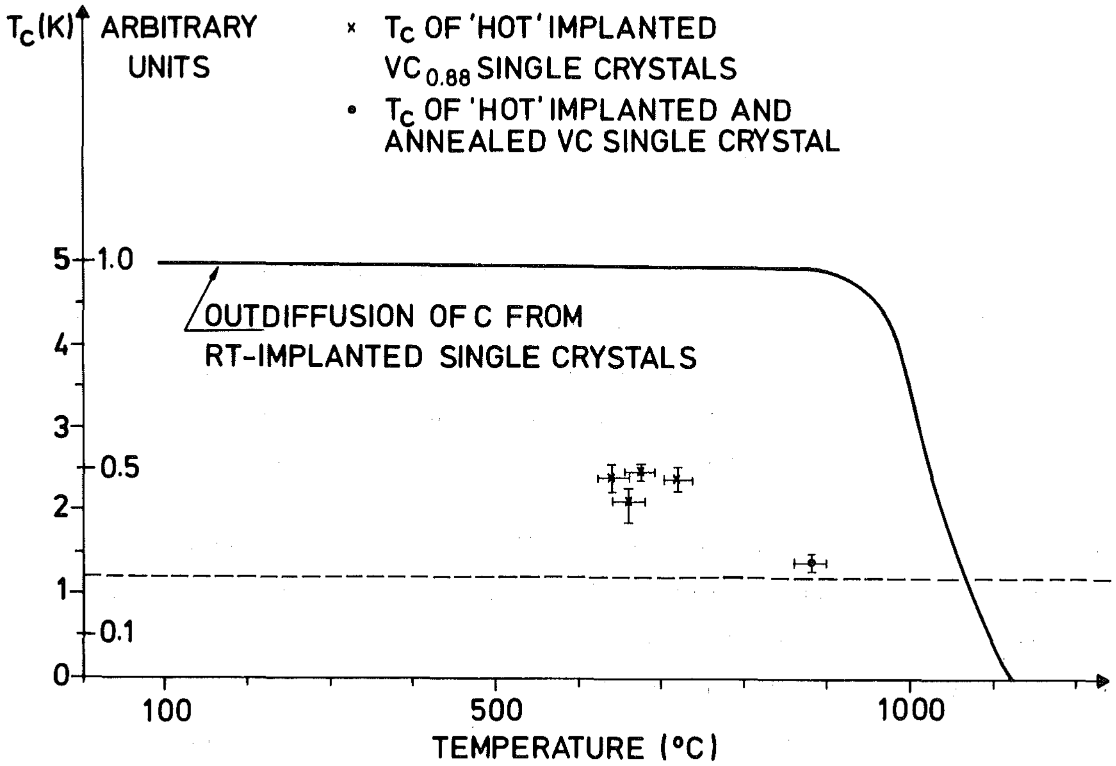

Fig. 1. Transition temperature $T_c$ of carbon implanted $VC_{0.88}$ single crystals as a function of implantation temperature.

till now was 2.5 ± .1 K. The temperature region of the 'hot' implantations in respect to the temperature region where outdiffusion of the implanted carbon occurs is shown in Fig. 1. The dotted line gives the lower temperature limit of the cryostat used for $T_c$ - measurements. The error bars of the $T_c$ - measurements denote the transition width of the samples.

## REFERENCES

/1/ D. W. Bloom, L. Finegold, R. G. Lye, R. Radebaugh and J. D. Siegwarth, Phys. Lett. 33A, 137 (1970).

/2/ E. Rudy, Elisab. Rudy and F. Benesovsky, Planseeberichte für Pulvermetallurgie 10, 42 (1962).

/3/ A. L. Giorgi, E. G. Szklarz, E. K. Storms, A. L. Bowmann and B. T. Matthias, Phys. Rev. 125, 837 (1962).

## 3.7. Crystal Structures and Superconducting Transition Temperature of Reactively Sputtered Vanadium Carbide Thin Films

*O. Meyer and F. Ratzel*

Bulk vanadium carbide produced with normal preparation techniques does not exhibit superconducting transitions down to 0.03 K. Additional C ion implantation /1/ however has lead to an increase of $T_c$ up to 2.5 K. Metastable carbides and nitrides (e.g. VC, TaN) with enhanced $T_c$-values have also been synthesized by rapid quenching from the liquid state and by reactive sputtering.

Here we report on the preparation of VC thin films by reactive sputtering of vanadium in an argon-methane plasma. The films are produced in a rf sputtering unit with an ultimate pressure of $10^{-9}$ Torr. During deposition a rf power of 600 W was applied. The partial pressure of the argon gas was kept constant at $1.5 \times 10^{-2}$ Torr, the methane partial pressure, $p(CH_4)$ was varied between $10^{-5}$ and $10^{-2}$ Torr and was monitored during sputtering by a selectively pumped quadrupole mass analyser. Graphite, quartz and sapphire substrates have been used; the substrate temperature was kept at 750 °C before and during the sputtering process.

The superconducting transition temperature, $T_c$, has been measured with the four-point resistance technique. X-ray diffraction results were obtained from a thin film camera. The ratio Y of the number of C atoms to the number of V atoms and the depth dependence of the composition have been determined by Rutherford backscattering of 2 MeV $^4He$ ions. Layer thickness has been measured with a stylus instrument.

The layer thicknesses of different charges deposited under the same preparation conditions were found to decrease with increasing $p(CH_4)$. The deposition rate was thus calculated to be about 2 Å/s at $p(CH_4) \simeq 10^{-4}$ Torr and 0.5 Å/s at $p(CH_4) = 10^{-2}$ Torr. The concentration ratio Y increased steeply with increasing $p(CH_4)$ as can be seen in Fig. 1. This strong dependence is partly responsible for the difficulties in producing layers with a high degree of homogeneity. The homogeneity is further influenced by $p(CH_4)$ variations which have to be compensated at the beginning of layer growth. The variation in composition with depth are included in Fig. 1 as error bars.

With increasing $p(CH_4)$ in the sputtering gas, layers which revealed five different types of X-ray patterns have been obtained, the results are presented in Fig. 1. For $P(CH_4) \leq 10^{-4}$ Torr the vanadium bcc and the $V_2C$ phase is visible,

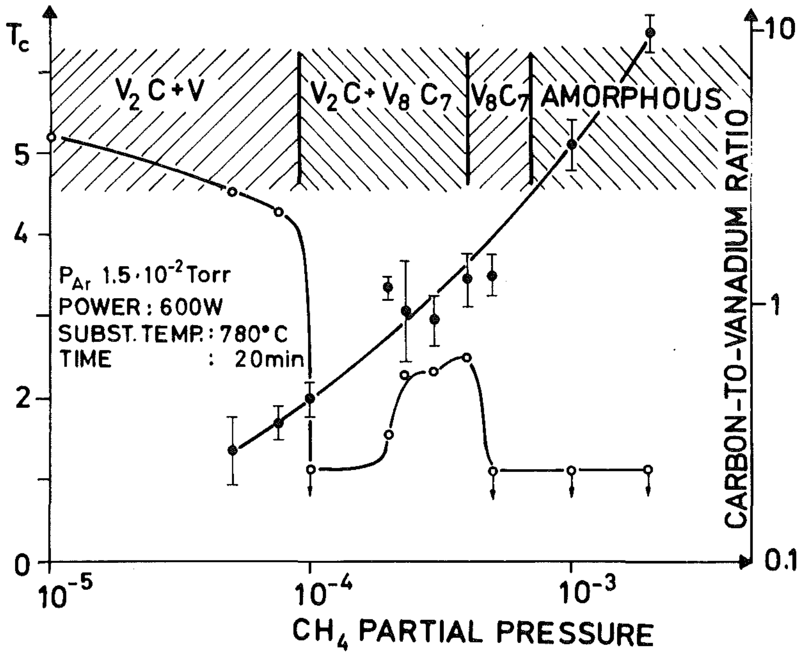

Fig. 1. Carbon to vanadium ratio, phases and $T_c$ versus methane partial pressure.

for $10^{-4} \leq p(CH_4) \leq 5 \times 10^{-4}$ Torr a mixture of $V_2C$ and the B-1 structure ($V_8C_7$) is observed, for $5 \times 10^{-4} \leq p(CH_4) \leq 8 \times 10^{-4}$ Torr the pure B-1 structure is present, for $p(CH_4) > 8 \times 10^{-4}$ Torr no diffraction lines could be seen; the layers seem to be amorphous.

The $T_c$ values are also presented in Fig. 1. $T_c$ is about 4 K in the $p(CH_4)$ range where the V bcc phase is present and was found to decrease below 1.2 K for $10^{-4} \leq p(CH_4) \leq 2 \times 10^{-4}$ Torr. In the pressure region from $2 \times 10^{-4}$ Torr to $6 \times 10^{-4}$ Torr $T_c$ increased up to 2.3 K, a value which also has been obtained by carbon ion implantation. This indicates, that the superconducting VC phase may have been formed.

In summary we have found that the B1 phase is formed only in a narrow methane partial pressure region. For samples having $T_c$ values above 1.2 K either a V bcc phase was present or a phase mixture of $V_2C$ and B1 phase exists. Further work is necessary to correlate the observed $T_c$-values with the observed phases.

## REFERENCES

/1/ K. G. Langguth and M. Kraatz: Superconducting VC Produced by Carbon Ion Implantation (3.6 in this report).

## 3.8. Annealing Effects in Carbon Ion Implanted Niobium Carbide

*K.-G. Langguth and J. Geerk*

Implantation of carbon ions into $NbC_{0.89}$ single crystals and subsequent annealing leads to a maximum superconducting transition temperature $T_c$ of 11.5 K /1/. This high $T_c$ is believed to be due to a carbon content very close to stoichiometry in the implanted surface region. In order to analyze the samples we performed backscattering measurements using 2 MeV α-particles. From the spectrum of the α-particles backscattered from niobium atoms we were able to determine the concentration profile of the carbon in the implanted surface layer. A detailed description of the evaluation technique was given in an earlier paper /2/.

The solid line in Fig. 1 shows the carbon concentration profile after implantation of $C^+$-ions with 80 keV and a fluence of 5 x $10^{16}$ $cm^{-2}$ and 200 keV with a fluence of 1.5 x $10^{17}$ $cm^{-2}$ into a $NbC_{0.89}$ single crystals. The two peaks correspond to the different implantation energies. The $T_c$ of this surface layer determined by resistivity measurement is 7.6 K. The aligned backscattering spectrum shows a strong defect peak within the implanted region.

Annealing at 1070 °C changes the shape of the concentration profile remarkably as is shown by the dashed line in Fig. 1. A considerable amount of carbon has diffused to the surface increasing the carbon concentration in the surface region to more than 15 % above stoichiometry. The aligned backscattering spectrum shows no defects in the first 1000 Å.

After annealing at 1160 °C $T_c$ reaches its maximum. The dotted line in Fig. 1 shows a gaussian shaped carbon concentration profile with a maximum concentration very close to stoichiometry in accordance with measurements of Giorgi et al. /3/ who determined $T_c$ as a function of carbon content. Most of the implanted carbon has diffused to the surface forming there an optically visible layer. The defect peak has disappeared in the aligned backscattering spectrum. The high $T_c$ surface layer causes only strong dechannelling of the incoming α-particles. This indicates that no longer interstitial Nb atoms, but internal strain fields and/or interstitial carbon are present in the implanted surface layer.

At higher annealing temperature the profile spreads out and carbon from the surface layer starts to diffuse back into the crystal. Thus the concentration profile obtained after annealing at 1260 °C (dashed and dotted) shows a typical

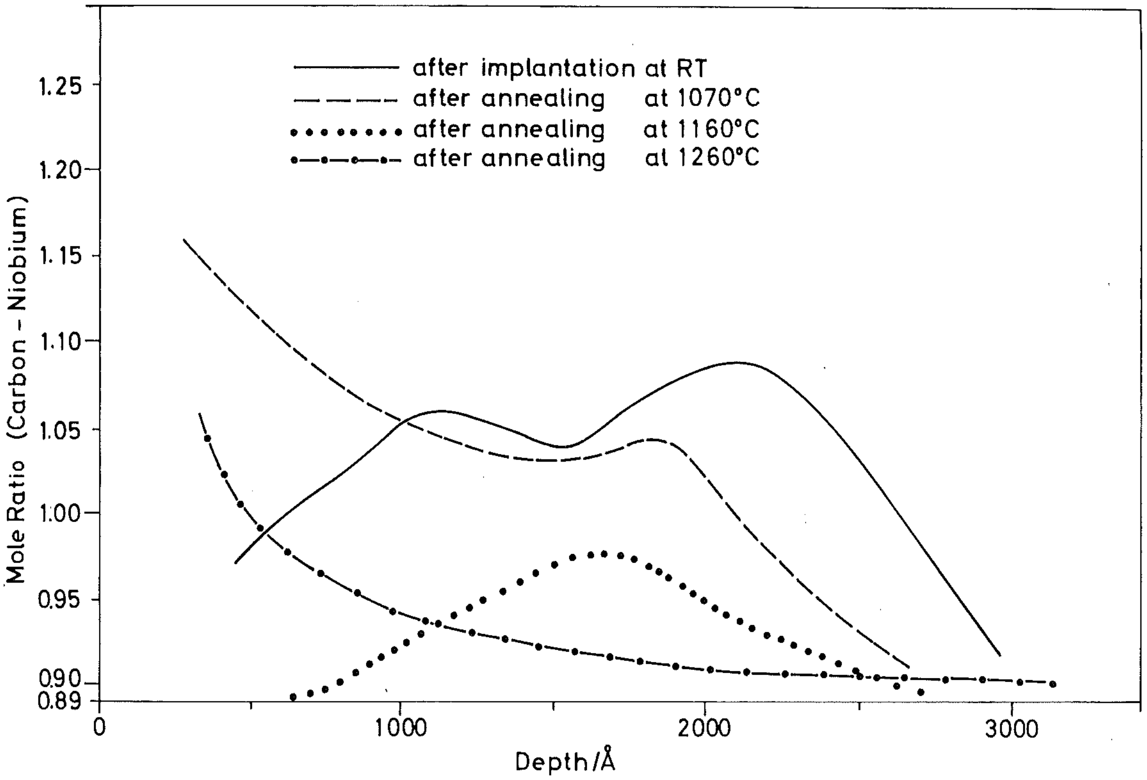

Fig. 1. Concentration profiles of implanted carbon after successive annealing steps.

diffusion like shape. At this temperature also carbon from evaporated carbon layers begins to diffuse into the crystal as we have reported previously /1/. After annealing at 1250 °C there is no evidence of crystalline defects in the aligned backscattering spectrum.

Our next aim is to implant only small amounts of carbon ions into single crystals of niobium carbide with a carbon content close to stoichiometry. Thus the defect production is strongly reduced and a maximum $T_c$ higher than 11.5 K is expected.

## REFERENCES

/1/ J. Geerk and K.-G. Langguth, in Progress Report of the Teilinstitut Nukleare Festkörperphysik,Ges. f. Kernforschung Karlsruhe (KFK 2183), p. 69 (1975).

/2/ K.-G. Langguth, G. Linker and J. Geerk, Ion Beam Surface Layer Analysis, Plenum Press, p. 273 (1976).

/3/ A. L. Giorgi, E. G. Szklarz, E. K. Storms, A. L. Bowman and B. T. Matthias, Phys. Rev. 125, 837 (1962).

## 3.9. First Results on the Superconducting Isotope Effect for VN

*B. Hofmann-Kraeft and F. Ratzel*

The influence of the optical phonons on the superconducting critical temperature $T_c$ has been calculated for NbX (X = light mass) /1/. From these calculations follows that a replacement of $^{14}N$ by $^{15}N$ should cause a $T_c$ enhancement of about 0.1 K in NbN.

In order to test this prediction, we have prepared thin films of the vanadium nitrides $V^{14}N$ and $V^{15}N$ by reactive sputtering. VN is chosen as a test material, as its superconducting NaCl phase is stable and the expected $T_c$ enhancement is also of the order of 0.1 K.

Reactive sputtering is a proofed method for producing layers of refractory nitrides /2/. The sputtering system used for the layer preparation has already been described elsewhere /3/. In order to perform precise inductive $T_c$ measurements, a sample holder was constructed (Fig. 1), consisting of a heatable copper box, a silicon-diode and an induction coil. The VN film, which is deposited on a semi-circle of quartz or sapphire - is in facing contact with the diode, and the remaining semicircle is filled by a Pb foil. Thus each measurement is controlled by the $T_c$ of Pb ($T_c$ = 7.23 K). The reproducibility was found to be ± 0.01 K.

The optimum preparation conditions for high $T_c$ VN layers have been already reported /3/. In contrast to the procedures described there, in the present work the sputtering has been performed in a closed system. The residual gas pressure was found to be mainly due to $H_2O$ vapor as determined with a quadrupole residual gas analyser. A cryopump around the heated anode plate was used to freeze out the $H_2O$ vapor. For each charge we used carbon, sapphire and quartz substrates distributed over the 750 $^{o}C$ hot anode plate. $T_c$ measurements have been performed for VN-layers on the quartz-substrates only, where fluctuations in $T_c$ of 0.12 K have been found for samples of the same charge. This effect is attributed to inhomogeneities in either the temperature of the molybdenum plate or the plasma. The layer with the maximum $T_c$ value however is always formed at about the same position on the plate. Therefore only samples which were situated at the same place during sputtering have been compared.

Fig. 2 shows the $T_c$ results for one such sample of each charge. When average $T_c$-values from these samples are taken we find an isotope shift of 0.08 K.

Rutherford backscattering of $\alpha$-particles revealed that the samples have different contents of oxygen, depending on the individual desorption conditions. $T_c$ decreases with increasing oxygen content, while the V/N ratio is kept constant.

For a more precise analysis of the samples, $T_c$ measurements will be performed on a larger number of samples from each charge and then related to backscattering results.

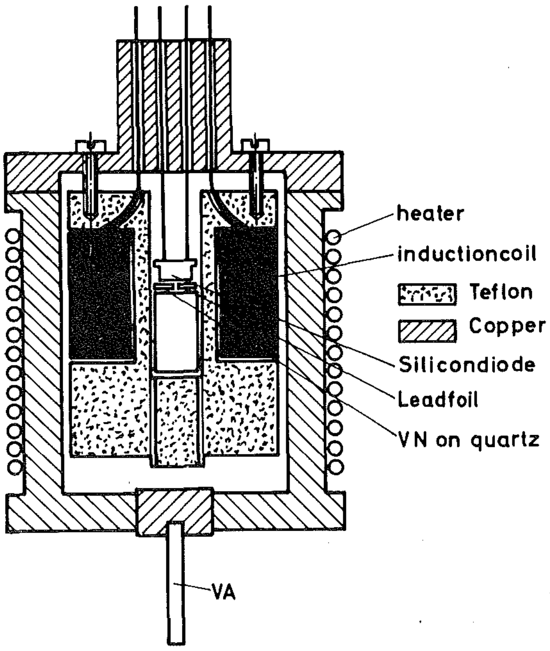

**Fig. 1: Sample holder for inductive $T_c$ - measurements**

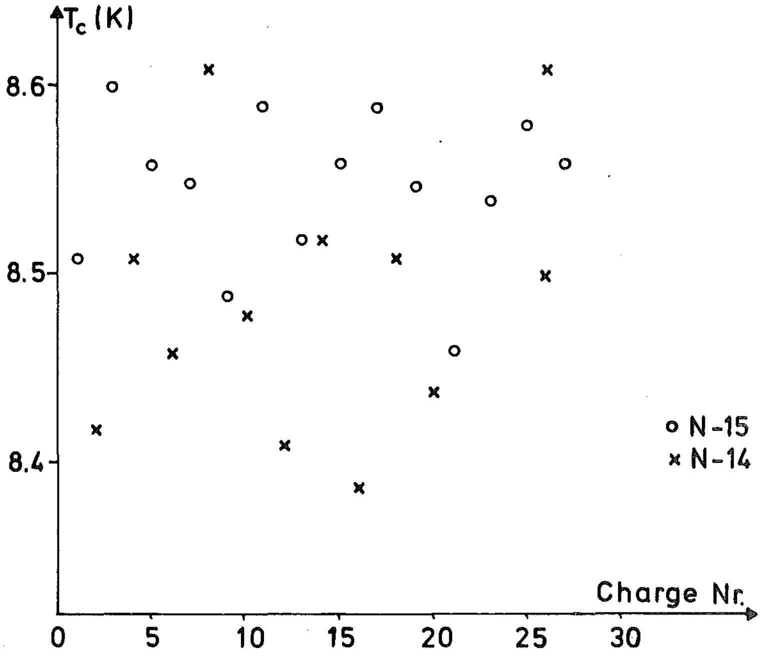

**Fig. 2: $T_c$ for VN on quartz**

REFERENCES

/1/ H. Rietschel, Z. Phys. B22, 133 (1975).

/2/ R. Somasundaram: The Structure and Superconducting Properties of Bulk and Thin Film Hard Superconductors, University of Minnesota, Ph. D. thesis (1974).

/3/ B. Hofmann-Kraeft, F. Ratzel and R. Smithey, in Progress Report of the Teilinstitut Nukleare Festkörperphysik, Ges. f. Kernforschung Karlsruhe (KFK 2183) p. 81 (1975).

## 3.10. High Sensitive Four Probe Arrangement for $T_c$ Measurements

*K.-G. Langguth and J. Geerk*

A frequently used method to measure the transition temperature $T_c$ is the four probe arrangement: a constant current is applied to the sample and the voltage drop between two other contacts attached to the sample is recorded as a function of temperature. For thick samples with low resistivity the voltage drop is very small and therefore difficult to measure.

In the special case of vanadium carbide single crystals /1/ for example the specific residual resistivity is about 10 μΩcm. Because of the critical current density of about $10^3$ A/cm$^2$ in the superconducting surface layer, the currents are restricted to a few mA. With typical sample dimensions of 10 x 5 x 2 mm this yields voltage drops in the 100 nV region. For measuring this small voltage the lock-in-amplifier technique is used which in addition eliminates problems associated with thermal electromotoric forces and temperature dependent contact resistances.

As the resistance of the sample is small compared with lead resistance (10 Ω) a common mode rejection ratio (cmr) better than 100 dB is necessary to measure the voltage drop at the sample accurately. The normal electronic arrangement, with differential amplifier (PAR 118), amplifier (PAR 211), selective amplifier (PAR 210 A) and lock-in-amplifier (PAR 220) yielded a cmr as a function of frequency shown in Fig. 1 (dashed), which is too small for our prupose. In order to increase the cmr of the equipment we use a shielded transformer with an amplification of 1 : 20 of the incoming signal. In addition the signal to noise ratio is improved considerably. The solid line in Fig. 1 shows the cmr of the system with transformer. As the maximum cmr is obtained for frequencies below 100 Hz we use the frequency of 80 Hz for our $T_c$ measurements. At 80 Hz the cmr is about 155 dB corresponding to $6 \times 10^7$. If the lead resistance is 10 Ω, errors are introduced in the measurements for sample resistances below .2 μΩ. Thus the system works successfully for bulk samples with high residual resistivities like compounds and alloys but the cmr may still be too low for very clean bulk samples of superconductors of the pure elements.

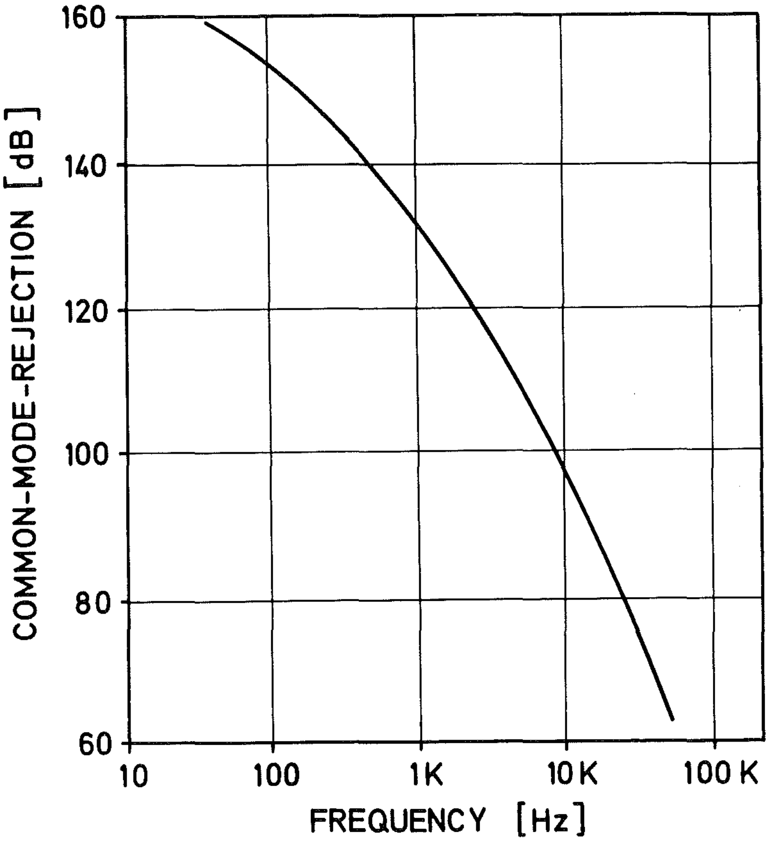

Fig. 1. Common mode rejection as a function of frequency

REFERENCES

/1/ K.-G. Langguth and M. Kraatz: Superconducting Vanadium Carbide Produced by Carbon Ion Implantation (3.6 in this report).

## 3.11. A New Approach to the Precise Determination of $\frac{dI}{dV}$ of Superconducting Tunneling Diodes

*J. Geerk*

The first derivative $\frac{dI}{dV}$ of the current-voltage characteristic of a superconducting tunneling diode is the quantity of primary interest in the tunneling experiment. The standard measuring technique for $\frac{dI}{dV}$ is the modulation technique

/1, /2/, /3/. Small structures in $\frac{dI}{dV}$ due to phonon effects occur usually at high energies (high above the energy gap) where the I-V characteristic shows generally an ohmic behaviour. Thus the phonon effects can easily be detected by balancing out the majority of the $\frac{dI}{dV}$ signal. This can be best accomplished by a conventional ac-bridge circuit. If the conductance data are used to determine the Eliashberg function $\alpha^2(\omega)F(\omega)$ and the coulomb pseudopotential $\mu^*$ by the inversion of the Eliashberg selfenergy equations the accuracy of the results (particularly of $\mu^*$) is strongly dependent on the accuarcy of $\frac{dI}{dV}$ measured at energies close to the energy gap. At these energies the I-V characteristic of a superconducting junction shows a strong deviation from ohmic behaviour and the conventional bridge circuits are not applicable. Therefore the determination of low bias conductance data has been so far a central problem in tunneling studies.

In this report a new approach to the solution of this experimental difficulty is presented. We use a self balancing ac-bride for the measurement of $\frac{dI}{dV}$. The self balancing ac-bridge does not primarily detect deviations from ohmic behaviour but automatically balances out completely at each bias and displays digitally the value of the balancing resistor. Thus the accuracy is not dependent on ohmic behaviour of the I-V characteristic that means the accuracy remains principally unchanged whether the measurement is taken near the gap edge or at high energies.

Recently self balancing ac-bridges designed for the four probe measurement of Ge-low temperature sensors have become avaiable. Such a bridge (Model PCB from SHE-Corporation, USA) was used in a circuity for the precise determination of $\frac{dI}{dV}$ as a function of bias. Fig. 1 shows a complete diagramme of the circuity. The bridge Model PCB measures the conductance applying constant voltage modulation signals from 10 $\mu$V to 300 $\mu$V of a frequency of 27.5 Hz to the sample. The digital readout covers 4 - 1/2 digits corresponding to a resolution of 1 part in 2 x $10^4$. The capacities $C_1$ to $C_4$ isolate the bridge input from the junction bias. The resistors $R_1$ to $R_4$ prevent dc-loading of the isolated sensor leads. The analog output of the bridge is connceted to the Y-input of a recorder. The function of the difference amplifier in the dc-detection circuit is to prevent noise currents from the recorder input generating noise across the junction. The low pass filters $F_1$ and $F_2$ prevent disturbance of the dc-readout by the modulation signal. The small error in conductance introduced by the resistors $R_1$ to $R_4$ and the capacities $C_1$ to $C_4$ has been determined as a function of junction conductance. After the measurement of the conductance

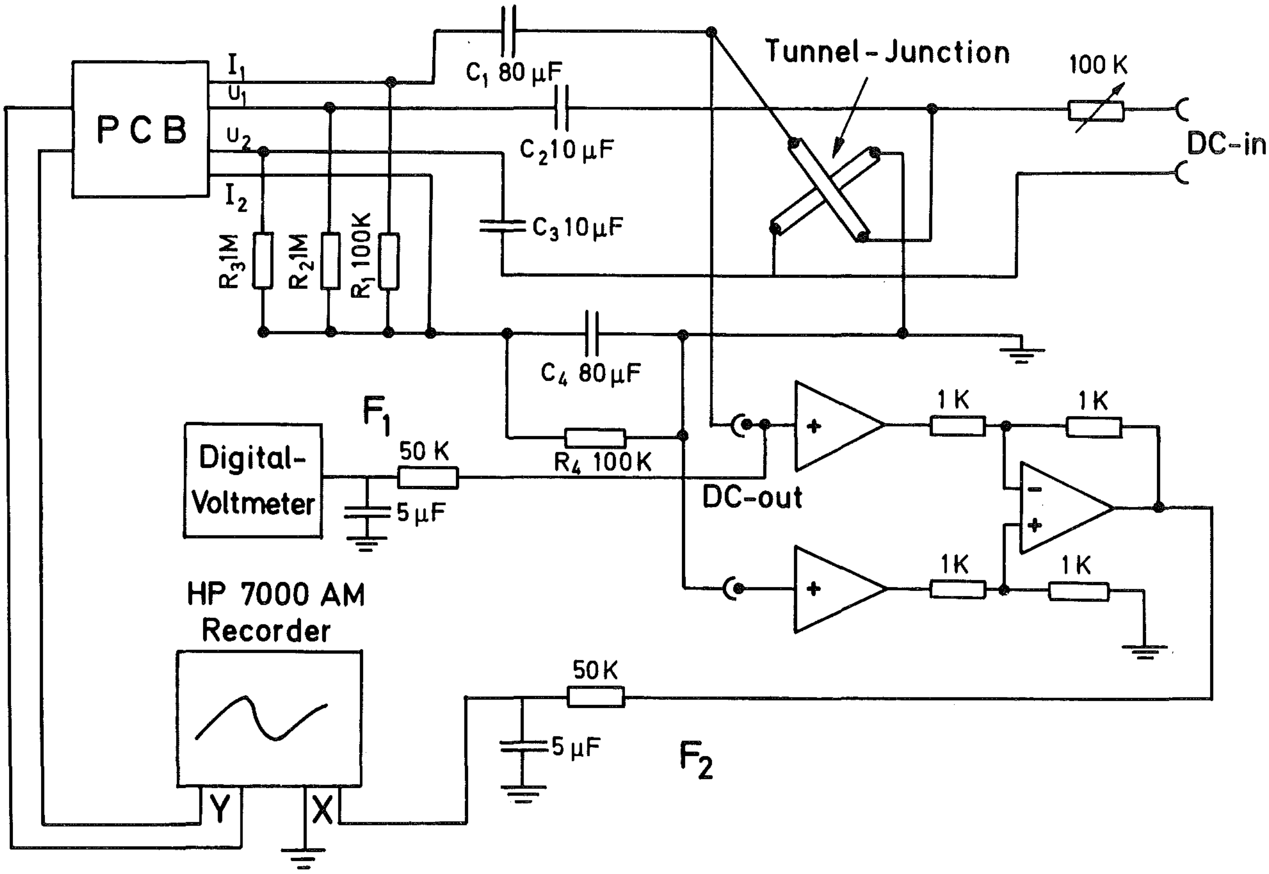

Fig. 1. Schematic diagram of the circuit for the determination of $\frac{dI}{dV}$

characteristic of a junction the data can easily be corrected with respect to this error.

First test measurements of the circuit using Ge-tunneling diodes immersed in liquid helium have been performed successfully.

REFERENCES

/1/ J. G. Adler and J. E. Jackson, Rev. Sci. Instrum. 37, 1049 (1966).
/2/ B. L. Blackford, Rev. Sci. Instrum. 42, 1198 (1971).
/3/ J. Geerk, Gesellschaft für Kernforschung Karlsruhe, KFK-2140 (1975).

## 3.12. The Preparation of Tunneling Contacts on $V_3Si$

*J. Geerk*

Only few tunneling experiments on the β-W superconductor $V_3Si$ have been reported in literature /1/, /2/. The tunnel junctions were always produced in unconventional manners. Levinstein and Kunzler /1/ used a point contact technique and Hauser et al. /2/ measured the energy gap induced in thin Al-films evaporated on $V_3Si$. As both types of junctions are not suited for a detailed measurement of the tunneling density of states, which is recommended for a determination of the Eliashberg function $\alpha^2(\omega)F(\omega)$, we tried to produce junctions of the conventional type namely: $V_3Si$ - $V_3Si$ Oxide-Ag.

A bulk single crystal of $V_3Si$ with a $T_c$ of 16 K was lapped with 7 μ diamond paste till a mirror like surface was obtained. Then the surface was electrolytically etched. Two different etchants were applied: a mixture of HF and $HNO_3$ (in the following called "wet" solution) and a mixture of $H_2SO_4$ and methanol (called "dry" solution). After this chemical preparation a tunneling barrier was formed on the crystal by oxidation in dry oxygen at atmospheric pressure. After masking with Formadur A6 the junctions were completed by the evaporation of Ag layers as counterelectrodes.

Room temperature oxidation resulted in completely shorted contacts and oxidation at 250 °C in high resistance (> 1 MΩ) "capacitor" diodes. Junctions with nominal resistances between 10 - 50 Ω were obtained after oxidation between 120 °C and 150 °C.

Junctions prepared using the "wet" solution showed even at the lowest measuring temperature (1.3 K) no energy gap but exhibited strong zero bias anomalies. Using the "dry" chemical preparation method junctions which reflected superconducting properties could be prepared. Fig. 1 shows $\frac{dI}{dV}$ as a function of voltage of such a junction. The high leakage current which may result from tunneling into normal conducting material and the smeared characteristic in the gap region indicate, that the tunneling surface is partly contaminated. From the distance of the peaks in the dI/dV curve a maximum energy gap of about 2.5 meV can be derived. For the ratio $\frac{2\Delta_o}{kT_c}$ one obtains 3.63, which seems too low for a high $T_c$ superconductor. Levinstein and Kunzler /1/ reported values

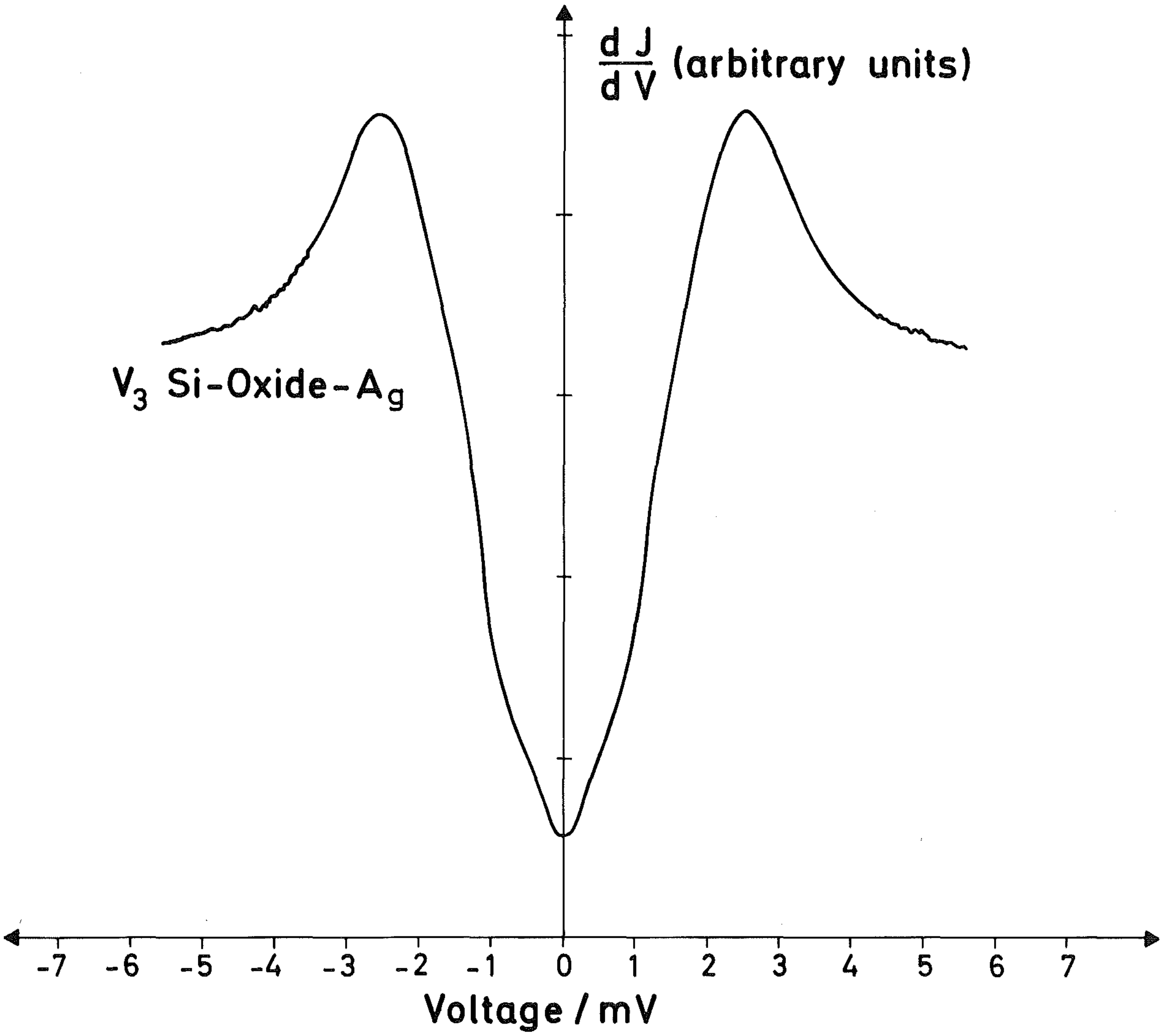

Fig. 1. First derivative $\frac{dI}{dV}$ as a function of voltage of a $V_3$Si-Oxide-Ag tunnel junction.

ranging from 1.8 to 4.2. Most of the values of Hauser et al. /2/ fell close to 3.8.

We conclude that it is possible to prepare tunnel junctions of the conventional type on $V_3$Si. The oxidation has to be carried out at elevated temperature. A serious problem still is the surface contamination which may be caused by the chemical preparation or by the following oxidation procedure.

REFERENCES

/1/ H. J. Levinstein and J. E. Kunzler, Phys. Lett. 20, 581 (1966).
/2/ J. J. Hauser, D. D. Bacon and W. H. Haemmerle, Phys. Rev. 151, 296 (1966).

## 3.13. Channelling Studies on Implanted $V_3Si$

*J. Geerk, G. Linker, O. Meyer and B. Seeber*[(a)]

[(a)] Forschungslaboratorium für Festkörperchemie,
Pelkovenstr. 148, D-8000 München 50

The superconducting transition temperature, $T_c$, of A15 compounds strongly decreases with increasing radiation damage produced by heavy ions /1/ and neutron irradiation /2/. It has been assumed that the results obtained from neutron irradiation are due to simple antistructure (antiside) defects. In contrast to this assumption it has been found that stoichiometry is not the crucial parameter for obtaining high $T_c$ values in sputtered A15 materials /3/.

We have performed channelling measurements on an irradiated $V_3Si$ single crystal in order to get information on the structure of the defects. Successful surface preparation was obtained by successively lapping with 15.7 and 0.5 µm diamond paste, vibratory polishing with 0.25 µm diamond paste and etching in 4 : 1 : 1, $H_2O$ : HF : $H_2O_2$ for 3 min.

The experiments have been performed with 2 MeV $^4He^+$ ions in the [100] and [110] directions. The critical angle, $\psi_{crit}$, and the minimum yield, $\chi_{min}$, have been measured in the [100] direction as a function of depth for the V sublattice. By extrapolating to the surface we determined $\psi_{crit} = 0.75^\circ$ and $\chi_{min} = 0.03$. The empirical formulas from Barrett /4/ were used to calculate $\psi_{crit}$ and $\chi_{min}$. Using an average phonon frequency of 500 K we obtained 0.85° and 0.01, for 300 K we obtained 0.75° and 0.032, respectively. The experimentally determined values are well described using an average phonon frequency of 300 K for the V sublattice, in accordance with results from neutron diffraction measurements /5/.

The strong influence of irradiation on the lattice is demonstrated in Fig. 1 showing random and [100] aligned backscattering spectra from a) an unimplanted b) an implanted and c) an implanted and afterwards annealed $V_3Si$ single crystal. The channelled spectra reveal peaks due to silicon and vanadium atoms, displaced from the rows by damage and oxidation. We determine the number of this atoms from the peak areas assuming that the number of scattering centers is proportional to the number of displaced atoms.

The results are summarized in Table I. For the unimplanted sample the number of displaced Si atoms is about a factor of 6.5 and that of V atoms a factor of 11 larger than the number of the surface atoms. The ratio of V to Si atoms is 3.3 for the [100] surface and 1.8 for the [110] surface. After implantation of 5 x $10^{15}$ Zr/$cm^2$, 140 keV at room temperature the channelled backscattering spectra indicate a completely disordered region in the range of the implanted ions. A single Zr ion was found to displace 63 V atoms and 17 Si atoms (these numbers are a lower limit, as we are already in the saturation region of the damage versus dose curve). The reason that the ratio of displaced V to Si atoms is 3.7 and not 3 maybe due to the simple linear background subtraction. A strong annealing of the disorder occurs at 920 °C for 3 min. The decrease of the number of displaced lattice atoms is accompanied by a 22 % decrease of the number of Zr atoms, probably due to outdiffusion.

Table I

| Surface | Number of surface atoms/$cm^2$ | Number of displaced atoms/$cm^2$ | | |
|---|---|---|---|---|
| | | unimplanted sample | implanted sample | implanted and annealed at 920 °C |
| [100] | | 11 x $10^{15}$ O | 6 x $10^{15}$ Zr | 4.7 x $10^{15}$ Zr |
| | 4.5 x $10^{14}$ Si | 2.6 x $10^{15}$ Si | 1 x $10^{17}$ Si | 1.2 x $10^{16}$ Si |
| | 9 x $10^{14}$ V | 8.7 $10^{15}$ V | 3.8 x $10^{17}$ V | 4.1 x $10^{16}$ V |
| [110] | 8 x $10^{14}$ Si | 6 x $10^{15}$ Si | | |
| | 9 x $10^{14}$ V | 11 x $10^{15}$ V | | |

From the results it may be concluded that heavy ion irradiation of $V_3Si$ produces heavy disorder and not simple antistructure defects. In contrast to results of similar experiments on transition metals, where a higher degree of crystallinity is still present after high dose implantation the damage production in $V_3Si$ resembles that of the semiconductor Si, where it is believed that the covalent bonding is responsible for the observed behaviour.

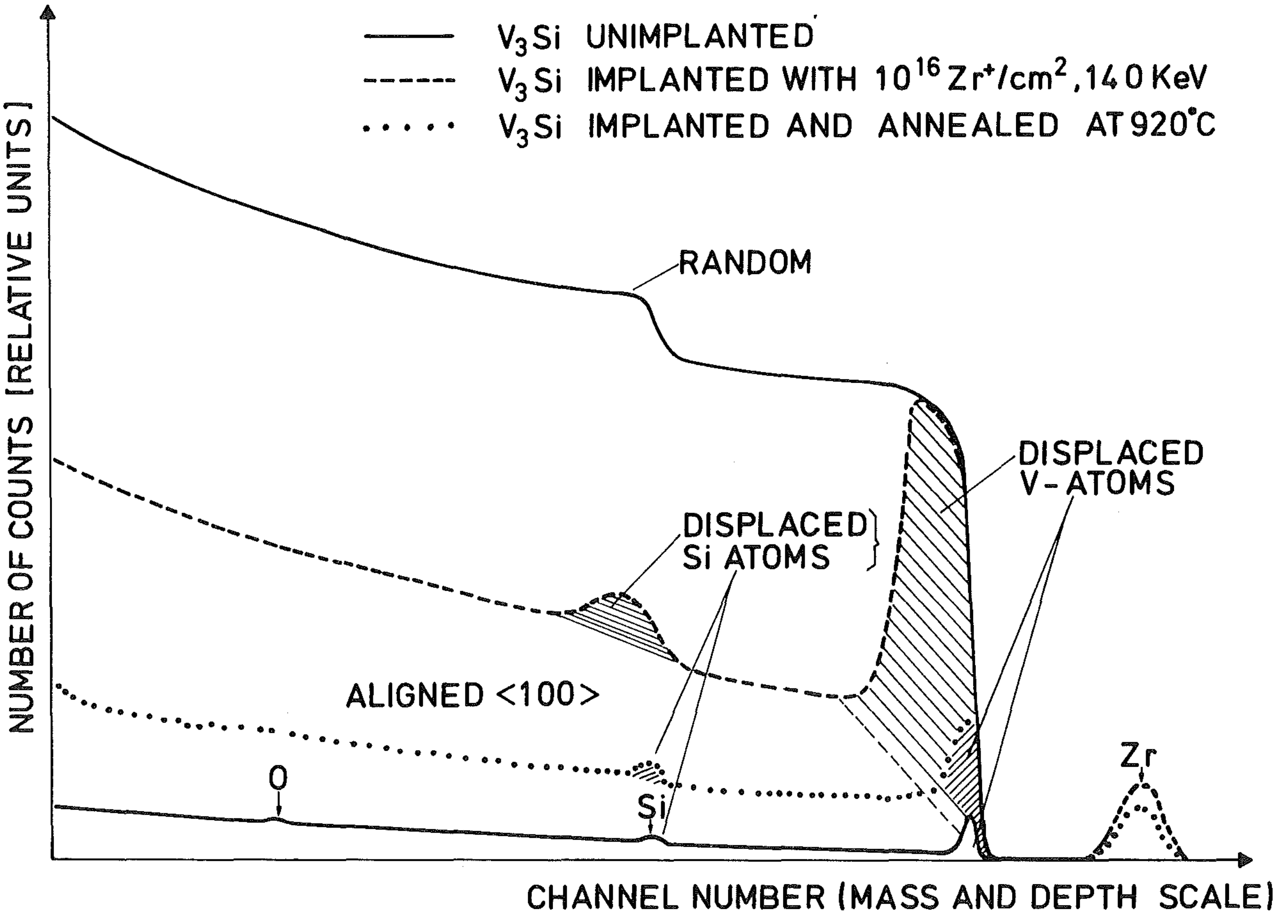

Fig. 1. Random and aligned backscattering spectra from implanted and umimplanted $V_3Si$ single crystal

REFERENCES

/1/ O. Meyer, Applications of Ion Beam to Metals; S. T. Picraux, E. P. EerNisse, F. L. Vook - Editors, Plenum Press, p. 21 (1974).

/2/ A. R. Sweedler, D. G. Schweitzer and G. W. Webb, Phys. Rev. Lett. 33, 168 (1974).

/3/ L. R. Testardi, R. L. Meek, J. M. Poate, W. A. Royer, A. R. Storm and J. H. Wernick, Phys. Rev. B11, 4304 (1975).

/4/ J. G. Barret, Phys. Rev. B3, 1527 (1971).

/5/ P. Schweiss, in Progress Report of the Teilinstitut Nukleare Festkörperphysik, Gesellschaft für Kernforschung Karlsruhe (KFK 2054), p. 12 (1974).

## 3.14. Ion Implantation Disorder in Some Transition Metal Superconductors Studied by the Channelling Effect Technique

*G. Linker and O. Meyer*

We have reported on changes of the superconducting transition temperature $T_c$ in evaporated transition metal layers V, Nb, Ta /1/ and Mo /2/,/3/ after bombardment with inert ($Ne^+$) and chemically active ($N^+$) ions. A decrease of $T_c$ has been observed in V, Nb and Ta by $Ne^+$ ion irradiation into and through the layers and had been referred to 'pure' defect generation; recent results however revealed that the $T_c$-decrease depend strongly on the layer purity (mainly oxygen content) and that in layers with low oxygen content equal doses of implanted $Ne^+$ or $N^+$ ions cause different depressions of $T_c$ the effect being more pronounced for the $N^+$ ions. In Mo-layers the inverse effect had been observed; in high purity layers an increase of $T_c$ occured only by implantation of chemically active ions ($N^+$), whereas oxygen contaminated layers showed a $T_c$-increase also by noble gas ion irradiation at low temperatures. These results indicate that different defect structures are generated by the implantation of different ions.

In order to obtain some information on the nature of the defects, channelling experiments with $He^+$ ions were performed on $Ne^+$ and $N^+$ implanted V and Mo single crystals. The results are demonstrated in Fig. 1. Here backscattering spectra from pure crystals aligned in [100] direction and randomly oriented are shown together with the spectra of $N^+$ and $Ne^+$ implaned and aligned crystals. Though these results are qualitativ at the present stage of investigation pronounced differences in the spectra of $Ne^+$ and $N^+$ implanted samples can be observed. Neon implantations result in a pure almost linear increase of the dechannelling rate while disorder peaks are observed in the spectra of the nitrogen implanted samples.

The former result indicates that long range order defects like dislocations are created by the Ne implantations while from the latter it can be concluded that direct backscattering of the $He^+$ ions occurs from locally displaced lattice atoms. It is thought that these displaced atoms are bound to their new positions by the implanted chemically active nitrogen forming impurity-defect complexes. Disorder introduced by this complex formation into the samples is to our opinion the primary reason for the observed changes in $T_c$.

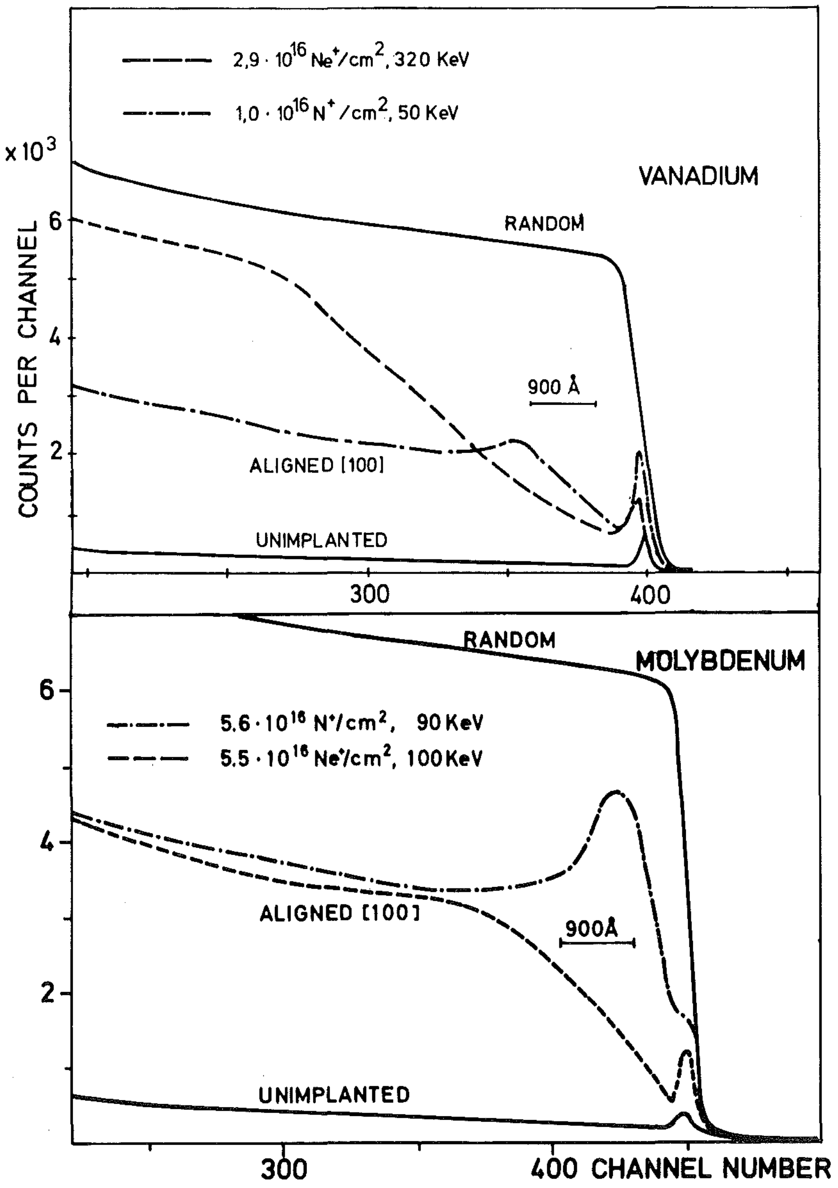

Fig. 1. Random and aligned backscattering spectra from implanted and unimplanted V and Mo single crystals. The Mo crystal has been implanted with similar amounts of $Ne^+$ and $N^+$ ions, while for V a higher $Ne^+$ fluence and a higher implantation energy than for $N^+$ have been chosen such that the $Ne^+$ ions penetrated a surface layer of about 2000 Å and came to rest deeper in the crystal.

## REFERENCES

/1/ G. Linker and O. Meyer, Ion Implantation in Semiconductors, S. Namba Ed., Plenum Press, p. 309 (1975).

/2/ O. Meyer, H. Mann and E. Phrilingos, Application of Ion Beams to Metals, S. T. Picraux, E. P. EerNisse, F. L. Vook-Editors, Plenum Press, p. 15 (1974).

/3/ O. Meyer, Applications of Ion Beams to Materials, Inst. of Physics, Conf. Series 28, p. 168 (1975).

## 3.15. Study of the Diffusion of Cesium in Stainless Steel Using Ion Beams

*Hj. Matzke*[a] *and G. Linker*

[a] European Institute for Transuranium Elements (EURATOM)
D-7500 Karlsruhe, Germany

Stainless steel has been selected as cladding material for oxide fuel elements of fast breeder reactors. However, inner clad corrosion causing a reduction in the effective strength of the clad is a serious problem when applying this material. The corrosion is due to a number of chemical agents and physical actions. A presently favoured hypothesis claims that fission product cesium, in combination with oxygen, is the agressive reactant in grain boundary corrosion reaction. Therefore kinetic data on Cs mobility in steel are of interst. In this study emphasis is put on lattice diffusion using ion beams for analysis.

Cs was introduced into samples of stainless steel by ion implantation with energies of 50 keV and total ion doses of 2 to 5 x $10^{15}$ ions/$cm^2$ were accumulated. The Cs distributions within the steel before and after annealing and the release of Cs from the steel were measured using Rutherford backscattering of 2 MeV $^4He^+$ ions. The fractional release values F were obtained by integrating the Cs-peak following subtraction of the background, and by dividing through the integral of the as-implanted peak. The knowledge of these values in isothermal or isochronal anneal cycles yields the diffusion coefficient D and the activation energy $\Delta H$. The mathematical formalism for the deduction of D and $\Delta H$ has been published before /1/, /2/.

Isochronal (15 min) release values for Cs in two types of stainless steel are presented in Fig. 1.

The release started at about 500 °C and was practically complete at 900 °C. A theoretical curve (dashed line) corresponding to

$$D = 0.3 \exp(-65000/RT) \ cm^2 sec^{-1} \qquad (1)$$

could be fitted reasonably well to these data. The temperature dependence of

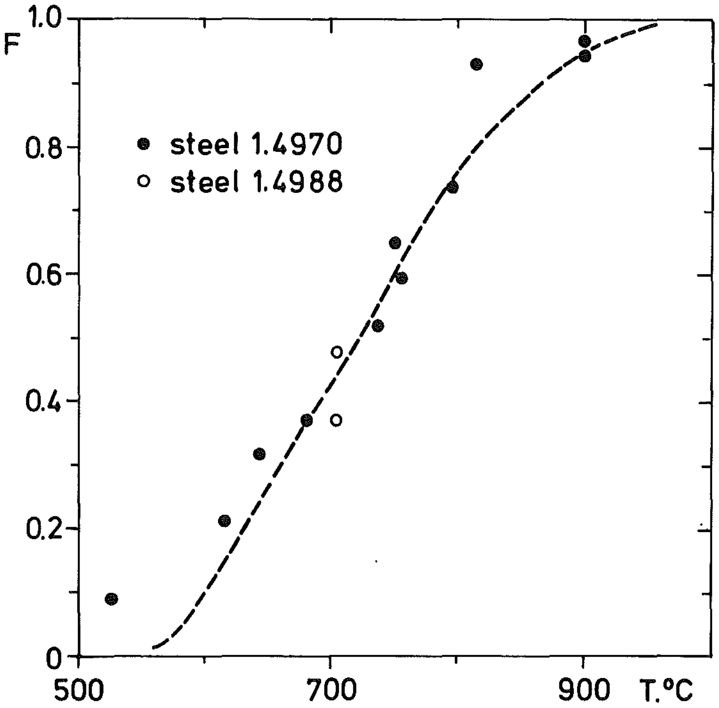

Fig. 1. Isochronal release curve for $C_s$ and stainless steel 1.4970 for 15 min anneal periods. Two measurement from steel 1.4988 are included in the figure.

D in (1) is comparable to that of self diffusion in other steels for which data are available thus indicating though not proving a vacancy diffusion mechanism for Cs.

The Cs-implanted areas of the steel specimens revealed an enhanced oxidation at temperatures above 700 °C. Such an effect was not observed on Ti-bombarded samples indicating the important role of Cs in clad corrosion. The approximate thickness (90 ± 25 Å) and composition (∿ Fe Cr $O_3$) of the oxide layer could be deduced from the backscattering spectra. Also a preferential sputtering of alloying elements from the steel was indicated by enrichment of Mo and Ta at the surface of the bombarded samples. Further a fast diffusion component along grain boundaries has been detected however could not be followed qualitatively due to the high background in the backscattering spectra arising from the heavy steel components (Mo, Ta).

Radioative tracers will be needed to obtain more information on Cs-penetration along grain boundaries.

REFERENCES

/1/ Hj. Matzke, Z. Naturforschung 22a, 507 (1976).
/2/ R. Kelly, Hj. Matzke, J. Nucl. Mat. 20, 171 (1966).

## 3.16. Herstellung von Einkristallen der tetragonalen $\gamma$-Phase des Niobnitrid

*B. Scheerer*

Für Messungen der Phononendispersion an Niobnitrid /1/ wurden Versuche zur Herstellung von Einkristallen durchgeführt.

Bisher war es uns nicht möglich, größere kubisch flächenzentrierte $\delta$-$NbN_{1-x}$-Einkristalle mit NaCl-Struktur herzustellen /2/. Die unter nachstehend beschriebenen Ziehbedingungen erhaltenen Einkristalle hatten die leicht tetragonal deformierte NaCl-Struktur der $\gamma$-$NbN_{1-x}$-Phase /2/.

Als Ausgangsmaterial wurde heißgepreßtes Pulver in Form von Stäben mit einem Durchmesser von ca. 12 mm und einer Länge von ca. 150 mm verwendet. Das Material wurde nach dem tiegelfreien Zonenziehverfahren aufgeschmolzen. Dazu wurde der Stab an beiden Enden in eine Halterung aus "Lavit" eingespannt und mit einer Geschwindigkeit von 8 mm/h vertikal nach unten durch die Hochfrequenzspule geführt. Zur induktiven Beheizung des Materials waren speziell geformte HF-Spulen erforderlich. Dadurch erzielte man ein gutes Ausschmelzverhalten und eine möglichst kleine Schmelzzone. Fig. 1 zeigt einen zonengezogenen $NbN_{1-x}$ Stab.

Um die beiden Schmelzpunkte von NbN /3/ beträchtliche Dekomposition bzw. um den Verlust von Stickstoff zu vermindern /4/, wurden die Versuche unter einer Stickstoffatmosphäre bei einem Druck von 20 bar durchgeführt.

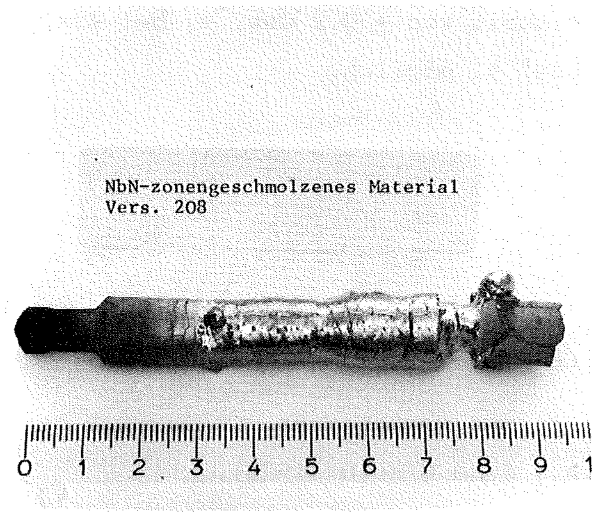

Fig. 1.

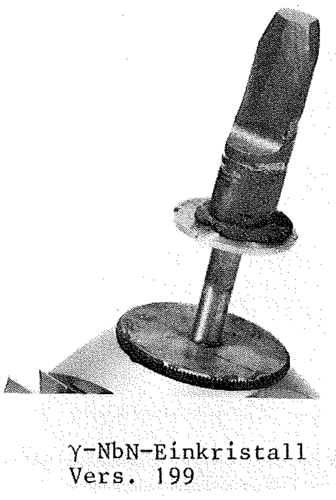

Fig. 2.

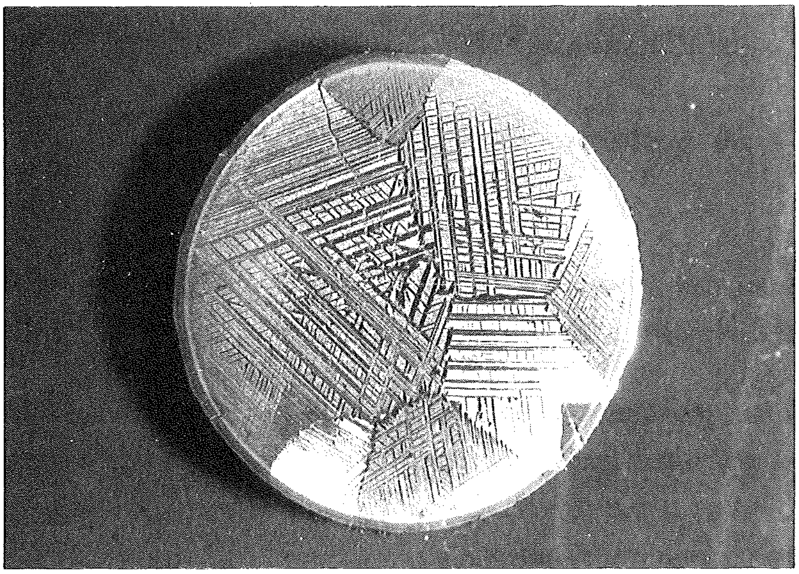

Fig. 3. Querschnitt eines gezonten Niobnitrid-Stabes

Zur strukturellen Analyse wurden die gezonten Stäbe auf einem Neutronendiffraktometer am FR2 in Karlsruhe untersucht.

Aus dem zonengezogenen Stab wurden die einkristallinen Bereiche mit Volumina > 1 $cm^3$ herausgeschnitten. Fig. 2 zeigt einen $\gamma$-$NbN_{.64}$-Einkristall. Fig. 3 zeigt den Querschnitt eines gezonten Niobnitrid-Stabes. Zu erkennen ist die lamellenartige Struktur, welche aus dem Übergang von der $\delta$-$NbN_{1-x}$ in die $\gamma$-$NbN_{1-x}$-Phase während des Abkühlvorganges resultiert.

Die chemische Analyse der Kristalle ergab ein Verhältnis N/Nb von 0.64. Die Analyse des Stickstoffs, nach dem Vakuum-Heißextraktions-Verfahren durchgeführt, ist im ungünstigsten Fall mit einer Genauigkeit von ± 0.2 Gew. %, bei einem angenommenen Gesamtstickstoffanteil von 11. Gew. %, möglich.

## REFERENCES

/1/ F. Gompf, L. Pintschovius, W. Reichardt und B. Scheerer, Conference on Neutron Scattering, Gatlinburg, U.S.A., June 6 - 10 (1976).

/2/ G. Brauer und R. Esselborn, Z. anorg. Chem. 309, 151 (1961).

/3/ P. Ettmayer, R. Kieffer und F. Hattinger, Metall 28, 1151 (1974).

/4/ R. W. Guard, J. W. Savage und D. G. Swarthout, Transact. of the Met. Soc. of AIME 239, 643 (1976).

# 4. DATA PROCESSING

## 4.1. An Interactive Computer Graphics Method for the Determination of the Phonon Density of States from Inelastic Coherent Neutron Scattering Data of Polycristalline Samples

*W. Abel*

It is well known that the analysis of the neutron scattering data is often a time-consuming process requiring complicated and laborious calculations. Accordingly, the application of interactive computer graphics methods has been led to a more effective evaluation of the scattering data. Moreover, the use of on-line computing with interactive graphics has enabled studies to be performed in much greater detail than is normally possible in a batch processing environment. An interactive computer program already exists to evaluate the phonon density of states from inelastic incoherent (partially incoherent) scattering data using Egelstaff's method /1/. Because in the overwhelming majority of cases the coherent scattering in inelastic scattering experiments predominates a new approach which is based upon a FORTRAN IV code /2/ has been developed to determine the phonon density of states using Bredov's method by averaging over a large range of the momentum transfer. Then, under certain conditions, the one-phonon scattering cross section is directly related to the phonon density of states /3/.

This method can be applied unless the multi-phonon contributions predominate so that a successful correction will not be achieved. Therefore an interactive control of the program flow enables the user to arrive at a most acceptable solution by observing the consequences of changes in various parameters which are summarized below:

1. Determination of the range of evaluation in the TOF-spectra.
2. Choice of the detectors which are taken into account to integrate over the range of the scattering angles.
3. Correction for time-dependent background.
4. Correction for constant background.
5. Variation of the mass of the scattering system.
6. Two iteration methods can be used alternatively.
7. Determination of the upper of the one-phonon spectra.
8. Correction for experimental resolution.

The TOF-data can be supplied to the program as a data set containing the detector spectra for each scattering angle or as a TOF-sum predefined by external programs. An on-line facility with an IBM/2250-1 display system connected to an IBM/370-168 computer is used. The communication of the user with the program is realized via a light pen and a programmed function keyboard.

## REFERENCES

/1/ W. Abel, in Progress Report of the Teilinstitut Nukleare Festkörperphysik, Ges. f. Kernforschung Karlsruhe (KFK 2054), p. 86 (1974).

/2/ W. Reichardt and J.-B. Suck, in Progress Report of the Teilinstitut Nukleare Festkörperphysik, Ges. f. Kernforschung Karlsruhe (KFK 2183), p. 94 (1975).

/3/ M M. Bredov et al., Sov. Phys. Sol. State 9, 241 (1967).

## 4.2. Connection of a NOVA-Computer with the Central IBM Computers under Test

*F. Barthel*[(a)] *and G. Ehret*

[(a)] Abt. Datenverarbeitung und Instrumentierung (ADI)

A way for connecting distributed minicomputers with the central batch- and time-sharing IBM computers has been designed and demonstrated by ADI. Standard high speed modems and specially designed line-handler hardware are used to exchange data with 300 K baud over standard twisted-pair telephone cables. The software driver package is an elaborated multitasking program allowing the use of several logically independent data paths simultaniously. It has been adapted to a Nova-line computer.

Due to the 4 K memory need of the software driver package it was decided not to incorporate it into the Real Time Disk Operation System RDOS, but to make it available as part of the user's program using standard linkage techniques. The software interface routines for the programming languages BASIC and FORTRAN have been written. A scheme for an intensive test of the hardware and software is started.

## 4.3. Übersichtsplots auf dem STATOS-Plotter

*R. Moser*

Es wurde eine FORTRAN IV Subroutine erstellt, die es ermöglicht, eine grobe Übersicht zu erhalten, wenn mehrere Spektren gleichzeitig betrachtet werden sollen.

Pro Aufruf verlangt die Subroutine als Argumente das zu zeichnende Datenfeld, die Anzahl der Punkte sowie die Minima und Maxima. Die Minima und Maxima können auch in der Routine selbst bestimmt werden.

Jedes Spektrum wird in etwa Postkartengröße dargestellt. Es werden nach Möglichkeit 256, maximal jedoch 350 Punkte geplottet; werden mehr Punkte angeliefert, so wird entsprechend gemittelt. Punkte, die oberhalb des vorgegebenen Maximums liegen, werden solange durch 10 dividiert, bis sie in die Zeichnung passen. Punkte, die unterhalb des vorgegebenen Minimums liegen, werden gleich dem Minimum gesetzt.

Die Achsenbeschriftung ist durch die Calcomp-Software normiert. Die Anordnung der einzelnen Zeichnungen auf dem Papier ist in der Subroutine festgelegt; es werden jeweils 4 Spektren übereinander geplottet (Abb. 1). In einem Lauf können bis zu 120 Spektren geplottet werden.

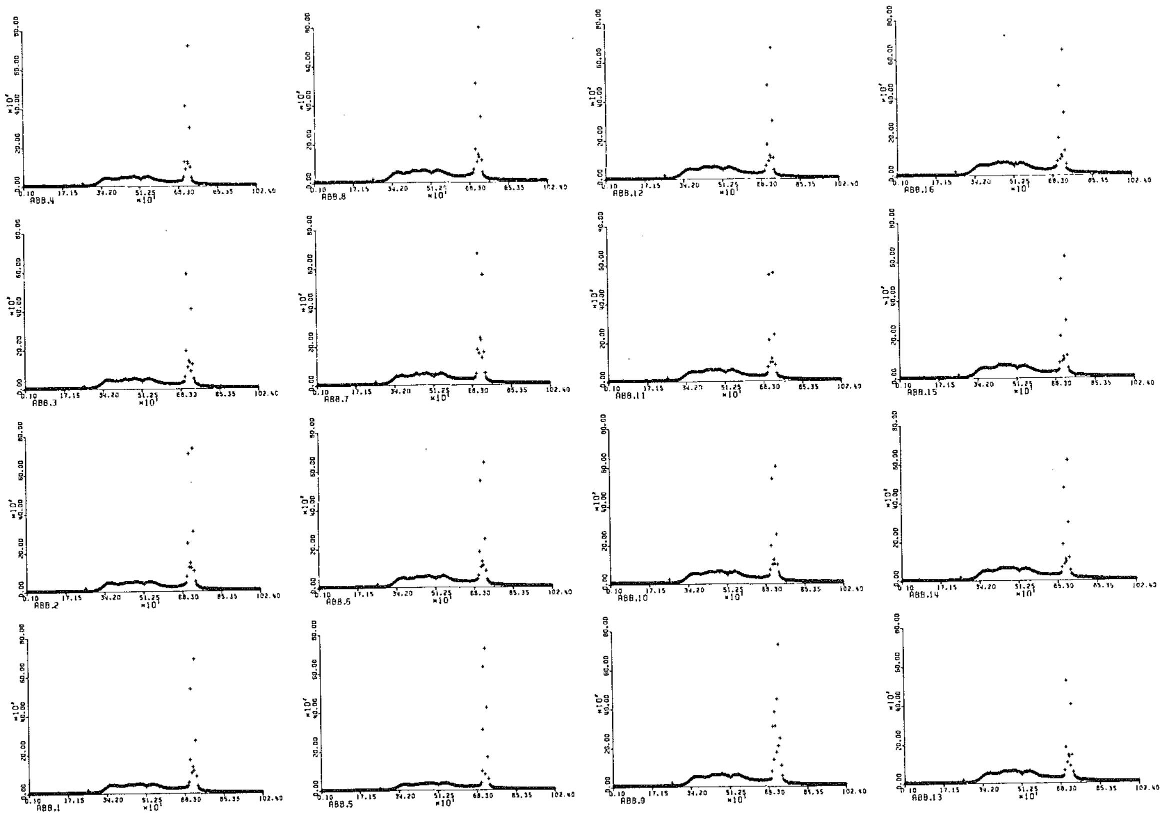

Abb. 1. Beispiel

## 4.4. Adaption of the X-RAY SYSTEM to the IBM 370/168 of the ADI/KFZ-Karlsruhe

*R. Kuhn*

From the University of Marburg we received a set of programs, called the X-RAY SYSTEM /1/. It is designed to carry out the calculations required to solve the structure of crystals by diffraction techniques.

The version we procured was working on an IBM-computer, so that we had only to adapt it to our installation, an IBM 370/168. The whole program resides on disks, the module being used is in the memory. There it takes only 300 K bytes, so that one can run it several times a day.

The SYSTEM was tested in part for X-RAY application using the enclosed example data decks and for the case of single crystal neutron diffraction by our data on $K_2Pt(CN)_4Br_{0.3} \cdot 3D_2O$ (KCP). The following programs have worked successfully:

| | |
|---|---|
| BONDLA | determination of contact and bond distances and angles with estimated errors |
| CRYLSQ | general crystallographic least squares program |
| DATRDN | preparation of binary data file and preliminary treatment of data and symmetry |
| DIFSET | generation of settings for gathering data on an automated diffractometer |
| FC | structure factor calculation |
| FOURR | fourier transformations to give Patterson, vector, electron density, difference, or E maps |
| LOADAT | load atomic parameters into the binary data file |
| NORMSF | preliminary data scaling, calculation of quasi-normalized structure factors (E), and estimation of overall temperature factor |
| SINGEN | forms triples for phase determination (centric or acentric). |

### REFERENCES

/1/ J. M. Stewart, G. J. Kruger, H. L. Ammon, C. Dickinson and S. R. Hall, Technical Report TR-192, THE X-RAY SYSTEM, Computer Science Center University of Maryland, June 1972.

## 4.5. Program System for the Development of Printed Card (PC)-Layouts

*G. Ehret and R. Moser*

Starting from the original program /1/ an extended version in form of a program system has been developed for the NOVA-computer. The system consists of to parts.

The first contains a set of 7 programs to check and prepare the input data.

1. The input data for the boreplan and interconnectionplan are converted into a fixed format.
2. The boreplan is concatenated with a separate file, containing a list of boreholes, common to all PC.
3. The interconnectionplan is tested for duplication.
4. The interconnections are compared with the boreplan to get a list of the missing IC's and a general library is searched for them.
5. Then the IC's that could be found are added to the boreplan and the duplicationtest will be repeated.
6. For further tests a listing of unused IC-pins can be produced.
7. A papertape for the boreplan and the interconnectionplan can be punched out, usable as input for the development of the layout.

In industry using this papertape two PC's have already been produced in multiwire technic.

In the second part of the program the search for interconnectionlines for the multiwire technic is done interactively. First the symbolic boreplan is converted to absolute coordinates and a matrix, which is used as a working area, is filled respectively. Then the program tries to draw a way and asks the user, if the solution is acceptable. In stepmode it is possible to draw a better line than the program has found or to try to draw an interconnection that could not be found automatically. After each run of the program the actual picture of the matrix is shown on display. In the stepmode the actual position is pointed by flashing. The ways that could not be drawn even stepwise are written into an outputfile and must be used in a second multiwire plane. Finally a NC-papertape may be punched, which is used to fabricate the PC.

### REFERENCES

/1/ R. Moser, in Progress Report of the Teilinstitut Nukleare Festkörperphysik, Ges. f. Kernforschung (KFK 2183), p. 98 (1975).

# 5. DEVELOPMENT OF MEASURING DEVICES AND TECHNIQUES

## 5.1. MAG 1 and MAG 2: Two Neutron Spectrometers for Elastic Diffuse and Inelastic Scattering

*P. v. Blanckenhagen, G. Ehret, J. Krisch*[(a)]*, N. Nücker, Chr. v. Platen*[+] *and K. Weber*

(a) Abteilung Reaktorbetrieb und Technik

Two neutron spectrometers have been installed at the FR2-reactor mainly for the investigation of magnetic neutron scattering from polycrystalline and single crystalline samples. One instrument (MAG 1) is installed at a thermal beam hole, the other (MAG 2) uses the beam of the cold source. Both spectrometers are designed for the following applications /1/:

1. Investigation of diffuse scattering with the possibility to separate the inelastic background.
2. Measurement of inelastic scattering by time-of-flight technique.
3. Inelastic measurements using triple axis technique.
4. Elastic and inelastic scattering experiments with polarized neutrons.

The basic mechanical construction of the spectrometers consists of two parts: A monochromator with movable crystals and an one-axis spectrometer with two arms bearing multidetectors for application 1. and 2. and a crystal analyser unit for 3. and 4. . The MAG 1 monochromator may be used either as single or as double-monochromator (track distance 35 - 65 cm, track length 90 cm). The MAG 2 double-monochromator has a track distance of 50 cm and a track length of 100 cm. The spectrometers are surrounded by shielding houses with 20 - 40 cm thick boron-paraffin walls. The counters are additionally shielded by 10 - 20 cm boron-paraffin and boron-carbide. All angle variations are accomplished by stepping motors and controlled by digitizers giving 1/100 degree resolution. The instruments may be

---

[+] Present address: I. Physikalisches Institut der Universität Heidelberg operated either with a NOVA 2 computer or manually. Some details of the spectrometers are given in the following table:

| | MAG 1 | MAG 2 |
|---|---|---|
| Energy range (with graphite monochromators) | 12 - 67 meV | 2 - 5 meV |
| Maximum neutron flux at the sample position (poorest primary resolution) | $\sim 10^5$ n/cm$^2$ sec | $\sim 10^7$ n/cm$^2$ sec |
| Background without sample (for one counter) | 4 cpm | 0.2 cpm |
| Secondary flight-path | 110 cm | 110 - 170 cm |
| Detectors ($He^3$, 1' Ø) | 20 x 8' long | 30 x 12' long |
| Angular range of the multidetectors | 30° | 2 x 60° |

The following ancillary equipment is available, which may be used at both spectrometers alternatively: An analyser-crystal-spectrometer; two high speed Fermi-choppers; a superconducting magnet and three electromagnets for field directions in the scattering plane and vertical to it; a continuous flow cryostat (6 - 300 K); a furnace up to 700 K, CoFe-polarizer and analyser with an RF-spin-flipper for time-of-flight measurements and two NOVA 2 computers with CAMAC-scalers or time-of-flight-unit as input.

Fermi-chopper /3/: High speed Fermi-choppers were developed for applications 1. and 2. (maximum rotating speed: 28 000 rpm; maximum beam cross-section: 3.9 x 7.9 cm). For the diffuse experiments a chopper with 6.5° angular acceptance is used, the chopper for inelastic measurements has an angular acceptance of 1.6°.

Superconducting magnet with target cryostat /4/: This magnet was designed to study large samples with a wide range of scattering angles. The field direction may be directed vertical (180° access) or parallel to the scattering plane (30° access). Polarized neutron experiments (asymmetric field distribution) are also possible. The characteristic features of the magnet are:

Maximum field: 4.5 T
Magnet sweep rate: 5 min
Residual field compensation: $-0.5\ A \leq I \leq 0.5\ A$
Max. usefull beam cross-section: 5 x 5 cm
Homogeneity of the field: 5.5 % at the sample position (3 cm Ø × 4 cm)
Liquid He consumption (with maximum field): ~ 0.5 l/h
Operation time with one He-filling and max. field: ~ 24 h
Target-temperature range: 1.5 - 300 K

Data recording and spectrometer control with NOVA 2 computer: Two CAMAC-crates with controllers of type A include up to 38 scalers, an input register (for temperature and field check), a decimal display unit, a clock generator and an adapter to the step-motor controller. A gate generator controlled by the chopper trigger signal allows to gate the scalers with a variable time window. The detector signals may be summed to groups of 2 - 20 counters. The time-of-flight unit /5/ has a 16 detector group capability. The CAMAC-moduls may be controlled by a manual controller /6/ with preset time. Normally the spectrometers are computer controlled. The programs are written in extended basic language, assembler subroutine execute the dialog with the CAMAC-crate and allow plotting of data on TV display.

Stepping-motor-controller /7/: This instrument consists of a power unit for the supply of 12 stepping-motors and a control-unit to control the stepping-motors, the end switches and the adapters for the digitizers. In the manual mode of operation in connection with the CAMAC-manual controller scans with constant increments using 4 stepping-motors can be done.

RF-flipper-chopper: The RF-flipper is similar to the Kjeller instrument /8/. A 20 A - power supply may be operated continuously or in a pulsed mode with a periodic pulse pattern of variable pulse length and frequencies or pseudorandom pulses. This chopper was tested with Co-Fe single crystal as polarizer and analyser and a secondary flight path of 50 cm. The shortest neutron pulse width obtained for 4 Å-neutrons of the cold source was 40 µsec.

## REFERENCES

/1/ P. v. Blanckenhagen et al., in Progress Report of the Teilinstitut Nukleare Festkörperphysik, Ges. f. Kernforschung Karlsruhe (KFK 2054), p. 54 (1974) and (KFK 2183), p. 51 and 54 (1975).

/2/ K. Weber et al., in Progress Report of the Teilinstitut Nukleare Festkörperphysik, Ges. f. Kernforschung Karlsruhe (KFK 2054), p. 97 (1974).

/3/ K. Weber, in Progress Report of the Teilinstitut Nukleare Festkörperphysik, Ges. f. Kernforschung Karlsruhe (KFK 2183), p. 104 (1975).

/4/ from Oxford Instruments

/5/ H. Hanak et al., in Progress Report of the Teilinstitut Nukleare Festkörperphysik, Ges. f. Kernforschung Karlsruhe, (KFK 2054), p. 81 (1974).

/6/ from Wenzel-Electronic

/7/ N. Nücker, in Progress Report of the Teilinstitut Nukleare Festkörperphysik, Ges. f. Kernforschung Karlsruhe (KFK 2183), p. 103 (1975).

/8/ A. Virjo et al., Kjeller-Report 125 (1968).

## 5.2. Monochromator für ein Dreiachsenspektrometer

K. Weber

Für das am R6-Strahlrohr des FR2 installierte 3-Achsenspektrometer /1/ wurde ein neuer Monochromator benötigt, um den ausnutzbaren Energiebereich zu vergrößern, die Intensität zu erhöhen und den Untergrund herabzusetzen. Es wurde ein Gerät entwickelt, das sowohl als Doppelmonochromator wie auch als Einfachmonochromator eingesetzt werden kann (Fig. 2 und 3).

Die Monochromatoranlage besteht aus einem stationär aufgebauten Abschirmhaus, dem auf Schienen beweglichen Monochromatorwagen (Fig. 1), sowie einer ebenfalls auf Schienen beweglichen Abschirmtür. Die gesamte, den Monochromatorwagen umhüllende Abschirmung wurde aus Blei-, Beton- und Paraffinsteinen aufgebaut. Die Abschlußtür ist ganz mit Schwerbeton ausgegossen. Sie kann mit einem Handrad bewegt werden. Die Dicke der Abschirmung um den Monochromator beträgt 50 cm. Der Monochromatorwagen, ebenfalls eine Stahlkonstruktion, auf Schienen beweglich, besitzt für die Aufnahme der Laufbahnen und Kollimatorwalze präzise gearbeitete Auflageflächen. Seine Hohlräume sind mit Schwerbeton ausgefüllt, die strahlseparierenden Abschirmformsteine wurden aus einer Mischung von Bleikugeln, Borkarbid und Gießharz hergestellt.

Die zur optimalen Einstellung der Monochromatorkristalle erforderlichen Bewegungen können in folgender Weise durchgeführt werden:

1. Die Translationsbewegung der beiden Kristalle geschieht durch zwei im Abstand von 60 cm parallel zueinander angeordneten Laufbahnschlittenführungen. Gesamthub des Schlittens 90 cm, kleinste Hubweite 0.02 mm.
2. Zur Einstellung des Bragg-Winkels wurden zwei Rundtische der Fa. Huber mit einer Einstellgenauigkeit von 0.01° verwendet.
3. Zur Kristalljustierung sind zwei durch Getriebemotoren angetriebene Goniometerköpfe der Fa. Huber eingesetzt.
4. Die Kollimation des monochromatischen Strahls erfolgt durch einen Soller-Kollimator, der von einer Abschirmwalze aufgenommen wird, die zwischen den beiden Monochromatorkristallen drehbar gelagert ist. Die Kollimation kann durch Entfernen von Blechen vergrößert werden. Kleinstmögliche Kollimation 20'. Die Einstellgenauigkeit des Kollimators beträgt 0.02°.

Alle zur Energieänderung notwendigen Bewegungen können durch einen Kleinrechner angesteuert werden, wobei die tatsächlichen Positionen durch Positionsmelder registriert werden. Der Bragg-Winkel $2\theta$ beträgt beim Einsatz als Einfachmonochromator 18.5° und beim Doppelmonochromator kann er zwischen 18.5 und 90° variiert werden, was einen Energiebereich von ca. 5 - 60 meV bei Verwendung von Graphiteinkristallen ergibt.

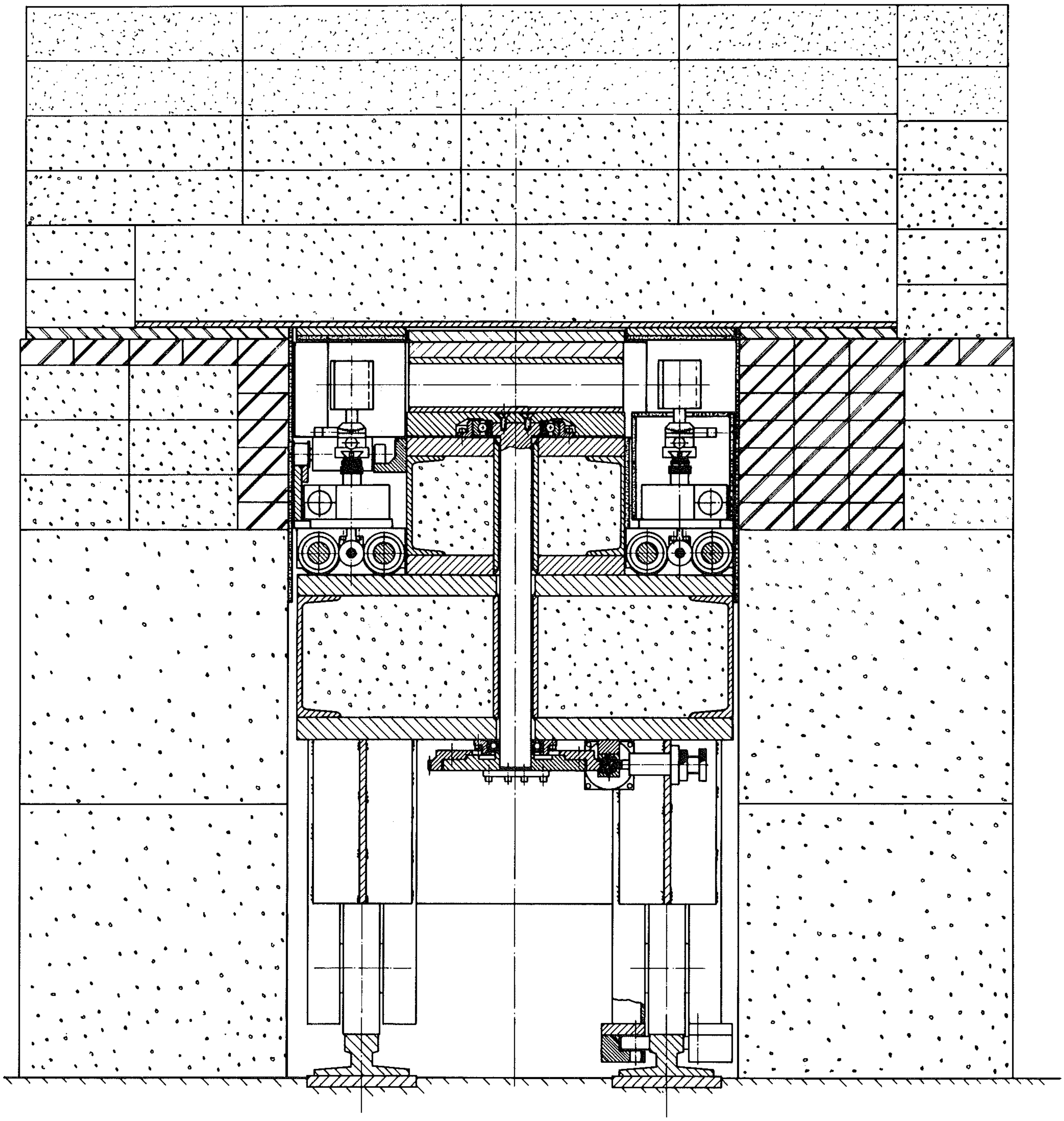

Fig. 1 Monochromatorenanlage (Vertikalschnitt)

REFERENCES

/1/ K. Weber, J. Krisch, H. Bialas and H.J. Stolz, in Progress Report of the Teilinstitut Nukleare Festkörperphysik, Ges. f. Kernforschung Karlsruhe,(KFK 2054), p. 97 (1974).

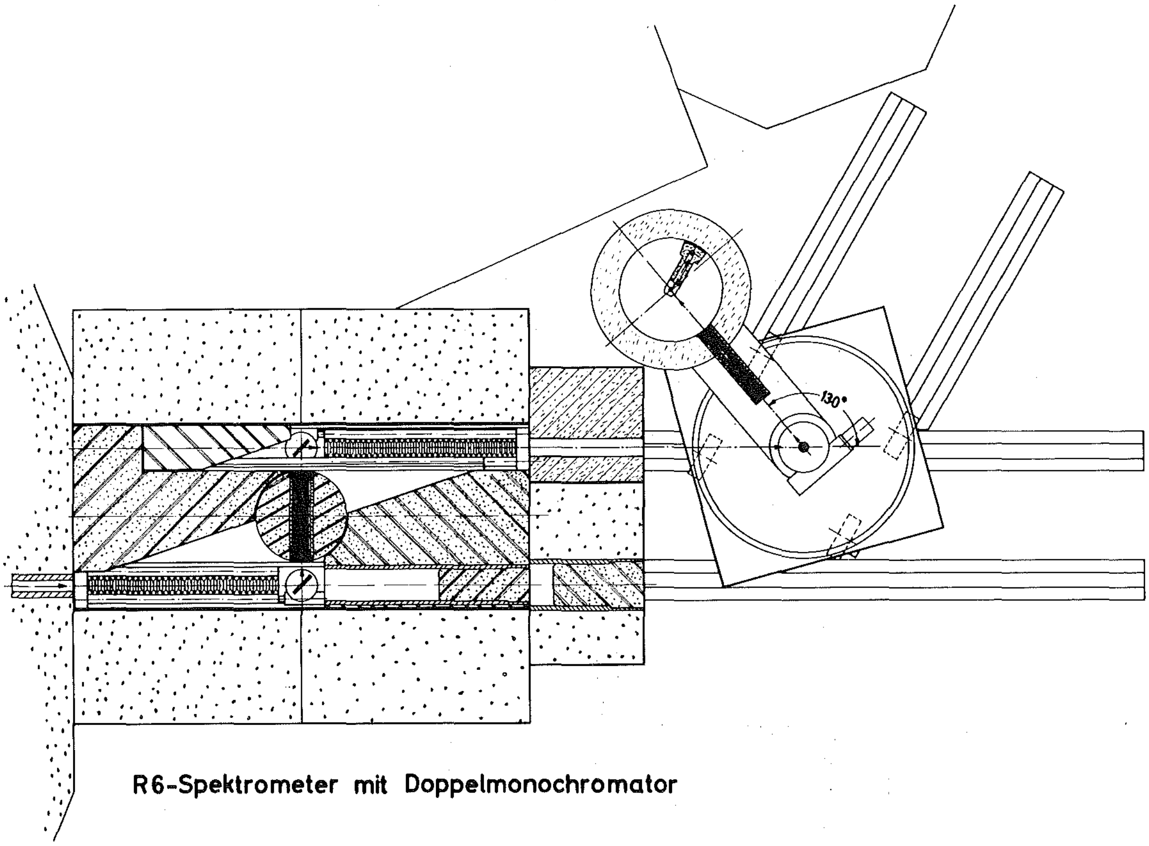

**R6-Spektrometer mit Doppelmonochromator**

Fig. 2

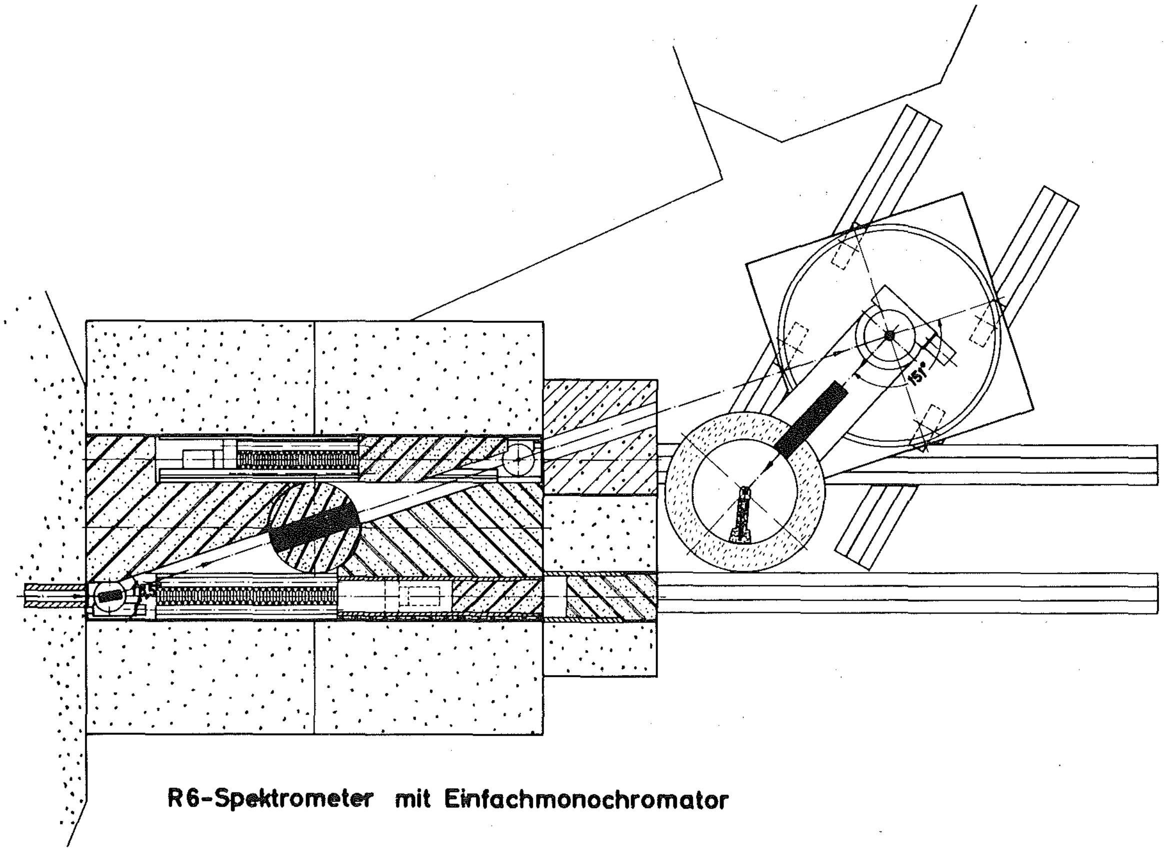

**R6-Spektrometer mit Einfachmonochromator**

Fig. 3

## 5.3. Interferometer for Absolute Velocity Calibration of Mößbauer Spectrometers

*H. Schmidt, J. Fink and G. Czjzek*

The application of interferometric methods for the calibration of constant acceleration Mößbauer spectrometers has been described by several authors /1-5/. These methods allow an absolute calibration of the velocity with high accuracy. The interferometer, Fig. 1, consist, in essential, of a He-Ne laser S, a beam splitter Sp, two mirrors $M_1$, $M_2$, one of which is mounted on the Mößbauer drive, and a photodiode as detector D. High accuracy, however, can only be obtained if the system contains a sufficient amount of noise. This has been pointed out in detail by Cranshaw /5/. The problem of noise has become most important since Mößbauer transducers with extremely low noise are available.

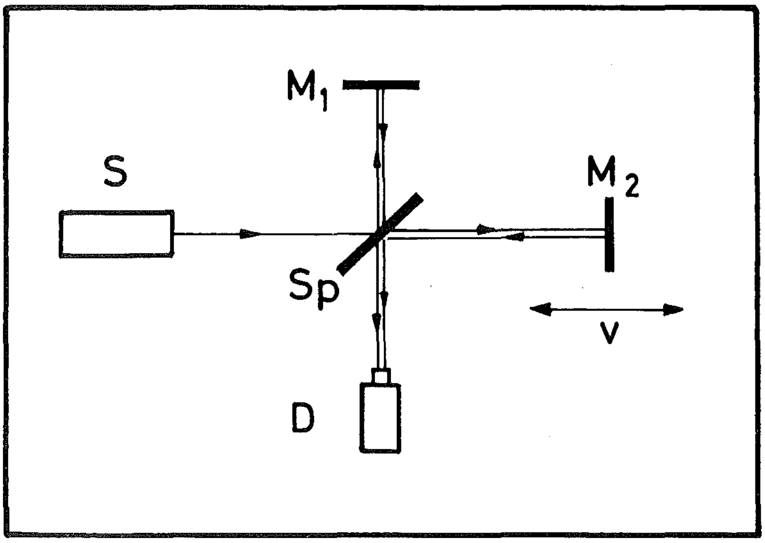

Fig. 1 Schematic diagram of the interferometer used for velocity calibration. S = He-Ne laser; Sp = beam splitter; $M_1$, $M_2$ = mirrors; D = detector. Precautions to avoid multiple reflextions from the exit mirror of the laser are omitted.

In some applications, e.g. Mößbauer spectroscopy with short lived nuclei, it is imperative to set up and adjust the interferometer within a very short time.

We have built up an interferometer which can cope with both problems. A rapid adjustment is accomplished by the use of corner cube prisms instead of the plane mirrors $M_1$, $M_2$. Thus it is possible to mount and adjust the interferometer within a few minutes.

In order to overcome the second problem a certain amount of noise is introduced into the interferometersystem by mounting one of the corner cube prisms (which is usually fixed) on a small loud speaker driven by a simple noise generator.

In Fig. 2, typical plots of the velocity function of a high quality Mößbauer transducer obtained with the interferometer operated in conjunction with a multichannel analyzer are shown. The transducer has been built at this Institute. Its non-linearity is < $5.10^{-4}$ and its noise is extremely low. In the upper three spectra, Fig. 2a, 2b, 2c, which are taken with the noise generator switched off at velocities of 1.8, 3.6, and 7.2 mm $\sec^{-1}$, respectively, the result of insufficient noise is clearly demonstrated. The patterns are persistent for periods of 10 to 30 minutes, depending on the conditions under which the transducer is operated. After introduction of a certain amount of noise by means of the noise generator the "interference patterns" completely disappear. This is shown in Fig. 2d. The velocity in this casewas 1.8 mm $\sec^{-1}$.

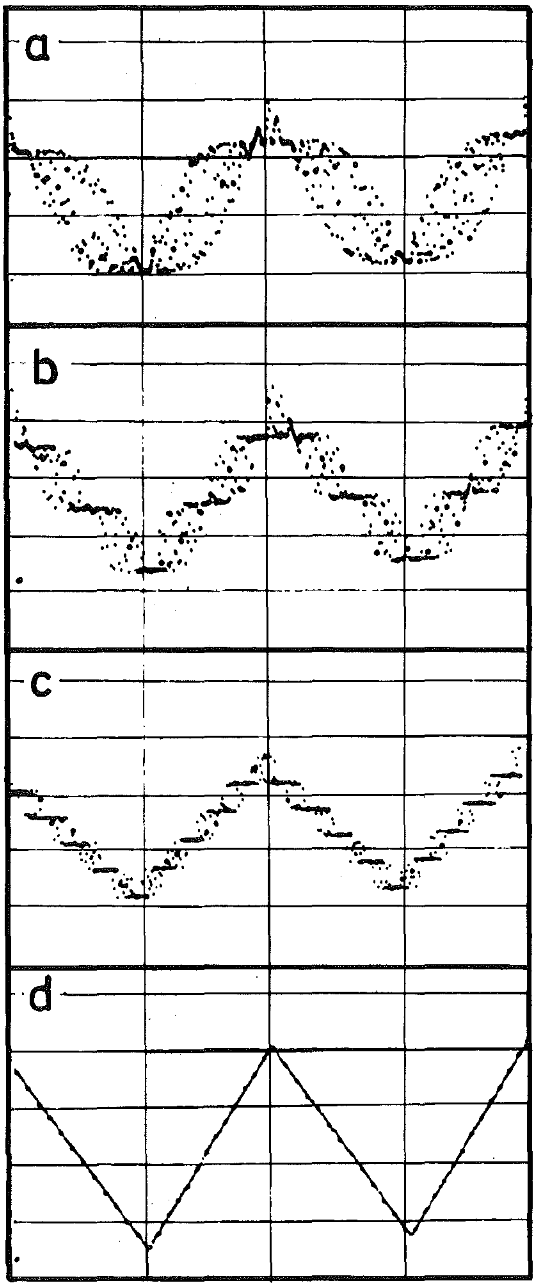

Fig. 2 Typical plots of the velocity function of a Mößbauer transducer as shown on the oscilloscope of a MCA. Figs. 2a, b,c = insufficient noise; Fig. 2d = noise introduced by a noise generator. Velocities in Fig. 2a, b, c, d are 1.8, 3.6, 7.2, 1.8 mm $\sec^{-1}$, respectively.

## References

/1/ H. de Waard, Rev.Sci. Instrum. 36, 1728 (1965).

/2/ R. Fritz and D. Schulze, Nucl. Instrum. Meth. 62, 317 (1968).

/3/ J.P. Biscar, W. Kündig, H. Bommet and R.S. Hargrove Nucl. Instrum.Meth. 75, 165 (1969).

/4/ J.G. Cosgrove and R.L. Collins, Nucl. Instrum. Meth.,95,269 (1971).

/5/ T.E. Cranshaw, J. Phys. E.6, 1053 (1973).

## 5.4. The NOVA2 Computer as a Multiscaler

*G. Ehret and H. Hanak*

In order to replace older timer-counter and multiscaler units or to upgrade them with computers a flexible unit with 16 scalers has been built on one NOVA Card. Some reasons to develop such a new scaler unit are:

1. The computer program has immediate access to the data because the computer memory is used to store the scalers.
2. Large and variable memory areas for multiscalers are assigned by software.
3. Specifications of an extended Mössbauer multiscaler-time setup can be met by a modified microprogram in the NOVA2 CPU /1/ rather than by additional hardware.
4. No special housing including power supply in necessary for a card.
5. Standard computer bus connection is used.

The scaler setup was designed for highest flexiblity which is possible in order to meet most of the demands of a computerized scaler-timer-system.

We placed 16 scalers with 16 bit length on the card. Each scaler can work independent gated by program or by external signals. Any contiguous array within the 16 scalers can be read-out via DMA using the add-to-memory mode of the modified CPU micro program. Read-out and re-set of "array" scalers does not affect the behaviour of "non-array" scalers. Each scaler uses 16 or 32 bit in the computer memory .

An array may be read either only once (single sweep) or in a cyclic manner, triggered either by an internal oscillator, or by program or by an external signal. In the cyclic read-out mode memory addressing is done either cyclic or contiguous, the latter is known as multiscaler mode. Special hardware has been added to avoid loss of counts during the read-out sequence. This feature is necessary in Mössbauer spectroscopy.

All these different modes are under program control. An extended software driver system has been written /2/, which supports the BASIC interpreter system.

### REFERENCES

/1/ G. Ehret, and H. Hanak, in Progress Report of the Teilinstitut Nulkeare Festkörperphysik, Ges. f. Kernforschung Karlsruhe (KFK 2183), p. 100 (1975).
/2/ G. Ehret and B. Volk, Program description (unpublished).

# 6. PUBLICATIONS, CONFERENCE CONTRIBUTIONS AND SEMINARS

## 6.1 PUBLICATIONS

*Czjzek, G.;. Fink, J.; Schmidt, H.; Krill, G.; Lapierre, M.F.; Panissod, P.; Gautier, F.; Robert, C.*
An Investigation of Magnetic Structures and Phase Transitions in $NiS_{2-x}Se_x$ by $^{61}$Ni-Mössbauer Spectroscopy
Journal of Magnetism and Magnetic Materials 3, 58-60 (1976)

*Geerk, J.*
Tunneluntersuchungen an supraleitenden Hartstoffen
KFK-Nachrichten, 7, No. 4, S. 7-11 (1975)

*Geserich, H.-P.; Pintschovius, L.*
Polymeric Sulfur Nitride, $(SN)_x$ - A New Type of a One-Dimensional Metal?
Festkörperprobleme XVI (1976), p. 65
Friedr. Vieweg + Sohn GmbH, P.O.B. 5829, D-6200 Wiesbaden, Germany (West)

*Heger, G.; Mullen, D.; Knorr, K.*
On the Importance of Hydrogen Bonding for the Structural Phase Transitions in $(CH_3NH_3)_2MnCl_4$. A Single Crystal Neutron Diffraction Study
phys. stat. sol. (a) 35, 627 (1976)

*Heger, G.; Mullen, D.;. Knorr, K.*
On the Second-Order Phase Transition in $(CH_3NH_3)_2MnCl_4$
A Single-Crystal Neutron Diffraction Study at 404 and 293 K
phys. stat. sol. (a) 31, 455 (1975)

*Heger, G.; Mullen, D.;. Reinen, D.*
Planar Dynamic Jahn-Teller Effects in Nitrocomplexes: A Single Crystal Neutron Diffraction Study of $Cs_2PbCu(NO_2)_6$ at 293 K
Solid State Commun., 17, pp. 1249-1252,(1975)

*Heger, G.; Renker, B.; Deiseroth, H.J.; Schulz, H.*
A Second Br-Site or a Third Water Position in the Crystal Structure of $K_2(Pt(CN)_4)Br_{0.3} \cdot 3\ H_2O$(KCP)?
Solid State Commun., 18, pp. 517-519 (1976)

*Krill, G.; Lapierre, M.F.; Gautier, F.; Robert, C.;*
*Czjzek, G.; Fink, J.; Schmidt, H.*
Electronic and Magnetic Properties of the Pyrite-Structure Compound $NiS_2$: Influence of Vacancies and Copper Impurities.
Journal of Physics C, 9, 761-782 (1976)

*Lehner, N.; Strobel, K.; Geick, R.; Heger, G.*
Lattice Dynamics in Perovskite-Type Layer Structures:
FIR Studies of $(CH_3NH_3)_2MnCl_4$ and $(CH_3NH_3)_2FeCl_4$
J. Phys. C: Solid State Phys. Vol. 8, 4096(1975)

*Linker, G., Käppeler, F.; Meyer, O.*
International Tagung 'Anwendung von Ionenstrahlen zur Materialanalyse'
KFK-Nachrichten, 7, No. 4, 23 (1975)

*Meyer, O.*
Ion Implantation in Superconductors
Ziegler, J.F. (Hrsg.): New Uses of Ion
Accelerators. New York (usw.): Plenum Press
p. 323-353 (1975)

*Möller, W.; Pintschovius, L.; Geserich, H.P.*
Optical Properties of Orientated $(SN)_x$-Films in the Visible and Near Infrared Region
Solid State Commun. 18, 791-794 (1976)

*Reichardt, W.; Wagner, V.; Kress, W.*
Lattice Dynamics of NiO
J. Phys. C. Solid State Phys. 8, 3955 (1975)

*Scheerer, B.; Fink, J.; Reichardt, W.*
Herstellung von TiC-Einkristallen
KFK-2139 (July 1975)

*Suck, J.-B.*
Streugesetze des polykristallinen und des flüssigen Rubidiums
Dissertation, Universität Karlsruhe 1975
KFK-2231 (Dezember 1975)

## 6.2 CONFERENCE CONTRIBUTIONS AND SEMINARS

*Abel, W.; Block, R.; Schommers, W.*
Bestimmung von Paarpotentialen mit Hilfe einer erweiterten Born-Green-Gleichung
Verhandlungen der DPG 6, 11, 680 (1976)

*Ahsbahs, H.; Denicke, K.; Heger, G.; Hellner, E.; Helmbolt, R.; Mullen, D.; Reinen, D.*
Cooperative Jahn-Teller Distortions in Nitrocomplexes $A_2PbCu(NO_2)_6$. (A = K, Rb, Cs, Tl)
10. International Congress of Crystallography,
Amsterdam, August 7 - 15, 1975
Acta Crystallographica, A, 31 Part S3, 190 (1975)

*Blanckenhagen, P. von; Hoenig, H.E.*
Magnetische Ordnung im verdünnten Van Vleck Antiferromagneten $La_{1-y}Tb_ySn_3$
Verhandlungen der DPG 6, 11, 720 (1976)

*Crecelius, G.;. Maletta, H.; Hauck, J.; Fink, J.; Czjzek, G.; Schmidt, H.*
Einfluß der Kristallstruktur und der Substitutionspartner auf die magnetischen Wechselwirkungen in intermetallischen Verdünnungsreihen
Verhandlungen der DPG, Magetismus, 6, 11, 289 (1976)

*Crecelius, G.; Maletta, H.; Hauck, J.; Fink, J.; Czjzek, G.; Schmidt, H.; Morariu, M.*
Elektronische Struktur und Hyperfeinwechselwirkungen in der Mischreihe $Dy(Fe_xNi_{1-x})_3$
Verhandlungen der DPG 6, 11, 625 (1976)

*Czjzek, G.; Fink, J.; Schmidt, H.; Blanckenhagen, P. von; Krill, G.; Lapierre, M.F.; Robert, C.; Panissod, P.; Gautier, F.*
Untersuchungen von magnetischen Strukturen und Phasenübergängen in $NiS_{2-x}Se_x$ durch Mössbauerspektroskopie an $^{61}Ni$ und Neutronenbeugung
Verhandlungen der DPG 6, 11, 533 (1976)

*Czjzek, G.; Fink, J.; Schmidt, H.; Gautier, F.; Krill, G.; Lapierre, M.F.; Panissod, P.; Robert, C.*
An Investigation of Magnetic Structures and Phase Transitions in $NiS_{2-x}Se_x$ by $^{61}$Ni-Mössbauer Spectroscopy
6. International Conference on Mössbauer Spectroscopy, Cracow/Poland, August 25-30, 1975

*Dachs, H.; Heger, G.; Steiner, M.*
Neutronenstreuexperimente an niederdimensionalen Magneten vom Institut für Kristallographie, Tübingen
Verhandlungen der DPG 6,10, 920 - 921 (1975)

*Dietrich, M.; Reichardt, W.; Rietschel, H.*
Phononenzustandsdichten der Thoriumhydride
Verhandlungen der DPG 6, 11, 739 (1976)

*Ehret, G.; Karbstein, W.; Kneis, W.*
Basic Soubroutines for CAMAC on NOVA2 Computers
2. Internat. Symposium über CAMAC für Datenverarbeitungsanwendungen, Brüssel, 14.-16. Oktober 1975

*Fink, J.; Czjzek, G.; Schmidt, H.*
Magnetic Hyperfine Interactions of $^{61}$Ni in NiMn Alloys
6. Internat. Conference on Mössbauer Spectroscopy, Cracow/Poland, August 25-30, 1975

*Fink, J.; Czjzek, G.; Schmidt, H.; Krill, G.; Lapierre, M.F.; Gautier, F.; Robert, C.*
An Investigation of $NiS_2$ by $^{61}$Ni-Mössbauer Spectroscopy: Influences of Vacancies and Copper Impurities
Discussion Meeting on Magnetic Semiconductors, Jülich, September 29 - October 1, 1975

*Geerk, J.; Gläser, W.; Gompf, F.; Reichardt, W.; Schneider, E.*
Comparison of the Eliashberg Function $\alpha^2(\omega)F(\omega)$ and the Phonon Density of States $F(\omega)$ of Niobium Carbide
Low Temperature Physics. Proc. of the 14. Internat. Conf. Otaniemi, Finland, August 14 - 20, 1975. Ed. by M. Krusius and M. Vuorio. Vol. 2: Superconductivity. Amsterdam (u.s.w.): North-Holland Publ. Co.; New York: American Elsevier Publ. Co. 411-414 (1975)

*Geerk, J.; Langguth, K.-G.*
Sprungtemperatur von $NbC_{89}$-Einkristallen nach Implantation von Kohlenstoffionen
Verhandlungen der DPG 6, 11, 714 (1976)

*Geserich, H.P.; Pintschovius, L.*
Polymeres Schwefelnitrid - ein neuer Typ eines "eindimensionalen Metalls"
Verhandlungen der DPG 6, 11, 519 (1976)

*Gompf, F.; Pintschovius, L.; Reichardt, W.; Scheerer, B.*
Investigations on the Lattice Dynamics of the Carbides and Nitrides of Niobium and Titanium
Conference on Neutron Scattering, Gatlinburg, June 6-10, 1976

*Gompf, F.; Reichardt, W.*
Vergleich der Phononenzustandsdichten von NbN und NbC
Verhandlungen der DPG, 6,11, 738 (1976)

*Heger, G.*
Wasserstoff-Bindungen und strukturelle Phasenübergänge in $(CH_3NH_3)_2MnCl_4$
Internat. Informal Meeting on Halide Perovskite Layer Structures, ETH/Universität Zürich, April 23-24, 1976

*Heger, G.; Mullen, D.*
Über die strukturellen Modifikationen von perowskitähnlichen Schichtstrukturen
Verhandlungen der DPG 6, 11, 449 - 450 (1976)

*Heger, G.; Mullen, D.*
Hydrogen Bonding and Structural Phase Transitions in $(CH_3NH_3)_2MnCl_4$
Conference on Neutron Scattering, Gatlinburg, June 5-10, 1976

*Heger, G.; Mullen, D.; Knorr, K.*
Structural Modifications of $(CH_3NH_3)_2MnCl_4$:
A Single Crystal Neutron Diffraction Study
10. Internat. Congress of Crystallography, Amsterdam, August 7-15, 1975, Acta Crystallographica A, 31, Part S3, 189 (1975)

*Hellner, E.; Mullen,D; Treutmann, W.; Heger, G.; Mateika, D.*
Zur Züchtung von Mischkristallen im System $Cr_{1+\delta}Sb$-$Fe_{1+\delta}Sb$
Kristallzuchttagung, Jülich, September 16-19, 1975

*Hellner, E.; Heger, G.; Mullen, D.; Treutmann, W.*
Combined X-Ray and Neutron Diffraction Studies of the Intermetallic System $(Cr_{1-x}Fe_x)_{1+\delta}Sb$
Conference on Neutron Scattering, Gatlinburg, June 6-10, 1976

*Hellner, E.; Heger, G.; Mullen, D.; Treutmann, W.*
On the Crystal Structures of the Intermetallic System $Cr_{1+\delta}Sb$-$Fe_{1+\delta}Sb$: A Combined Single Crystal X-Ray and Neutron Diffraction Study
10. Internat. Congress of Crystallography, Amsterdam, August 7-15 (1975)
Materials Research Bulletin, 10, 91-94 (1975)

*Hofmann, B.*
Lokalisierte Schwingungen in $Bi_{1-x}Sb_x$ Einkristallen
Verhandlungen der DPG 6, 11, 487 (1976)

*Langguth, K.-G.; Geerk, J.; Linker, G.; Meyer, O.*
Determination of Implanted Crabon Profiles in NbC Single Crystals from Random Backscattering Spectra
Internat. Conference on Ion Beam Surface Layer Analysis, Karlsruhe, September 15-19, 1975

*Langguth, K.-G.; Meyer, O.*
Herstellung von supraleitendem Vanadiumkarbid durch Ionenimplantation und Kathodenzerstäubung
Verhandlungen der DPG 6, 11,715 (1976)

*Lehner, N.*
Neue Ergebnisse an der perowskitähnlichen Schichtstrukturen $(CH_3NH_3)_2MnCl_4$ und $(C_2H_5NH_3)MnCl_4$
Internat. Informal Meeting on Halide Perovskite Layer Structures, ETH/Universität Zürich, April 23 -24, 1976

*Lehner, N.; Geick, R.; Heger, G.*
Neue Ergebnisse an den perowskitähnlichen Schichtstrukturen $(CH_3NH_3)_2MnCl_4$ und $(C_2H_5NH_3)_2MnCl_4$
Verhandlungen der DPG 6, 11, 450 (1976)

*Linker, G.; Meyer, O.*
Stickstoff-Implantation in Molybdän - Supraleitende Eigenschaften und Phasenumwandlungen
Verhandlungen der DPG 6, 11, 715 (1976)

*Linker, G.; Meyer, O.*
Nitrogen Implantation into Molybdenum: Superconducting Properties and Compound Formation
Internat. Conference on the Application of Ion Beams to Materials, Coventry, September 8-12, 1975

*Maletta, H.; Crecelius, G.; Hauck, J.; Fink, J.; Czjzek, G.; Schmidt, H.*
Magnetische Wechselwirkungen in der intermetallischen Mischreihe $Dy(Fe_xNi_{1-x})_2$
Verhandlungen der DPG 6, 11,625 (1976)

*Meyer, O.*
Herstellung und Untersuchung aufgestäubter supraleitender Schichten
Fort- und Weiterbildungszentrum Technische Akademie Esslingen, 4. Februar 1976

*Meyer, O.*
Enhancement of the Superconducting Transition Temperature by Ion Implantation in Molybdenum Thin Films
Internat. Conference on the Applications of Ion Beams to Materials, Coventry, September 8-12, 1975

*Nösselt, J.; Heger, G.*
Untersuchung des Spinflop-Überganges und des trikritischen Punktes im 2-dimensionalen Antiferromagneten $(C_2H_5NH_3)_2MnCl_4$
Verhandlungen der DPG, 6, 11,304, (1976)

*Nücker, N.*
Phononenzustandsdichte von Lanthan
Verhandlungen der DPG 6, 11,740 (1976)

*Parisot, G.I.; Coey, J.M.D.; Brusetti, R.; Gompf, F.;*
*Czjzek, G.; Fink, J.*
Electron-Phonon Coupling and the Loss of Magnetism in NiS
21. Annual Conference on Magnetism and Magnetic Materials,
Philadelphia, December 9-12, 1975

*Pintschovius, L.; Renker, B.; Comès, R.*
Investigation of the Dynamical Structure Factor of
$K_2Pt(CN)_4Br_3 \cdot 3.2D_2O$ KCP
Conference on Neutron Scattering, Gatlinburg, June 6-10, 1976

*Pintschovius, L.; Reichardt, W.; Scheerer, B.*
Vergleich der Phononendispersion von Vanadiumkarbid,
Titankarbid und Niobkarbid
Verhandlungen der DPG 6, 11, 738 (1976)

*Pintschovius, L.; Wendel, H.*
Akustische Phononen des eindimensionalen Metalls
Polyschwefelnitrid $(SN)_x$
Verhandlungen der DPG 6, 11, 761 (1976)

*Reichardt, W.; Rieder, K.H.*
Phononendispersion von $\alpha$-Arsen
Verhandlungen der DPG 6, 11, 451 (1976)

*Reichardt, W.; Rieder, K.H.*
Lattice Dynamics of $\alpha$-Arsenic
Conference on Neutron Scattering, Gatlinburg, June 6-10, 1976

*Renker, B.; Pintschovius, L.; Comès, R.*
Untersuchungen des dynamischen Strukturfaktors von
$K_2Pt(CN)_4Br(0.3) \cdot 3\ D_2O$
Verhandlungen der DPG 6, 11, 760 (1976)

*Renker, B.; Pintschovius, L.; Comès, R.*
Inelastic Neutron Scattering Study of the $2K_F$ Instability
in $K_2Pt(CN)_4Br_3 \cdot 3D_2O$ (KCP)
Internat. Conference on Low Lying Lattice Vibrational Modes
and their Relationship to Superconductivity and Ferroelectricity,
San Juan, Puerto Rico, December 1-4, 1975

*Renker, B.; Schweiss, P.; Fischer, O.*
Untersuchungen der Phononenzustandsdichte des Hochfeldsupraleiters
Bleimolybdänsulfid
Verhandlungen der DPG 6, 11, 738-739 (1976)

*Ruebenbauer, K.; Czjzek, G.; Fink, J.; Schmidt,H.*
Mössbauerspektroskopie mit $^{155}$Gd in $Gd_xCe_{1-x}Ru_2$ zur
Frage der Koexistenz von Supraleitung und Magnetismus
Verhandlungen der DPG 6, <u>11</u>, 719-720 (1976)

*Scheerer, B.*
Herstellung von Karbid-Einkristallen, am Beispiel von TiC, NbC
und VC
Kristallzuchttagung, Jülich 16.-19. September 1975

*Scheerer, B.*
Methoden zur Herstellung von Einkristallen.
(Schmelzverfahren; Karbide und Nitride).
Neutronenbeugungs-Seminar, Institut für Kernphysik,
Universität Frankfurt, 13. Mai 1976

*Schneider, E.*
Temperaturabhängigkeit der Phononenzustandsdichten von $Nb_3Al$
Verhandlungen der DPG 6, <u>11</u>, 740 (1976)

*Schneider, E.; Schweiss, P.; Reichardt, W.*
Temperature Dependence of the Phonon Densities of States
of some A-15 Compounds
Conference on Neutron Scattering, Gatlinburg, June 6-10, 1976

*Schweiss, P.; Schneider, E.; Renker, B.; Reichardt, W.*
Phonon Spectra of A-15 Compounds and Ternary Molybdenum
Chalcogenides
2. Conference on Superconductivity in d- and f-Band Metals,
Rochester, April 30 - May 1, 1976

*Stolz, H.-J.; Otto, A.; Pintschovius, L.*
On the Interaction between Chains in $(SN)_x$
Proc. III Int. Conf. Light Scatt. Solids,
July 1975, Campinas (Brazil), ed. M. Balkanski
R.C.C. Leite, S.P.S. Porto, Flammarion Science, Paris 1976

*Wagner, V.; Reichardt, W.; Kress, W.*
Gitterschwingungen in MnO
Verhandlungen der DPG 6, <u>11</u>, 453 (1976)

*Wagner, W.; Reichardt, W.; Kress, W.*
Lattice Dynamics of MnO
Conference on Neutron Scattering, Gatlinburg, June 6-10,1976

# 7. LIST OF THE NEUTRON SPECTROMETERS AT THE FR2 AT KARLSRUHE

DIF 1 : Four circle diffractometer, $\lambda = 1.035$ Å

DIF 2 : Two circle diffractometer, 1 Å $\leq \lambda <$ 2.6 Å

DIF 3 : Powder diffractometer, $\lambda = 1.28$ Å or 1.09 Å

DIF 4 : Two circle diffractometer, $\lambda \geq 4$ Å (cold neutrons)

TAS 1 : Three-axis spectrometer, 13 meV $\leq E_o \leq$ 120 meV

TAS 2 : Three-axis spectrometer, 8 meV $\leq E_o <$ 65 meV

TOF 1 : Time of-flight spectrometer with Fermi-Chopper, 100 detectors, thermal neutrons

TOF 2 : Time of-flight spectrometer with rotating crystal, 100 detectors, cold neutrons

TOF 3 : Time of-flight spectrometer with Fermi-Chopper, 10 detectors, thermal neutrons

TOF 4 : Time of-flight spectrometer with rotating crystal. 6 detectors, cold neutrons

MAG 1 : Spectrometer for diffuse scattering, 20 detectors, thermal neutrons

MAG 2 : Multipurpose spectrometer, 20 detectors, cold neutrons.

## 8. STAFF MEMBERS

### Professional Staff

*Blanckenhagen, P. von*
*Czjzek, G.*
*Fink, J.*
*Geerk, J.*
*Gompf, F.*
*Haase, E.L.*
*Heger, G.*
*Linker, G.*
*Meyer, O.*
*Nücker, N.*
*Pintschovius, L.*
*Reichardt, W.*
*Renker, B.*
*Rietschel, H.*
*Schmidt, H.*
*Schommers, W.*
*Schweiß, P.*

### Technical Staff

*Abel, W.*[+]
*Blum, B.*[+]
*Ehret, G.*[+]
*Hanak, H.*[+]
*Kraatz, M.*
*Kuhn, R.*[+]
*Moser, R.*[+]
*Ratzel, F.*
*Richelsen, H.*[+]
*Scheerer, B.*
*Smithey, R.*
*Weber, K.*

### Visiting Scientiests

*Klein, S.; Guest from SFB127, Universität Marburg*
*Lombaard, J.; Guest from Physics Department, University of Pretoria, South Africa*
*Ruebenbauer, K.; Guest from Institute of Physics, Cracow, Poland*
*Tomala, K.; Guest from Institute of Physics, Cracow, Poland*

### Research Students

*Block, R.; Universität Karlsruhe*
*Feld, R.; Universität Marburg*
*Gauß, C.; Universität Karlsruhe*
*Guth, H.; Universität Karlsruhe*
*Hofmann, B.; Universität Karlsruhe*
*Hofmann-Kraeft, B.; Universität Karlsruhe*
*Käfer, K.; Universität Karlsruhe*
*Langguth, K.-G.; Universität Karlsruhe*
*Lehner, N.; Universität Würzburg*
*Ziemann, P.; Universität Karlsruhe*

---

[+] Member of infrastructure